Theoretical investigation of the interaction of ultra-high intensity laser pulses with near critical density plasmas towards the optimization of secondary sources

Iuliana-Mariana Vladisavlevici

THÈSE EN COTUTELLE PRÉSENTÉE

POUR OBTENIR LE GRADE DE

DOCTEUR
DE L'UNIVERSITÉ DE BORDEAUX ET DE L'UNIVERSITÉ D'OUEST DE TIMISOARA

École doctorale: UBX - Sciences Physiques et de l'Ingénieur et UVT - Physique

Spécialité: UBX - Astrophysique, Plasmas, Nucléaire et UVT - Physique

Par Iuliana-Mariana VLADISAVLEVICI

Theoretical investigation of the interaction of ultra-high intensity laser pulses with near critical density plasmas towards the optimization of secondary sources

Direction: Prof. dr. Emmanuel D'HUMIÈRES et Prof. dr. Daniel VIZMAN

Soutenue le 16 décembre 2022

Membres du jury:

Mme. Dana PERCEC	Professeure	UVT (Romania)	Présidente (UVT)
M. João Jorge SANTOS	Professeur	UBX (France)	Président (UBX)
Mme. Michèle RAYNAUD-BRUN	Directrice de recherche	CEA - LSI (France)	Rapporteur
M. Daniel URSESCU	Directeur de recherche	ELI-NP (Romania)	Rapporteur
M. Calin UR	Directeur de recherche	ELI-NP (Romania)	Examinateur
M. Paolo TOMASSINI	Directeur de recherche	ELI-NP (Romania)	Examinateur
M. Emmanuel d'HUMIÈRES	Professeur	UBX (France)	Direction de thèse
M. Daniel VIZMAN	Professor	UVT (Romania)	Direction de thèse
M. Gheorghe ADAM	Directeur de Recherche	IFIN-HH (Romania)	Invité
M. Xavier RIBEYRE	Directeur de Recherche	UBX (France)	Invité

EN

Title: Theoretical investigation of the interaction of ultra-high intensity laser pulses with near critical density plasmas towards the optimization of secondary sources

Summary: The main goal of this thesis is to develop a theoretical model for the transfer of energy from the laser pulse to plasma constituents in the ultra-high intensity laser pulse regime and for near critical density targets with focus on the optimization of the secondary sources. As a first application of our model, we studied the proton acceleration for a laser of intensity 10^{22} W/cm^2 which will be soon available on experiments at laser facilities like Apollon and ELI. Laser driven ion acceleration is important for various applications like hadron therapy, radioisotope production, and ion fast ignition for inertial confinement fusion. As a second application of our model, we investigated the emission of high energy radiation in laser-plasma interaction for a laser intensity up to $5 \cdot 10^{23}$ W/cm^2, towards the creation of electron-positron pairs through the linear Breit-Wheeler process, which is an extremely important phenomenon occurring at astrophysical scales.

Keywords: ultra-high intensity regime, near-critical density targets, laser energy absorption, electron and proton acceleration, high energy photons, electron-positron pair creation

FR

Titre : Étude théorique de l'interaction des impulsions laser à ultra-haute intensité avec des plasmas à densité presque critique vers l'optimisation des sources secondaires

Résumé : L'objectif principal de cette thèse est de développer un modèle théorique pour le transfert d'énergie de l'impulsion laser aux constituants du plasma dans le régime d'impulsion laser à ultra-haute intensité et pour des cibles de densité quasi critique en mettant l'accent sur l'optimisation des sources secondaires. Comme première application de notre modèle, nous avons étudié l'accélération de proton pour un laser d'intensité 10^{22} W/cm^2 qui sera disponible dans des installations laser Apollon et ELI. L'accélération des ions par laser est importante pour les applications comme : la protonthérapie, la production de radio-isotopes, et l'allumage rapide des ions pour la fusion par confinement inertiel. Comme deuxième application de notre modèle,

nous avons étudié l'émission de rayonnement de haute énergie dans l'interaction laser-plasma pour une intensité laser jusqu'à $5 \cdot 10^{23}$ W/cm^2, utilisable pour étudier la création de paires électron-positon par le processus linéaire de Breit-Wheeler, qui est un phénomène extrêmement important se produisant à des échelles astrophysiques.

Mots clés : régime ultra-haute intensité, cibles de densité quasi-critiques, absorption d'énergie laser, accélération des électrons et des protons, photons de haute énergie, création de paires électron-positon

RO

Titlu: Studiul teoretic al interacțiunii unui impuls laser de intensitate ultra-înaltă cu plasme de densitate cvasi-critică spre optimizarea surselor secundare

Rezumat: Obiectivul principal al acestei teze este de a dezvolta un model teoretic pentru transferul de energie de la impulsul laser la constituenții plasmei în regimul de impulsuri laser de intensitate ultra-înaltă și pentru ținte de densitate cvasi-critică, cu accent pe optimizarea surselor secundare. Ca o primă aplicație a modelului nostru, am studiat accelerația protonilor pentru un laser de intensitate 10^{22} W/cm^2 care va fi disponibil în instalațiile laser Apollon și ELI. Accelerarea ionilor cu laser este importantă pentru aplicații precum: terapia cu protoni, producerea de radioizotopi și aprinderea rapidă a ionilor pentru fuziunea inerțială. Ca o a doua aplicație a modelului nostru, am studiat emisia de radiații de înaltă energie în interacțiunea laser-plasmă pentru intensitatea laser de până la $5 \cdot 10^{23}$ W/cm^2, utilizabile pentru a studia crearea de perechi electron-pozitron prin procesul liniar Breit-Wheeler, care este un fenomen extrem de important ce are loc la scala astrofizică.

Cuvinte cheie: regim de intensitate ultra-înaltă, ținte cu densitate cvasi-critică, absorbție de energie laser, accelerare a electronilor și protonilor, fotoni de înaltă energie, crearea de perechi electron-pozitron

Abstract

EN

At the interaction of an ultra-high intensity laser pulse with a plasma, the plasma constituents will absorb a significant part of the laser energy and will be accelerated up to relativistic velocities for electrons. The most predominant mechanisms of energy transfer from the laser pulse to the plasma constituents are collisionless in this regime, being done by collective effects in plasma. There are various collisionless mechanisms of laser energy absorption, each being dependent on the laser or target parameters.

In this thesis we analyse the case of an ultra-high intensity, ultra-short laser pulse interacting with a near critical density target. Our main goal is to describe and model the energy transfer from laser to particles, from the transparent to less transparent regime of laser-plasma interaction in the ultra-high intensity regime, and using the results obtained to optimize the characteristics of the secondary sources.

We propose a theoretical model for maximizing the energy conversion from the laser pulse to the plasma constituents, assuming that the transfer is made via hot electrons. Considering a Gaussian spatial and temporal profile for the laser pulse and a fully ionized target made of electrons and protons, we developed a model which includes the variation of all laser and target parameters in the ultra-short high laser intensity regime for near critical density targets. The theoretical model is tested and corrected through the observations made from 2D Particle-in-cell simulations performed with SMILEI for a wide range of parameters: the target density varies in $0.5-24$ $\mathrm{n_c}$ (where $n_c = 1.1 \cdot 10^{21}$ cm^{-3} for a laser of 1 μm wavelength), the laser peak intensity in $10^{20}-10^{23}$ $\mathrm{W/cm^2}$ (for a laser pulse duration of 20 fs) and laser pulse duration in

$6.5 - 100$ fs (for a laser intensity of 10^{22} W/cm^2). This model could be used to optimize all processes that rely on the energy stored in the electrons.

The laser absorption mechanisms determine the characteristics of the accelerated particles. As a first application of our model, we studied the proton acceleration for a laser intensity of 10^{22} W/cm^2 and a pulse duration of 20 fs. Based on the state-of-the-art literature and the new findings from our model, we predict the optimum thickness for proton acceleration and the maximum proton energies for an expansion like mechanism. Laser driven proton acceleration is important for various applications like hadron therapy, radioisotope production, fast ignition for inertial confinement fusion. These results can be used for applications requiring high energy ions and for preparations of experiments at the Apollon and ELI laser facilities.

As a second application of our model, we investigated the emission of high energy radiation in laser-plasma interaction for a laser intensity varying from 10^{22} W/cm^2 to $5 \cdot 10^{23}$ W/cm^2. Using our absorption model, we focused on optimization of the emission of high energy radiation in the forward direction which was further used for the creation of electron-positron pairs. There are multiple processes to create electron-positron pairs in the laboratory from the interaction of the high energy photons - with the laser electromagnetic field (the nonlinear Breit-Wheeler process), with the Coulomb field of the target (the Bethe-Heitler process) and with another high energy photon (the linear Breit-Wheeler process). We studied the total number of pairs produced by each of these processes in laser-plasma interaction with the focus on the optimization of the linear Breit-Wheeler process. This is an extremely important process occurring in the astrophysical scales which can be used to measure the magnitude of the intergalactic infrared radiation field. Compared to the other pair production processes mentioned, the linear Breit-Wheeler process was not yet proved experimentally in the laboratory. Our results discuss the suitability of the detection the linear Breit-Wheeler pairs in experiments at Apollon and ELI laser facilities.

FR

Lors de l'interaction d'une impulsion laser d'ultra-haute intensité avec un plasma, les constituants du plasma absorberont une partie importante de l'énergie laser et seront accélérés jusqu'à des vitesses relativistes pour les électrons. Les mécanismes les plus prédominants de transfert d'énergie de l'impulsion laser aux constituants du plasma sont sans collision dans ce régime, étant effectués par des effets collectifs dans le plasma. Il existe divers mécanismes d'absorption d'énergie laser sans collision, chacun dépendant du paramètre laser ou cible.

Dans cette thèse, nous analysons le cas d'une impulsion laser ultra-haute intensité et ultra-courte interagissant avec une cible de densité quasi critique. Notre objectif principal est de décrire et de modéliser le transfert d'énergie du laser aux particules, du régime transparent au régime moins transparent de l'interaction laser-plasma dans le régime des ultra-haute intensités, et d'utiliser les résultats obtenus pour optimiser les caractéristiques des sources secondaires.

Nous proposons un modèle théorique pour maximiser la conversion d'énergie de l'impulsion laser aux constituants du plasma, en supposant que le transfert se fait via des électrons chauds. En considérant un profil spatial et temporel gaussien pour l'impulsion laser et une cible entièrement ionisée composée d'électrons et de protons, nous avons développé un modèle qui inclut la variation de tous les paramètres du laser et de la cible dans le régime d'impulsions laser ultra-courtes et à ultra haute intensité pour des cibles de densité quasi critique. Le modèle théorique est testé et corrigé grâce aux observations faites à partir de simulations 2D Particle-in-cell réalisées avec SMILEI pour une large gamme de paramètres : la densité cible varie de $0,5-24$ $\mathrm{n_c}$ (où $n_c = 1,1 \cdot 10^{21}$ cm^{-3} pour un laser de longueur d'onde 1 μm), l'intensité du pic laser de $10^{20}-10^{23}$ $\mathrm{W/cm^2}$ (pour la durée d'impulsion laser de 20 fs) et la durée d'impulsion laser en $6,5-100$ fs (pour l'intensité du pic laser de 10^{22} $\mathrm{W/cm^2}$). Ce modèle pourrait être utilisé pour optimiser tous les processus qui dépendent de l'énergie stockée dans les électrons.

Les mécanismes d'absorption laser déterminent les caractéristiques des particules accélérées. Comme première application de notre modèle, nous avons étudié l'accélération de protons pour une intensité laser de 10^{22} $\mathrm{W/cm^2}$ et une durée d'impulsion de 20 fs. Sur la base de l'état de l'art et des nouvelles découvertes de notre modèle, nous prédisons l'épaisseur optimale pour l'accélération des protons et les énergies maximales des protons pour un mécanisme de type expansion. L'accélération des protons par laser est importante pour diverses applications

telles que la protonthérapie, la production de radio-isotopes, et l'allumage rapide pour la fusion par confinement inertiel. Ces résultats peuvent être utilisés pour des applications nécessitant des ions de haute énergie et pour la préparation d'expériences sur les installations laser Apollon et ELI.

Comme deuxième application de notre modèle, nous avons étudié l'émission de rayonnement de haute énergie dans l'interaction laser-plasma pour une intensité laser variant de 10^{22} W/cm^2 – $5 \cdot 10^{23}$ W/cm^2. En utilisant notre modèle d'absorption, nous nous sommes concentrés sur l'optimisation de l'émission de rayonnement de haute énergie collimaté qui a ensuite été utilisée pour la création de paires électron-positon. Il existe plusieurs processus pour créer des paires électron-positon en laboratoire à partir de l'interaction des photons de haute énergie - avec le champ électromagnétique laser (le processus non linéaire de Breit-Wheeler), avec le champ coulombien de la cible (le processus Bethe-Heitler) et avec un autre photon de haute énergie (le processus linéaire de Breit-Wheeler). Nous avons étudié le nombre total de paires produites par chacun de ces processus dans le contexte de l'interaction laser-plasma en mettant l'accent sur l'optimisation du processus linéaire de Breit-Wheeler. Il s'agit d'un processus extrêmement important qui se produit à l'échelle astrophysique et qui peut être utilisé pour mesurer l'ampleur du champ de rayonnement infrarouge intergalactique. Comparé aux autres procédés de production de paires mentionnés, le procédé linéaire de Breit-Wheeler n'a pas encore été prouvé expérimentalement en laboratoire. Nos résultats permettent de discuter de la pertinence de la détection des paires Breit-Wheeler linéaires dans les expériences des installations laser Apollon et ELI.

Le résumé détaillé en français se trouve en annexe E.

RO

La interacțiunea unui impuls laser de intensitate ultra-înaltă cu o plasmă, constituenții plasmei vor absorbi o parte semnificativă a energiei laserului și vor fi accelerați până la viteze relativiste pentru electroni. Mecanismele cele mai predominante ale transferului de energie de la pulsul laser la constituenții plasmei sunt fără coliziune în acest regim, fiind realizate prin efecte colective în plasmă. Există diverse mecanisme fără coliziune de absorbție a energiei laser, fiecare fiind dependent de parametrii laserului sau țintei.

În această lucrare de doctorat analizăm cazul unui impuls laser de intensitate ultra-înaltă și durată ultra-scurtă, care interacționează cu o țintă de densitate cvasi-critică. Scopul nostru principal este de a descrie și modela transferul de energie de la laser la particule, de la regimul transparent la cel mai puțin transparent al interacțiunii laser-plasmă în regim de intensitate ultra-înaltă, și folosind rezultatele obținute să optimizăm caracteristicile surselor secundare.

Propunem un model teoretic pentru maximizarea conversiei energiei de la impulsul laser la constituenții plasmei, presupunând că transferul se face prin intermediul electronilor. Considerând un profil spațial și temporal gaussian pentru impulsul laser și o țintă complet ionizată formată din electroni și protoni, am dezvoltat un model care include variația tuturor parametrilor laser și țintă în regimul de intensitate laser mare ultra-scurtă pentru ținte cu densitate cvasi-critică. Modelul teoretic este testat și corectat prin observațiile făcute din simulări 2D Particle-in-cell efectuate cu SMILEI pentru o gamă largă de parametri: densitatea țintei variază în $0.5 - 24$ n_c (unde $n_c = 1.1 \cdot 10^{21}$ cm^{-3} pentru o laser cu lungimea de undă de 1 μm), intensitatea maximă a laserului în $10^{20} - 10^{23}$ W/cm^2 (pentru durata impulsului laser de 20 fs) și durata impulsului laser în $6.5 - 100$ fs (pentru intensitatea maximă a laserului de 10^{22} W/cm^2). Acest model poate fi folosit pentru a optimiza toate procesele care se bazează pe energia stocată în electroni.

Mecanismele de absorbție a energiei laserului determină caracteristicile particulelor accelerate. Ca o primă aplicație a modelului nostru, am studiat accelerația protonilor pentru o intensitate laser de 10^{22} W/cm^2 și o durată a impulsului de 20 fs. Pe baza literaturii de specialitate și a noilor descoperiri din modelul nostru, putem prezice grosimea optimă pentru accelerarea protonilor și energiile maxime ale protonilor pentru un mecanism asemănător expansiunii plasmei. Accelerarea protonilor condusă de laser este importantă pentru diverse aplicații, cum

ar fi terapia cu protoni, producția de radioizotopi, aprinderea rapidă a ionilor pentru fuziunea inerțială. Aceste rezultate pot fi utilizate pentru aplicații care necesită ioni de înaltă energie și pentru pregătirea experimentelor la instalațiile laser Apollon și ELI.

Ca o a doua aplicație a modelului nostru, am investigat emisia de radiații de înaltă energie în interacțiunea laser-plasmă pentru o intensitate laser de 10^{22} W/cm^2 – $5 \cdot 10^{23}$ W/cm^2. Folosind modelul nostru de absorbție, ne-am concentrat pe optimizarea emisiei de radiații de înaltă energie în direcția înainte, care a fost folosită în continuare pentru crearea perechilor electron-pozitron. Există mai multe procese pentru a crea perechi electron-pozitron în laborator din interacțiunea fotonilor de înaltă energie – cu câmpul electromagnetic laser (procesul neliniar Breit-Wheeler), cu câmpul Coulomb al țintei (procesul Bethe-Heitler) și cu un alt foton de înaltă energie (procesul liniar Breit-Wheeler). Am studiat numărul total de perechi produse de fiecare dintre aceste procese în interacțiunea laser-plasmă cu accent pe optimizarea procesului liniar Breit-Wheeler. Acesta este un proces extrem de important care are loc la scala astrofizică și care poate fi folosit pentru a măsura mărimea câmpului de radiație infraroșu intergalactic. În comparație cu celelalte procese de producție de perechi menționate, procesul liniar Breit-Wheeler nu a fost încă dovedit experimental în laborator. Rezultatele noastre discută caracterul adecvat al detectării perechilor electron-pozitron prin procesul liniar Breit-Wheeler în experimente la instalațiile laser Apollon și ELI.

Table of Contents

Introduction

Laser-plasma interaction

A laser is an optical device which allows the Light Amplification by Stimulated Emission of Radiation (LASER). One important property of the emitted radiation is its coherence, meaning that all emitted photons have the same frequency and the same phase which allows its amplification. The first laser in the world was made by Mainman in 1960 [1]. The setup consisted of a high-power flash lamp which irradiated a 1 cm ruby crystal coated on two paralel faces with silver. The chromium ions are excited by the energy of the flash-lamp and by de-excitation they emit sponatneously a doublet at 6929Å and 6943Å wavelengths. By increasing the power of the lamp, the emission at 6943Å was dramatically increasing.

The lasers built in 1960 had a pulse duration of 10 μs and a peak power in the order of kW range [2]. The advances in the peak power came with the reduction of the pulse duration by changing the laser cavity modes. From 1960 to 1964 the lasers achieved the picosecond scale, corresponding to a peak power in the GW range. Despite decreasing further the laser pulse duration, the laser peak power intensity obtained was about 10^{15} W/cm^2 due to the nonlinear optic efects which damaged the properties of the laser. The change came in 1985, when Donna Strickland and Gérard Mourou proposed a novel method to create shorter, more energetic and, consequently more intense laser pulses [3]. They used a Nd YAG short low-energy linearly chirped laser pulse of pulse duration 300 ps. In a first step of the process, the pulse is streched to obtain a longer laser pulse with a smaller peak power. In the second step the streched pulse is amplified and further, in a third step is compressed by a double grating compressor. The authors obtained a 2 ps laser pulse with an energy of a few mJ. The process is represented schematically in Fig.1. This process is called Chirped Pulse Amplification (CPA) and nowadays is used in

laboratories worldwide to create the shortest and the most intense laser pulses. The authors were awarded the Nobel Prize for Physics in 2018 [4].

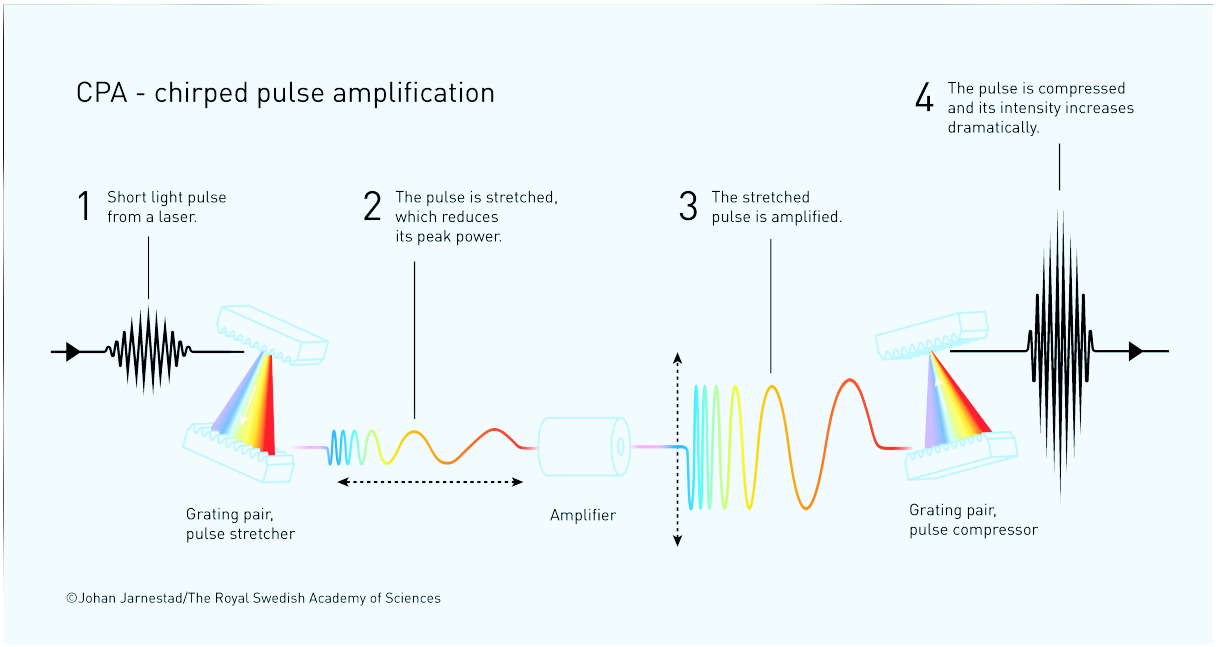

Figure 1: Chirped Pulse Amplification (CPA) scheme. Credit photo: Johan Jarnestad, The Royal Swedish Academy of Sciences

Nowadays the most powerfull lasers in the world are Ti:Sapphire lasers [5]. The most intense laser is CoReLS - PW laser which in 2021 reached a peak intensity of $\sim 10^{23}$ W/cm^2 and a short pulse duration of ~ 19 fs FWHM corresponding to a peak power of 2.7 PW [6]. Multiple lasers around the world in the PW level reached an intensity of 10^{22} W/cm^2 and new projects are aiming at higher power like Apollon (peak power 10 PW; peak intensity $\sim 2 \cdot 10^{22}$ W/cm^2, pulse duration 15 fs FWHM) [7], ELI-NP (peak power $2 \cdot 10$ PW; peak intensity $10^{22} - 10^{23}$ W/cm^2, pulse duration $15 - 22.5$ fs FWHM) [8] and SEL (peak power 100 PW; peak intensity 10^{24} W/cm^2) [9]. The latest experimental results obtained at ELI-NP laser facility this year reported a 10 PW peak power and a pulse duration of 21.7 fs, corresponding to a laser intensity of $10^{22} - 10^{23}$ W/cm^2 [10, 11]. Nowadays, ELI-NP is the most powerfull laser in the world.

At the interaction of a high intensity laser with a target (solid, liquid or gas), a plasma made of electrons and ions is created. Plasma by definition is the fourth state of matter in which the electrons and the ions are freely moving. Over 99% of the visible universe is made of plasmas, from polar lights or Earth ionosphere up to the stars, galaxies or the intergalactic space [12]. In the laboratory a plasma can be created by increasing the temperature of an object up to

its ionization. In the interior of a star, the temperature and the density are so high that the ions start to fusion forming heavier elements and releasing energy. If one could control the nuclear fusion process on Earth, the energy problems of the 21^{st} century would be solved. Very hot plasmas are created nowadays in the laboratory with tokamaks or with lasers. However, further experimental and theoretical studies are needed in order to reach the self-sustained nuclear fusion process and be energy efficient.

As previously mentioned, when a laser irradiates a target, a plasma is created through target heating and ionization. Further the plasma constituents are accelerated, the acceleration depending on the laser and target initial characteristics. For intensities $> 10^{18}$ W/cm^2, the electron motion is relativistic. For example, for a laser intensity of 10^{19} W/cm^2 and a wavelength of 1 μm, the average energy of the most energetic electrons is about 1 MeV. The increase of the laser intensity comes with a change of the interaction regime, opening up new regimes of laser-plasma interaction where relativistic effects are important and can dominate the motion of particles [2].

Further in this thesis the words *target* and *plasma* will be interchangeable as we will always consider our target being initially fully ionized.

Numerical simulations

Numerical simulations are a powerful tool to study real systems and to gain detailed information on the physical phenomena. A short time after the first numerical experiment of a physical system was made in 1955 [13], the first numerical simulation of a plasma was published by Dawson in 1962 [14]. The 1-dimensional simulation setup consisted of 1000 sheets representing charged particles moving into one direction. The goal was to study physical phenomena like thermal relaxation of the system, Debye screening and Landau damping. The computation results obtained showed good agreement with the theory with relatively small errors.

Since then, the computational setup advanced as well as plasma codes. The computer used in 1955 was MANIAC I (Mathematical Analyzer Numerical Integrator and Automatic Computer Model I) which had a processing power of 2048 instructions per second [15]. Nowadays, the most powerful computing machine is the Frontier system from the Oak Ridge National

Laboratory which is made of more than 8.7 million cores and a computation speed of 1.102 Exaflops corresponding to more than 10^{18} instructions per second [16]. This is the first computer to surpass the exascale barrier [17]. The numerical simulations for plasma physics require complex, high performance computing codes to have a complete description of billions of particles and their interactions. Numerical simulations of plasma can be made either kinetic, by solving the Maxwell-Vlasov system of equations, or fluid, by solving the fluid equations of a plasma, depending on the time scales of the processes we want to investigate. As we are interested in the very short timescale of high intensity laser-plasma interaction, in the range of hundreds of fs up to a ps, we will further consider the kinetic approach.

Thesis objectives

The acceleration of particles with a laser pulse is an alternative to conventional radio-frequency accelerators. The huge acceleration gradients in a laser based accelerator are in the order of $\mathrm{MeV}/\mu\mathrm{m}$, compared with the ones in a radio-frequency accelerators of the order of hundreds of MeV/m. Consequently, the particles can be accelerated to very high energies over sub-mm distances, by many orders of magnitude shorter than required in conventional accelerators. This brings the opportunity to study new applications of the accelerated beams. However, issues like the conversion efficiency of the laser energy into the particles, the spectral and angular distribution of the particle beam as well as their energy are still to be resolved [18].

The main goal of this thesis is to study theoretically and numerically the interaction of the new generation high power laser pulses with near-critical density targets. There can be identified three interconnected subjects:

1. *The energy transfer from the laser to the plasma constituents.* Our main goal is to describe and model the energy transfer from laser to particles, from the transparent to less transparent regime of laser-plasma interaction in the ultra-high intensity regime.
2. *Laser-driven proton acceleration.* Our main goal is to predict the optimum thickness for proton acceleration and the maximum proton energies based on the absorption of laser energy.
3. *Emission of high energy radiation and pair creation.* Our main goal is to investigate

the high energy radiation emitted by electrons in the laser-plasma interaction, eventually leading to production of electron-positron pairs via the linear and nonlinear Breit-Wheeler processes.

Thesis structure

The thesis contains six chapters, two theoretical chapters in which the personal contributions are restricted to two sections as commented below and three chapters of original results obtained during the doctoral studies:

Chapter 1 entitled *Laser-plasma interaction on ultra-high intensity regime* contains a brief summary of the literature regarding laser-plasma interaction. The theoretical description of a plasma and a laser electromagnetic field is also introduced, along with the most important concepts like plasma frequency, critical density or normalized field amplitude. Further, the most important laser energy absorption mechanisms in the ultra-high intensity regime are summarized as well as different optimization models proposed for specific target density regimes. In the domain of interest for this thesis, the near-critical density regime, all described mechanisms play a role in the transfer of energy. In addition, the transfer of laser energy determines the acceleration of particles. In Section 1.3 we discuss the ion acceleration mechanisms, different models and scalings to predict and to optimize the maximum ion energy and some applications of these beams. As the electron motion is highly relativistic, in Section 1.4 are described the emission of high energy radiation and its effect on the electron motion. For very strong laser fields, the radiation emitted by the electron can decay into an electron-positron pair under different processes as described in the last section of this chapter.

In Chapter 2 entitled *Particle-in-cell simulations* (PIC) is detailed the kinetic approach of laser-plasma interaction. The chapter starts by describing the PIC method and a typical PIC time step in a simulation, followed by the PIC code used in this work SMILEI. Further, in Section 2.2 the path from the continuous theoretical description of a plasma to discontinuous numerical quantities is detailed. We describe the numerical method used for the integration of the equations on the particles and of the fields and another important concept in PIC codes, the macroparticles. Other aspects of a code are introduced, like the boundary conditions ap-

plied to the particles and to the fields as described in SMILEI and the normalization of the units. The physical quantities are stored in the so-called Diagnostics which are presented in Section 2.5. In the last theoretical section of this chapter, the special Physical modules which are not self-contained by solving the Maxwell-Vlasov system of equations are briefly described. Two modules are representative for this thesis and will be used: Radiation Reaction and nonlinear Breit-Wheeler pair creation. The last two sections are dedicated to our studies of numerical aspects performed with SMILEI: the convergence of the physical quantities for the variation of two numerical parameters, the number of particles per cell and the cell length, (Section 2.7) and the estimation of the total consumed power of our simulations (Section 2.8).

Chapter 3 entitled *Theoretical model of laser-energy absorption* collects the results obtained from the theoretical and the numerical study of the interaction of the new generation high power laser pulses with near-critical density targets. In Section 3.1, we propose a theoretical model for maximizing the energy conversion from the laser pulse to the plasma constituents, assuming that the transfer is made via hot electrons. Considering a Gaussian spatial and temporal profile for the laser pulse and a fully ionized target, we developed a model which includes the variation of all laser and target parameters in the ultra-short high laser intensity regime for near critical density targets. In the following sections, the theoretical model is tested and corrected through the observations made from 2D Particle-in-cell simulations performed for a wide range of parameters: the target density varies in $0.5 - 24$ n_c, the target thickness varies in $0.5 - 200$ μm, the target width is 30 μm, the laser peak intensity varies in $10^{20} - 10^{23}$ W/cm^2 (for a laser pulse duration of 20 fs), the laser pulse duration varies in $6.5 - 100$ fs (for a laser intensity of 10^{22} W/cm^2), the laser transversal waist is 12.5 μm FWHM and the laser wavelength is 1 μm. The laser transveral width and the plasma transversal width are almost equal in the model developed. In Section 3.4 we discuss the applicability of our model when the laser transversal width is much smaller than the plasma width and the possible applications of our model for electron acceleration and the emission of high energy radiation.

In Chapter 4 entitled *Proton acceleration for $a_0 = 85$* we use our model to study the proton acceleration for a laser intensity of 10^{22} W/cm^2, a pulse duration of 20 fs fWHM, a laser waist of 12.5 μm FWHM and a laser wavelength of 1 μm. The target characteristics are varying like in the previous chapter. The proton acceleration depends on the absorption of the laser energy in the hot electrons as presented in Section 4.2. We further analyze the optimum

target thickness for proton acceleration, which is found to be smaller than the optimum target thickness to maximize laser energy absorption as presented in Section 4.3. Based on the state-of-the-art literature and the new findings from our theoretical model, we predict the optimum thickness for ion acceleration and the maximum ion energies for an expansion like mechanism. We also discuss the origin of the most energetic protons, which corresponds to an expansion like mechanism as illustrated in the proton trajectories from the 2D PIC simulation.

Chapter 5 entitled *High energy synchrotron radiation and electron-positron pair creation* contains a detailed study on the emission of high energy radiation in laser-plasma interaction with the perspectives of studying nonlinear quantum electrodynamic effects like pair-creation. In Subsection 5.1.1 we analyze the radiation energy losses of an electron beam which interacts in head-on collision with an ultra-high intensity laser pulse as obtained in 2D PIC simulations and we compare it with the theoretical prediction. We studied multiple parameters: the energy of the electron beam varied in $0.5 - 1.5$ GeV and the laser intensity varied in $10^{19} - 10^{23}$ W/cm^2, while the laser pulse duration was kept constant at 30 fs FWHM. In addition, we compared the continuous and discontinuous radiation models implemented in SMILEI with the theoretical scaling. In Subsection 5.1.2 we study the radiation emitted in the case of an ultra-high intensity laser pulse interacting with a near critical density plasma. The laser and target characteristics are the same as the ones from the previous chapter. We discuss the different regimes of high energy radiation emission, which are dependent on the target density, and the optimum target thickness to maximize the conversion coefficient from the laser energy to the emitted γ-photons. In Section 5.2 we look at a further step of the laser-plasma interaction, namely the production of electron-positron pairs. In the optimal configuration for laser energy transfer to γ-photons from the previous section, we investigated the pair production by three different processes: nonlinear Breit-Wheeler, linear Breit-Wheeler and Bethe-Heitler with the aim of optimizing the linear Breit-Wheeler process. An experimental setup consisting of two identical γ-photons colliding under an angle θ is introduced in Subsection 5.2.1. Further we analyze the total number of pairs and their collimation for different angles θ. In Section 5.3 we extend our study for laser intensities in $10^{22} - 5 \cdot 10^{23}$ W/cm^2. We analyze the optimum target thickness to maximize the conversion coefficient from the laser to the emitted γ-photons and afterwards we study the total number of pairs and their collimation in the setup explained above.

In Chapter 6 are summarized the most important findings of this work and are given some perspectives for the open questions to be solved in the future.

The chapters are followed by the Bibliography, in which the references used are listed and by the Acknowledgements in which the gratitude for the profesional, moral and financial support provided are expressed.

The thesis ends with five Appendixes. The first one, Appendix A consists of additional information needed for the development of the theoretical absorption model, namely the explicit variation of the absorption coefficient, of the average hot electron energy and of the optimum thickness with the laser and target parameters. The second one, Appendix B contains a few typical electron trajectories in the bidimensional space as well as their energy variation as obtained in 2D PIC simulations. In addition, we discuss the variation of the target density which may influence the proton acceleration. In Appendix C are summarized the positron characteristics produced by the nonlinear Breit-Wheeler process as obtained from 2D PIC simulations. Finally, in Appendix D, the scientific activity is listed and in Appendix E a summary of the thesis in French is written.

Chapter 1

Laser-plasma interaction on ultra-high intensity regime

In this chapter we introduce the basic concepts of laser-plasma interaction and we make a summary of the existent literature which will be used later in this thesis. In Section 1.1 we describe theoretically the electromagnetic field, the plasma and the particle dynamics in the laser-plasma system. Further, in Section 1.2 we summarize the most important laser energy absorption mechanisms in the ultra-high intensity regime and in Section 1.3 we introduce the main laser ion acceleration mechanisms. Finally, Section 1.4 is dedicated to the emission of high energy radiation with perspectives for applications to electron-positron pair creation, a phenomenum specific to ultra-intense electromagnetic fields.

This chapter is inspired by the following literature: [19, 20, 21, 22], if not otherwise indicated.

1.1 Introductory Notions

1.1.1 Electromagnetic field & Maxwell equations

In 1865 James Clerk Maxwell achieved the unification of electric and magnetic phenomena in a set of 20 equations representing the theory of Electromagnetic Field [23]. The theory describes the idea that electric and magnetic bodies can interact at a distance, between them being present an electromagnetic field, which can be in vacuum or in matter. Based on the propagation velocity of magnetic disturbances in a medium, he also proposed that light and radiant heat are electromagnetic phenomena. The theory was formulated by coupling the laws based on experimental observations on stationary phenomena (Coulomb law on electric field, Ampere law on magnetic field) and Faraday law of induction. In 1880, Olivier Heaviside reduces the set of equations to 4, which are widely known as Maxwell equations, and in vacuum they can be written as (in SI units):

$$\vec{\nabla}\cdot\vec{E} = \frac{\rho}{\varepsilon_0} \tag{1.1}$$

$$\vec{\nabla}\cdot\vec{B} = 0 \tag{1.2}$$

$$\vec{\nabla}\times\vec{E} = -\frac{\partial\vec{B}}{\partial t} \tag{1.3}$$

$$\vec{\nabla}\times\vec{B} = \mu_0\vec{J}+\frac{1}{c^2}\frac{\partial\vec{E}}{\partial t} \tag{1.4}$$

We can define an electromagnetic field as a superposition of electric and magnetic field which generates itself and evolve according to these equations. The theory of electromagnetic fields was proved experimentally in 1888 by Heinrich Rudolf Hertz.

The laser radiation can be fully described by using the Maxwell equation. They describe the evolution of the electromagnetic waves in vacuum. In order to describe the evolution in matter, the vacuum permitivity and permeability should be replaced by the material characteristics.

1.1.2 Plasma kinetic description - Vlasov equation

A plasma is a neutral system of electrons and ions coupled to each other by their electromagnetic fields. An important parameter to describe a plasma is the Debye length, which represents the length over which the fields generated by a particle are shielded by the neighbouring particles. A collisionless plasma represents a plasma in which the one-to-one particle interaction is negligible, which is true when the number of particles in a sphere with the radius equal to the Debye length is very large.

The full description of a plasma can be made by providing in detail the evolution in time of the motion (position and momentum) of each particle. However, due to the large number of particles in a system, a practical approach to the problem is done using a statistical distribution function $f(\vec{r},\vec{p},t)$ which describes how the particles are distributed in a position $\vec{r}$ and momentum $\vec{p}$ space called phase space, at a given time t. Integrating the distribution function, we can find the following quantities:

- the total number of particles:

$$N = \int\int f(\vec{r},\vec{p},t)d\vec{r}d\vec{p} \tag{1.5}$$

- the total density in the configuration space:

$$n(\vec{r},t) = \int f(\vec{r},\vec{p},t)d\vec{p} \tag{1.6}$$

- the average velocity of a particle:

$$\vec{u}(\vec{r},t) = \frac{1}{n}\int \vec{v}\cdot f(\vec{r},\vec{p},t)d\vec{p} \tag{1.7}$$

  where $\vec{v} = \vec{p}/(m\gamma)$ is the velocity of a particle and $\gamma = \sqrt{\frac{1}{1-(v/c)^2}}$ is the Lorentz factor of the particle.

We consider a plasma made of multiple particle species α. The description of our system can be made with a distribution function $f_\alpha(\vec{r},\vec{p},t)$ which contains all information (position and velocity) for each particle species α at a given time. In a collisionless system, the distribution

function must obey the following continuity equation:

$$\frac{df_\alpha}{dt} = 0 \Rightarrow \left(\frac{\partial}{\partial t} + \frac{\partial}{\partial \vec{r}} \cdot \vec{v_\alpha} + \frac{\partial}{\partial \vec{p}} \cdot \vec{F_\alpha}\right) f_\alpha = 0 \tag{1.8}$$

The electromagnetic force which acts on the particles is given by the Lorentz force:

$$\vec{F_\alpha} = q_\alpha \left(\vec{E} + \frac{\vec{v_\alpha}}{c} \times \vec{B}\right) \tag{1.9}$$

where the electric and magnetic fields are obtained from the Maxwell equations (1.1) - (1.4).

Substituting Eq.(1.9) in Eq.(1.8), we will obtain the Vlasov equation:

$$\frac{\partial f_\alpha}{\partial t} + \vec{v_\alpha} \cdot \frac{\partial f_\alpha}{\partial \vec{r}} + q_\alpha \left(\vec{E} + \frac{\vec{v_\alpha}}{c} \times \vec{B}\right) \cdot \frac{\partial f_\alpha}{\partial \vec{p}} = 0 \tag{1.10}$$

which describes the evolution of the distribution function of a particle species in a collisionless plasma.

In order to compute the electric and magnetic fields, one must obtain the charge ρ and current densities $\vec{J}$ of the particles from the distribution function as following:

$$\rho = \sum_\alpha q_\alpha \int f_\alpha(\vec{r}, \vec{p}, t) d\vec{p} \tag{1.11}$$

$$\vec{J} = \sum_\alpha q_\alpha \int \vec{v_\alpha} f_\alpha(\vec{r}, \vec{p}, t) d\vec{p} \tag{1.12}$$

The full plasma description is made by using the Vlasov Eq.(1.10) for the time evolution of the particles and the Maxwell Eqs. (1.1) - (1.4) for the self-generated electromagnetic fields. This system of equations will be referred to as the Maxwell-Vlasov equations.

In a system where the particles are neither destroyed nor created, the equation of conservation of electric charges must be fulfilled. Consider applying $\vec{\nabla}$ on Maxwell - Ampere

Eq.(1.4):

$$\vec{\nabla}\cdot(\vec{\nabla}\times\vec{B}) = \vec{\nabla}\cdot(\mu_0\vec{J})+\vec{\nabla}\cdot\left(\frac{1}{c^2}\frac{\partial\vec{E}}{\partial t}\right) \quad (1.13)$$

$$= \mu_0\vec{\nabla}\cdot\vec{J}+\frac{1}{c^2}\frac{\partial}{\partial t}\vec{\nabla}\cdot\vec{E} \quad (1.14)$$

$$= \mu_0\vec{\nabla}\cdot\vec{J}+\frac{1}{\varepsilon_0 c^2}\frac{\partial\rho}{\partial t} \quad (1.15)$$

where we introduced the Maxwell - Poisson Eq.(1.1). Using the vector identity $\vec{\nabla}\cdot(\vec{\nabla}\times\vec{B})=0$ and $c=1/\sqrt{\mu_0\varepsilon_0}$, we will obtain:

$$\frac{\partial\rho}{\partial t}+\vec{\nabla}\cdot\vec{J}=0 \quad (1.16)$$

which is the equation of conservation of charges.

1.1.3 Non-relativistic electron motion in a monochromatic plane wave

We consider an electron moving in an electromagnetic plane wave. The electric and magnetic fields of the plane wave are given by:

$$\vec{E}(\vec{r}) = E_0\cdot\exp\left[i(\vec{k}\vec{r}-\omega t)\right] \quad (1.17)$$

$$\vec{B}(\vec{r}) = B_0\cdot\exp\left[i(\vec{k}\vec{r}-\omega t)\right] \quad (1.18)$$

where $\vec{k}$ is the wave vector and ω is the wave angular frequency.

Considering the Lorentz force Eq.(1.9) which acts on the electron, we can write the equation of motion, in the non-relativistic limit $v << c$, as following:

$$m_e\frac{d\vec{v}}{dt}=-e\left(\vec{E}+\frac{\vec{v}}{c}\times\vec{B}\right) \quad (1.19)$$

In this limit, the motion of the electron will only be due to the electric component. Thus, we can derive the electron velocity as:

$$\int d\vec{v}=\frac{-e}{m_e}\int E_0\cdot\exp\left[i(\vec{k}\vec{r}-\omega t)\right]dt \Rightarrow \vec{v}=\frac{-ie}{m_e\omega}\vec{E}. \quad (1.20)$$

and the electron position as:

$$\vec{v} = \frac{d\vec{r}}{dt} \Rightarrow \vec{r} = \frac{e\vec{E}}{m_e\omega^2}. \tag{1.21}$$

The solutions Eqs. (1.20) - (1.21) describe the motion of an electron in an electromagnetic plane wave in the non-relativistic limit ($\vec{v} << c$). The peak amplitude of the velocity is $v_0 = eE_0/m_e\omega$. We will define the normalized field amplitude a_0 as:

$$a_0 = \frac{eE_0}{m_e\omega c} \tag{1.22}$$

which for the non-relativistic case fulfils the condition $a_0 << 1$. The normalized field amplitude a_0 can be written as a function of laser peak intensity and wavelength as:

$$a_0 = 0.85\left(\frac{I\lambda^2}{10^{18}W/cm^2}\right)^{1/2} \tag{1.23}$$

where I is the laser pulse peak intensity and λ is the laser pulse wavelength in μm.

1.2 Laser energy absorption in plasma

1.2.1 Electron plasma frequency & critical density

We consider a neutral plasma of a given length L made of electrons and immobile ions. We induce a displacement x of the electrons, thus we will create a charge separation similar to a capacitor. The electric field created between the charges is given by:

$$E = \frac{\sigma_s}{\varepsilon_0} = \frac{n_{e0}ex}{\varepsilon_0} \tag{1.24}$$

where σ_s is the surface charge density, n_{e0} the electron density and ε_0 the vacuum permittivity. The electrons will start to oscillate under the electric force $F = -eE$ and their motion will be described by the following oscillator equation:

$$\frac{d^2x}{dt^2} = -\frac{n_{e0}e^2x}{m_e\varepsilon_0} \tag{1.25}$$

where we define the oscillation frequency:

$$\omega_{pe} = \sqrt{\frac{n_{e0}e^2}{m_e\varepsilon_0}} \tag{1.26}$$

as the electron plasma frequency.

The oscillation of the electrons will create an electromagnetic wave which will propagate in the plasma. The dispersion relation of an electromagnetic wave in a plasma is given by [21]:

$$\omega^2 - \omega_{pe}^2 - k^2c^2 = 0. \tag{1.27}$$

The electromagnetic wave can propagate in the plasma only if $|k|$ is a real number which occurs when $\omega > \omega_{pe}$.

We define the critical density as the density for which the electromagnetic wave frequency is equal to the electron plasma frequency:

$$\omega = \omega_{pe} \rightarrow n_c = \frac{\omega_{pe}^2\varepsilon_0 m_e}{e^2} = 1.1 \cdot 10^{21} cm^{-3} \cdot \frac{1}{\lambda_{\mu m}^2}. \tag{1.28}$$

If the electron plasma density $n_e < n_c$ for a given wavelength λ, the electromagnetic wave can propagate and the plasma is called underdense. In the opposite case, for $n_e > n_c$ for a given λ, the electromagnetic wave cannot propagate and the plasma is called overdense. For an overdense plasma, the electromagnetic wave will vanish exponentially as $\exp(-x/l_s)$ where l_s is the plasma skin depth and is given by:

$$l_s = \frac{c}{\omega_{pe}} \tag{1.29}$$

However, if the laser pulse is intense enough to accelerate the electrons to velocities comparable with the velocity of light, the laser can propagate even in overdense plasmas as shown in [24, 25]. Thus, in the relativistic regime, the critical density will be corrected by considering the relativistic electron mass: $n_{c,rel} = \gamma n_c$, where γ is the Lorentz factor.

1.2.2 Laser energy absorption mechanisms

When an ultra-high intensity laser pulse ($I \geq 10^{18}$ W/cm^2) interacts with a plasma, the plasma constituents will absorb a significant part of the laser energy and electrons will be accelerated up to relativistic velocities. The most predominant mechanisms of energy transfer from the laser pulse to the plasma constituents are collisionless at relativistic intensities, being done by collective effects in the plasma. This fact is due to the very long electron and ion collission times compared to the time of laser-plasma energy transfer, which is on the order of laser pulse duration. For example, in a plasma of density of 10 n_c and temperature of 10 keV, the electron and ion collision times is 3 ps, respectively 189 ps, while for a temperature of 1 MeV, the collision times are 3 ns for electrons and 189 ns, which in both cases are much higher than the laser pulse durations of our interest, in the order of tens of femtoseconds.

There are various collisionless mechanisms of absorption, each being dependent on the laser or target parameters. For an obliquely incident laser pulse at sub-relativistic intensities and when there is a preplasma, the most predominant mechanism is the resonant absorption, which can convert up to 60% of the laser energy into electron energy [26]. In this mechanism, the intense pulse is absorbed in the vicinity of the critical surface by the hot electrons. The resonant absorption model predicts the hot electron temperature is dependent on the laser intensity and wavelength and on the background electron temperature as $T_H \sim 14(I\lambda^2)^{1/3}T_c^{1/3}$. The results obtained showed a good agreement with the observations in the $10^{15} - 10^{16}$ W/cm^2 intensity range [27].

For an obliquely incident laser light and an overdense target with no preplasma, the dominant absorption mechanism is Brunel absorption [28]. The absorption will take place at the focal spot where the laser drags the electrons out of the plasma, and when the field reverses, the electrons go back into the plasma.

Another absorption mechanism is $\mathbf{J} \times \mathbf{B}$ heating, which is caused by the oscillating component of the ponderomotive force of the laser light [29]. This mechanism is efficient only for high-intensity light, showing about 15% conversion efficiency for $I\lambda^2 = 10^{18}$ Wμm^2/cm^2.

Further studies were performed addressing the absorption of an ultra-high intensity laser pulse ($I \geq 10^{18}$ W/cm^2) in an overdense plasma [30]. The light pressure of the laser creates a

hole into the target. As the hole increases in time, the absorption coefficient increases and, with a mix of the previously explained absorption mechanisms, can lead to the conversion of 50% of the laser energy to hot electrons.

During the interaction process, as the electrons are heated and accelerated, the target characteristics are dynamic. The target transparency or opacity depends on the interaction process itself: a slightly overdense target can absorb or reflect the laser energy according to the laser amplitude [31]. The transition between the two regimes (transparent and opaque) is determined by the critical laser strength or normalized amplitude, which depends on the target density $a_{0c} = 1.65(n_e/n_c - 0.5)$. Under this value, the laser wave will push the plasma surface, creating a large density increase which will lead to a higher reflection of the laser waves. Over the critical value, the laser waves will propagate in the target, accelerating the electrons.

Further studies on the absorption of an ultra intense laser pulse have shown a decrease of the absorption coefficient as a_0/n_e under the critical value $a_0/n_e = 0.07$, corresponding to the opaque regime earlier discussed. Above this value, the absorption coefficient increases as a_0^3/n_e^3 [32].

A recent analytical study for the energy absorption of an intense short-pulse laser by a near-critical density plasma in the transparent regime was made by Debayle et al. [33]. The model shows good agreement between the analytical study and the simulations performed in the density range of $0.1\ \mathrm{n_c} - 2\ \mathrm{n_c}$.

However, due to the complexity of the laser-plasma interaction process, a simple general analytical model for optimizing the energy transfer from the laser pulse to the target and particle beams characteristics (energy, direction of propagation), comprising all regimes (classical and relativistic, transparent or opaque) cannot be formulated.

1.3 Ion acceleration mechanisms

1.3.1 Target Normal Sheath Acceleration

When an ultra-high intensity laser pulse interacts with the plasma, the electrons will be accelerated by the laser ponderomotive force:

$$F_p = -m_e c^2 \nabla \gamma_a \tag{1.30}$$

where $\gamma_a = \sqrt{1 + (a_0^2/2)}$ and a_0 is the normalized field amplitude of the laser pulse.

The oscillating part of the ponderomotive force will push electrons to oscillate at twice the laser frequency and the electrons will absorb the laser energy and will be accelerated up to relativistic velocities. The fastest electrons will be propagating through the target and eventually escape at the rear side. This displacement will lead to the creation of a quasi-electrostatic charge-separation field at the rear side of the target which will accelerate the ions and reinject the slower electrons into the target, forming a return current. This acceleration process is called Target Normal Sheath Acceleration (TNSA) [34, 35]. The process is schematically presented in Fig.1.1.

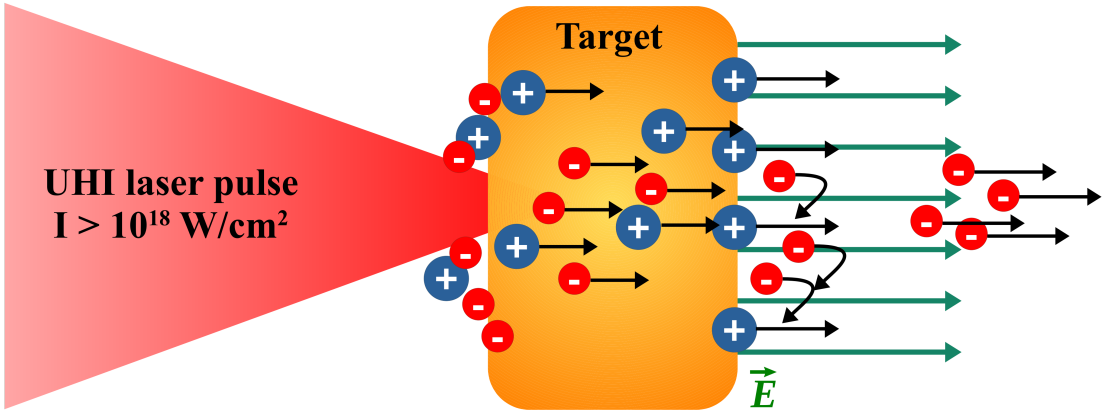

Figure 1.1: Ultra-high intensity laser pulse interacting with a target

One of the first models to theoretically describe the TNSA mechanism was made by Mora [36]. Based on an electron-ion plasma expansion in vacuum, the model predicts the

maximum electric field at the back of the target and the ion energy cutoff as a function of the electron temperature, the electron density distribution and time.

Further, Fuchs et al. [37] describes the optimization of the maximum proton energy and laser-proton energy conversion efficiency as a function of target thickness and laser intensity, energy and pulse duration. The model is based on an isothermal plasma expansion model similar to the previously mentioned approach, where the protons are accelerated by the TNSA mechanism. The model shows good agreement with experimental data in the intensity range of $10^{18} - 10^{20}$ W/cm^2 and for short laser pulses [38]. However, for higher laser intensities the model overestimates the maximum proton energy [39] and a revised Mora model should be used [40]. Moreover, a recently empirical model to predict the maximum proton energy as a function of laser energy, pulse duration, focal spot size and target thickness was reported in [41]. The model is based exclusively on experimental data obtained from previously published studies for a laser intensity in $10^{16} - 10^{21}$ W/cm^2, a pulse duration varying from 30 fs to 1 ps and a laser energy varying from 10 mJ to 400 J.

1.3.2 Radiation Pressure Acceleration

In the ultra high intensity regime other acceleration mechanisms may become dominant: Radiation Pressure Acceleration (RPA) [42] and Collisionless Shock Acceleration (CSA) [43].

In the RPA process, the laser pressure pushes masses of electrons, creating a strong electric field which accelerates the ions from the front side in the forward direction. This process can be very efficient for high intensity circularly polarized laser pulses, producing high energy monoenergetic ion beams [44].

In CSA, the radiation pressure of the laser launches an RPA piston that can become a shock in certain conditions and reflect upstream ions. In this case, the target density will be compressed at more than twice its initial density and reflect the ions at twice the initial shock wave velocity. This phenomena was studied through PIC simulations in solid target densities [45, 46] and near-critical underdense targets [47]. Collissionless Shock Acceleration can provide high energy, low divergence proton beams, as observed experimentally in [48] (up to 20 MeV) [49] (up to 6 MeV).

1.3.3 Optimization of laser-driven ion acceleration

The interaction of high intensity lasers in the range $10^{18} - 10^{21}$ W/cm^2 with thin foils was studied by E. d'Humières et al. [50]. Both interaction regimes were considered, opaque and transparent. In the opaque case, some energetic ions are first accelerated by the shock created by the laser pulse at the front side of the target, and after propagating inside the target, they are reaccelerated by the charge separation field created at the rear side, while others are directly accelerated at the back of the target by the charge separation field. In the transparent case, the ions are accelerated by the plasma expansion driven by the hot electrons. In both cases, the most energetic ions are originating from the back of the target. The optimum target thickness for ion acceleration was found to be at the point where the laser is strongly absorbed, but still able to pass through the target and efficiently heat the electrons. A further study [51] lead to the same conclusion for a higher laser pulse intensity. The optimum target thickness for ion acceleration was found to depend on the laser field amplitude as $l = 0.5\lambda a_0 n_c/n_{e0}$.

Brantov et al. [52] analyzed the influence of the laser polarization. The circularly polarized laser pulse were found more effective in the case of low density targets, where the maximum proton energy can be increased by 60% compared to the results with linearly polarized lasers, by enhancing the volumetric heating of hot electrons. The optimum target thickness was corresponding to the transition between the two regimes of interaction: opaque and transparent, where the acceleration mechanisms work together.

This transition was also studied by Mishra et al. [53] for the case of linear polarized laser pulses. The maximum proton energy in this case can be 2 times higher than in the opaque regime. The ion energy depends on an optimal electron areal density, which according to the analytical model depends on the laser parameters as $n_{e0}/n_c L_0(\mu m) \approx \tau_p I_0^{3/4}$. This regime is efficient only if the target becomes transparent when the laser is interacting around its peak intensity.

The enhancement of laser absorption into hot electrons can be also achieved by using double-layer targets, composed by a near-critical density thick plasma in front of an ultrathin solid foil [54, 55]. A theoretical model for the optimization of ion acceleration using double-layer targets was made in [56], based on the absorption of the laser energy in the hot electrons. In this case, superponderomotive electrons are generated in the thick absorbing layer of the

target and travel behind the laser pulse. When the laser hits the solid foil, the radiation pressure acceleration mechanism accelerates the ions. The hot electrons escaping the target will give rise to a charge separation field at the back of the target, accelerating the back surface ions, and the RPA ions can be reaccelerated.

1.3.4 Applications of laser-driven ion acceleration

An important medical application of the ion beams is hadrontherapy which was first proposed for cancer treatment in 1946 and treated more than 170000 patients by the end of 2017 [57]. However, in 2020 there was almost 20 million cancer patients worldwide out of which almost 10 million died of cancer [58]. Laser driven ion accelerator have the advantage of being more compact than the standard ones [59], providing a less expensive solution. Typical maximum proton energies for hadrontherapy are in $230-250$ MeV, with a proton beam intensity of $10^{10}-5\cdot10^{10}$ protons/s [60]. Theoretical studies have shown that proton energies ≥ 200 MeV can be achieved with lasers of intensity $2\cdot10^{21}$ W/cm^2 [61]. An important characteristic of the proton beam is the low energy spread which can be controlled by shaping the laser pulse and the target [60].

Another application of the laser driven ion beams for medical applications is radioisotope production [62, 63]. Protons with energies of a few MeV's can be used to induce nuclear reactions in secondary targets and create radionuclides suited for positron emission tomography (PET) like ^{11}C, ^{13}N, ^{15}O and ^{18}F. Experimental studies demonstrated the production of ^{11}C and ^{13}N using a laser pulse with the intensity up to 10^{20} W/cm^2 and a solid density target [64, 65]. Theoretical studies have shown that using a laser intensity of 10^{21} W/cm^2, the production rate of ^{18}F can be two orders of magnitude larger than by the standard cyclotron method [66].

Laser driven ion beams can also have applications in other fields, among which are: proton induced X-ray emission spectroscopy (PIXE) for cultural heritage [67, 68] and ion fast ignition for inertial confinement fusion [69].

1.4 High energy radiation

1.4.1 Emission of high energy radiation by a moving particle

We consider a particle with the charge e moving along a trajectory $\vec{r} = \vec{r_0}(t)$ with a velocity $\vec{v}$. Starting with the Lienard-Wiechert potentials for the field produced by this particle in Gaussian units [19],

$$\Phi = \frac{e}{R - \frac{\vec{v}\vec{R}}{c}} \tag{1.31}$$

$$\vec{A} = \frac{e\vec{v}}{c\left(R - \frac{\vec{v}\vec{R}}{c}\right)} \tag{1.32}$$

we can deduce the expressions for the electric and magnetic field produced by this particle:

$$\vec{E} = e\frac{1-\frac{v^2}{c^2}}{\left(R - \frac{\vec{R}\vec{v}}{c}\right)^3}\left(\vec{R} - \frac{\vec{v}}{c}R\right) + \frac{e}{c^2\left(R - \frac{\vec{R}\cdot\vec{v}}{c}\right)^3}\vec{R} \times \left\{\left(\vec{R} - \frac{\vec{v}}{c}\right) \times \vec{\dot{v}}\right\} \tag{1.33}$$

$$\vec{H} = \frac{1}{R}\vec{R} \times \vec{E} \tag{1.34}$$

where $\vec{R}$ is the vector until the point of our observation.

The expressions (1.31)-(1.32), consequently (1.33)-(1.34) are valid with respect to the retarded time $t' = t - R(t')/c$.

The electromagnetic wave radiated by the particle will carry off energy. If we consider the reference frame in which the particle is initially at rest, the total energy and momentum radiated will be [19]:

$$\Delta\mathscr{E} = \frac{2e^2}{3c^3}\vec{\dot{v}}^2 dt \tag{1.35}$$

$$d\vec{P} = 0 \tag{1.36}$$

However, in an arbitrary reference frame, the total radiated energy is [19]:

$$\Delta\mathscr{E} = \frac{2e^2}{3c^3}\int_{-\infty}^{\infty} \frac{\vec{\dot{v}}^2 - \frac{(\vec{v}\times\vec{\dot{v}})^2}{c^2}}{\left(1 - \frac{v^2}{c^2}\right)^3} dt \tag{1.37}$$

Using the Lienard-Weichert expressions for the fields, we can calculate the intensity radiated inside the solid angle $d\Theta$ [19]:

$$dI = \frac{e^2}{4\pi c^3}\left\{\frac{2(\vec{n}\cdot\vec{\dot{v}})(\vec{v}\cdot\vec{\dot{v}})}{c\left(1-\frac{\vec{v}\cdot\vec{n}}{c}\right)^5} + \frac{\vec{\dot{v}}^2}{\left(1-\frac{\vec{v}\cdot\vec{n}}{c}\right)^4} + \frac{\left(1-\frac{v^2}{c^2}\right)(\vec{n}\cdot\vec{\dot{v}})^2}{\left(1-\frac{\vec{v}\cdot\vec{n}}{c}\right)^6}\right\}d\Theta \tag{1.38}$$

where $\vec{n}$ is the unit vector in the direction of the radiation.

Integrating (1.38) over time, we will obtain the angular distribution of the total radiation throughout the whole motion of the particle.

An ultra-relativistic particle will emit radiation mainly along the direction of its own motion, with a small range of angles around the direction of its velocity:

$$\theta \sim \sqrt{1-\frac{v^2}{c^2}} \tag{1.39}$$

1.4.2 Radiation Reaction

The radiation emitted by the particle will be acting on the particle itself. This force can be seen as a damping force acting on the particle. In order to describe it, we will consider the reference frame in which the particle is at rest. In this case, using (1.35), the force acting on the particle is [19]:

$$\vec{f} = \frac{2e^2}{3c^3}\vec{\dot{v}} \tag{1.40}$$

The equation of motion of the particle, under interaction with the force (1.40) is given by:

$$m\vec{\dot{v}} = \frac{2e^2}{3c^3}\vec{\dot{v}} \tag{1.41}$$

This equation has two solutions: the trivial solution $v = constant$ and a solution in which the acceleration increases indefinitely with time $a \approx \exp(3mc^3t/2e^2)$. The runaway solution means that a charged particle passing through a field will be self-accelerated indefinitely.

In a reference frame where the particle has a small velocity compared to c, the equation

of motion in an external field and in the field created by the particle itself, will be:

$$m\vec{v} = e\vec{E} + \frac{e}{c}\vec{v}\times\vec{H} + \frac{2e^2}{3c^3}\vec{v} \tag{1.42}$$

where $\vec{E},\vec{H}$ represent the intensity of the external electric, respectively magnetic fields.

The damping force will be [19]:

$$\vec{f} = \frac{2e^3}{3mc^3}\dot{\vec{E}} + \frac{2e^4}{3m^2c^4}\vec{E}\times\vec{H} \tag{1.43}$$

Eq.(1.42) is valid only if the damping force acting on the particle is small compared to the force of the electric field. This condition can be expressed as the following:

$$\lambda \gg \frac{e^2}{mc^2} \tag{1.44}$$

where λ is the wavelength of the external electromagnetic field.

In order words, Eq.(1.42) is valid if the wavelength of the incident radiation on the particle is much larger than the radius of the particle. Also, the field itself cannot be very large:

$$H \ll \frac{m^2c^4}{e^3} \tag{1.45}$$

In the ultra-relativistic case, the damping force (1.43) will become [19]:

$$\begin{aligned}\vec{f} = {} & \frac{2e^3}{3mc^3}\left(1-\frac{v^2}{c^2}\right)^{-1/2}\left\{\left(\frac{\delta}{\delta t}+\vec{v}\cdot\nabla\right)\vec{E} + \frac{1}{c}\vec{v}\times\left(\frac{\delta}{\delta t}+\vec{v}\cdot\nabla\right)\vec{H}\right\} \\ & + \frac{2e^4}{3m^2c^4}\left\{\vec{E}\times\vec{H} + \frac{1}{c}\vec{H}\times(\vec{H}\times\vec{v}) + \frac{1}{c}\vec{E}(\vec{v}\cdot\vec{E})\right\} \\ & - \frac{2e^4}{3m^2c^5\left(1-\frac{v^2}{c^2}\right)}\vec{v}\left\{\left(\vec{E}+\frac{1}{c}\vec{v}\times\vec{H}\right)^2 - \frac{1}{c^2}(\vec{E}\cdot\vec{v})^2\right\}\end{aligned}$$

The previous force is called the Landau-Lifshitz force and can be used only when quantum effects can be neglected. However, this classical description is not valid anymore when the electric field of the electron approaches the Schwinger field:

$$E_s = \frac{m_e^2c^3}{e\hbar} = 1.3\times10^{16}\ V/cm \tag{1.46}$$

The Schwinger field is used as a reference for non linear quantum electrodynamics effects such as pair production in vacuum. This field corresponds to an intensity of $I = 10^{29}$ W/cm^2, which is far away from what we can achieve in the present laser facilities. However, in [70] it was shown that the intensity is much higher in the rest frame of the relativistic electrons, in such a way that radiation reaction effects can be studied at laser facilities like Apollon [71] and ELI [72].

1.4.3 Thomson scattering

We consider the case of an electromagnetic wave scattered by a system of charges. The charges will move under the action of the incident wave and will produce radiation in all directions. The effective cross-section of the scattering is the ratio between the amount of energy emitted by the scattering system in a given direction per unit of time, to the energy flux density of the incident radiation.

For an unpolarized wave scattered by a free charge, the cross section is given by the Thomson formula [19]:

$$d\sigma = \frac{1}{2}\left(\frac{e^2}{mc^2}\right)^2 (1+\cos\theta^2) d\Theta \tag{1.47}$$

where $d\Theta$ is the solid angle of scattering and θ is the angle between the directions of the incident and scattered waves.

Eq.(1.47) is valid only for non-relativistic particles, Thomson scattering being the low energy limit of Compton scattering.

The total Thomson cross section is:

$$\sigma = \frac{8\pi}{3}\left(\frac{e^2}{mc^2}\right)^2 \tag{1.48}$$

For an electron at rest, with $m_e = 9.1 \cdot 10^{-31}$ kg and electric charge $e = -1.6 \cdot 10^{-19}$ C, the Thomson cross section is $0.665 \cdot 10^{-24}$ cm^2.

1.4.4 Inverse Compton scattering

At the scattering of an electromagnetic wave with a high energy electron, the electron can emit radiation with a higher frequency than the one of the incident wave:

$$e^- + n\gamma_l \rightarrow e^- + \gamma \tag{1.49}$$

where γ_l represents a laser photon, n - the number of laser photons participating in the process and γ - the photon emitted by the incident electron.

The process is called nonlinear inverse Compton scattering and is described schematically in Fig. 1.2 a).

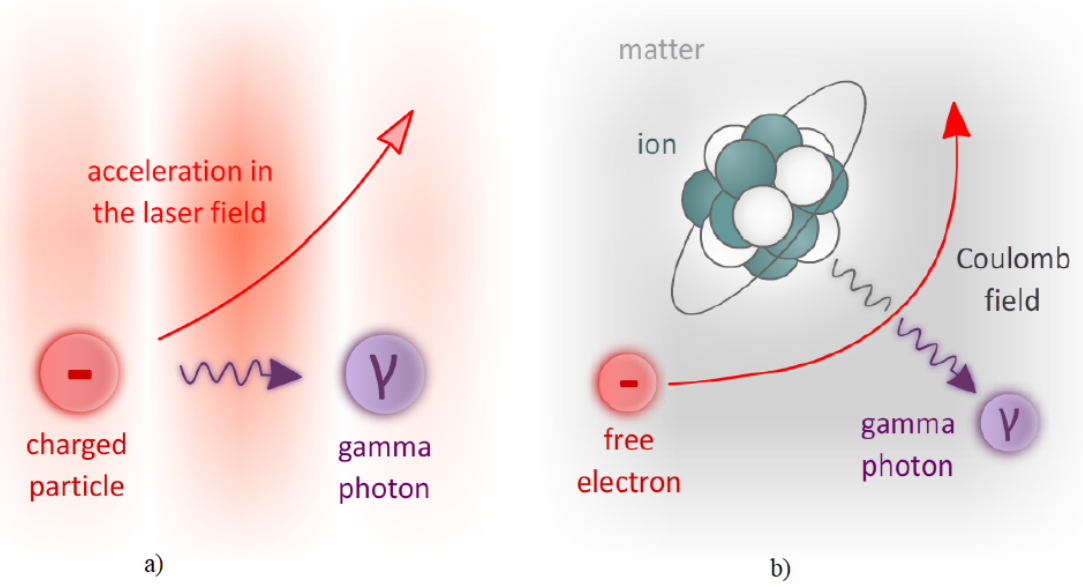

Figure 1.2: a) Inverse Compton Scattering b) Bremsstrahlung emission [73]

In the case of dense targets, the electrons will interact with the Coulomb field of the atoms, and will lose energy via the Bremsstrahlung process. This process is represented schematically in Fig. 1.2 b). In the case of ultra-high intensities (above 10^{22} W/cm^2), the electrons will predominantly lose energy via nonlinear inverse Compton scattering.

1.4.5 Emission of high energy radiation in laser-plasma interaction

The generation of intense γ-photon beams from the interaction between an accelerated electron beam and an ultra-high intensity laser is a well-known phenomena [74, 75, 76]. Recently, various theoretical and numerical studies have been performed to optimize the generation of high energy γ-photons using ultra high intensity lasers interacting with matter. At the interaction between an ultra-high intensity laser ($I > 10^{22}$ W/cm^2) with a plasma, high energy particle beams can be obtained (protons, electrons, gamma photons, neutrons, etc.). The electrons will be accelerated up to ultra-relativistic velocities and will emit a copious amount of synchrotron gamma photons.

Studies on the absorption mechanisms of the laser energy, using different target configurations, showed a conversion efficiency of the laser energy to γ-photons that strongly depends on the laser and target parameters. The highest absorption coefficient of the laser energy to γ-photons are obtained when the laser normalized field amplitude a_0 is much higher than the target density normalized by the critical density n_c. In [77] was shown that using a cylindrical channel target, the laser energy transfer to the generated high energy radiation can be increased thanks to the generation of strong magnetic fields. The authors reported a maximum absorption coefficient in high energy photons of 15% obtained for a target bulk density of 100 n_c and channel density of 10 n_c, and a laser intensity of $5 \cdot 10^{22}$ W/cm^2.

Studies involving near-critical density targets have also shown promising results regarding the conversion efficiency to gamma photons. In [78] a total conversion coefficient of the laser energy to high energy photons of 13% was obtained for a target density of 17 n_c and a laser pulse intensity of 10^{22} W/cm^2, which soon will be available experimentally. Moreover, for a target density of 32 n_c and using a laser intensity of 10^{24} W/cm^2, a total conversion coefficient of laser energy to high energy photons of 72% was reported [79]. An overview of the emission of high energy radiation in laser-plasma interaction among other high energy radiation sources (e.g. laser-electron beam interaction), comprising theoretical and experimental data, was discussed recently [80, 81].

1.5 Electron-positron pair creation

The generation of high-energy radiation in laser-plasma interaction brings the possibility to study in the laboratory the creation of electron-positron pairs. There are multiple processes which can lead to the creation of the electron-positron pairs, each being discussed below.

1.5.1 Linear Breit-Wheeler pair production

The linear Breit-Wheeler process consists of the creation of an electron-positron pair by the collision of two high energy photons. The process was first described in 1934 [82] and it can be represented as:

$$\gamma_1 + \gamma_2 \rightarrow e^- + e^+ \tag{1.50}$$

The linear Breit-Wheeler (LBW) process occurs naturally in astrophysical scales. In [83] is discussed the linear Breit-Wheeler process in the intergalactic space, considering the high energy photons coming from a star at a distance of $6.6 \cdot 10^{26}$ cm, with energies in $0.1 - 50$ TeV, colliding with the thermal intergalactic photons with energy of 1 eV. The maximum probability of the process to occur is for the photon energy of 1 TeV. Moreover, the absorption of high-energy γ photons from a blazar by infrared photons, which results in the creation of pairs, can be used to measure the magnitude of the intergalactic infrared radiation field [84].

Thanks to the latest advances in laser technology, experimental setups for the production and the detection of the linear Breit Wheeler process in the laboratory were proposed.

One setup was proposed by Pike et al. [85]: one high energy collimated photon beam interacts with the thermal photons from a Holhraum. The energetic photon beam is produced by the interaction of a high energy electron beam accelerated by laser wakefield acceleration in a gas jet, with a mm-thick solid gold target. The laser will accelerate the electrons up to GeV energies, and these electrons will emit about 40% of their energy producing high energy photons through the Bremsstrahlung process. The total number of emitted photons is about 10^8 with energies in the range of 500 MeV $-$ 2 GeV. On the other hand, another laser, with a high energy and a nanosecond pulse duration, will irradiate the Hohlraum which will emitt black-body radiation with an energy in the range of $100 - 400$ eV. The authors reported $10^4 - 10^5$

pairs produced by the linear Breit-Wheeler process.

Another setup is the one proposed by Ribeyre et al. [86]: two high intensity laser pulses irradiating two targets and creating two high-energy γ-photon beams, which collide between each other and produce pairs. Considering the laser energy in $5-100$ J, and the production of the two γ-photons through different processes, the authors estimate the creation of up to 10^4 pairs per laser shot. The optimum case to create the pairs is based on the syncrotron radiation emitted by the electrons at the interaction of a laser pulse of intensity 10^{23} W/cm^2 with either a solid target, or a near-critical density target. The maximum number of linear Breit-Wheeler pairs created is 10^3, respectively 10^4 at 500 μm far away from the γ-photon source.

In Wang et al. [87], the two experimental setups have been compared using an ultra-high intensity laser of peak intensity $5 \cdot 10^{22}$ W/cm^2, a laser peak power of 4 PW irradiating a channel-type target with the bulk density of 100 n_c and the channel density of 20 n_c. The authors reported a laser energy transfer to gamma photons of 1.5%, for photons with energies higher than 1 MeV. The photon beam was further used for the creation of the electron-positron pairs by the linear Breit-Wheeler process by the two previously mentioned setups: considering the collision of two identical gamma ray beams at a distance of 250 μm from the laser-plasma interaction area and under a collision angle of 90°, which lead to the creation of 10^4 linear Breit-Wheeler pairs, and considering the collision of one gamma ray beam with a black body radiation of 400 eV, which lead to the creation of 10^5 linear Breit-Wheeler pairs. Moreover, the authors reported scaling laws for the number of pairs, according to the laser peak power, for the two setups used for the linear Breit-Wheeler pair creation: in the case of two gamma ray beams colliding with each other the number of pairs is $N_{pairs} \propto P^{2.4}$, and for one gamma ray beam interacting with black body radiation the number of pairs is $N_{pairs} \propto P^{4.5}$, both valid for laser peak powers smaller than 4 PW.

Numerical study of $\gamma - \gamma$ interaction

To study numerically the interaction between two γ-photon beams, we will consider the code proposed by X. Ribeyre et al. [88, 89]. It consists of two identical conical γ-photon beams (prior obtained in laser-plasma interaction) interacting with each other under a collision angle θ, as shown in Figure 1.3. Each photon beam has an initial beam radius R_{ini}, a total energy

E_γ and a half-opening angle ϕ, and the $\gamma-\gamma$ interaction occurs at a given distance D from the laser-plasma interaction area.

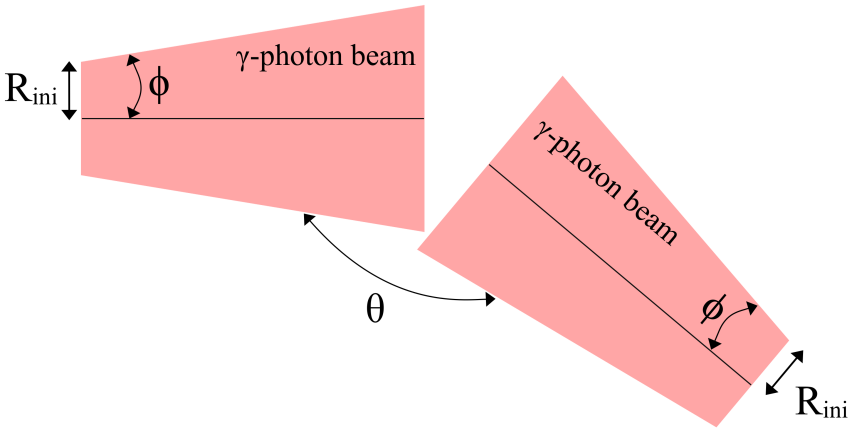

Figure 1.3: Numerical setup: two high energy γ-photon beams with total energy E_γ, beam initial radius R_{ini} and half-opening angle ϕ interacting under a collision angle θ.

An estimate of the total number of pairs created by the linear Breit-Wheeler process is given by [86]:

$$N_p = N_\gamma^2 \frac{\sigma_{\gamma\gamma}(\phi)}{2\pi D^2\left(1-\cos\theta\right)} \tag{1.51}$$

where N_γ represents the total number of photons in each beam. The total cross section of the LBW process $\sigma_{\gamma\gamma}(\theta)$ is given by [90]:

$$\sigma_{\gamma\gamma} = \frac{\pi}{2} r_e^2 \left(1-\beta^2\right)\left[-2\beta\left(2-\beta^2\right)+\left(3-\beta^4\right)\ln\frac{1+\beta}{1-\beta}\right] \tag{1.52}$$

where $\beta = \sqrt{1-1/s}$ and $s = E_\gamma^2(1-\cos\theta)/2m_e^2c^4$.
The cross section is maximum if $s \simeq 2$ [86].

Given the characteristics of the two γ-photon beams (the number of γ-photons, the energy spectrum and the opening angle), the code discretizes the information in each photon beam and solves the total cross section to compute the total number of pairs. In addition, the code solves the angular distribution of the pairs, which depends on the collision angle θ. The numerical algorithm is presented in details in [88, 89].

1.5.2 Nonlinear Breit-Wheeler pair production

The nonlinear Breit-Wheeler process or multiphoton Breit-Wheeler process [91, 92] represents the creation of an electron-positron pair by the decay of a high energy photon in a strong electromagnetic field:

$$\gamma + n\gamma_l \rightarrow e^- + e^+ \tag{1.53}$$

where γ represents an incident high energy photon, n - the number of laser photons participating in the process and γ_l represents a laser photon.

Numerical studies have shown that the production of multiphoton Breit-Wheeler pairs can be achieved by using ultra-high intensity laser pulses interacting with solid targets [93]. The study consisted of the irradiation of an aluminum target by a laser of intensity $4 \cdot 10^{23}$ W/cm^2. The laser energy was converted in a burst of γ-rays with an efficiency of 35% which produced about $8 \cdot 10^9$ pairs by the interaction with the laser electromagnetic field.

The first experimental observation of this process was made at SLAC in 1997 [94]. The experiment consisted of a laser of intensity $I = 10^{19}$ W/cm^2 and 527 nm wavelength colliding with an electron beam of energy 46.6 GeV. In the first step of the process, the enegetic electrons undergo Inverse Compton scattering Eq.1.49 and produce high energy photons, which in a second step, interact with the laser field and produce electron-positron pairs. The simulations performed indicated that, in average, about 1.5 laser photons per electron participate in the first step and 4.7 laser photons per high energy photon participate in the second step of the process. The total number of pairs detected for 20000 laser shots is 106 ± 14.

The numerical study of the nonlinear Breit-Wheeler process in PIC simulations is detailed in Subsection 2.6.5.

1.5.3 Bethe-Heitler pair production

The Bethe-Heitler process [95] consists of the creation of an electron-positron pair by the decay of an energetic photon in the Coulomb field of a nucleus:

$$\gamma + \gamma_Z \rightarrow e^- + e^+ \tag{1.54}$$

where γ represents an incident high energy photon and γ_Z represents a photon of the nucleus Coulomb field.

This process is dominant in high Z materials used in laser-plasma interaction. Experimental studies of a high intensity laser with a solid target have shown the production of $2 \cdot 10^{10}$ pairs in a laser shot [96]. The laser intensity varied in $3 \cdot 10^{19} - 2 \cdot 10^{20}$ W/cm^2, the pulse duration between $0.7 - 10$ ps and the laser energy between $120 - 250$ J. There were multiple targets used: high Z targets (gold and tantalum) and low Z targets (tin, copper, aluminum) with thicknesses varying between $0.1 - 1$ mm. The maximum number of pairs ($2 \cdot 10^{10}$) was obtained for a 1 mm thick gold target. In addition, the number of pairs in the rear direction was about 10 times higher than the one from the front side of the target. There were no pairs observed for the low Z targets considered, and neither for thicknesses < 250 μm.

Another competing process in high Z materials is the trident process, corresponding to the interaction of a high energy electron with the Coulomb field of an atom, which results in the creation of a pair:

$$e^- + \gamma_Z \rightarrow e^- + e^+ e^- \tag{1.55}$$

where γ_Z represents a photon of the atom Coulomb field.

A numerical study comparing the two competing processes in the interaction of a high intensity laser pulse with a gold foil was performed in [97]. The cross section of the trident process is about 100 times smaller than the one of Bethe-Heitler process. However, for a fixed laser pulse intensity of 10^{20} W/cm^2 and variable thickness of the gold foil in $10 - 40$ μm, the authors found that the dominant pair creation process is dependent on the target thickness: up to a thickness of < 20 μm, the trident process dominates; above 20 μm, the number of Bethe-Heitler pairs is higher than the trident pairs (for a thickness of 40 μm, the authors found a total number of Bethe-Heitler pairs of $3.1 \cdot 10^9$, while the number of trident pairs is $1.4 \cdot 10^9$). In addition, the variation of the total number of pairs with the laser intensity was studied. The laser energy was kept constant at 280 J and the target thickness was 125 μm. The intensity was varying in $10^{19} - 10^{21}$ W/cm^2. The maximum number of pairs was $5 \cdot 10^{10}$ for the highest intensity considered.

Estimation of the total number of pairs produced by Bethe-Heitler process

We consider a high Z target irradiated by a high intensity laser pulse. The electrons will be accelerated and will emit high energy radiation, which, in the Coulomb field of the target, will undergo the Bethe-Heitler process generating pairs. The total number of pairs created is given by:

$$N_{e^+_{BH}} = N_i \cdot N_\gamma \cdot \frac{\sigma_{BH}}{S} \tag{1.56}$$

where N_i, N_γ - are the numbers of ions, respectively photons inside the interaction volume, σ_{BH} - the total Bethe-Heitler cross section and S - the target surface.

The total Bethe-Heitler cross section can be estimated as:

$$\sigma_{BH} \approx Z^2 \cdot r_e^2 \cdot \alpha \tag{1.57}$$

where $r_e = 2.8 \cdot 10^{-13}$ cm is the electron radius and $\alpha = 1/137$ is the fine structure constant.

The number of ions in the target is:

$$N_i = \frac{\rho}{A \cdot m_p} \cdot V \tag{1.58}$$

where $V = S \cdot L$ is the target volume with L the target thickness, ρ - the target density, A - the atomic mass number, m_p - the proton mass.

Introducing Eq.(1.57) and Eq.(1.58) in Eq.(1.56) and normalizing the units, we will obtain the total number of Bethe-Heitler pairs as:

$$N_e^+ = 6.36 \cdot 10^{-7} \cdot Z \cdot \frac{n_e}{n_c} \cdot N_\gamma \cdot L_{cm} \cdot \frac{1}{\lambda_\mu^2} \tag{1.59}$$

where n_e - the target density, $n_c = 1.1 \cdot 10^{21}$ cm$^{-3}/\lambda^2_{\mu\mathrm{m}}$ - the critical density and λ is the laser wavelength.

Given the target and the laser characteristics and the total number of photons generated in the laser-target interaction, we can estimate from Eq.(1.59) the total number of the Bethe-Heitler pairs produced. However, to obtain Eq.(1.59) we assumed that all photons generated in the laser-plasma interaction will suffer the Bethe-Heitler process, which may not be the case in

real experiments due to other processes which can occur. Consequently, Eq.(1.59) may lead to an overestimation of the total number of Bethe-Heitler pairs produced.

Chapter 2

Particle-in-cell simulations

This chapter aims to introduce the concepts of computer simulations for plasma physics, mainly the Particle-in-cell method. In Section 2.1 we describe the main ingredients of the Particle-in-cell (PIC) recipe and the PIC code used for this work: SMILEI. In Section 2.2, the numerical integration of the physical quantities is explained. Further, the practical aspects of the SMILEI code are pointed out in Section 2.3 and Section 2.4. The physical quantities computed are presented in Section 2.5 and the additional physical modules in Section 2.6. The following two sections are dedicated to numerical studies performed with SMILEI: convergence studies of the physical quantities of interest in Section 2.7 and consumed power of the computing system in Section 2.8.

This chapter is inspired by the following literature [98, 21, 99], as well as the SMILEI official website [100], if not otherwise indicated.

2.1 PIC method

A Particle-in-Cell code consists in solving the Maxwell-Vlasov system of equations. Consider a plasma made of particle species α of charge q_α which interact between each other through their self-generated electromagnetic fields (no laser is considered). In order to solve numerically the evolution in time of this system, two mathematical grids are used: a temporal grid to follow the particle evolution and a spatial grid to follow the fields evolution. The physical

quantities will be discretized and computed in time step by step for a given number of steps. At the initial time step, the position and the velocity of the particles are known (the initial profile of the plasma), as shown in Fig.2.1.

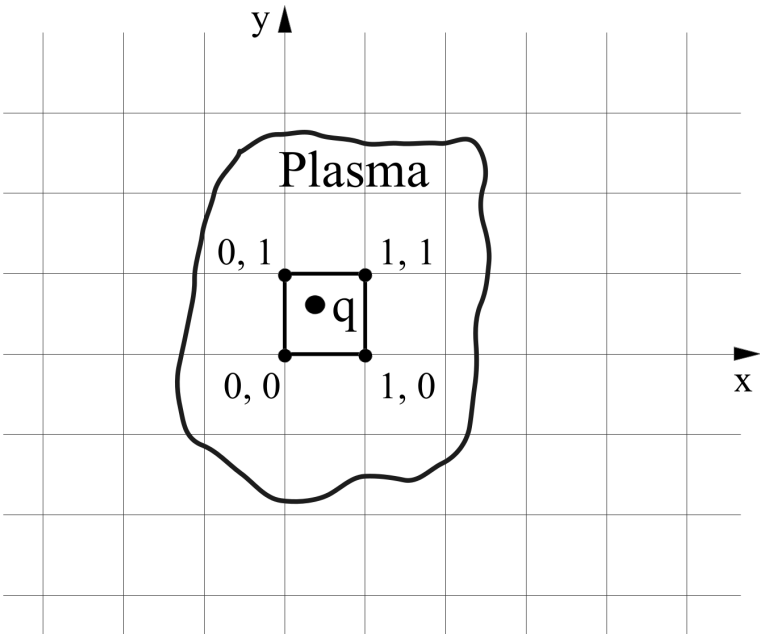

Figure 2.1: A mathematical grid to measure charge and current densities. The particle q will contribute to the charge density in all nearby grid points and to the current density at the faces between these points. Adapted from [98].

The discretization of the particle properties is made by a distribution function which sums all N_α computational particles for each species of the plasma:

$$f_\alpha(\vec{r},\vec{p},t) = \sum_{i=1}^{N_\alpha} w_i S\big(\vec{r}-\vec{r}_i(t)\big)\,\delta\big(\vec{p}-\vec{p}_i(t)\big) = 0 \tag{2.1}$$

where w_i is the weight of a computational particle, $S(\vec{r}-\vec{r}_i)$ is the shape function of all computational particles, $\vec{r}_i$ its position, $\vec{p}_i$ its momentum, δ is the Dirac distribution. More information about the computational particles will be explained in the Macroparticles section.

A particle q_i will contribute to the electric and magnetic fields on all nearby grid points. Its contribution will be quantified in the grid quantities charge and current densities using Eqs.((1.11)) - ((1.12)), from which the electric and magnetic fields will be computed through Maxwell equations ((1.1)) - ((1.4)). In the end of the initialization time step, the forces which act on the particles will be computed with the Lorentz formula ((1.9)). In the next time step, the equations of motions will be integrated from which the positions and the velocities of the

particles will be updated and the whole procedure will start over again. This procedure is called PIC loop and is repeated for a given number of time steps as shown in Fig.2.2.

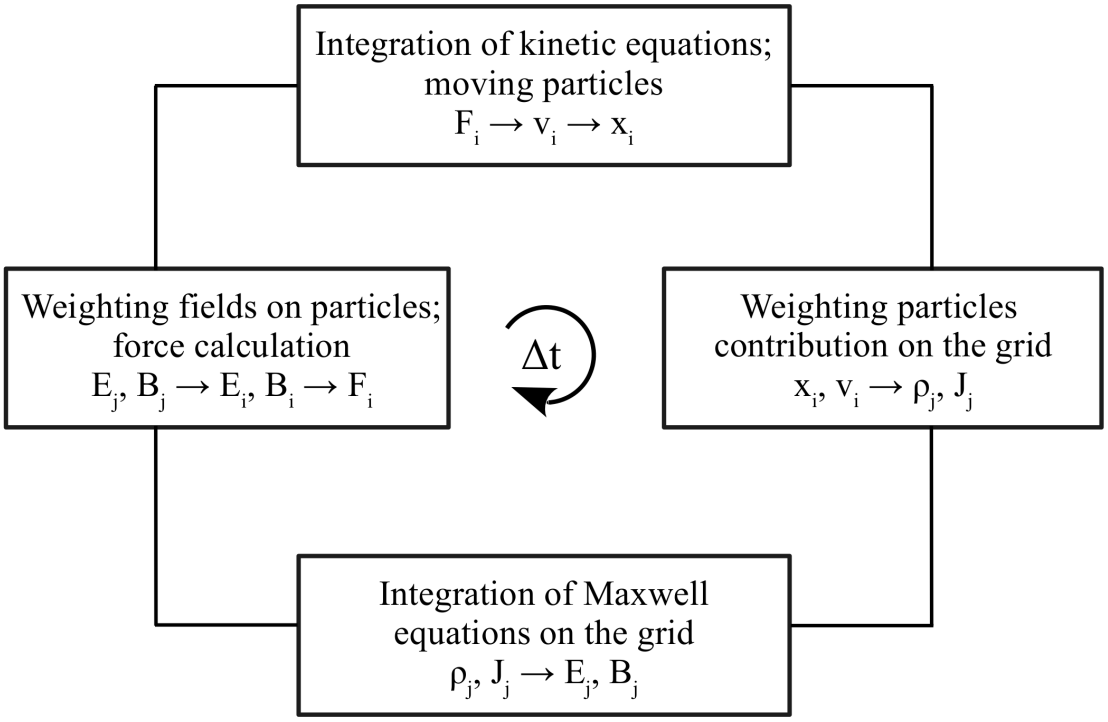

Figure 2.2: The PIC cycle; particles are numbered with i and grid points are numbered with j. Adapted from [98].

2.1.1 SMILEI

SMILEI (Simulating Matter Irradiated by Light at Extreme Intensities) [99] is an open-source, fully-relativistic PIC code designed for high performance computing on massively parallel supercomputers. It was developed to study new regimes of laser-plasma interaction and matter under extreme conditions, where the non-linear quantum effects are important. SMILEI can be used to study a wide range of physics problems: laser driven ion acceleration [101, 102], relativistic acceleration of electrons [103] and astrophysics [104, 105].

SMILEI needs an appropriate environment for high-performance computing (HPC) tasks. Prior to SMILEI installation, a set of mandatory dependencies should be installed like a C++ compiler, MPI and HDF5 libraries, Python3. There are also other supplementary optional dependencies, which are needed for post processing the data obtained like the happi and pint python modules. SMILEI was successfully installed, with all its mandatory and supplementary dependencies, on the Curta machine from the Mésocentre de Calcul Intensif Aquitain (MCIA)

of the Université de Bordeaux and of the Université de Pau et des Pays de l'Adour [106] and on the HybriLIT Platform of the Laboratory of Information Technologies of the Joint Institute for Nuclear Research [107].

2.2 Numerical integration of particles and fields

In the following section, each step of the PIC method will be detailed. The computational particles will be referred to as macroparticles and the grid spatial discretization will be referred to as grid cell or cell. For simplicity, we will use the normalization $c = 1$ in the Maxwell equations.

2.2.1 Macroparticles

A computational particle or a macroparticle is a computational representation of a real particle from the studied system. The macroparticles can represent a large number of real particles. Each macroparticle contributes to the distribution function of the particle species of our plasma through a statistical weight, which is computed at the initialization of the simulation as:

$$w_\alpha = \frac{n_{\alpha 0}}{N_\alpha} \cdot V_c \tag{2.2}$$

where $n_{\alpha 0}$ is the density of the particle species, N_α the number of macroparticles per cell and V_c the volume of the cell.

In order to compute the charge and current contribution of a macroparticle to the grid points (as seen in Fig.2.1), a shape function is assigned to each particle. Different shape functions $S(\vec{r})$ can be used (e.g. triangular, quadratic, spline), having the following properties:

- symmetry with respect to $\vec{r}$, where $\vec{r}$ is the position vector to the center of mass
- $S(\vec{r}) \neq 0$ in a region centered around $\vec{r} = 0$ that extends over the cell size
- normalization to 1:

$$\int S(\vec{r}) d\vec{r} = 1 \tag{2.3}$$

2.2.2 Characteristic equations of motion

To obtain the equations of motion for the macroparticles, we introduce Eq.(2.1) in the Eq.(1.10) and first we multiply by $\vec{p}$ and integrate over $d\vec{p}$:

$$\begin{aligned}\int \frac{\partial}{\partial t}\sum_{i=1}^{N_\alpha} w_i S\big(\vec{r}-\vec{r}_i(t)\big)\,\delta\big(\vec{p}-\vec{p}_i(t)\big)\,\vec{p}\,d\vec{p}+ \\ +\int \vec{v}_i\cdot\frac{\partial}{\partial \vec{r}}\sum_{i=1}^{N_\alpha} w_i S\big(\vec{r}-\vec{r}_i(t)\big)\,\delta\big(\vec{p}-\vec{p}_i(t)\big)\,\vec{p}\,d\vec{p}+ \\ +\int \cdot\frac{\partial}{\partial \vec{p}}\sum_{i=1}^{N_\alpha} w_i S\big(\vec{r}-\vec{r}_i(t)\big)\cdot q_\alpha\cdot(\vec{E}+\vec{v}_i\times\vec{B})\cdot\delta\big(\vec{p}-\vec{p}_i(t)\big)\,\vec{p}\,d\vec{p}=0\end{aligned} \tag{2.4}$$

and using the properties of the Dirac function:

$$\int \delta(\vec{p}-\vec{p}_i(t))d\vec{p} = 1 \tag{2.5}$$

$$\int \vec{p}\,\delta(\vec{p}-\vec{p}_i(t))d\vec{p} = \vec{p}_i(t) \tag{2.6}$$

we will obtain:

$$\begin{aligned}\sum_{i=1}^{N_\alpha} w_i S\big(\vec{r}-\vec{r}_i(t)\big)\frac{\partial \vec{p}_i(t)}{\partial t}+\sum_{i=1}^{N_\alpha} w_i S\big(\vec{r}-\vec{r}_i(t)\big)\,\vec{p}_i(t)\cdot\vec{v}_i\Bigg[\frac{\partial S\big(\vec{r}-\vec{r}_i(t)\big)}{\partial \vec{r}}- \\ -\frac{\partial S\big(\vec{r}-\vec{r}_i(t)\big)}{\partial \vec{r}_i}\Bigg]-\sum_{i=1}^{N_\alpha} w_i S\big(\vec{r}-\vec{r}_i(t)\big)\cdot q_\alpha\cdot(\vec{E}+\vec{v}_i\times\vec{B})=0\end{aligned} \tag{2.7}$$

We will integrate Eq.(2.7) over $d\vec{r}$ and using the property of the shape function Eq.(2.3), we will obtain the equations of motion:

$$\frac{d\vec{p}_i}{dt} = q_\alpha\left(\vec{E}_i+\frac{\vec{p}_i}{m_\alpha\gamma_i}\times\vec{B}_i\right) \tag{2.8}$$

$$\frac{d\vec{r}_i}{dt} = \vec{v}_i \tag{2.9}$$

where we introduced the macroparticle Lorentz factor $\gamma_i=\sqrt{1+(\vec{p}_i/m_\alpha)^2}$ and the fields are interpolated at the particle position as:

$$\vec{E}_i = \int S\big(\vec{r}-\vec{r}_i(t)\big)\vec{E}(\vec{r})d\vec{r} \tag{2.10}$$

$$\vec{B}_i = \int S\big(\vec{r}-\vec{r}_i(t)\big)\vec{B}(\vec{r})d\vec{r} \tag{2.11}$$

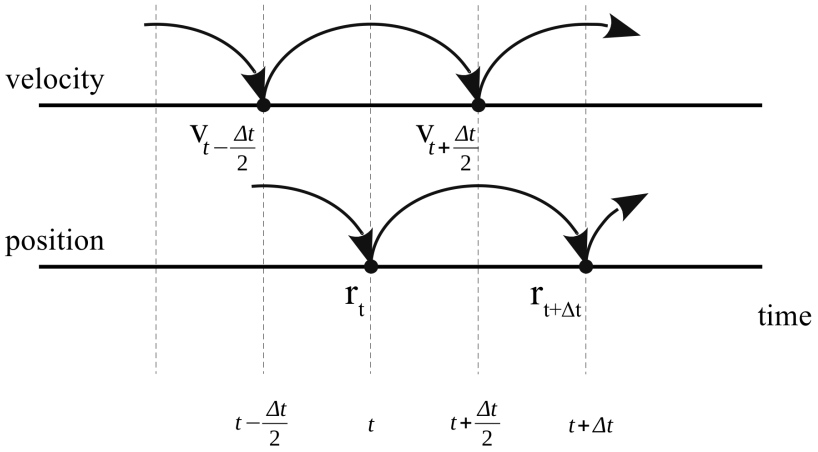

Figure 2.3: Leapfrog method. The particles advance from time step t to time step $t+\Delta t$: particles position r is computed at integer time steps Δt, while their velocity v is computed at half-integers time steps. Adapted from [98].

We consider the distribution of the macroparticles from which we know their velocities $\vec{v}_t$ and positions $\vec{r}_t$ at the time step t, and we want to compute their new positions and velocities at the time step $t+\Delta t$. The numerical integration of the equations (2.8) and (2.9) is made according to a leapfrog method, where we replace the equations of motion by their equivalent finite-difference equations. The leapfrog method is illustrated in Fig.2.3.

The velocity of the macroparticles will be computed at half integer time steps:

$$\frac{\vec{p}_i^{(t+\frac{\Delta t}{2})} - \vec{p}_i^{(t-\frac{\Delta t}{2})}}{\Delta t} = q_\alpha \left[\vec{E}_i^{(t)} + \left(\frac{\vec{p}_i^{(t+\frac{\Delta t}{2})}}{\gamma_i^{(t+\frac{\Delta t}{2})}} - \frac{\vec{p}_i^{(t-\frac{\Delta t}{2})}}{\gamma_i^{(t-\frac{\Delta t}{2})}} \right) \frac{1}{2m_\alpha} \times \vec{B}_i^{(t)} \right] \tag{2.12}$$

while their position will be computed at integer time steps:

$$\frac{\vec{r}_i^{(t+\Delta t)} - \vec{r}_i^{(t)}}{\Delta t} = \vec{v}_i^{(t+\frac{\Delta t}{2})} \tag{2.13}$$

In SMILEI, three different leap-frog schemes have been implemented: the Boris pusher [108], the J.-L. Vay pusher [109] and the Higuera and Cary pusher [110]. For laser intensities $> 10^{24}$ W/cm^2, as the electron motion will be ultra-relativistic, the Boris pusher may induce errors, except if a very fine resolution is used. We studied the influence of the particles pushers on the emission of high energy radiation in the case of a laser intensity of 10^{23} W/cm^2 interacting with an electron beam of energy 0.5 GeV and we did not observe any difference between

the three particle pushers. The particle pusher used further in all our simulations is the one proposed by J.-L. Vay.

2.2.3 Integration of fields

To find the electric and magnetic fields at the macroparticle position, we need to compute first the charge and the current density from the distribution function of the macroparticles. Implementing Eq.(2.1) in Eq.(1.11) and Eq.(1.12), and using the property given in Eq.(2.5) we will obtain the charge and current density for each macroparticle species:

$$\rho_\alpha(\vec{r},t) = \sum_{i=1}^{N_\alpha} q_\alpha w_i S\big(\vec{r}-\vec{r}_i(t)\big) \tag{2.14}$$

$$\vec{J}_\alpha(\vec{r},t) = \sum_{i=1}^{N_\alpha} q_\alpha \vec{v}_i w_i S\big(\vec{r}-\vec{r}_i(t)\big) \tag{2.15}$$

The total charge and current density will be given by the sum of all macroparticle species contribution. According to their definition by the above equations, the charge density will be computed at integers time steps and the current density will be computed at the half integers time steps.

The leapfrog method is also used for the numerical integration of the electric and magnetic fields. The electric field will be computed at integers time steps by integrating Eq.(1.4):

$$\frac{\vec{E}^{(t+\Delta t)}-\vec{E}^{(t)}}{c^2\Delta t} = \big(\vec{\nabla}\times\vec{B}\big)^{(t+\frac{\Delta t}{2})} - \mu_0\vec{J}^{(t+\frac{\Delta t}{2})} \tag{2.16}$$

while the magnetic field will be computed at half integers by integrating Eq.(1.3):

$$\frac{\vec{B}^{(t+\frac{3\Delta t}{2})}-\vec{B}^{(t+\frac{\Delta t}{2})}}{\Delta t} = -\big(\vec{\nabla}\times\vec{E}\big)^{(t+\Delta t)} \tag{2.17}$$

The numerical integration of the ∇ operations is done by using the finite-difference time-domain (FDTD) [111]. This method implies a Courant-Friedrich-Lewy condition for the spatial and temporal time step as following:

$$c\Delta t < \Delta x \tag{2.18}$$

which has the physical interpretation that the information cannot propagate through more than one cell during one time step. In addition, the size of the cell should be chosen small enough to resolve a Debye length.

2.2.4 Numerical Cherenkov

Cherenkov radiation occurs when the velocity of a high-energy particle in a medium is higher than the phase velocity of the light in that medium. Numerical Cherenkov radiation occurs due to the reduced velocity of light in vacuum or in a plasma due to the Maxwell solvers. In particular it can occur for very low density plasmas and can affect the energy spectrum of the accelerated particles. This radiation can be suppressed by using a temporal filtering for the electric field and a spatial filtering for the current density.

In SMILEI, the electric field in the Maxwell-Faraday solver is replaced by the temporally filtered electric field from [112] given at time step n by:

$$E^{(n)} = \big(1+\frac{\theta}{2}\big)E^{(n)} - \big(1-\frac{\theta}{2}\big)E^{(n-1)} + \frac{1}{2}(1-\theta)^2\overline{E}^{(n-2)} \tag{2.19}$$

where $\overline{E}^{(n-2)} = E^{(n-2)} + \theta\overline{E}^{(n-3)}$ and $\theta \in [0,1]$ is a defined input parameter.

The current density is spatially filtered by a multi-pass function. Each pass consists in a N-point spatial averaging (in one or all spatial dimensions) of the current densities. The filtered current density will be given by:

$$J_{f,i} = \sum_{n=-(N-1)/2}^{(N-1)/2} K_{(N-1)/2+n} J_{i+n} \tag{2.20}$$

where i is the location of the grid and the number of passes f is a defined input parameter.

2.3 Boundary conditions

Boundary conditions must be applied to our simulation, one set for the macroparticles and one set for the electromagnetic fields.

The boundary conditions for the macroparticles can be:

- periodic: the macroparticles loop around the simulation box
- reflective: the macroparticles are reflected at the boundary
- stop: the momentum of the macroparticles is set to zero
- remove: the macroparticles are deleted from the memory
- thermalize: the macroparticles are set back inside the simulation box with a randomly sampled momentum from a Maxwellian distribution

The boundary conditions for the electromagnetic fields can be:

- Silver - Müller: the electromagnetic fields are injected or are absorbed
- reflective: the electromagnetic fields are reflected
- periodic: the electromagnetic fields are injected from the opposite boundary

2.4 Normalized units

To avoid performing calculations with very small or very large numbers, PIC codes are usually normalized to some reference units. Some basic normalization units used in SMILEI are the following: the velocities are normalized to c, the particles charge and mass are normalized to the elementary charge e respectively mass m_e. Consequently, the particle momentum will be normalized to $m_e c$ and the particle energy to $m_e c^2$.

In addition, SMILEI proposes an arbitrary normalization for time and space. All temporal and spatial quantities will be normalized to an arbitrary factor called reference frequency ω_r which, according to our problem, can be the plasma or the laser angular frequency. Some of the quantities normalized to ω_r are:

- the time $T_r = 1/\omega_r$

- the length $L_r = c/\omega_r$
- the electric field $E_r = m_e c\omega_r/e$
- the magnetic field $B_r = m_e\omega_r/e$
- the particle density $N_r = \varepsilon_0 m_e\omega_r^2/e^2$
- the current density $J_r = ceN_r$
- the pressure $P_r = m_e c^2 n_r$
- the Poynting flux $S_r = m_e c^3 n_r/2$

2.5 Diagnostics

The goal of a simulation is to gain detailed information regarding the physics of plasmas, the data collection being performed by the diagnostics. These diagnostics are part of the input file, hence they must be chosen before the simulation runs. Having total control of the input and output data, one could choose to save all the data obtained at each time step in order to obain the full information of the numerical experiment. However, this can lead to the storage of hundreds of gigabytes of data which may be difficult to analyze. Therefore, the diagnostics chosen for our simulation should be representative for the phenomena under study.

At minimum, the diagnostics can give us information regarding the particles (position, momentum, energy distribution), the fields (the electric and magnetic fields) or a global picture of the energy balance during the simulation. Sometimes, the raw data requires a postprocessing in order to obtain the physical information of interest.

The diagnostics of interest for this work are the following:

- **Scalar diagnostic**

  It collects a wide range of averaged or integrated in space or in time quantities regarding the particles or the electromagnetic fields. The following quantities are important for our postprocessing:

  - the total kinetic energy of all particle species
  - the total radiated energy of the particles
  - the total electromagnetic energy of the fields
  - the total energy in the simulation box
  - the instanteneous Poynting vector exchanged at the boundaries
  - the kinetic energy exchanged at the boundaries

- **Field diagnostic**

  It collects data for the grid quantities like the electric and magnetic fields (which we are mostly interested in), and the particle densities and currents.

- **Particle binning**

  It collects averaged quantities regarding the macroparticles in a chosen grid. The important quantities used in this thesis are:

  - the density map of the particles
  - the energy density map of the particles
  - the phase space of the particles
  - the energy distribution of the particles
  - the energy angle distribution of the particles

- **Track particles**

  It collects the position and the momentum of macroparticles selected using specific conditions on their momentum or on their position.

2.6 Additional physical modules in PIC codes using the Monte Carlo method

Depending on the phenomena of interest, the PIC code may not contain all physical information needed and additional modules should be considered. Multiple physical modules are implemented in SMILEI, some of them using a statistical approach to the theory like a Monte Carlo scheme to calculate the probability of one event to occur. In the following section each module will be shortly presented.

2.6.1 Field ionization

At the interaction between a laser and a solid target, the target ionization will occur prior to particle acceleration. This phenomena can have an impact on the spectrum of the accelerated particles, which is not included in the standard PIC method. To account for this, a Monte Carlo scheme is implemented in SMILEI inspired by [113]. This scheme can allow multiple ionization events to occur in the same time step. The cumulative probability to ionize from 0 to k times a macro-ion with initial charge state Z^* during the time step Δt is given by:

$$F_k^{Z^*} = \sum_{j=0}^{k} p_j^{Z^*} \tag{2.21}$$

where $p_j^{Z^*}$ is the probability of the macro-ion to be ionized j times given by the ADK (Ammosov Delone Krainov) theory [114].

The Monte Carlo scheme consists in sampling a random number $r \in [0,1]$, which is compared with the probability to not ionize the macro-ion p_0^{Z*}. If $r < p_0^{Z*}$, then the macro-ion is not ionized. Otherwise, we sum over all number of ionization events k. Finally, the macro-electron is created with the weight k times of that of macro-ion and with the same velocity. The macro-ion charge is also increased by k.

2.6.2 Collisions

In a collisionless plasma the collective effects dominate over one-to-one particle collisions, consequently a PIC code solves the Maxwell-Vlasov system of equations where collisions are neglected. However, in dense and cold targets, collisions may occur and may lead to small deviations on particles trajectories. To simulate these effects, the additional module in SMILEI uses the following algorithm, inspired by [115]:

- the macroparticles species are randomly paired so each collides with one another at a given time step
- the collision rate is computed as:

$$s =< \theta^2 > N/2 \tag{2.22}$$

  where N is the total number of collisions in a time step and θ is the expected value for the deflection angle for a single collision given by [116]:

$$< \theta^2 >= 8 \int_0^1 \tan^{-1}\left[\frac{\theta_{min}}{2\eta}\right]^2 \eta d\eta \tag{2.23}$$

  with θ_{min} the minimal deflection angle corresponding to a Rutherford scattering.

- the deflection angle χ of the scattered macroparticles is computed as:

$$\sin^2\frac{\chi}{2} = \begin{cases} \alpha U/\sqrt{1-U+\alpha^2 U}, & s < 4 \\ 1-U, & \text{otherwise} \end{cases} \tag{2.24}$$

  where U is a random number in $[0,1]$ and $\alpha = 0.37s - 0.005s^2 - 0.0064s^3$

- the macroparticles are deflected and their momentum is updated.

2.6.3 Nuclear Reaction

In order to study inertial confinement fusion or radioisotope production with a PIC code, an additional module is needed. In SMILEI, the nuclear reactions represent a particular case of

the collisions module, where are introduced the cross sections of the reaction. The algorithm consists in the following steps:

- the cross-section of the reaction σ_{AB} is interpolated, given the kinetic energies of the two macroparticles A and B (the cross-sections are tabulated)
- the probability for a nuclear reaction to occur at a given time step Δt in a volume V [117] is given by:

$$P_{fusion} = F_{mult} \cdot N_{ratio} \cdot W_{max} \cdot \sigma_{A,B} \cdot v_{AB} \cdot \frac{\Delta t}{V} \tag{2.25}$$

  where:

  - $v_{AB} = |v_A - v_B|$ is the relative velocity between the macroparticles
  - N_{ratio} a factor to ensure nuclear reaction between only one pair of macroparticles
  - W_{max} the maximum value of the weight of the two macro-particles
  - F_{mult} is a multiplication factor to increase the statistical probability of the event.

- a random number $u \in [0,1]$ is sampled:

  - if $u < P_{fusion} \Rightarrow$ fusion event occurs
  - if $u > P_{fusion} \Rightarrow$ normal collision

  If the nuclear reaction occurs, the new macroparticles are created and their angles are sampled from a tabulated distribution and their momenta are calculated from the conservation of the total energy and momentum.

2.6.4 Radiation Reaction

As pointed out in the previous chapter, a charged particle moving in an electromagnetic field will start to lose energy by emitting electromagnetic radiation. The radiation emitted can influence the dynamics of the particle. This phenomena is known as radiation reaction effect. There are different regimes for the emission of radiation and its effect on the particle dynamics implemented in SMILEI. They are characterized by the particle quantum parameter:

$$\chi = \frac{\gamma}{E_s} \sqrt{(\vec{E} + \vec{v} \times \vec{B})^2 - \frac{(\vec{v} \cdot \vec{E})^2}{c^2}} \tag{2.26}$$

where $\gamma = \varepsilon/m_e c^2$ is the particle Lorentz factor and $\vec{v}$ is the particle velocity.

Classical radiation emission - Landau-Lifshitz

The first description of radiation reaction is the classical one of Landau and Lifshitz (discussed also in the previous chapter), where the particles lose continuously energy by radiating. In this case, the energy of the emitted photons is much smaller than the energy of the emitting electrons and the parameter $\chi \sim 10^{-3}$. The radiation reaction is approached as a damping force acting on particles [118]:

$$\vec{F}_{rad} = -P_{cl} \cdot \frac{\vec{v}}{\vec{v}^2 c} \tag{2.27}$$

where $P_{cl} = 2q^2 mc^2 \chi^2/(2\tau_e)$ is the classical Larmor power with $\tau_e = r_e/c$, the time needed for a photon to cross the classical radius of the electron. Eq.(2.27) is valid as long as $\gamma >> 1$.

Semi-classical radiation emission - corrected Landau-Lifshitz

For $\chi \sim 10^{-2}$, we have a field which is close to the Schwinger field, but the energy of the emitted photons is not yet comparable with the energy of the emitting electrons. In this case, a correction is needed to the previous formula. The radiated power will be [100]:

$$P_{rad} = P_{cl} \cdot g(\chi) \tag{2.28}$$

with

$$g(\chi) = \frac{9\sqrt{3}}{8\pi} \int_0^{+\infty} d\nu \left[\frac{2\nu^2}{(2+3\nu\chi)^2} K_{5/3}(\nu) + \frac{4\nu(3\nu\chi)^2}{(2+3\nu\chi)^4} K_{2/3}(\nu) \right] \tag{2.29}$$

where $K_{5/3}, K_{2/3}$ are the modified Bessel functions and $\nu = 2\chi_\gamma/[3\chi(\chi_\gamma - \chi)]$.

Weak quantum regime - Niel's model

In the case of a weak quantum regime, $\chi \sim 10^{-1}$, the continuous models cannot be used anymore, the emission of photons being more appropriately described by a stochastic event. However, the energy of the photons remains small with respect to that of the emitting electrons.

The description of this intermediate regime was made by F. Niel et al. [118]. In this case, we will consider the corrected Landau Lifshitz model in which we will add a term linked to the stochasticity of the emission of photons. The new 'damping' force will be:

$$\vec{F}_{rad}dt = \left[-P_{cl}g(\chi)dt + mc^2\sqrt{R(\chi,\gamma)}dW \right] \frac{\vec{v}}{\vec{v}^2 c} \tag{2.30}$$

where dW is a Wiener process of variance dt,

$$R(\chi,\gamma) = \frac{2}{3}\frac{\alpha^2}{\tau_e}\gamma h(\chi) \tag{2.31}$$

with α - the fine structure constant and

$$h(\chi) = \frac{9\sqrt{3}}{4\pi}\int_0^{+\infty} d\nu \left[\frac{2\chi^3\nu^3}{(2+3\nu\chi)^3}K_{5/3}(\nu) + \frac{54\chi^5\nu^4}{(2+3\nu\chi)^5}K_{2/3}(\nu) \right] \tag{2.32}$$

Quantum regime - Monte Carlo model

When $\chi \sim 1$, the emitted photon energies are of the order of the emitting electron energies. In this case, the emission of photons is described only by a stochastic process, which is computed as a function of the particle field and energy. In this case, the electron dynamics is governed by the Lorentz force between two emission events.

The Monte Carlo algorithm is divided in the following steps [100]:

- An incremental optical depth τ is assigned to each particle. Emission occurs for $\tau = \tau_f$ where τ_f is sampled from $\tau_f = -\log\xi$ and ξ is a random number in $[0,1]$.
- The optical depth evolves according to:

$$\frac{d\tau}{dt} = \frac{2}{3}\frac{q^2}{\tau_e}\int_0^{\chi_\pm} \frac{S(\chi_\pm, \chi/\chi_\pm)}{\chi} d\chi = \frac{2}{3}\frac{q^2}{\tau_e}K(\chi_\pm) \tag{2.33}$$

  where $\chi_\pm$ is the emitting electron or positron quantum parameter and ξ the integration variable.

$S(\chi,\xi)$ is the quantum emissivity:

$$S(\chi_\pm,\xi_\pm) = \frac{\sqrt{3}}{2\pi}\xi_\pm\left[\int_\nu^\infty K_{5/3}(y)dy + \frac{\xi^2}{1-\xi}K_{2/3}(\nu)\right] \tag{2.34}$$

with $\xi_\pm = \chi_\gamma/\chi_\pm = \gamma_\gamma/\gamma$.

- The quantum parameter χ_γ of the emitted photon is computed by inverting the cumulative distribution function:

$$\xi = P(\chi_\pm,\chi_\gamma) = \frac{\int_0^{\chi_\gamma} d\chi S(\chi_\pm,\chi/\chi_\pm)/\chi}{\int_0^{\chi_\pm} d\chi S(\chi_\pm,\chi/\chi_\pm)/\chi}. \tag{2.35}$$

- The energy of the emitted photon is computed as:

$$\varepsilon_\gamma = mc^2\gamma_\gamma = mc^2\gamma_\pm\chi_\gamma/\chi_\pm. \tag{2.36}$$

- The particle momentum is then updated as:

$$\vec{p} = -\frac{\varepsilon_\gamma}{c}\frac{\vec{p}_\pm}{\|\vec{p}_\pm\|}. \tag{2.37}$$

then the force which acts on the particle is computed.

2.6.5 Nonlinear Breit-Wheeler pair creation

At the interaction between a strong electromagnetic field and a high-energy photon, the later one can decay into an electron-positron pair. This process is known as the multiphoton Breit-Wheeler process or nonlinear Breit-Wheeler process and will be experimentally reachable with ultra-high intensity lasers (multipetawatt lasers).

The simulation of this process requests an additional module which, in SMILEI, consists of the following Monte Carlo algorithm similar to the radiation reaction one:

- An incremental optical depth τ is assigned to each macro-photon. The decay occurs for $\tau = \tau_f$ where τ_f is sampled from $\tau_f = -\log\xi$ and ξ is a random number in $[0,1]$.

- The optical depth evolves according to:

$$\frac{d\tau}{dt} = \frac{dN_{BW}}{dt}\chi_\gamma \tag{2.38}$$

where χ_γ is given by Eq.(2.26) and the production rate of pairs is given by:

$$\frac{dN_{BW}}{dt} = \frac{\alpha_f m_e^2 c^4}{\hbar\varepsilon_\gamma}\cdot\frac{1}{\pi\sqrt{3}\chi_\gamma}\cdot\int_0^\infty\left[\int_x^\infty \sqrt{s}K_{1/3}\left(\frac{2}{3}s^{3/2}\right)ds - \right.$$
$$\left. - \left(2-\chi_\gamma x^{3/2}K_{2/3}\left(\frac{2}{3}x^{2/3}\right)d\chi_-\right)\right] \tag{2.39}$$

with α_f - the fine structure constant.

- The quantum parameter of the emitted electron χ_- is computed by inverting the cumulative distribution function:

$$\varepsilon' = P(\chi_-,\chi_\gamma) = \frac{\int_0^{\chi_-}\frac{d^2N_{BW}}{d\chi dt}d\chi}{\int_0^{\chi_\gamma}\frac{d^2N_{BW}}{d\chi dt}d\chi} \tag{2.40}$$

where ε' is a random number in $[0,1]$. The positron quantum parameter is $\chi_+ = \chi_\gamma - \chi_-$.

- The energy of the emitted electron is computed as:

$$\varepsilon_- = mc^2\gamma_- = mc^2[1+(\gamma_\gamma-2)\chi_-/\chi_\gamma] \tag{2.41}$$

- The photon momentum is then updated and the pairs are created at the same position as of the photon.

2.7 Convergence studies

We studied the convergence of physical quantities for the variation of different numerical parameters. This set of simulations aims at describing the influence of the cell length and of the total number of particles in each cell of the simulation grid, on the physical quantities.

We consider the interaction between an ultra high intensity laser pulse and a near critical density plasma. The laser pulse has a temporal and spatial Gaussian profile of peak intensity

$I = 10^{22}$ W/cm^2($a_0 = 85$), pulse duration $\tau = 20$ fs FWHM, laser wavelength $\lambda = 1$ μm and laser waist $w_0 = 12.5$ μm. The plasma initially cold is made of electrons and protons with a density $n_{e0} = 10$ n_c (where $n_c = 1.1 \cdot 10^{21}$ cm^{-3} for a laser wavelength of 1 μm), a thickness of 15 μm and a transversal width of 30 μm. The laser will irradiate the plasma at normal incidence and will transfer a significant part of its energy to the plasma constituents. At this ultra-high intensity, the motion of electrons will be relativistic, in consequence they will emit high energy radiation. The 2D PIC simulations were performed on the Curta machine - MCIA [106] and on the HybriLIT supercomputer [107].

We are interested in the variation of the total energy absorbed by the plasma constituents and of the total high energy radiation emitted by the electrons, both divided by the initial laser energy, with the numerical parameters previously mentioned.

2.7.1 The influence of the cell length

In Fig.2.4 is shown the variation of the absorption coefficient of the laser energy to plasma constituents with the longitudinal cell length. When the cell length is too large, the total energy in the simulation box is not conserved and the absorbed energy is much higher than the initial electromagnetic energy. The cell length has the opposite effect on the total energy absorbed in high energy photons, which decreases when the cell length increases as shown in Fig.2.5. The unphysical behaviour of the simulation results is known as numerical heating, which occurs when the cell size is much larger than the plasma skin depth (for a target density of 10 n_c, the plasma skin depth is 50 nm according to Eq.(1.29)).

2.7.2 The influence of the number of particles per cell

In Fig.2.6 is shown the variation of the absorption coefficient of the laser energy to plasma constituents with the number of particles per cell. The absorption coefficient of the laser energy to plasma constituents is constant for more than 10 particles per cell. Under this value, it decreases slowly. The absorption coefficient of the laser energy to high energy photons does not vary significantly with the number of particles per cell as shown in Fig.2.7.

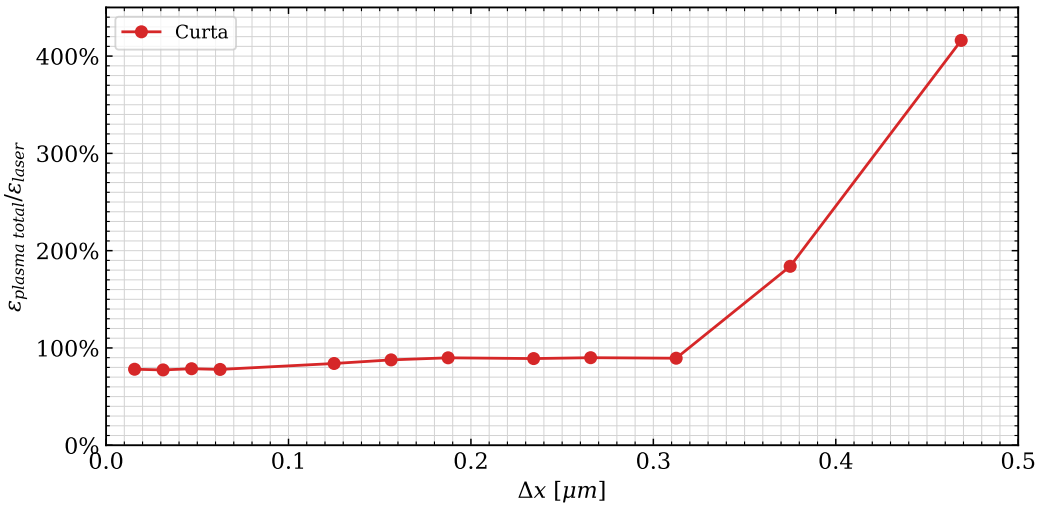

Figure 2.4: Absorption coefficient of the laser energy to plasma constituents vs longitudinal cell length as obtained in 2D PIC simulations. Target parameters: density $n_{e0} = 10$ n$_c$, thickness $L_x = 15$ μm and width $L_y = 30$ μm. Laser parameters: normalized field amplitude $a_0 = 85$, laser wavelength $\lambda = 1$ μm, laser pulse duration $\tau = 20$ fs FWHM and laser waist $w_0 = 12.5$ μm.

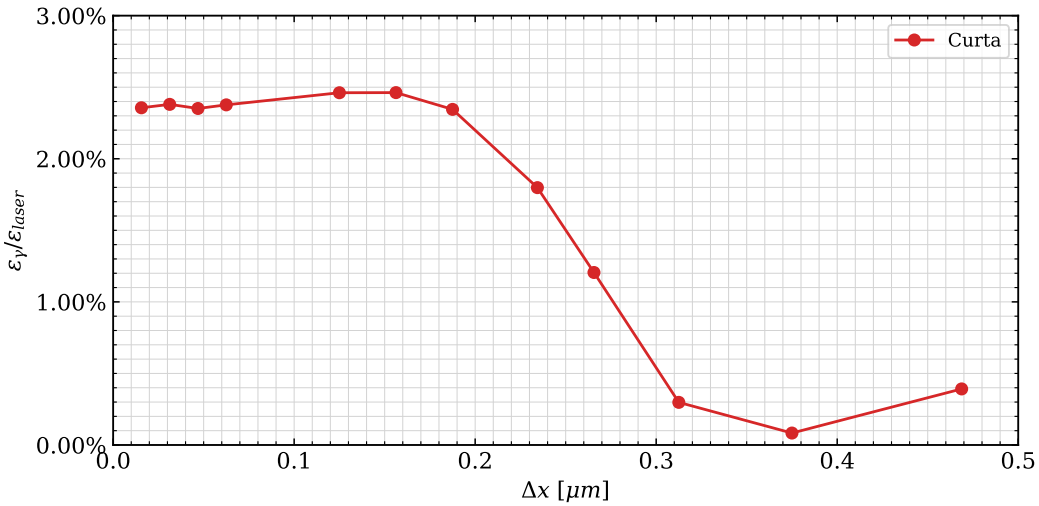

Figure 2.5: Absorption coefficient of the laser energy to photons vs longitudinal cell length as obtained in 2D PIC simulations. Target parameters: $n_{e0} = 10$ n$_c$, $L_x = 15$ μm and $L_y = 30$ μm. Laser parameters: $a_0 = 85$, $\lambda = 1$ μm, $\tau = 20$ fs FWHM and $w_0 = 12.5$ μm.

Such convergence studies are needed to find a compromise between the simulation time and the accuracy of the results.

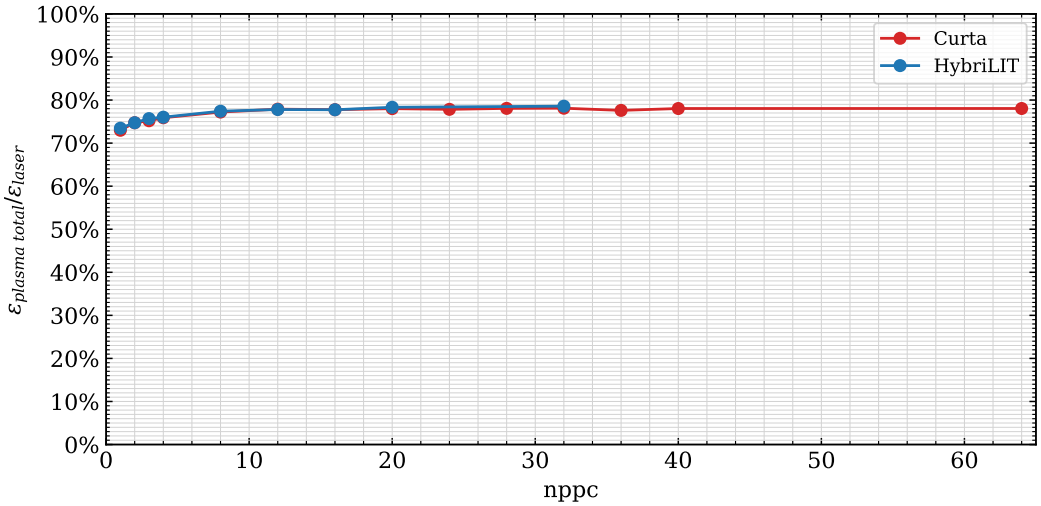

Figure 2.6: Absorption coefficient of the laser energy to plasma constituents vs the number of particles per cell as obtained in 2D PIC simulations. Target parameters: density $n_{e0} = 10$ n$_c$, thickness $L_x = 15$ μm and width $L_y = 30$ μm. Laser parameters: normalized field amplitude $a_0 = 85$, laser wavelength $\lambda = 1$ μm, laser pulse duration $\tau = 20$ fs FWHM and laser waist $w_0 = 12.5$ μm.

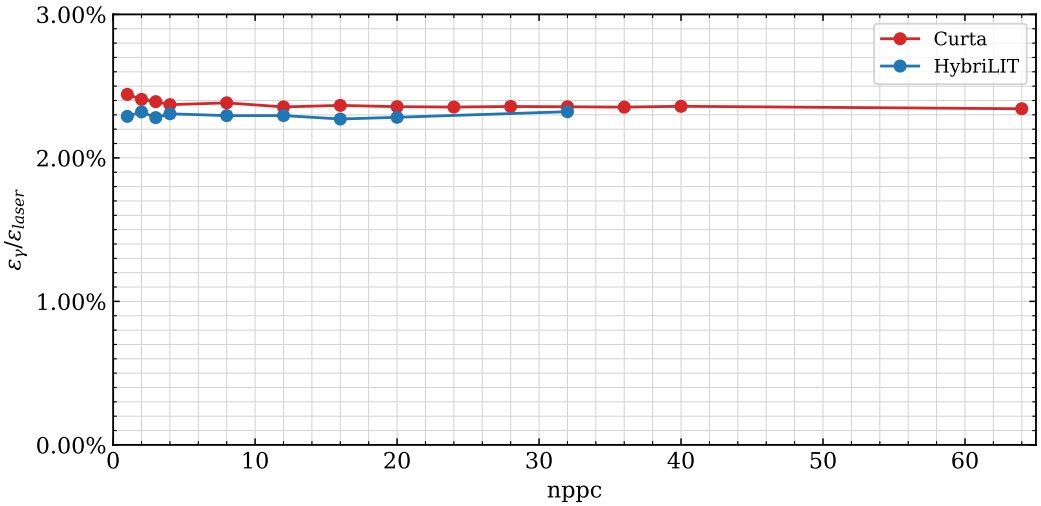

Figure 2.7: Absorption coefficient of the laser energy to photons vs the number of particles per cell as obtained in 2D PIC simulations. Target parameters: $n_{e0} = 10$ n$_c$, $L_x = 15$ μm and $L_y = 30$ μm. Laser parameters: $a_0 = 85$, $\lambda = 1$ μm, $\tau = 20$ fs FWHM and $w_0 = 12.5$ μm.

2.8 Energy scope project: optimization of the energetic profile of HPC calculation

The digital world is an expanding system with more than 4.1 billions users in 2019. The Information and Communications Technologies (ICT) industry was responsible for 3.8% of the total greenshouse emission in 2019, with 1400 millions tonnes of CO_2 equivalent emissions (CO_2 + other relevant greenhouse gasses). The greenhouse emission of the ICT industry is

estimated to grow with a factor of 1.6 by 2025 [119]. It is therefore of paramount importance to measure and reduce the environmental impact of digital services and equipment. Energy Scope [120] is a software developed to measure the energetic profile of a High Performance Computing Application and to optimize it [121, 122]. It was developed at INRIA [123] and is available on the Curta machine - MCIA [106].

We consider the interaction between an ultra high intensity laser pulse and a near critical density plasma. The plasma is made ef electrons and protons with a variable density and thickness as mentioned in Table 2.1 and a transversal width of 30 μm. The laser pulse has a temporal and spatial Gaussian profile of pulse duration $\tau = 20$ fs FWHM, laser wavelength $\lambda = 1$ μm and laser waist $w_0 = 12.5$ μm. The laser peak intensity is $I = 10^{22}$ W/cm^2($a_0 = 85$), with two exceptions: for the case 10 n_c and 22 μm the peak intensity is $5 \cdot 10^{22}$ W/cm^2 and for the case 10 n_c and 30 μm the peak intensity is 10^{23} W/cm^2. The 2D PIC simulations were performed on the Curta machine - MCIA [106].

The Energy scope software collects the information about the energy consumed by an application during its running and all the information is summarized in a report. The information aquired consists of the consumed power of the CPU used and of the Dynamic Random Access Memory (DRAM), as well as information regarding the core temperature. In Fig.2.8 is shown the power consumed by one CPU and DRAM during the simulation for a target of 10 n_c and a thickness of 12 μm. The measurements are acquired each 750 ms.

In Fig.2.9 is shown the temperature of the cores inside the node. One node contains two CPUs and each CPU contains 16 physical cores. The average temperature of the left CPU is 68.2° C and the average temperature of the right CPU is 54.4° C.

In Table2.1 is summarized the consumption of energy for multiple 2D PIC simulations. The TDP (Thermal Design Power) represents the average power, in watts, the processor dissipates under an intense workload.

In Fig.2.10 are shown the variation of the total energy consumption and respectively, the total emission of CO_2 calculated for France with the computational time expressed in CPU hours as obtained from Table 2.1. We observe a linear growth of the total energy consumed, respectively of the total CO_2 emissions with the computational time.

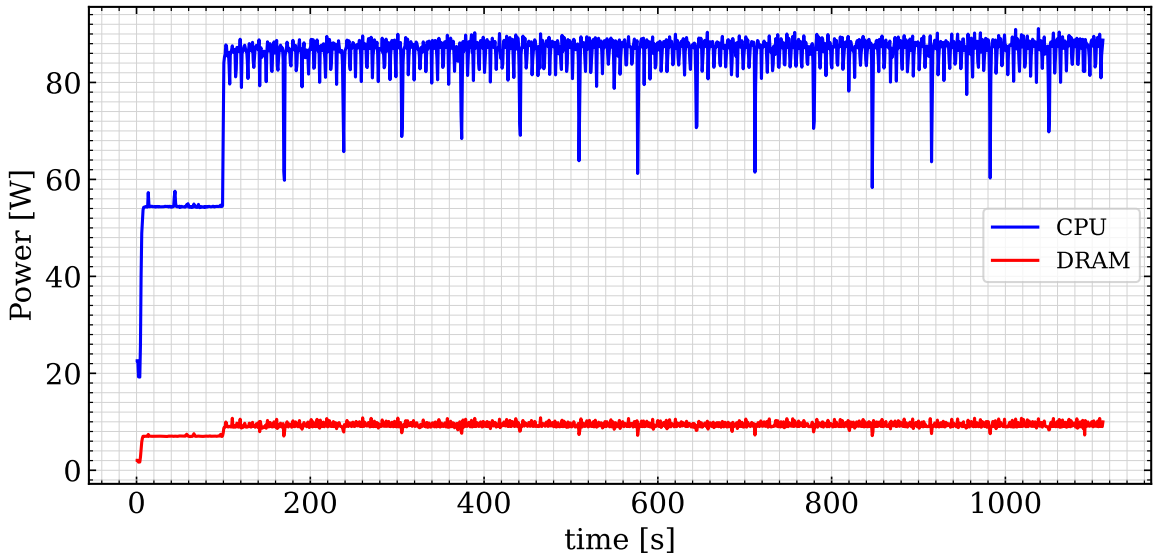

Figure 2.8: The power consumed during the first 1100s on one CPU of one node for a 2D PIC simulation as obtained from the Energy Scope Reports. Target parameters: $n_{e0} = 10$ n$_c$, $L_x = 12$ μm and $L_y = 30$ μm. Laser parameters: $a_0 = 85$, $\lambda = 1$ μm, $\tau = 20$ fs FWHM and $w_0 = 12.5$ μm. The measurements are acquired each 750 ms.

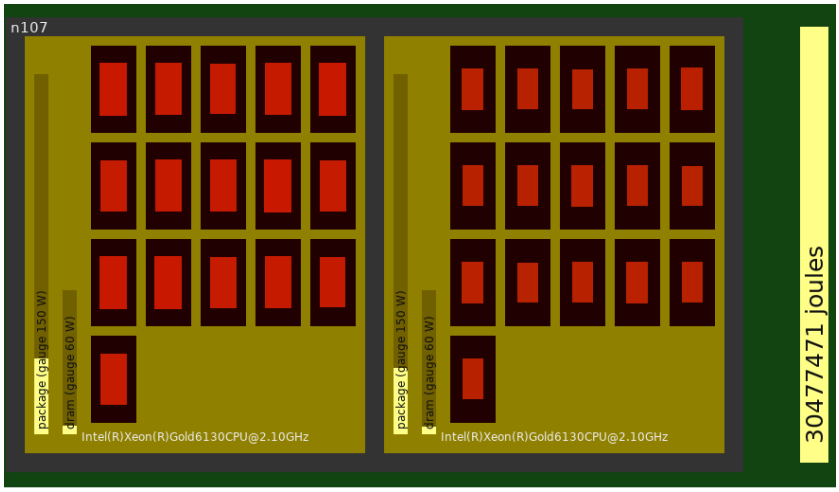

Figure 2.9: The core temperature of one node for a 2D PIC simulations as obtained from the Energy Scope Reports. Target parameters: $n_{e0} = 10$ n$_c$, $L_x = 12$ μm and $L_y = 30$ μm. Laser parameters: $a_0 = 85$, $\lambda = 1$ μm, $\tau = 20$ fs FWHM and $w_0 = 12.5$ μm. Credit photo: Energy Scope.

The total computation time used on Curta for the full PhD duration (taken from 1st September 2018 to 1st September 2022) is: 2658276 CPU hours which accounts for more than 300 simulations. Extrapolating the results from Fig.2.10, the total computation time corresponds to a total amount of consumed energy of 22.52 MWh and a total emission of 1.15 tonnes CO_2 (France). This relatively low energy consumption, for the amount of simulations performed, emphasizes the importance of performing PIC simulations to get trends and behaviors which can be searched for in real experiments. Moreover, the energy consumption of the

Table 2.1: Energetic profile for 2D PIC simulations as obtained from the Energy Scope Reports.

Target $[n_c \times \mu m]$	Number of nodes	Duration [s]	Energy consumed [kWh]	Energy efficiency TDP [%]
10×3	1	26636	2.1395	91.67
15×8	2	48372	7.2099	83.32
20×6	2	39709	6.1044	86.69
10×12	3	49002	10.916	82.93
5×20	3	66425	14.9827	84.27
10×22	3	81999	18.4576	76.93
10×30	4	92477	27.2758	75.25
1×40	3	105429	23.7512	77.67
1×30	4	61270	18.1972	82.92
0.5×60	6	81230	37.4055	86.52

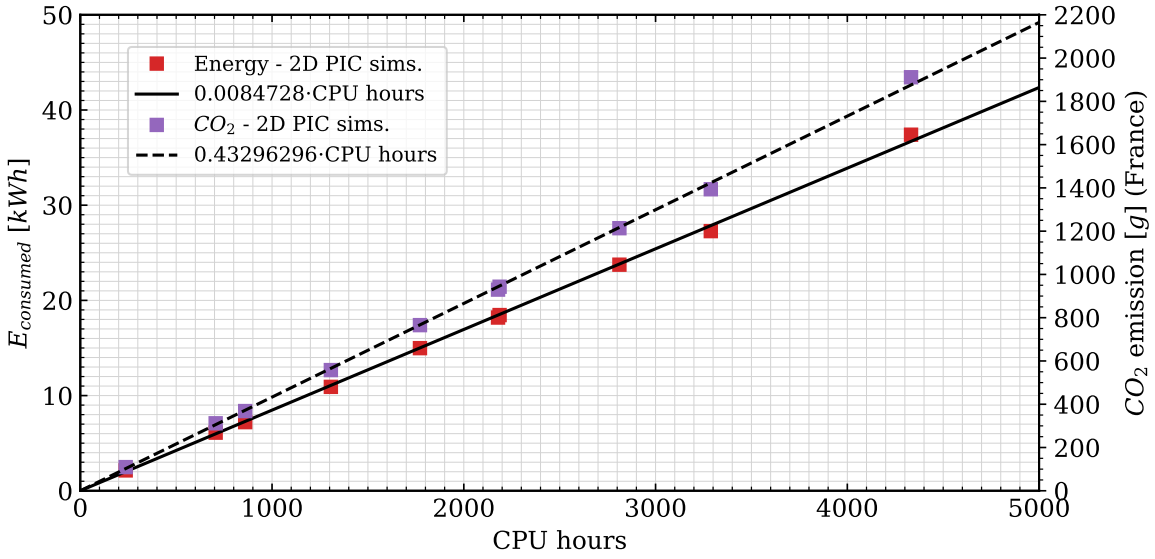

Figure 2.10: The total energy consumption and the total emission of CO_2 (France) vs computational time for 2D PIC simulations as obtained from the Energy Scope Reports.

simulations performed is even lower than the average energy consumption of driving a car. For example, the average journey of a person with a diesel car in France in 2019 is 14392 km/year [124]. The CO_2 equivalent emission of a diesel car is 190 g/km [125], which gives a total amount of 2.73 tonnes CO_2 equivalent per year.

Chapter 3

Theoretical model of laser-energy absorption

As introduced in Section 1.2 from Chapter 1, there are various mechanisms for the absorption of laser energy, each depending on the laser and target parameters. In this chapter we analyze the case of an ultra-high intensity, ultra-short laser pulse interacting with a near critical density target. Our main goal is to model the energy transfer from the laser pulse to plasma constituents, in the transition from the transparent to less transparent regime.

In Section 3.1 we propose a theoretical model of energy transfer, assuming that most of the laser energy will be transferred to hot electrons. The model proposed is further tested and corrected through 2D particle-in-cell (PIC) simulations in Section 3.2. We found a dependence of the laser to plasma energy transfer on target density and laser parameters (intensity, pulse duration). These results are presented in Section 3.3 and in Section 3.4 we discuss the model applicability. Finally, the main conclusions of the model are summarized in Section 3.5.

3.1 Analytical model

We consider the interaction between an ultra high intensity laser pulse of peak intensity I_0, normalized field amplitude a_0, pulse duration τ and a plasma target made of electrons and

protons with the initial density n_{e0}, where n_{e0} is smaller than the relativistic critical density, and thickness L_0 as shown in Fig.3.1.

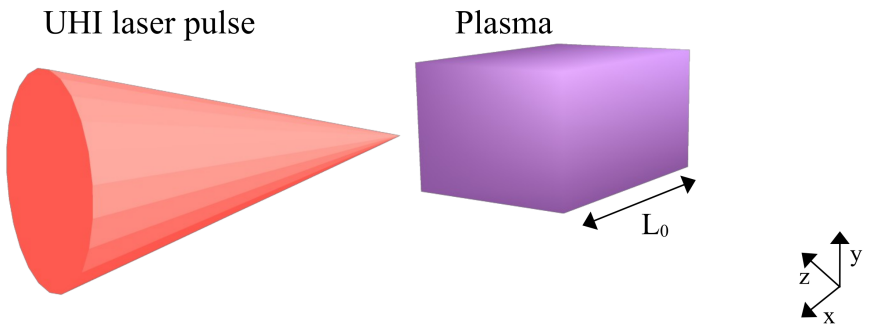

Figure 3.1: Experimental setup for the analytical model: an ultra-high intensity laser pulse interacting with a near-critical density plasma of thickness L_0.

The total energy of a Gaussian laser pulse is given by:

$$W_l = \int P dt = \int I(t) \exp\left(-2\frac{y^2+z^2}{{w_0}^2}\right) dt dy dz \tag{3.1}$$

where w_0 is the laser waist and:

$$I(t) = I_0 \exp\left[-4\ln 2\left(\frac{t}{\tau}\right)^2\right] \tag{3.2}$$

We will solve separately the two integrals using the Gauss integral:

$$\int_{-\infty}^{\infty} \exp(-\alpha x^2) dx = \sqrt{\frac{\pi}{\alpha}} \tag{3.3}$$

The time integral is:

$$\begin{aligned} \int_{-\infty}^{\infty} I(t) dt &= I_0 \int_{-\infty}^{\infty} \exp\left[-4\ln 2\left(\frac{t}{\tau}\right)^2\right] dt = \\ &= I_0 \cdot \sqrt{\frac{\pi\tau^2}{4\ln 2}} = I_0 \cdot \tau \cdot \sqrt{\frac{\pi}{4\ln 2}} \end{aligned} \tag{3.4}$$

The space integral is:

$$\begin{aligned}\int_{-\infty}^{\infty}\exp\left(-2\frac{r^2}{w_0^2}\right)dydz &= \int_{-\infty}^{\infty}\exp\left(-2\frac{y^2+z^2}{w_0^2}\right)dydz = \\ &= \int_{-\infty}^{\infty}\exp\frac{-2y^2}{w_0^2}dy\cdot\int_{-\infty}^{\infty}\exp\frac{-2z^2}{w_0^2}dz = \\ &= \sqrt{\frac{\pi w_0^2}{2}}\cdot\sqrt{\frac{\pi w_0^2}{2}} = \frac{\pi w_0^2}{2}\end{aligned} \tag{3.5}$$

Finally, using Eq.(3.4) and Eq.(3.5), the laser energy will be given by:

$$W_l = \int P dt = I_0\cdot\tau\cdot\sqrt{\frac{\pi}{4\ln 2}}\cdot\frac{\pi w_0^2}{2} = I_0\cdot\tau\cdot w_0^2\cdot\frac{\pi^{3/2}}{4\sqrt{\ln 2}} \tag{3.6}$$

The plasma target will be heated over a volume which corresponds to a cylinder, where the radius is represented by the spatial FWHM of the laser pulse and the length is the corresponding absorption length of the target L, with L smaller than or equal to L_0. The energy retrieved in the plasma constituents as a result of the interaction process depends on the distribution function of the particles as:

$$W_p = \sum_{\alpha}\int \varepsilon_{kin,\alpha} f_\alpha(\vec{r},\vec{v},t)d\vec{r}d\vec{v} \tag{3.7}$$

where α represents the particle species (electrons, ions), $\varepsilon_{kin,\alpha}$ - the average kinetic energy of each species and $f_\alpha(\vec{r},\vec{v},t)$ - the distribution function of each species.

The main assumption of our theoretical model is that the absorption of the laser energy will be predominantly made by electrons. In consequence, the plasma energy will be:

$$W_p = n_{e0}\cdot L\cdot\pi\cdot FWHM^2\cdot\varepsilon_{electrons_{avg}} \tag{3.8}$$

where $\varepsilon_{electrons_{avg}}$ is the average kinetic energy of the electrons.

Assuming that η is the saturation point of the absorption coefficient of the laser energy to plasma constituents, we can write:

$$W_p = \eta W_l \tag{3.9}$$

Using Eq.(3.6) and Eq.(3.8) in Eq.3.9, for a linearly polarized laser pulse with $w_0 = FWHM/\sqrt{2\ln 2}$ and $a_0 = 0.85\sqrt{I_{18}\lambda_{\mu m}^2}$, we will obtain:

$$n_{e0} \cdot L \cdot \varepsilon_{electrons_{avg}} = \eta \cdot \frac{a_0^2}{0.85^2} \cdot \tau \cdot \frac{1}{8} \cdot \left(\frac{\pi}{\ln 2}\right)^{3/2} \cdot 10^{18} \frac{W}{cm^2} \cdot \frac{1}{\lambda_{\mu m}^2} \tag{3.10}$$

Eq.(3.10) can be normalized:

$$\frac{n_{e0}}{n_c} \cdot \frac{L}{\lambda} \cdot \frac{\varepsilon_{electrons_{avg}}}{m_e c^2} = \eta \cdot \frac{a_0^2}{0.85^2} \cdot \frac{\tau}{t_0} \cdot t_0 \cdot \frac{1}{8} \cdot \left(\frac{\pi}{\ln 2}\right)^{3/2} \cdot \frac{1}{\pi} \cdot \frac{1}{n_c} \cdot \frac{1}{\lambda} \cdot \frac{1}{m_e c^2} \cdot 10^{18} \frac{W}{cm^2} \cdot \frac{1}{\lambda_{\mu m}^2}$$

where we used the following constants:

$$m_e c^2 = 511 \cdot 10^3 \cdot 1.6 \cdot 10^{-19} J \tag{3.11}$$

$$t_0 = \lambda/c = 3.3 \cdot 10^{-15} s \tag{3.12}$$

$$n_c = 1.1 \cdot 10^{21} cm^{-3} \tag{3.13}$$

$$m_e = 9.1 \cdot 10^{-31} kg \tag{3.14}$$

$$c = 3 \cdot 10^8 m/s \tag{3.15}$$

$$e = 1.6 \cdot 10^{-19} C \tag{3.16}$$

$$\omega = 2\pi c/\lambda \tag{3.17}$$

After the calculation of the numerical values, one can find a simplistic way to couple the target characteristics with the laser's ones:

$$\frac{n_{e0}}{n_c} \cdot \frac{L}{\lambda} = 0.195 \cdot \eta \cdot a_0^2 \cdot \frac{\tau}{t_0} \cdot \frac{m_e c^2}{\varepsilon_{electrons_{avg}}} \cdot \frac{1}{\lambda_{\mu m}^3} \tag{3.18}$$

where t_0 represents the laser period, λ - the laser wavelength and η - the saturation point of the absorption coefficient.

Eq.(3.18) can predict the target areal density $n_{e0}L$ needed to maximize the absorption of the laser energy. In the next section, Eq.(3.18) is tested by performing 2D PIC simulations. The main goal is to predict the target thickness needed for maximizing the laser energy absorption in the case of near critical density targets.

3.2 2D PIC simulation setup

The 2D simulation setup consists of a near-critical density target irradiated by an ultra-high intensity ultra-short laser pulse coming from the left side of the simulation box, as shown in Fig.3.2. The laser laser of wavelength $\lambda = 1$ μm is linearly polarized and has the following characteristics: a transversal waist of 4π μm, a pulse duration of 20 fs FWHM (6 t_0) for the laser intensity varying in $10^{20} - 10^{23}$ W/cm^2 (correpsonding to a normalized field amplitude of $a_0 = 8.5 - 268.8$) and a laser intensity of 10^{22} W/cm^2 for the pulse duration varying in $6.5 - 100$ fs FWHM ($2\ t_0 - 30\ t_0$). The target is considered fully ionized, being made of protons and electrons. The density of the target varies from 0.5 n_c to 24 n_c (where $n_c \approx 1.1 \cdot 10^{21}$ cm$^{-3}/\lambda^2_{\mu\mathrm{m}}$, with $\lambda_{\mu m}$ being the wavelength divided by one micron, is the critical density), while the thickness is adjusted to achieve full laser absorption (aprox. from 500 nm to 200 μm). The transversal width of the target is kept constant at 30 μm. The simulation box has 60 μm in the y direction, while in the x direction it is changed according to the thickness L_x of the target from 120 μm to 300 μm. The cell length is $dx = dy = 15.625$ nm and the number of particles per cell is 30 for each species. The particles are deleted while crossing the domain boundaries and the fields are absorbed. The simulations were performed with Simulating Matter Irradiated by Light at Extreme Intensities (SMILEI) [99] on the Curta machine - MCIA [106].

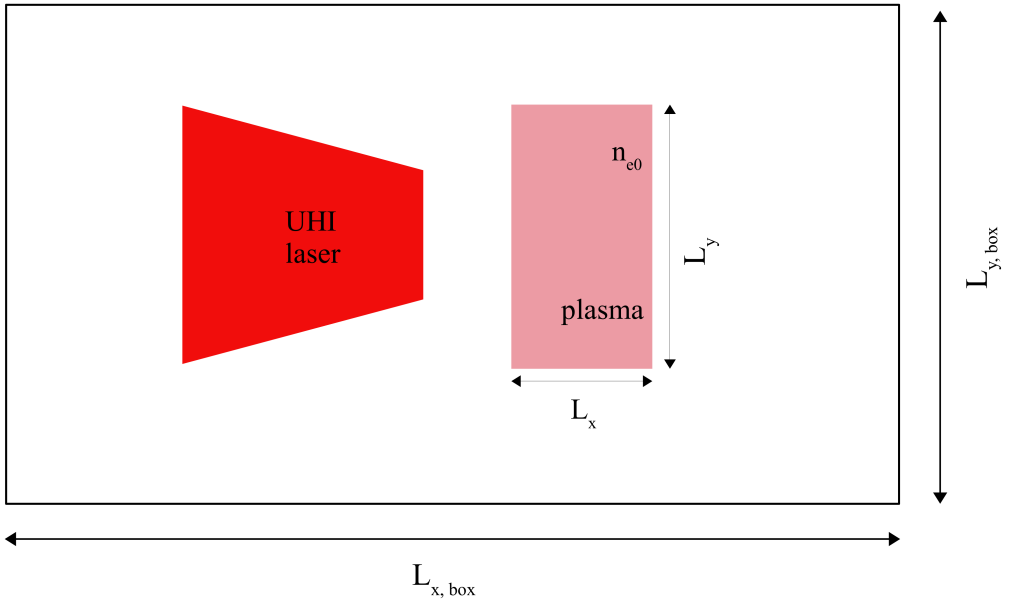

Figure 3.2: 2D simulation setup: an ultra high intensity laser pulse irradiating a near critical density plasma. The simulation box parameters: $L_{x,box} : \{120\ \mu\text{m} - 300\ \mu\text{m}\}$ and $L_{y,box} = 60\ \mu$m. Target parameters: $n_{e0} : \{0.5\ \text{n}_\text{c} - 24\ \text{n}_\text{c}\}$, $L_x : \{500\ \text{nm} - 200\ \mu\text{m}\}$ and $L_y = 30\ \mu$m. Laser parameters: $\lambda = 1\ \mu$m, $w_0 = 4\pi\ \mu$m, $\tau = 20$ fs FWHM (for $a_0 : \{8.5 - 268.8\}$) and $a_0 = 85$ (for $\tau : \{2\ \text{t}_0 - 30\ \text{t}_0\}$).

3.3 Results

3.3.1 Absorption of the laser energy

In Fig.3.3 is shown the evolution of the total energy in the simulation box. The initial energy in the box is the laser electromagnetic energy. When the laser reaches the target, the energy will be converted into plasma energy and finally retrieved at the end of the simulation in three coefficients: absorption, reflection and transmission.

In Fig.3.4 is shown the conversion of the electromagnetic energy into kinetic energy. The laser transfers its energy to the electrons, which afterwards lose energy by two channels: creation of the quasi-electrostatic field at the back of the target and emission of high energy radiation.

The absorption coefficient will be defined as the total plasma energy: the total kinetic energy of the particles (electrons, protons and photons), the radiation emitted by the relativistic electrons and the electromagnetic energy of the plasma fields, divided by the initial laser energy. The emission of radiation is simulated by two models, depending on the quantum parameter of

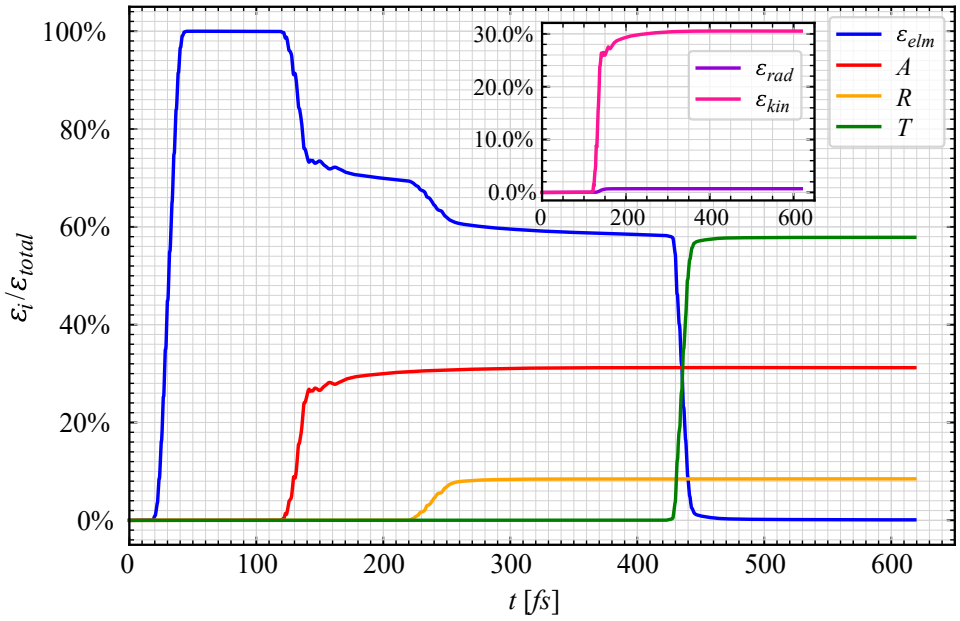

Figure 3.3: Time evolution of the energy from a 2D PIC simulation of a laser pulse of $a_0 = 85$, $\tau = 6$ t$_0$, $\lambda = 1$ μm, $w_0 = 12.5$ μm interacting with a plasma of $n_{e0} = 10$ n$_c$, L$_x = 3$ μm, $L_y = 30$ μm. The blue line represents the electromagnetic energy ε_{elm}, the red line - the absorption coefficient A, the orange line - the reflection coefficient R, the green line - the transmission coefficient T, the pink line - the total kinetic energy of the particles ε_{kin} and the purple line - the energy radiated by electrons ε_{rad},.

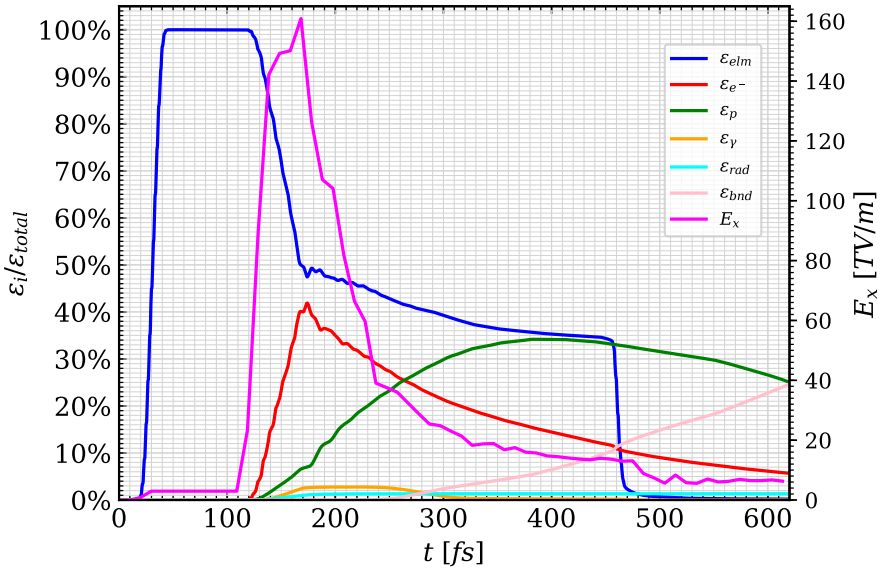

Figure 3.4: Temporal evolution of the electromagnetic energy and particles kinetic energy from a 2D PIC simulation; temporal evolution of the longitudinal electric field of the laser. Target parameters: $n_{e0} = 5$ n$_c$, $L_x = 10$ μm and $L_y = 30$ μm. Laser parameters: $a_0 = 85$, $\tau = 6$ t$_0$, $\lambda = 1$ μm, w$_0 = 12.5$ μm. The blue line represents the electromagnetic energy ε_{elm}, the red line - the kinetic energy of the electrons ε_{e^-}, the green line - the kinetic energy of the protons ε_p, the orange line - the kinetic energy of the γ-photons ε_γ, the cyan line - the energy radiated by the electrons ε_{rad}, the pink line - the kinetic energy retreived at the boundaries of the simulation box ε_{bnd} and the magenta line - the longitudinal component of the electric field E_x.

the electrons χ_{e^-}: for $\chi_{e^-} \leq 10^{-3}$ the radiation will be emitted according to the continuous Landau Lifshitz model (ε_{rad} in fig.3.3) [126], otherwise, a photon will be created by the Monte Carlo scheme ($\varepsilon_{kin,photon}$ - not shown) [126]. The reflection coefficient is defined as the electromagnetic energy measured at the left side of the simulation box, after the laser pulse is reflected by the target, and the transmission coefficient represents the electromagnetic energy measured at the right side of the simulation box, after the laser pulse has passed through the target, both divided by the initial laser energy. To compute the reflection and the transmission coefficients, the instantaneous Poynting vector at the left and right boundaries of the simulation box was used.

For all target densities considered in the 2D PIC simulations performed, the absorption coefficient increases when the target thickness increases, eventually reaching a plateau and additional plasma into the target will not affect it significantly as shown in fig.3.5.

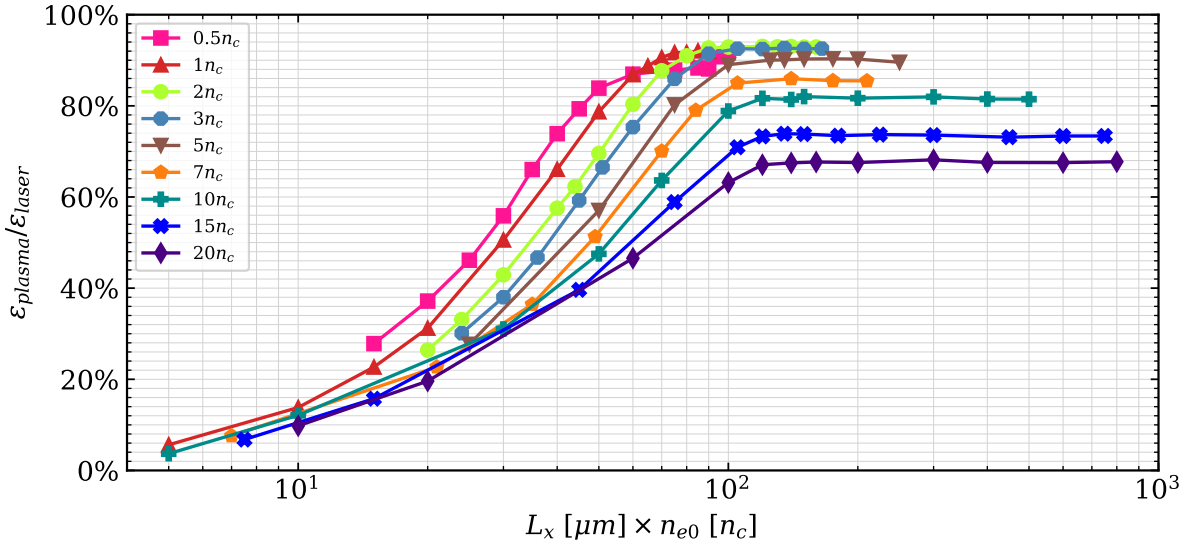

Figure 3.5: Absorption coefficient vs initial target areal density from 2D PIC simulations. Target parameters: $L_y = 30\ \mu$m. Laser parameters: $a_0 = 85$, $\tau = 6\ t_0$, $\lambda = 1\ \mu$m, $w_0 = 12.5\ \mu$m.

The transmission coefficient variation with the target areal density is shown in Fig.3.6. The increase of the absorption coefficient corresponds to a decrease of the transmission coefficient.

We are interested in modeling the variation of the maximum value of the absorption coefficient. We define the saturation point of the absorption coefficient η as the point where the absorption does not change with more than 2%. We define the optimum target thickness for

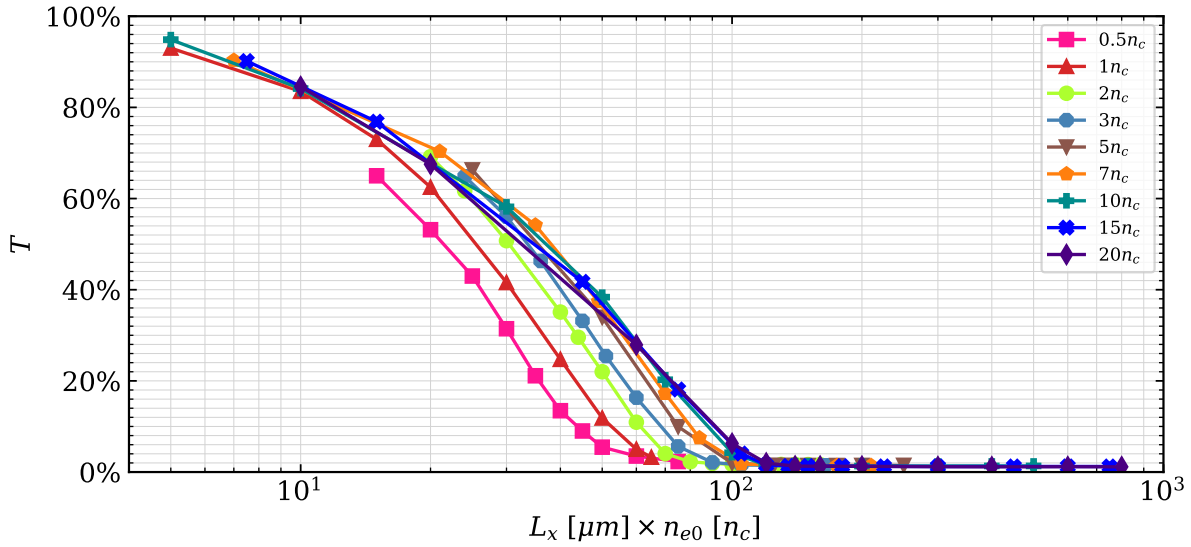

Figure 3.6: Transmission coefficient vs initial target areal density. Target parameters: $L_y = 30\ \mu$m. Laser parameters: $a_0 = 85,\ \tau = 6\ \mathrm{t_0},\ \lambda = 1\ \mu$m, $\mathrm{w_0} = 12.5\ \mu$m.

maximizing the absorption L_0 as the thickness corresponding to η . For various target densities, the saturation point of the absorption coefficient η shows two behaviours. For low target densities, in the range of $0.5 - 3\ \mathrm{n_c}$, when the reflection coefficient is negligible, η is almost independent on the density, presenting a small variation between $90 - 95\%$. For higher densities, when the reflection coefficient is higher than 5% and it cannot be neglected, η decreases strongly. The variation of the reflection coefficient with the areal density is shown in Fig.3.7.

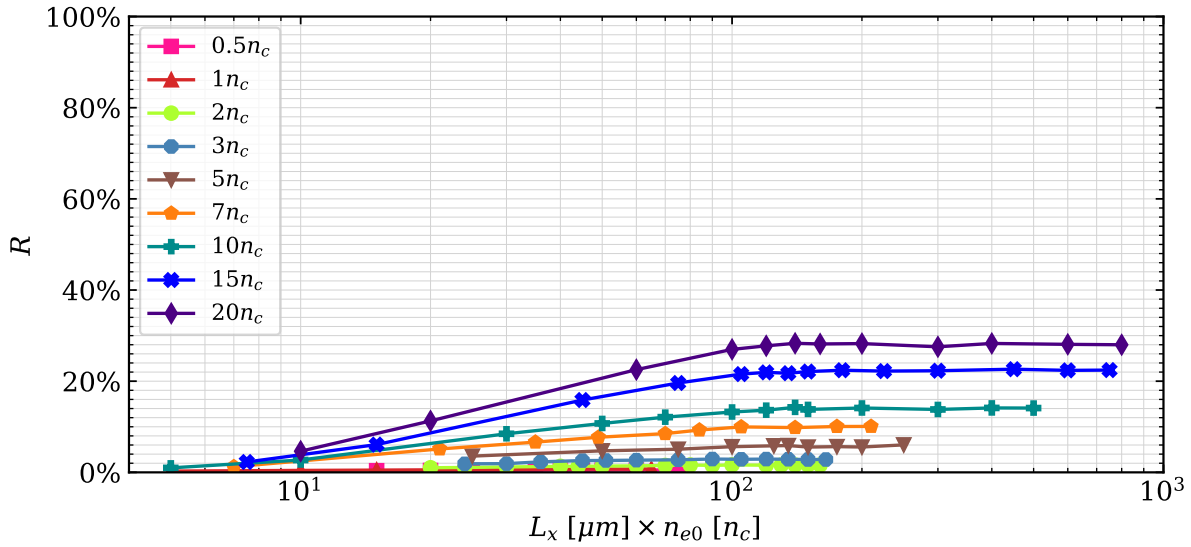

Figure 3.7: Reflection coefficient vs initial target areal density. Target parameters: $L_y = 30\ \mu$m. Laser parameters: $a_0 = 85,\ \tau = 6\ \mathrm{t_0},\ \lambda = 1\ \mu$m, $\mathrm{w_0} = 12.5\ \mu$m.

It is important to note that the absorption coefficient does not reach 100% due to the

losses of electromagnetic radiation on the top and bottom boundaries of the simulation box, which are not considered in the reflection and transmission coefficients and can reach a value of up to 5% of the total energy in the simulation box.

The saturation point of the absorption coefficient does not only depend on the target density, but also on the laser parameters. We studied its variation with two laser parameters: intensity (for a fixed pulse duration of 6 t_0) and pulse duration (for a fixed intensity of 10^{22} W/cm^2), in both cases varying also the target density. Using the 2D PIC simulation results (see Section A.3 of Appendix A), we have found the following semi-empirical formula:

$$\eta = 1 - \frac{4}{a_0}\frac{n_{e0}}{n_c}\sqrt{\frac{t_0}{\tau}} \tag{3.19}$$

where the second term corresponds to the reflection coefficient.

According to (3.19), the saturation point of the absorption coefficient goes negative for $n_{e0}/(n_c a_0) \geq \sqrt{\tau/t_0}/4$, which for $\tau = 20$ fs FWHM (6 t_0) corresponds to $n_{e0}/(n_c a_0) \geq 0.61$. The ratio $n_{e0}/(n_c a_0)$ was defined by S. Gordienko and A. Pukhov [127] as a similarity parameter $S = n_{e0}/(n_c a_0)$, which describes the laser-plasma interaction in the relativistic regime.

For a fixed laser pulse duration of 6 t_0, we varied the laser intensity in the range of $10^{20} - 10^{23}$ W/cm^2, corresponding to a normalized field amplitude of $8.5 - 268.8$. The results are shown in Fig.3.8: the colorscale represents the semi-empirical formula Eq.(3.19) and the circles represent the 2D PIC simulation results. All cases are shown at the optimum target thickness. In Section A.2 of Appendix A is shown the variation of the absorption coefficient with the target areal density for different laser pulse intensities up to the saturation value. For $a_0 >> n_{e0}/n_c$, we are in a highly transparent regime, and the absorption coefficient is maximized independently of the target density. As we are decreasing a_0, the regime is changing towards a less transparent - more opaque one, where the target reflects the laser light. For $a_0 = 85$, the differences between the simulation results and Eq.(3.19) are small, a few percents only, while towards the opaque regime, for $a_0 = 26.88$, the differences can be up to $\approx 50\%$ (see also Fig.A.11 and Fig.A.12 of Section A.3 - Appendix A).

For a fixed normalized field amplitude $a_0 = 85$, we varied the pulse duration in the range $2 - 30$ t_0 ($6.5 - 100$ fs FWHM). The results are shown in Fig.3.9: the colorscale represents the semi-empirical formula (3.19) and the circles represent the 2D PIC simulation results. All cases

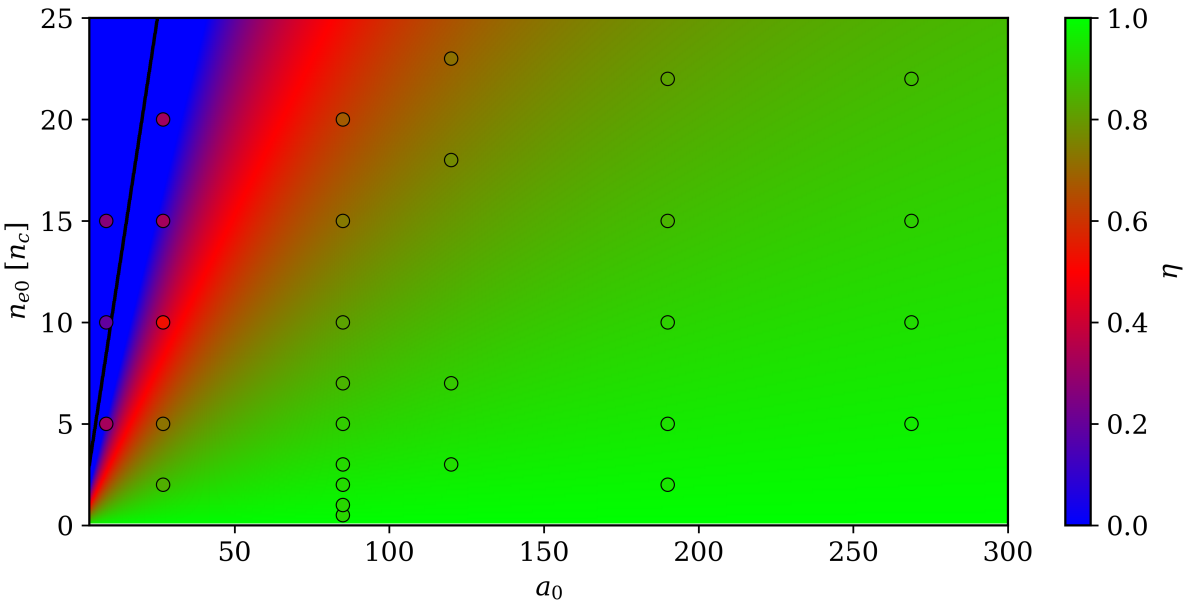

Figure 3.8: Saturation point of absorption coefficient vs target density and laser normalized field amplitude. Target parameters: $L_y = 30$ μm. Laser parameters: $\lambda = 1$ μm, $\tau = 6$ t$_0$ and $w_0 = 12.5$ μm. The simulation results are shown in circles while the results of Eq. (3.19) are shown with the colorscale. The black line represents the $a_0 = n_{e0}/n_c$ limit of the transparent regime. All negative values of η are considered zero.

are shown at the optimum target thickness. In Section A.1 of Appendix A is shown the variation of the absorption coefficient with the target areal density for different laser pulse durations up to the saturation value. For low densities, independently of the pulse duration, the laser energy is strongly absorbed and η reaches maximum values. For short pulses and high density targets, η is decreasing strongly with the density. The differences between the simulation results and (3.19) vary from a few percents up to 20% for the smallest pulse duration considered, $\tau = 2$ t$_0$ (see also Fig.A.13 and Fig.A.14 of Section A.3 - Appendix A).

The detailed graphs corresponding to the colormaps are shown in Section A.3 of Appendix A.

3.3.2 Average energy of the hot electrons

For the same parameters previously mentioned, the variation of the average energy of the hot electrons was studied. In the ultra-high intensity regime, the ponderomotive scaling $\varepsilon_{ponderomotive} = \sqrt{1+\frac{a_0^2}{2}} m_e c^2$ slightly underestimates the average energy of the hot electrons. Moreover, for the range of parameters studied and based on the 2D PIC simulation results (see Section A.4 of the Appendix A), we added a correction to the ponderomotive scaling which

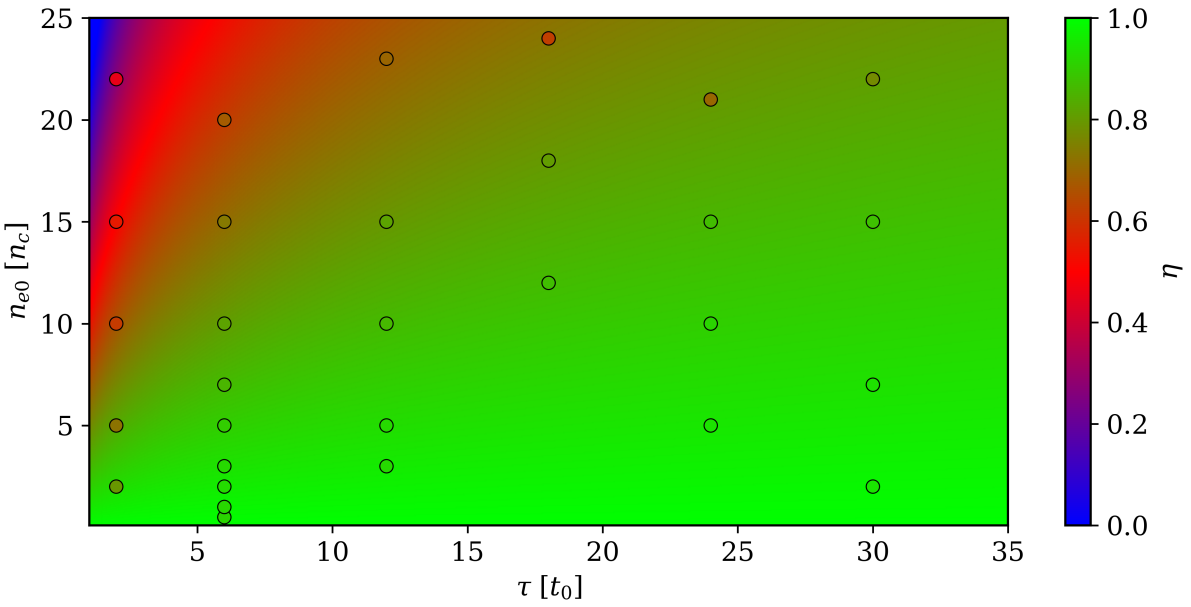

Figure 3.9: Saturation point of absorption coefficient vs target density and laser pulse duration. Target parameters: $L_y = 30$ μm. Laser parameters are $\lambda = 1$ μm, $a_0 = 85$ and $w_0 = 12.5$ μm. The simulation results are shown in circles while the results of Eq. (3.19) are shown with the colorscale.

depends on the initial target density as follows:

$$\varepsilon_{electrons_{avg}} = \sqrt{1 + \frac{a_0^2}{2}} m_e c^2 \left(1 + \frac{n_c}{n_{e0}}\right) \tag{3.20}$$

The average energy of the hot electrons from the simulations was computed for electrons with energies higher than 5 MeV as the absorption in these electrons represents $> 97\%$ of the total absorption in electrons for almost all cases considered. In Fig.3.10 is shown the variation of the absorption coefficient of the laser energy to electrons with the target areal density for various laser pulse durations. Two cases are considered: total absorption in electrons and absorption in electrons with energies > 5 MeV. As can be observed in Fig.3.10, there is no significant difference between the two cases.

In Fig.3.11 is presented the variation of the absorption coefficient of the laser energy to electrons with the target areal density for various laser pulse intensities. The previous behaviour is present: the absorption of laser energy in electrons with energies > 5 MeV is predominant. However, there are some exceptions for the lowest laser intensities: for $a_0 = 27$ the minimum value of the absorption coefficient in hot electrons with energies over 5 MeV varies from 93% to 56% of the total absorption coefficient, for $a_0 = 8.5$ it varies from 28% to 6%.

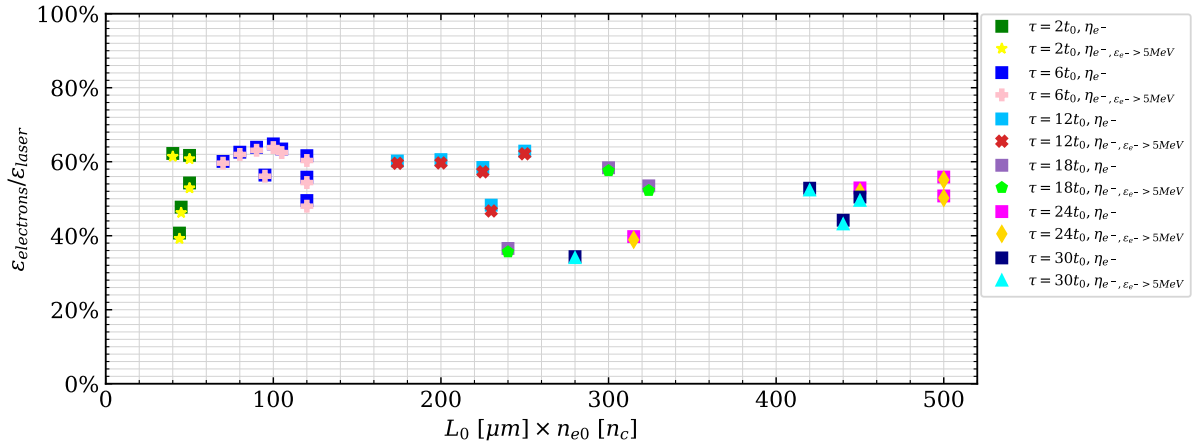

Figure 3.10: Absorption coefficient of the laser energy to electrons at the optimum target thickness vs target areal density for various laser pulse durations. Target parameters: $L_y = 30\ \mu$m. Laser parameters are $\lambda = 1\ \mu$m, $a_0 = 85$ and $w_0 = 12.5\ \mu$m.

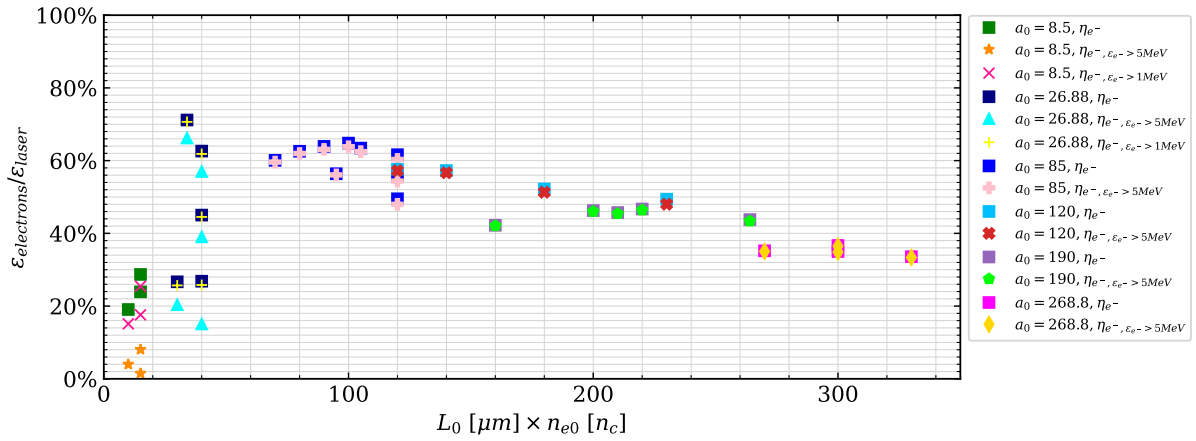

Figure 3.11: Absorption coefficient of the laser energy to electrons at the optimum target thickness vs target areal density for various laser pulse intensities. Target parameters: $L_y = 30\ \mu$m. Laser parameters are $\lambda = 1\ \mu$m, $\tau = 6$ t$_0$ and $w_0 = 12.5\ \mu$m.

The variation of $\varepsilon_{electrons_{avg}}$ with the laser intensity and with the target density is shown in Fig.3.12 using Eq.(3.20) and using our 2D PIC simulation results. For high a_0 and low target density, in the transparent regime, the electrons can achieve easily energies of hundreds of MeV - GeV. For $a_0 = 85$, the differences between the simulation results and (3.20) are a few percents up to 12% (see also Fig.A.15 and Fig.A.16 of Section A.4 - Appendix A), while in the highly transparent regime, for $a_0 >> n_{e0}/n_c$ we overestimate the average energy of the hot electrons (for $a_0 = 268.88$ and $n_{e0} = 22$ n$_c$ the differences are up to 65%). This overestimation is due to the strong and rapid energy losses suffered by the electrons to produce high energy radiation [128], which are taken into account in the simulations but not in the original assumptions of our theoretical model. This effect is also present in the transfer of the energy from the laser pulse

to gamma photons, which increases from a value of $\leq 5\%$ ($a_0 = 85$) to 30% ($a_0 = 268.8$). In addition, this coefficient depends also on the laser pulse duration. The emission of high energy radiation for the cases studied will be detailed in Subsection 3.4.2.

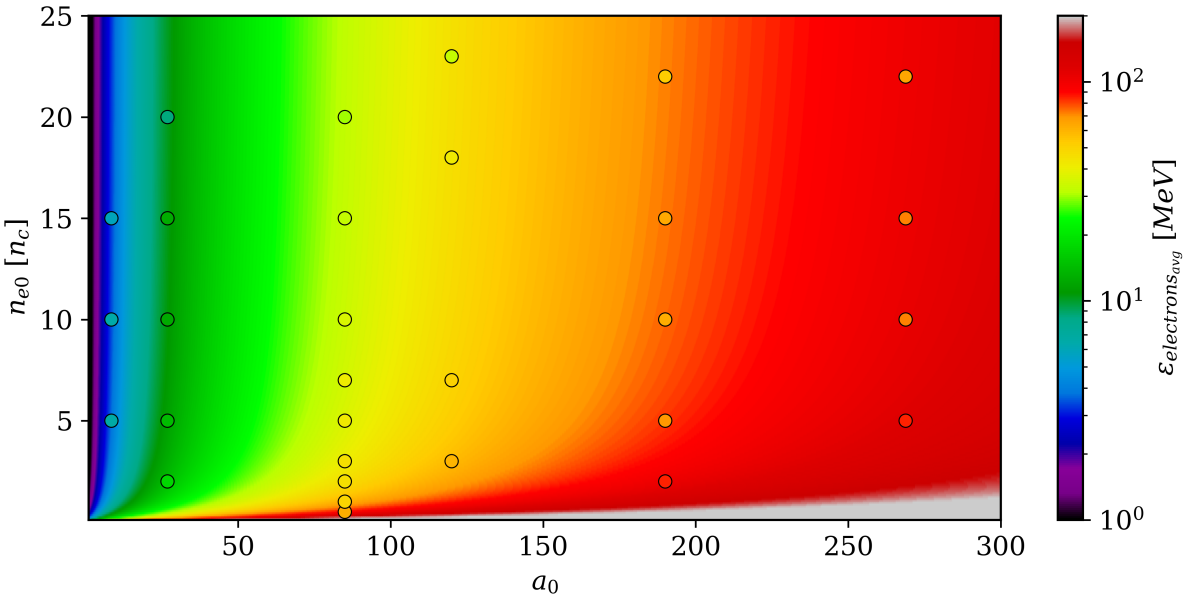

Figure 3.12: Average electron energy at the optimum target thickness vs target density and laser normalized field amplitude. Target parameters: $L_y = 30$ μm. Laser parameters: $\lambda = 1$ μm, $\tau = 6$ t_0 and $w_0 = 12.5$ μm. The simulation results are shown in circles while the results of Eq.(3.20) are shown with the colorscale.

For the range of parameters studied, there was no significant variation of the $\varepsilon_{electrons_{avg}}$ with the pulse duration, as can be seen in Fig.3.13 (see also Fig.A.17 and Fig.A.18 of Section A.4 - Appendix A).

The detailed graphs corresponding to the colormaps are shown in Section A.4 of Appendix A.

3.3.3 Optimum target thickness for maximizing laser energy absorption

Including Eq.(3.20) for the hot electron energy and Eq.(3.19) for the saturation point of the absorption coefficient in Eq.(3.18), we can predict the target thickness needed to maximize the absorption of an ultra-high intensity laser pulse in a near-critical plasma:

$$\frac{L_0}{\lambda} = 0.195 \cdot a_0^2 \cdot \frac{\tau}{t_0} \cdot \frac{n_c}{n_{e0}} \cdot \left(1 - \frac{4n_{e0}}{a_0 n_c}\sqrt{\frac{t_0}{\tau}}\right) \cdot \frac{1}{\sqrt{1 + \frac{a_0^2}{2}\left(1 + \frac{n_c}{n_{e0}}\right)}} \cdot \frac{1}{\lambda_{\mu m}^3} \tag{3.21}$$

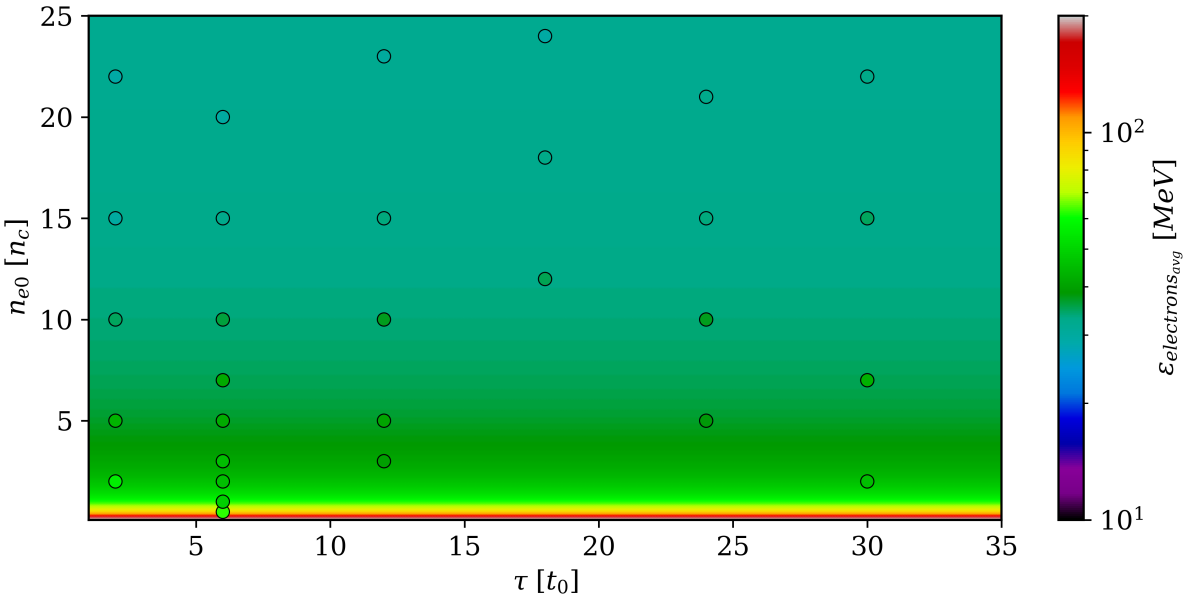

Figure 3.13: Average electron energy at the optimum target thickness vs target density and pulse duration. Target parameters: $L_y = 30$ μm. Laser parameters: $\lambda = 1$ μm, $a_0 = 85$ and $w_0 = 12.5$ μm. The simulation results are shown in circles while the results of Eq.(3.20) are shown with the colorscale.

The variation of the optimum target thickness with the laser normalized field amplitude is shown in fig.3.14 using Eq.(3.21) and using our 2D PIC simulation results. As can be seen in Fig.3.14, there is a good agreement between the simulation results and the prediction made by Eq.(3.21) for a wide range of parameters (see also Fig.A.19 and Fig.A.20 of Section A.5 - Appendix A). However, the differences between the simulation results and Eq.(3.21) vary from a few percents up to tens percents (50% for $a_0 = 120$ and $n_{e0} = 23$ n_c).

The detailed graphs corresponding to the colormaps are shown in Section A.5 of Appendix A.

Eq.(3.21) cannot predict the target thickness in the opaque regime when $n_{e0}/n_c >> a_0$ as η will be negative for $n_{e0}/n_c >> 0.61a_0$ according Eq.(3.19). Nevertheless, in this regime the laser can propagate up to the skin depth and a part of its energy will be transferred to the electrons, as we can also observe in the simulations. In the highly radiative regime, Eq.(3.21) overestimates the target thickness needed for maximizing the absorption. This can be due to the fact that an electron can absorb multiple times the laser energy and lose more energy through radiation.

The variation of the optimum target thickness with laser pulse duration is shown in Fig.3.15 using Eq.(3.21) and using our 2D PIC simulation results. Eq.(3.21) is in good agree-

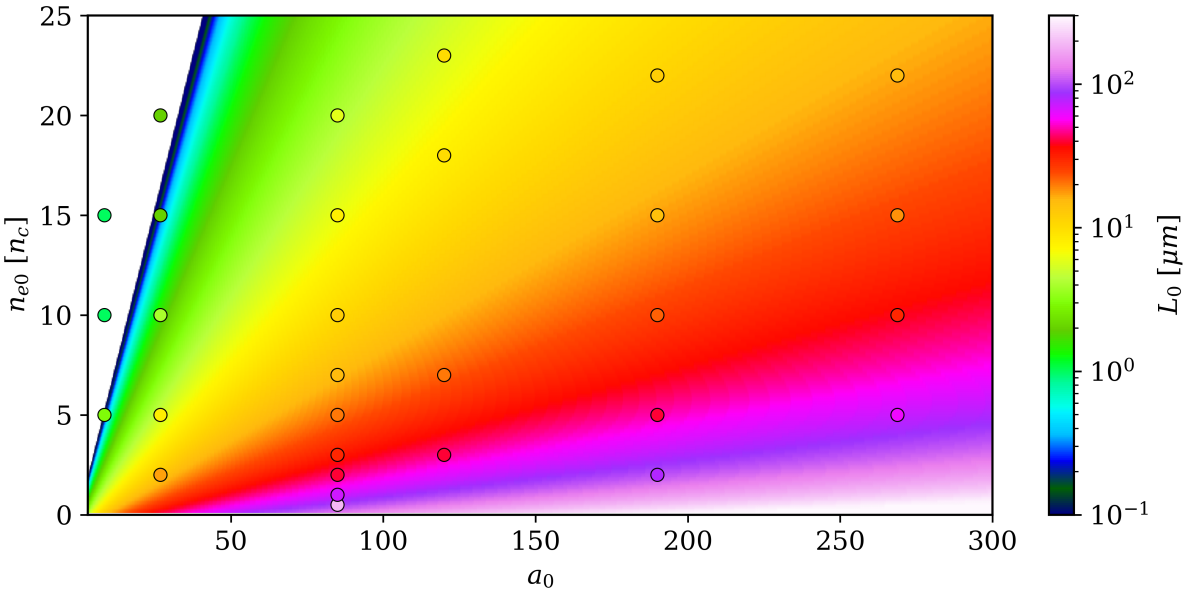

Figure 3.14: Optimum target thickness vs target density and laser normalized field amplitude. Target parameters: $L_y = 30$ μm. Laser parameters: $\lambda = 1$ μm, $\tau = 6$ t_0 and $w_0 = 12.5$ μm. The simulation results are shown in circles while the results of Eq.(3.21) are shown with the colorscale.

ment with the simulation results for a wide range of parameters: for τ in $2-24$ t_0 and n_{e0} in $1-20$ n_c, the differences between the simulation results and (3.21) are from a few percents up to 30%. For densities out of this interval and for the longest pulse duration considered, the differences are much higher than 50% (see also Fig.A.21 and Fig.A.22 of Section A.5 - Appendix A). The overestimation of the optimum thickness for long pulse duration ($\tau = 30$ t_0) can be due to the generation of high energy radiation (see Subsection 3.4.2).

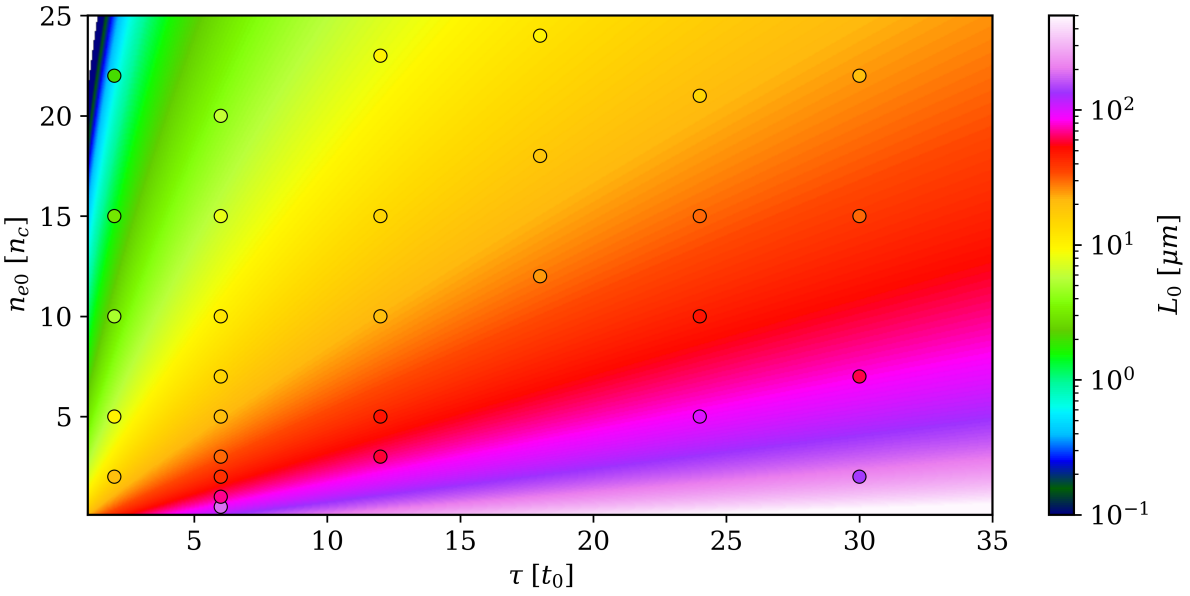

Figure 3.15: Optimum target thickness vs target density and pulse duration. Target parameters: $L_y = 30$ μm. Laser parameters: $\lambda = 1$ μm, $a_0 = 85$ and $w_0 = 12.5$ μm. The simulation results are shown in circles while the results of Eq.(3.21) are shown with the colorscale.

3.4 Perspectives

3.4.1 Model applicability

Our theoretical model was validated in the previous sections using always the same transversal width for the plasma and for the laser pulse. In this section, we test the model for different values of the transversal width of the laser pulse, keeping the plasma transversal width the same.

We consider the case of a near-critical density plasma of 2 n_c density and 40 μm thickness and 30 μm transversal width. The laser parameters are: the laser wavelength $\lambda = 1$ μm, the laser pulse intensity 10^{22} W/cm^2 and the laser pulse duration 20 fs FWHM. The laser pulse tranvsersal width (w_0) varies in the range $\{\pi, 2\pi, 4\pi, 8\pi\}$ μm.

Fig.3.16 shows the energy density map of the heated plasma region in all cases at the same time. The laser heats completely the plasma in the transverse direction, in all cases.

The electron spectra obtained in the simulations are shown in Fig.3.17. The low energy population is the same in all cases, the electron energies varying from a few MeV up to tens of MeV, while the high energy population is increasing when the laser width increases, from

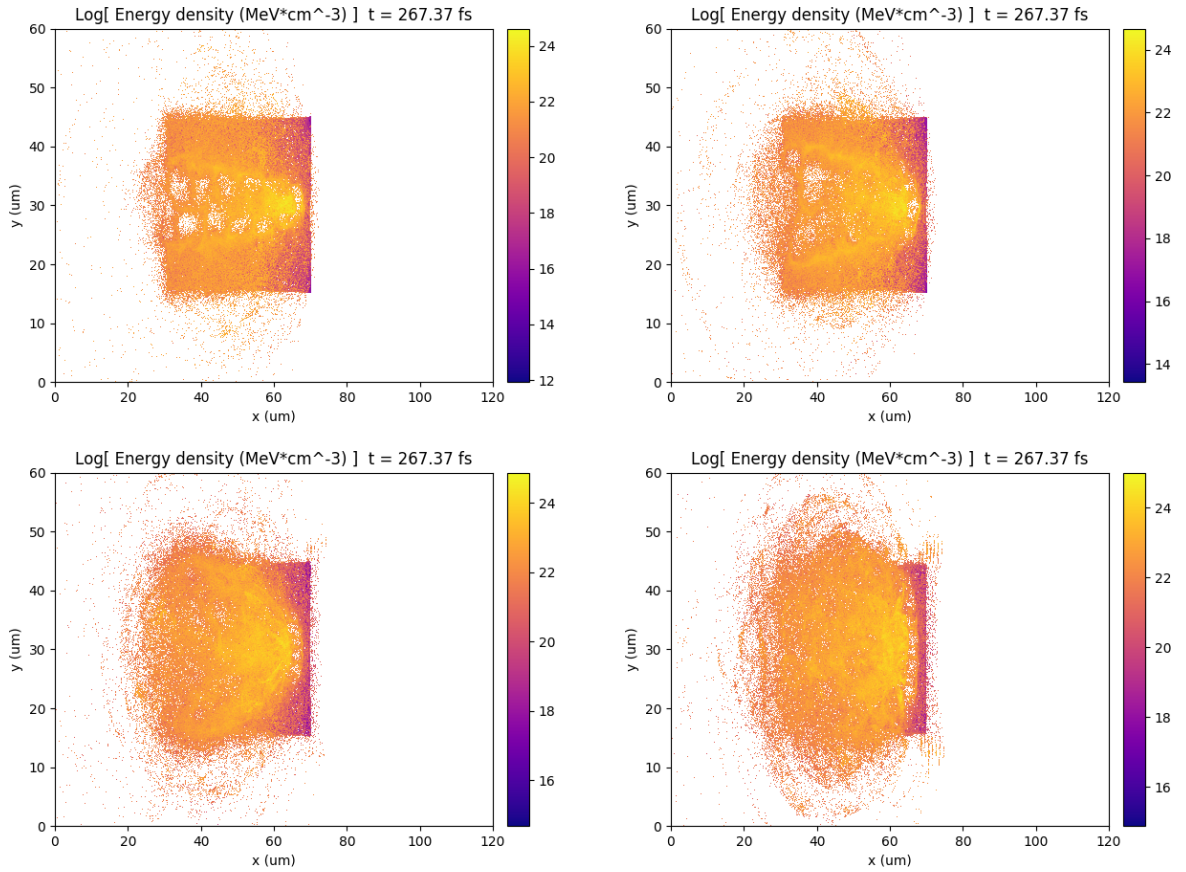

Figure 3.16: Electron energy density map from 2D PIC simulations for 4 different cases: (up left) $w_0 = \pi\ \mu$m, (up right) $w_0 = 2\pi\ \mu$m, (down left) $w_0 = 4\pi\ \mu$m and (down right) $w_0 = 8\pi\ \mu$m. Target parameters: $n_{e0} = 2$ n$_c$, $L_x = 40\ \mu$m and $L_y = 30\ \mu$m. Laser parameters: $\lambda = 1\ \mu$m, $a_0 = 85$ and $\tau = 20$ fs FWHM.

400 MeV up to $>$ 800 MeV. This can be explained by the increase of the laser energy when increasing the laser waist, from 32 J for a laser waist of $w_0 = \pi\ \mu$m up to 2 kJ for $w_0 = 8\pi\ \mu$m, while keeping all other parameters constant.

The characteristics of the electrons are presented in Table3.1. The total absorption of energy in hot electrons is comparable in all cases, except the case of $w_0 = 8\pi\ \mu$m, when the laser width is 2 times bigger than the plasma width and a part of it does not interract with the plasma. Between the total absorption of energy in hot electrons and the absorption in energy in electrons with energy $>$ 5 MeV, the only difference occurs at $w_0 = \pi\ \mu$m.

In order to study the applicability of our model for smaller laser transversal widths than the plasma width, we consider the case of an ultra high intensity laser pulse of $a_0 = 85$, $\tau = 20$ fs FWHM and $w_0 = \pi\ \mu$m interacting with a near critical density plasma with density in $1 - 20$ n$_c$. For each density, we considered two plasma thicknesses: one given by Eq.(3.21) and one which is about 25% smaller than the prediction of Eq.(3.21). In Fig.3.18 is shown the variation of the

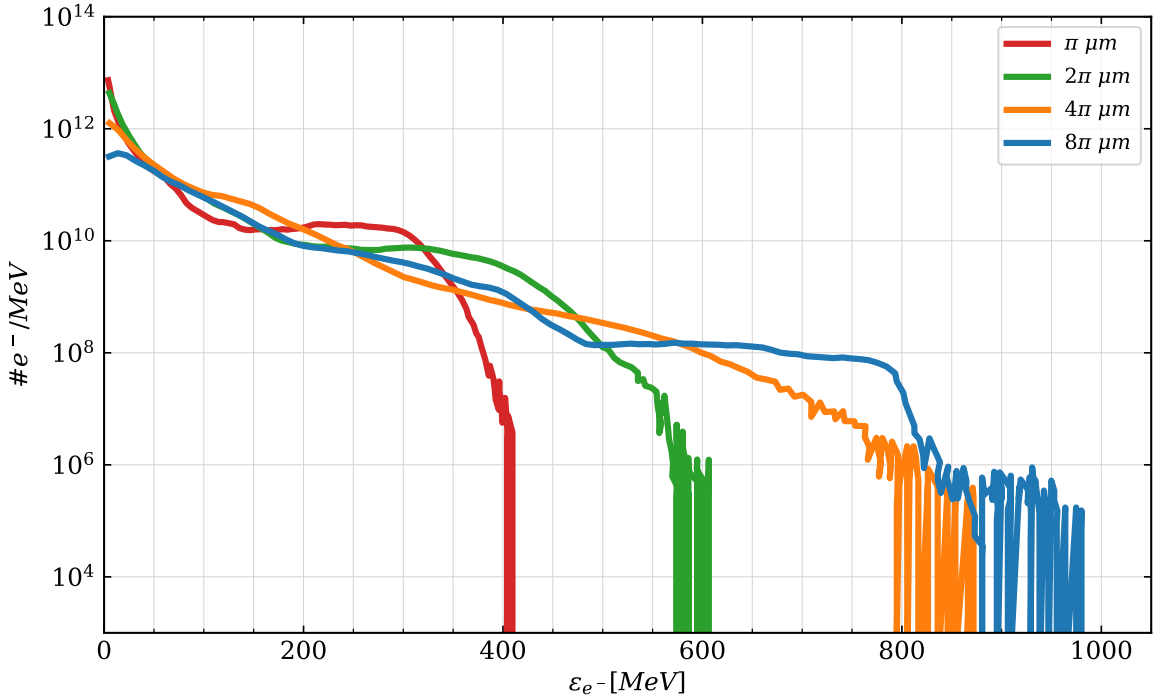

Figure 3.17: Electron spectra for different laser waists from 2D PIC simulations. Target parameters: $n_{e0} = 2$ n$_c$, $L_x = 40$ μm and $L_y = 30$ μm. Laser parameters: $\lambda = 1$ μm, $a_0 = 85$ and $\tau = 20$ fs FWHM.

Table 3.1: Electron characteristics from 2D PIC simulations for different laser waists. Target parameters: $n_{e0} = 2$ n$_c$, $L_x = 40$ μm and $L_y = 30$ μm. Laser parameters: $\lambda = 1$ μm, $a_0 = 85$ and $\tau = 20$ fs FWHM.

w_0 [μm]	π	2π	4π	8π
ε_{laser} [J]	32.67	130.7	522.8	2091.2
η_{e^-} [%]	59.04	63.55	63.21	49.7
$\eta_{\varepsilon_{e^-}>5\text{ MeV}}$ [%]	52.95	61.02	62.59	49.5
$\varepsilon_{e^-,avg}$ [MeV]	34	32.68	46.5	65.92

absorption and transmission coefficients with the target areal density. The absorption coefficient increases when increasing the target thickness and moreover, the transmission coefficient decreases and in all cases reaches a value below 3%. As a further increase of the target thickness will not significantly change the absorption coefficient, consequently the optimum target thickness to maximize the absorption is the one predicted by our model.

We compare the results obtained at $w_0 = \pi$ μm with the ones obtained at $w_0 = 4\pi$ μm, when the laser transversal width is equal to the plasma transversal width. The absorption coefficient variation with the target density at the same optimum target thickness in both cases is shown in Fig.3.19. The absorption coefficient is almost equal in both cases considered and in good agreement with Eq.(3.19) for a wide range of parameters: for $w_0 = 4\pi$ μm the differences

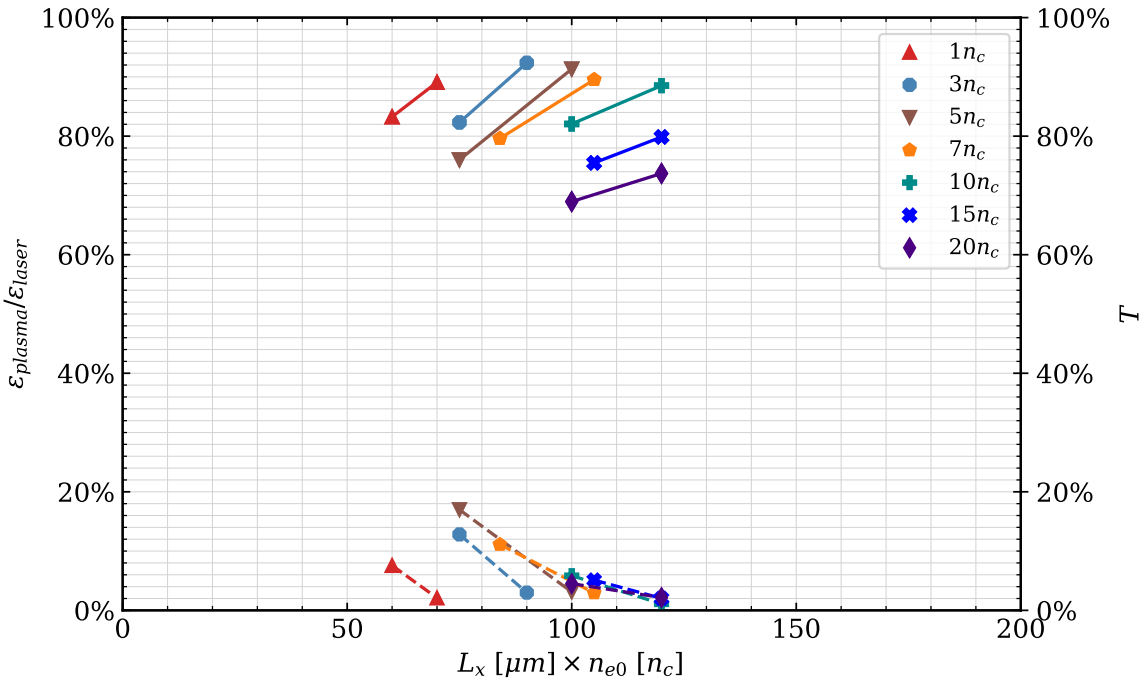

Figure 3.18: Absorption (continuous lines) and transmission (dashed lines) coefficients vs target areal density from 2D PIC simulations. Target parameters: $L_y = 30$ μm. Laser parameters: $\lambda = 1$ μm, $a_0 = 85$, $\tau = 20$ fs FWHM and $w_0 = \pi$ μm.

between the simulation results and Eq.(3.19) vary from a few percents up to 10% for the highest density considered, while for $w_0 = \pi$ μm, the differences can go up to 20%.

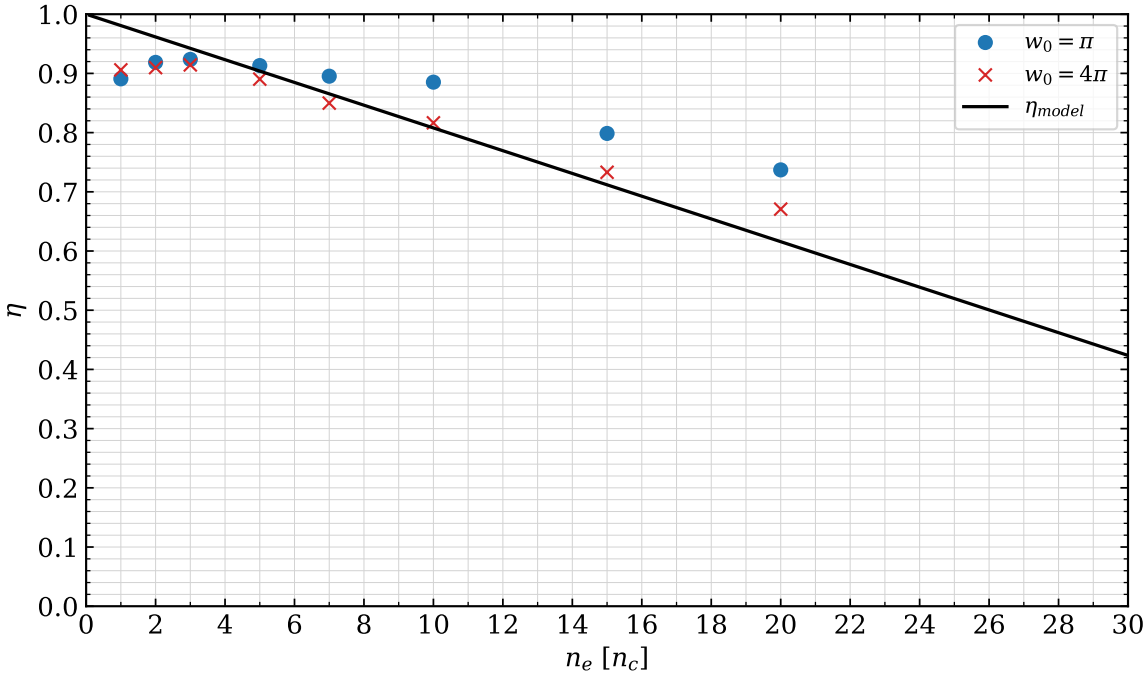

Figure 3.19: Saturation point of the absorption coefficient from 2D PIC simulations vs target density for different laser waists. Target parameters: $L_y = 30$ μm. Laser parameters: $\lambda = 1$ μm, $a_0 = 85$ and $\tau = 20$ fs FWHM. The black line represents the prediction made by Eq.(3.19).

Fig.3.20 presents the variation of the average electron energy (with energies > 5 MeV) with the target density at the same optimum target thickness in both cases. There is a difference between the results obtained for the case $w_0 = \pi$ μm and the prediction made by Eq.(3.20). These results are consistent with the observations made from Fig.3.17.

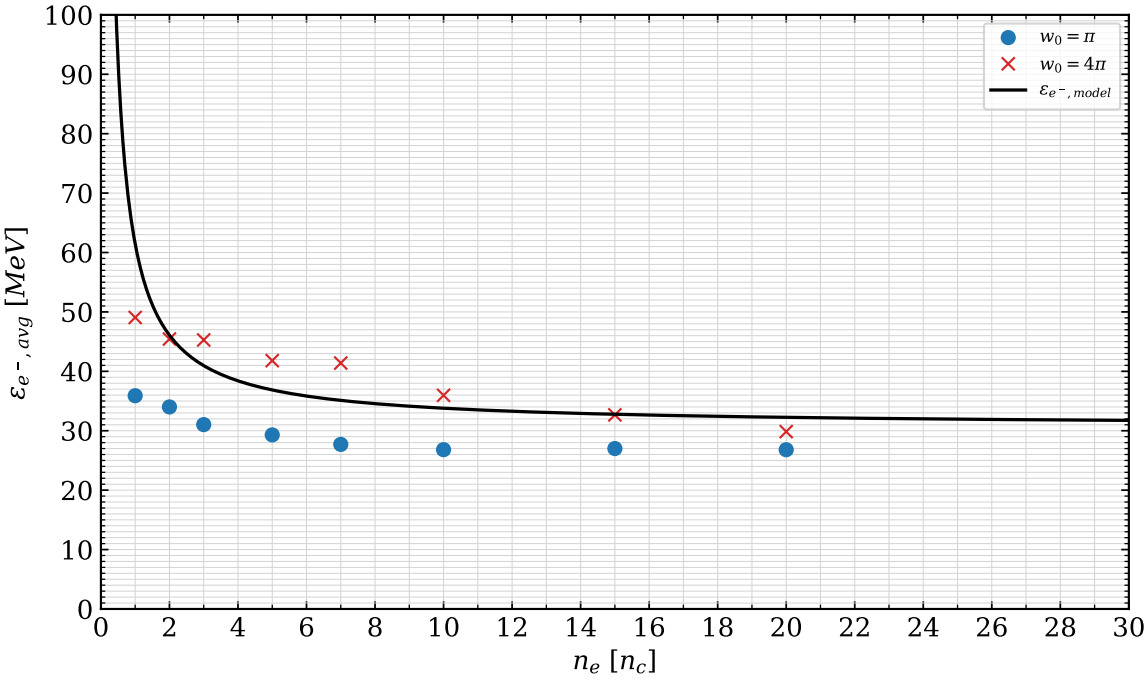

Figure 3.20: Average energy of the hot electrons at the optimum target thickness vs target density from 2D PIC simulations for different laser waists. Target parameters: $L_y = 30$ μm. Laser parameters: $\lambda = 1$ μm, $a_0 = 85$ and $\tau = 20$ fs FWHM. The black line represents the prediction made by Eq.(3.20).

Despite the difference for the electron average energy, the optimum target thickness is the one predicted by our model in all cases, as shown in Fig.3.21 and also observed from Fig.3.18.

3.4.2 Model applications

The proposed theoretical model can be used to optimize all processes that rely on the energy stored in the electrons. In this section are presented additional electrons and high energy photons characteristics.

The electrons present a broad spectrum, as shown in Fig.3.22 with two main populations: a less energetic one, with the energy between 5 MeV and 400 MeV, and a high energy one, with

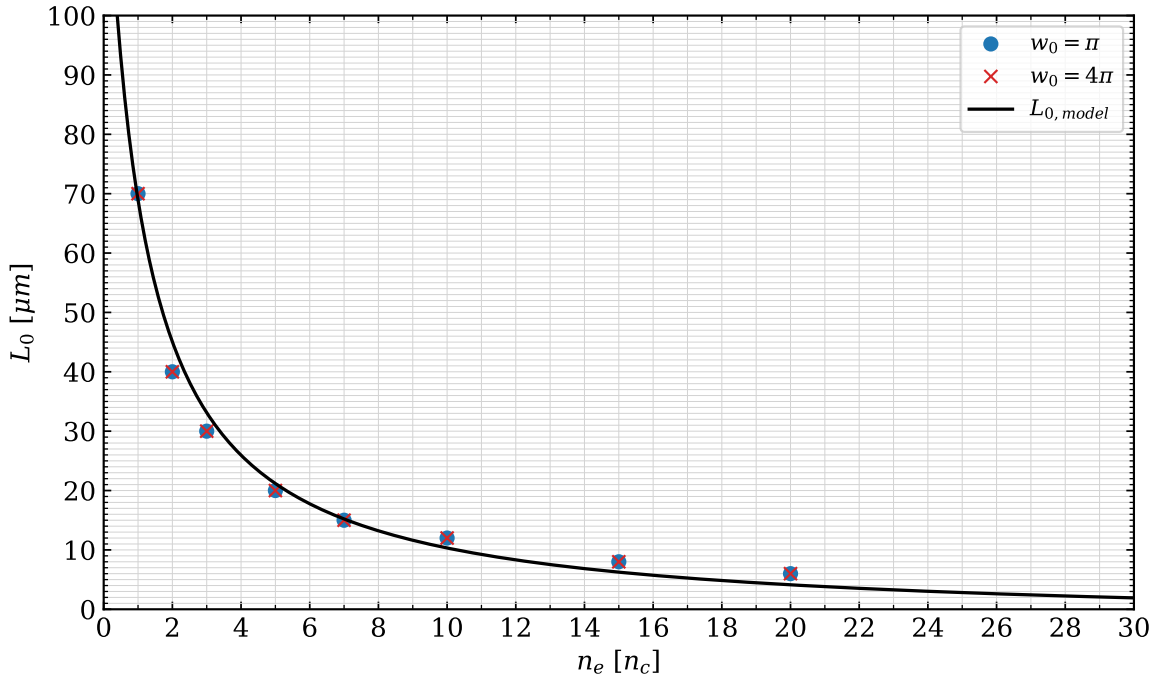

Figure 3.21: Optimum target thickness vs target density from 2D PIC simulations for different laser waists. Target parameters: $L_y = 30\ \mu$m. Laser parameters: $\lambda = 1\ \mu$m, $a_0 = 85$ and $\tau = 20$ fs FWHM. The black line represents the prediction made by Eq.(3.21).

the energy $>$ 400 MeV.

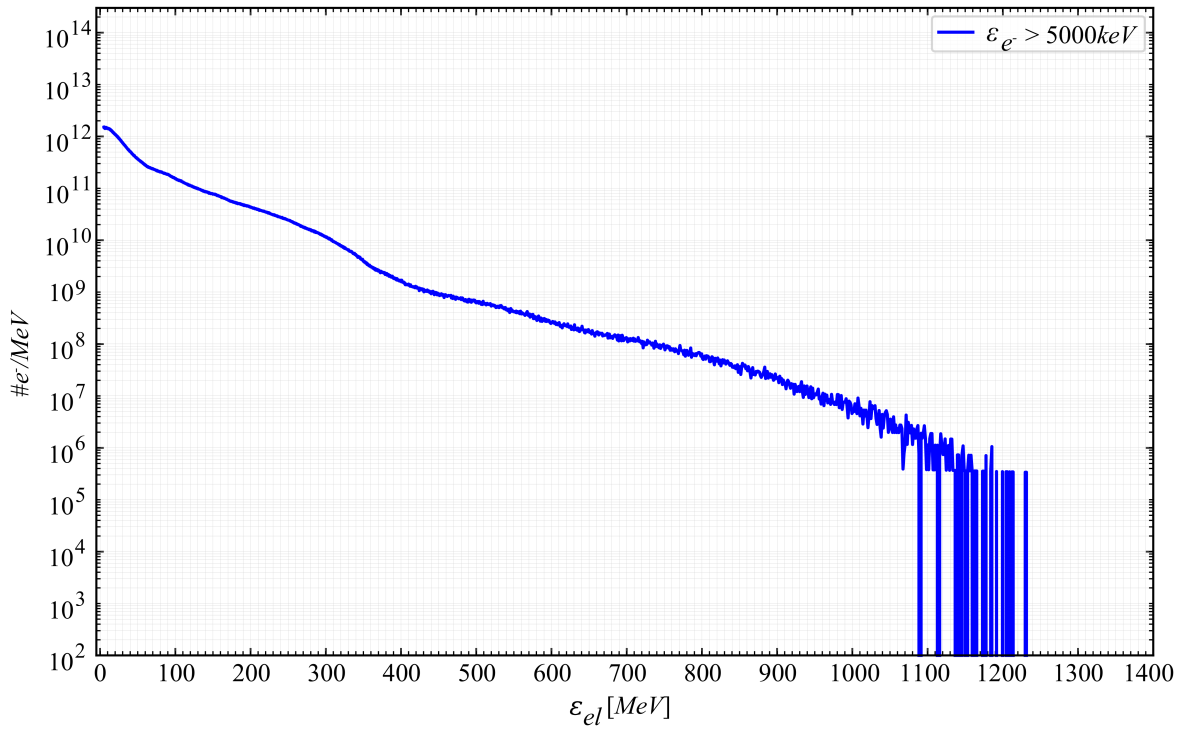

Figure 3.22: Electron spectra from a 2D PIC simulation. Target parameters: $n_{e0} = 3$ n$_c$, $L_x = 40\ \mu$m and $L_y = 30\ \mu$m. Laser parameters: $\lambda = 1\ \mu$m, $a_0 = 85$, $\tau = 20$ fs FWHM and $w_0 = 12.5\ \mu$m.

The maximum energy of the electrons depends on the laser and target parameters. In Fig.3.23 is shown the variation of the maximum electron energy with the target areal density for various laser intensities.

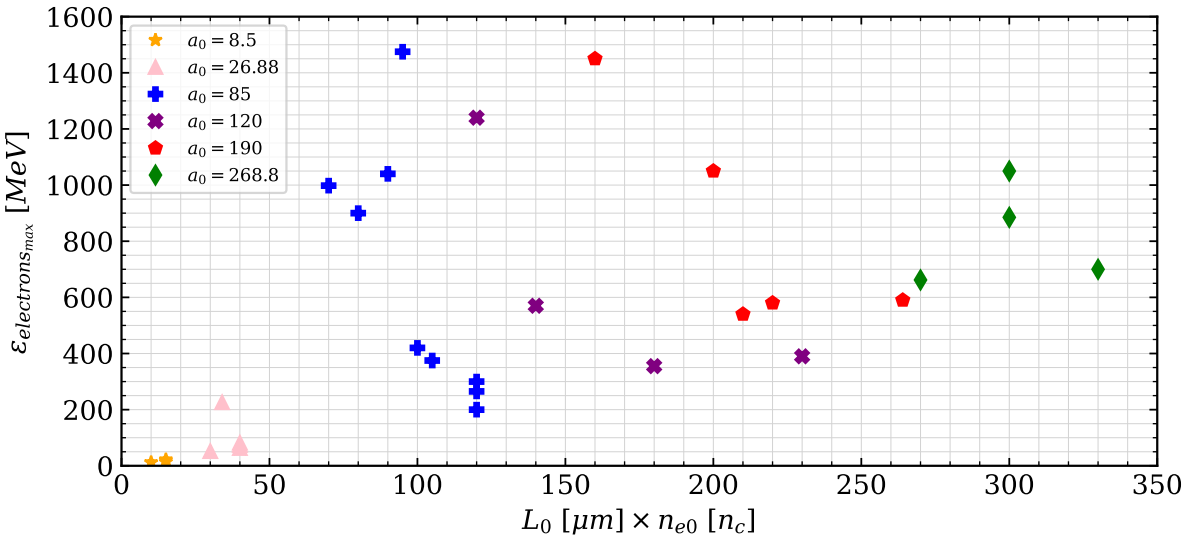

Figure 3.23: Maximum electron energy at the optimum target thickness vs target areal density for various laser pulse intensities. Target parameters: $L_y = 30$ μm. Laser parameters: $\lambda = 1$ μm, $\tau = 20$ fs FWHM and $w_0 = 12.5$ μm.

The maximum electron energy varies from a few tens of MeV for low laser intensities up to > 1 GeV for ultra-high laser intensities. In addition, for similar areal density we have a strong variation of the maximum energy: from 200 MeV to 1.5 GeV for $a_0 = 85$. This is due to the dependence of the maximum electron energy on the target density, as shown in Fig.3.24. The maximum energies are obtained for the lowest target density. For targets with densities > 10 n_c, the maximum electron energy varies slowly for the same laser pulse intensity.

In Fig.3.25 is shown the variation of the maximum electron energy with the target areal density for various laser pulse durations.

The maximum electron energy varies from a few hundreds of MeV up to 1.5 GeV. In addition, the previously explained behaviour is present: for the same areal density, the maximum electron energy varies dramatically due to the target density, as shown in Fig.3.26. The highest electron energy is obtained for the longest pulse duration, corresponding to the highest laser energy used in this variation, and the lowest target density considered. For targets with densities > 10 n_c, the maximum electron energy varies slowly for the same laser pulse duration.

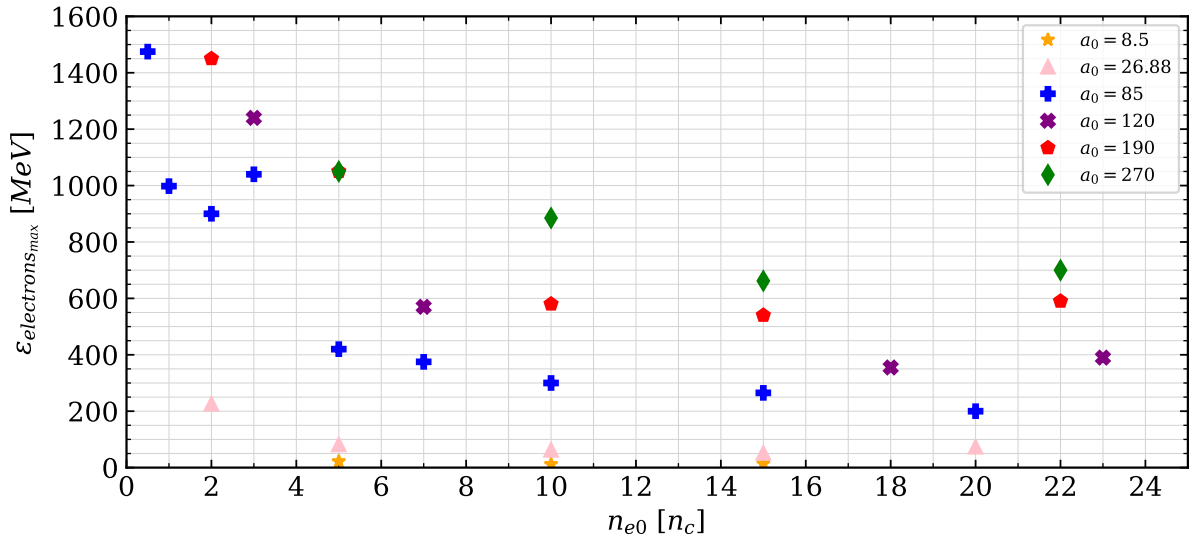

Figure 3.24: Maximum electron energy at the optimum target thickness vs target density for various laser pulse intensities. Target parameters: $L_y = 30$ μm. Laser parameters: $\lambda = 1$ μm, $\tau = 20$ fs FWHM and $w_0 = 12.5$ μm.

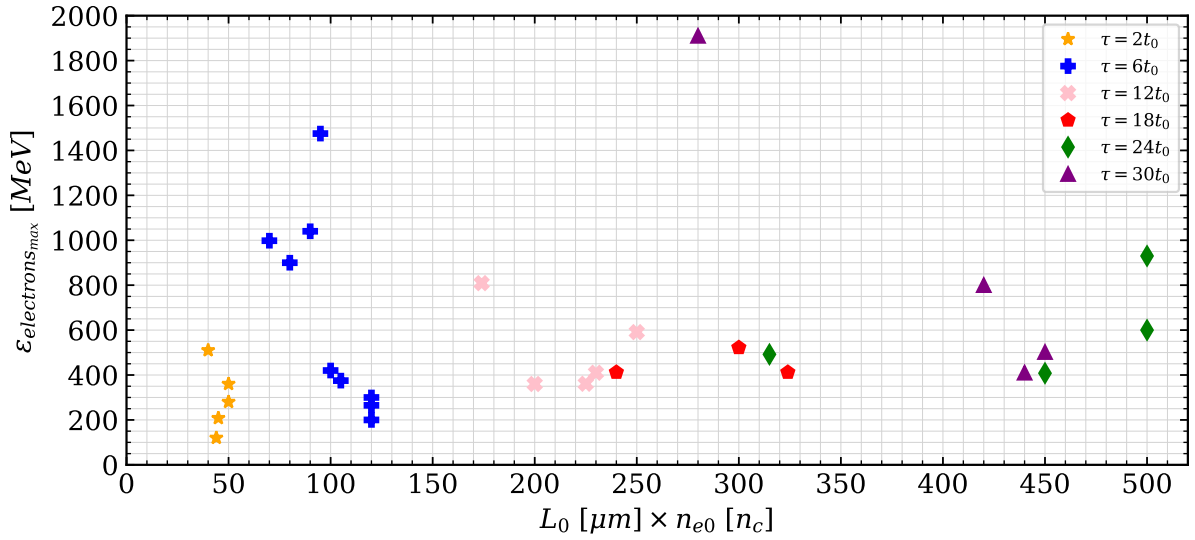

Figure 3.25: Maximum electron energy at the optimum target thickness vs target areal density for various laser pulse durations. Target parameters: $L_y = 30$ μm. Laser parameters: $\lambda = 1$ μm, $a_0 = 85$ and $w_0 = 12.5$ μm.

As previously mentioned, the relativistic electrons will emit a copious amount of high energy radiation. Fig.3.27 shows the variation of the absorption coefficient of the laser energy to high energy photons with the target areal density for various laser pulse intensities. The absorption coefficient in high energy photons increases from $\leq 1\%$ for a laser intensity of $I = 10^{20}$ W/cm^2 ($a_0 = 8.5$) to 30% for ultra-high intensity laser pulses $I = 10^{23}$ W/cm^2 ($a_0 = 268.8$).

In Fig.3.28, it is shown the variation of the absorption coefficient of the laser energy

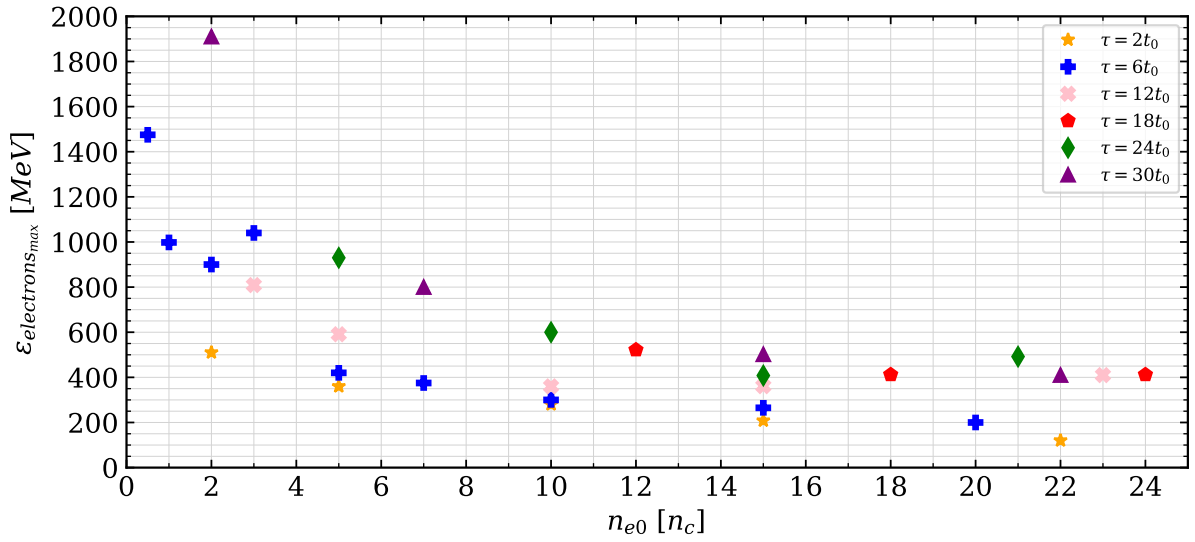

Figure 3.26: Maximum electron energy at the optimum target thickness vs target density for various laser pulse durations. Target parameters: $L_y = 30$ μm. Laser parameters: $\lambda = 1$ μm, $a_0 = 85$ and $w_0 = 12.5$ μm.

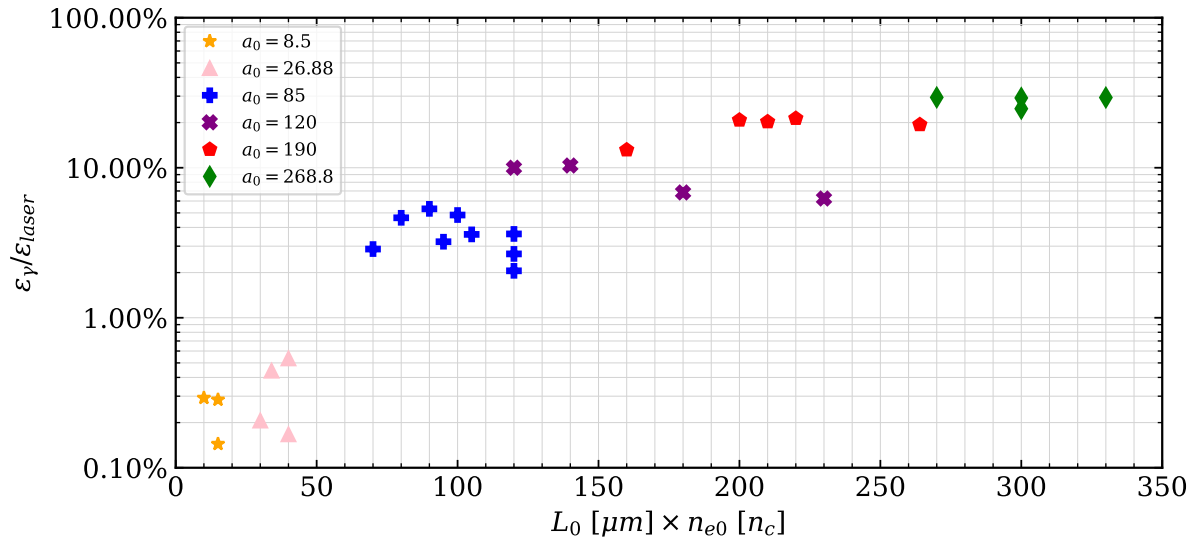

Figure 3.27: Absorption coefficient from the laser pulse to high energy photons at the optimum target thickness vs target areal density for different laser intensities. Target parameters: $L_y = 30$ μm. Laser parameters: $\lambda = 1$ μm, $\tau = 20$ fs FWHM and $w_0 = 12.5$ μm.

to high energy photons with the target areal density for various laser pulse durations. The absorption coefficient in high energy photons increases from $\leq 1\%$ for very short pulse duration ($\tau = 2$ t$_0$) to 10% for longer pulse durations ($\tau = 30$ t$_0$).

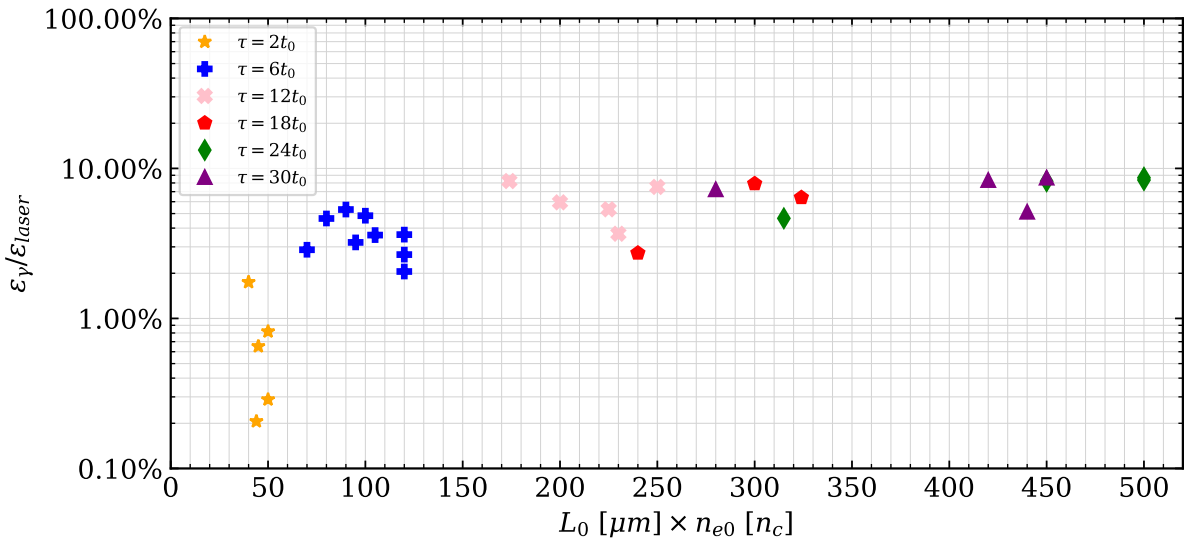

Figure 3.28: Absorption coefficient from the laser pulse to high energy photons at the optimum target thickness vs target areal density for different laser pulse durations. Target parameters: $L_y = 30\ \mu$m. Laser parameters: $\lambda = 1\ \mu$m, $a_0 = 85$ and $w_0 = 12.5\ \mu$m.

3.5 Summary of the results

We studied the maximum absorption of the laser energy in the case of near critical density targets with areal densities between $5 - 800\ n_{e0}L_x$. For a laser intensity of 10^{22} W/cm^2, the optimum areal density was found to be in the interval $70 - 120\ n_{e0}L_x$, corresponding to a maximum absorption coefficient of $67 - 95\%$. Minimizing the transmission coefficient at saturation, we found a semi-empirical model for the absorption coefficient, dependent on the target density, the laser intensity and the pulse duration. For the same areal density, we estimated the average energy of the hot electrons with the ponderomotive scaling, corrected by a factor which depends on the target density. Finally, we formulated a model for maximizing the laser energy absorption in the case of near critical density targets.

The theoretical model proposed shows good agreement with the simulation results obtained for a large set of parameters: laser pulse duration $\tau : 2 - 30\ t_0$ (for $a_0 = 85$), laser normalized field amplitude $a_0 : 26.88 - 268.8$ (for $\tau = 6\ t_0$) and target density $n_{e0} : 0.5 - 24\ n_c$. The model proposed by Eq.(3.21) is useful to guide maximum absorption in plasma, for studies involving generation of hot electrons and generation of high energy radiation [129, 93, 130, 131, 77, 132, 87].

These results can also be used to optimize the target areal density for maximizing pro-

ton acceleration. The maximum proton energy and the main acceleration mechanisms will be further discussed in Chapter 4.

Chapter 4

Proton acceleration for a_0=85

The laser absorption mechanisms determine the characteristics of the accelerated particles. In this chapter we analyze the particle acceleration, especially proton acceleration, in the case of an ultra-high intensity laser pulse interacting with a near-critical density target. In Section 4.1, the 2D simulation setup is presented and in Section 4.2 the main acceleration mechanisms are studied. Based on the literature and new findings from our model, the optimum thickness for proton acceleration and the maximum proton energies for an expansion like mechanism are predicted in Section 4.3. Finally, the main findings of this study are summarized in Section 4.4.

4.1 2D PIC simulation setup

We studied laser proton acceleration in the near-critical density regime. The 2D PIC simulation setup is similar to the one from Fig.3.2. The laser is linearly polarized and has the following characteristics: a wavelength of 1 μm, a transversal waist of 4π μm, a pulse duration of 20 fs FWHM (6 t_0) and a laser pulse intensity of 10^{22} W/cm^2 ($a_0 = 85$). The target is considered fully ionized, being made of protons and electrons. The density of the target varies from 0.5 n_c to 20 n_c, the target thickness varies from 500 nm to 200 μm and the transversal width of the target is 30 μm. The simulation box has 60 μm in the y direction, while in the x direction it is changed according to the thickness L_x of the target from 120 μm to 300 μm. The

cell length is $dx = dy = 15.625$ nm and the number of particles per cell is 30 for each species. The particles are deleted while crossing the domain boundaries and the fields are absorbed. The simulations were performed with Simulating Matter Irradiated by Light at Extreme Intensities (SMILEI) [99] on the Curta machine - MCIA [106].

4.2 Electron heating and proton acceleration mechanisms

At the interaction of the laser pulse with the target, the electrons (being lighter than the protons) will be accelerated by the laser ponderomotive force $f_p = -m_e c^2 \gamma_a$, where $\gamma_a = (1 + a_0^2/2)^{1/2}$ and a_0 is the laser normalized field amplitude. The oscillating part of the ponderomotive force will push the electrons with an angular frequency of $2\omega_l$, as can be observed in the electron density map and the electron phase space from Fig.4.1. A few examples of individual electron trajectories are shown in Section B.1 from Appendix B.

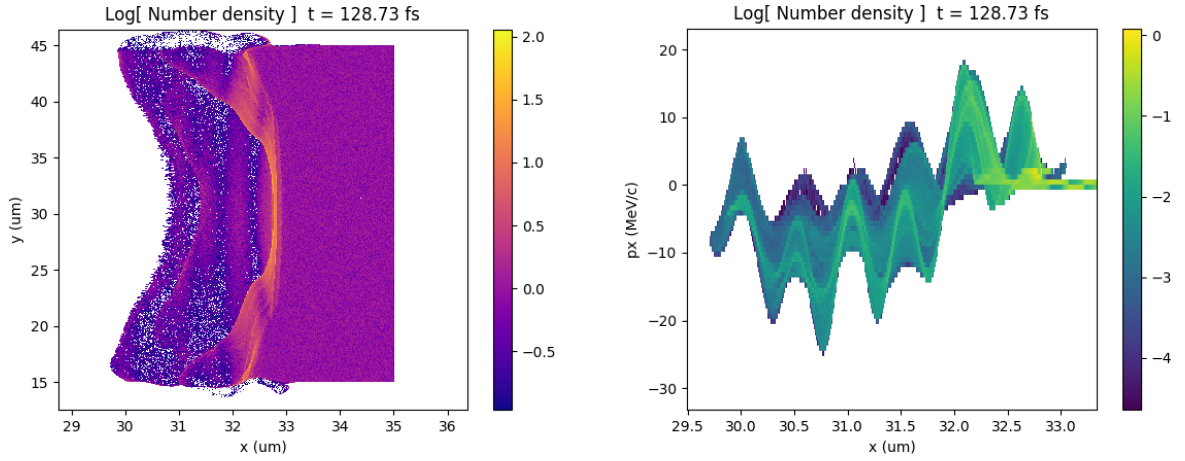

Figure 4.1: Electron density map (left) and phase space (right) from a 2D PIC simulation. Target parameters: $n_{e0} = 1$ n_c, $L_x = 20$ μm and $L_y = 30$ μm. Laser parameters: $\lambda = 1$ μm, $a_0 = 85$, $\tau = 20$ fs FWHM and $w_0 = 12.5$ μm.

As in all our cases $a_0 >> n_{e0}/n_c$, the laser propagates inside the target and while propagating inside the target, the laser can be modulated and focused by the target. We consider the case of a 15 μm target thickness of two densities: 1 n_c and 7 n_c to represent the transparent regime and the transition to the opaque one. In Fig.4.2 is represented the evolution in time of the electric field for both cases. For the 1 n_c target density, the laser will be focused, and its normalized field amplitude will increase from $a_0 = 85$ up to $a_0 = 100$. The laser focusing is taking place at the beginning of the interaction, and 22% of the laser energy will be absorbed

into the plasma. After passing through the target, the laser will continue unperturbed its propagation, maintaining a high value of the electric field. In this regime, the laser transmission is very high, around 72%, and the reflection is less than 1%. In the case of a 7 n_c target density, the focusing and the absorption of the laser will occur very fast, 85% of its energy being transferred to the particles. The electrons will be pushed forward and form a denser area, which will reflect around 10% of laser energy, and less than 2% will be transmitted to the end of the simulation box.

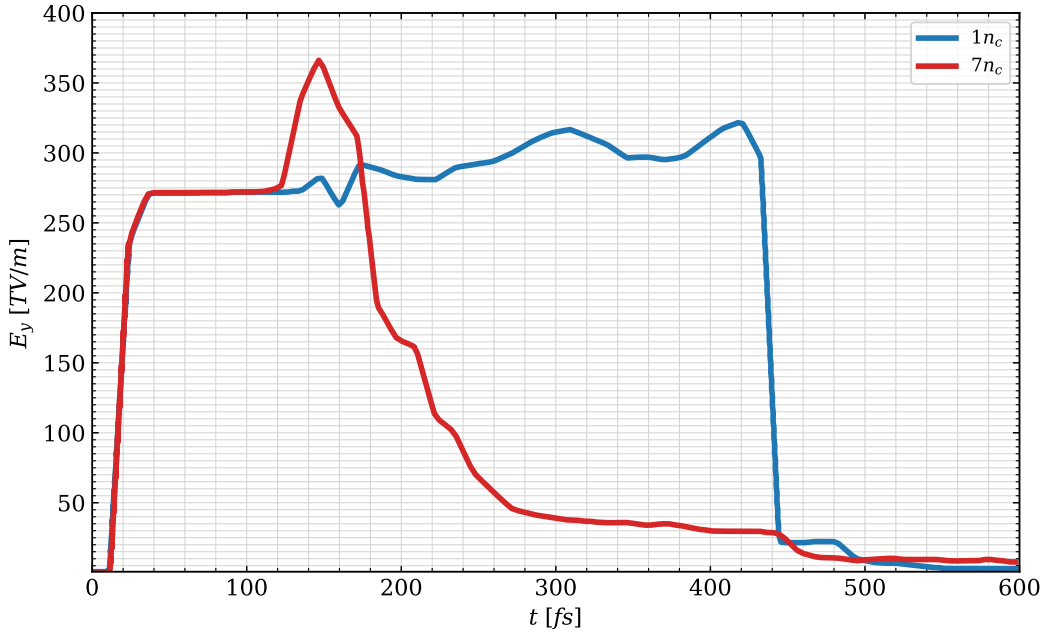

Figure 4.2: Temporal evolution of the transversal component of the laser electric field from 2D PIC simulations for two different target densities. Target parameters: $L_x = 15$ μm and $L_y = 30$ μm. Laser parameters: $\lambda = 1$ μm, $a_0 = 85$, $\tau = 20$ fs FWHM and $w_0 = 12.5$ μm.

The denser area in front of the laser pulse is present in mutliple simulations. However, the average density in this region is at most 27% higher than the initial target density as detailed in Section B.2 from Appendix B.

The electrons are pushed forward by the laser field much faster than the protons. The later ones, having a small charge-to-mass ratio will be left behind. This charge displacement occurring inside the target will create a very strong quasi-static charge separation field at the back of the target as shown in Fig.4.3.

In order to understand the dependence of the electric field on the target density, we will take the case of 30 μm thickness for various densities. The maximum value of the longitudinal

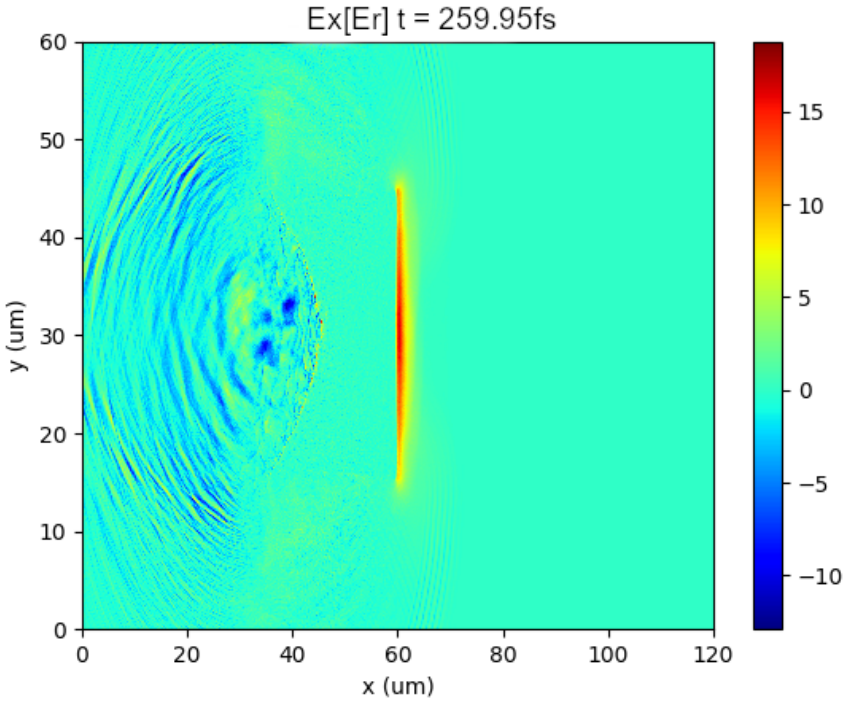

Figure 4.3: 2D map of the longitudinal electric field as obtained in a 2D PIC simulation. Target parameters: $n_{e0} = 10$ n$_c$, $L_x = 30$ μm and $L_y = 30$ μm. Laser parameters: $\lambda = 1$ μm, $a_0 = 85$, $\tau = 20$ fs FWHM and $w_0 = 12.5$ μm.

electric field E_x is shown in Fig.4.4.

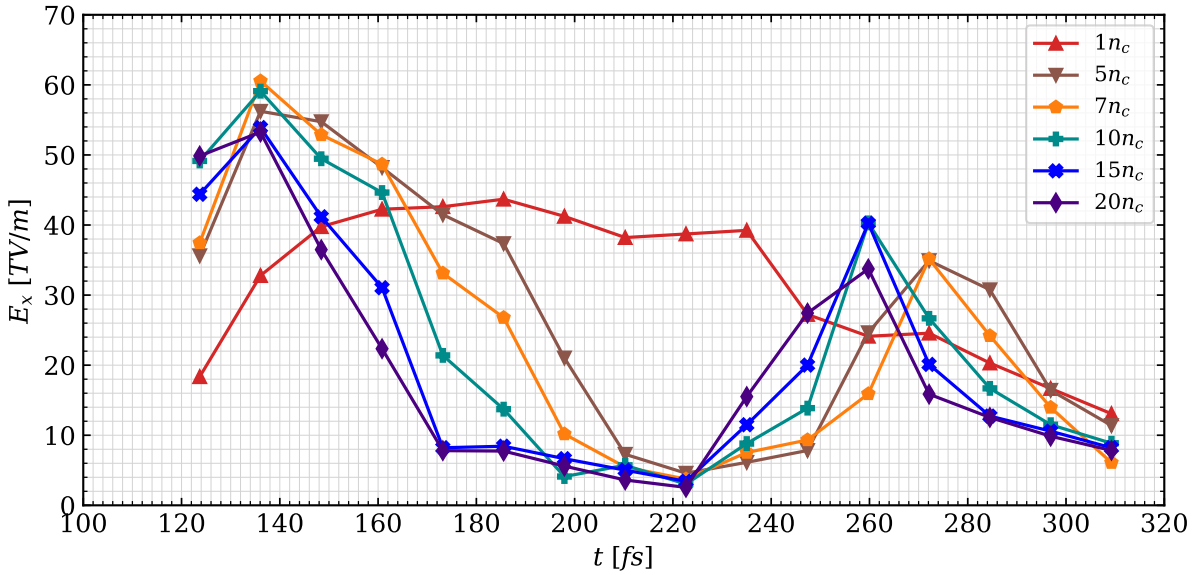

Figure 4.4: The temporal variation of the maximum value of the longitudinal electric field from 2D PIC simulations for various target densities. Target parameters: $L_x = 30$ μm and $L_y = 30$ μm. Laser parameters: $\lambda = 1$ μm, $a_0 = 85$, $\tau = 20$ fs FWHM and $w_0 = 12.5$ μm.

As we can observe, the electric field shows two peaks: one representing the x-component

of the initial electric field of the laser, and the second one representing the charge separation field due to the displacement of the electrons. The value of the second peak reaches in average around 65% of the value of the first one. For a denser target (20 n_c), the second peak can reach 75% of the initial peak. The corresponding position of the peaks is represented in Fig.4.5.

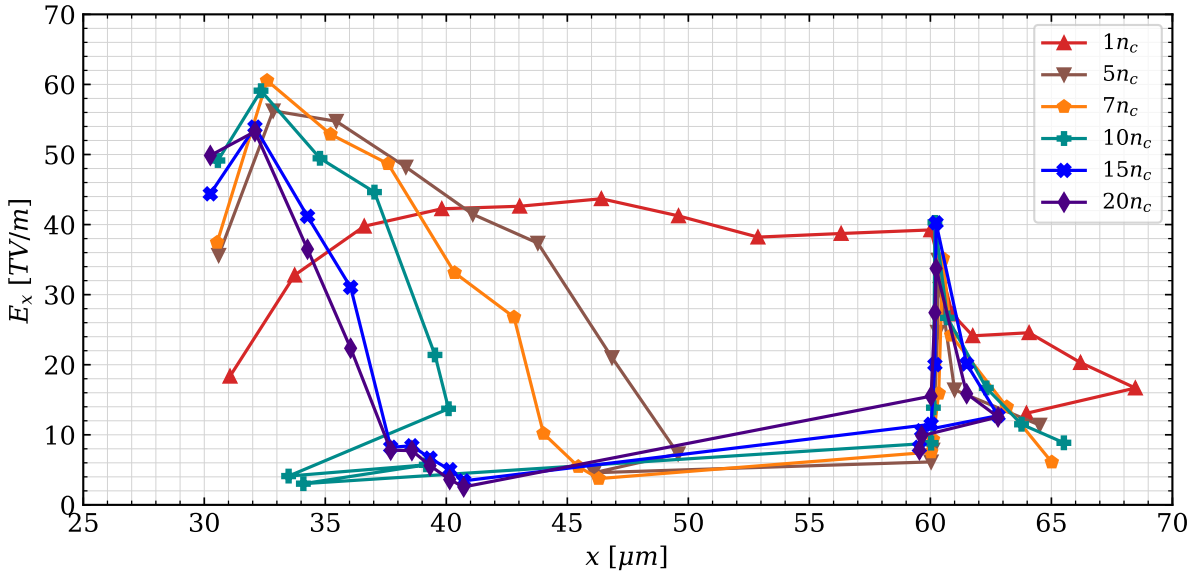

Figure 4.5: The spatial variation of the maximum value of the longitudinal electric field from 2D PIC simulations for various target densities. Target parameters: $L_x = 30$ μm and $L_y = 30$ μm. Laser parameters: $\lambda = 1$ μm, $a_0 = 85$, $\tau = 20$ fs FWHM and $w_0 = 12.5$ μm.

The target original position is from $x = 30$ μm to $x = 60$ μm. For a target of 1 n_c initial density, the electric field from the beginning of interaction maintains its high values due to the laser propagation and focusing inside the plasma. The value of the electric field at the back of the target $x = 60$ μm is related to a superposition of the laser electric field and the charge separation one.

The electric field at the back of the target will have two effects on the plasma dynamics: the deceleration of the electrons and the acceleration of the protons, as explained in Section 1.3.

At ultra-high intensities, the electron energy can be much higher than the ponderomotive scaling. The faster electrons will escape the potential created at the back of the target, meanwhile the slower ones will be reinjected in the target, forming a counterpropagating current. In Fig.4.6 is shown the electron phase-space as obtained in 2D PIC simulations for a target thickness of 5 μm at two target densities: $n_{e0} = 1$ n_c (left) and $n_{e0} = 10$ n_c (right). The high energy electrons can be seen escaping the target, while the lower energy ones are recirculating back

inside the target. Moreover, for the lower density case, a higher number of the electrons escape the target potential.

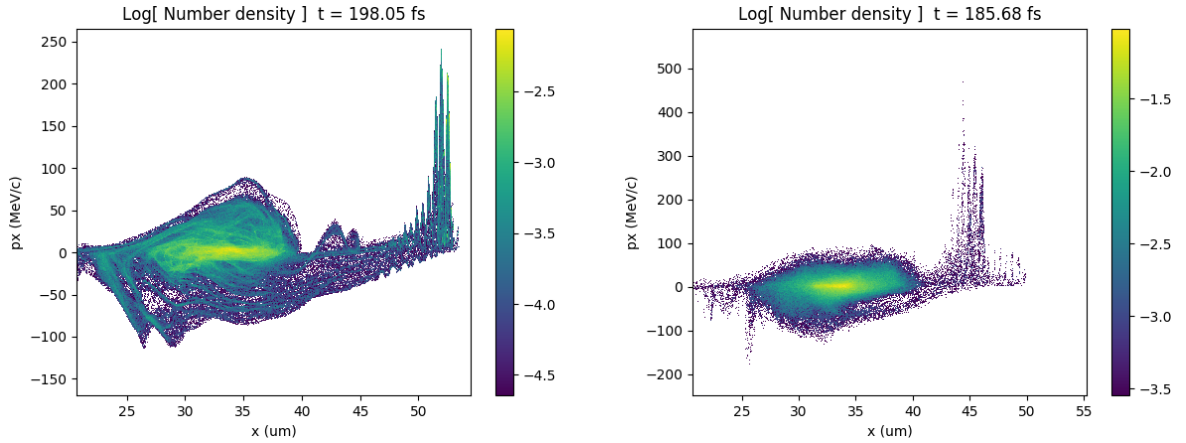

Figure 4.6: Electron phase-space from 2D PIC simulations for a target density of $n_{e0} = 1$ n_c (left) and $n_{e0} = 10$ n_c (right). Target parameters: $L_x = 5$ μm and $L_y = 30$ μm. Laser parameters: $\lambda = 1$ μm, $a_0 = 85$, $\tau = 20$ fs FWHM and $w_0 = 12.5$ μm.

The energetic electrons will be subject to Inverse Compton Scattering, emitting radiation at the interaction with the high intensity laser field. The emission of the radiation will be mainly in the direction of the electron propagation. This subject will be further treated in Section 5.1 of Chapter 5.

4.2.1 Electron characteristics

The absorption coefficient of the laser energy to electrons vs target areal density is shown in Fig.4.7. The dependence of the absorption coefficient of the laser energy to electrons is very similar with the total absorption coefficient dependence on the target areal density from Fig.3.5. This supports the fact that the laser absorption is made mainly via the electrons. Moreover, as long as the laser normalized field amplitude is smaller than the ratio between the ion mass and the electron mass, the laser electromagnetic fields will not directly accelerate the ions.

The electrons are accelerated to relativistic velocities, their maximum energy being in the range of hundreds of MeV - GeV, as shown in Fig.4.8. The maximum energy of the electrons as a function of the target areal density shows an optimum, which is reached before the saturation of the laser-to-electrons conversion coefficient. For a thicker and denser target than the optimum values for acceleration, the electrons will be heated in a larger volume, which will

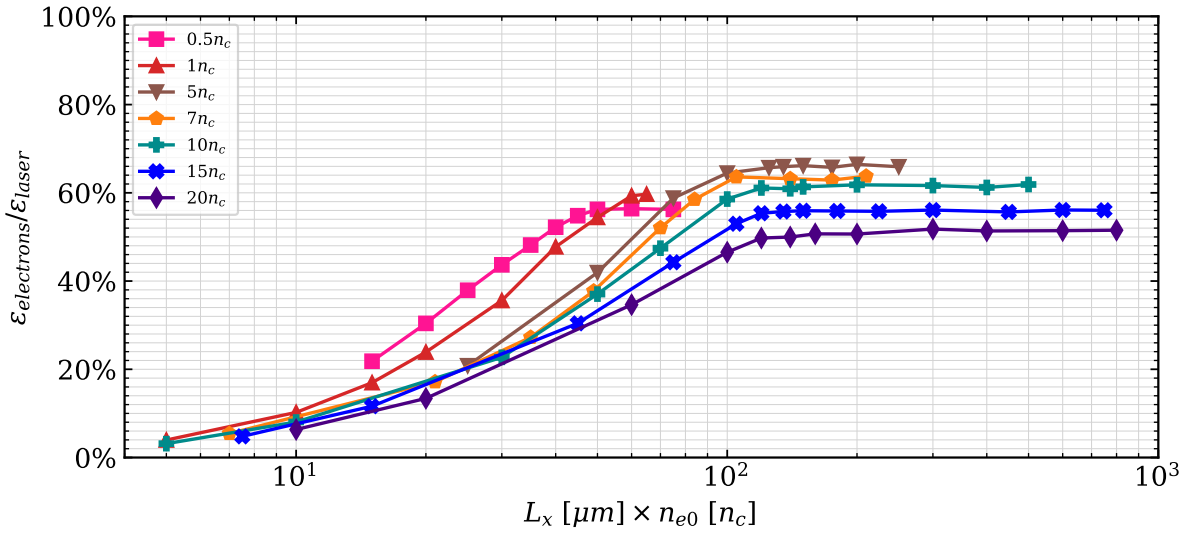

Figure 4.7: Energy conversion coefficient from the laser to electrons vs target areal density as obtained in 2D PIC simulations. Target parameters: $L_y = 30\ \mu$m. Laser parameters: $\lambda = 1\ \mu$m, $a_0 = 85$, $\tau = 20$ fs FWHM and $w_0 = 12.5\ \mu$m.

lead to a lower electron energy density.

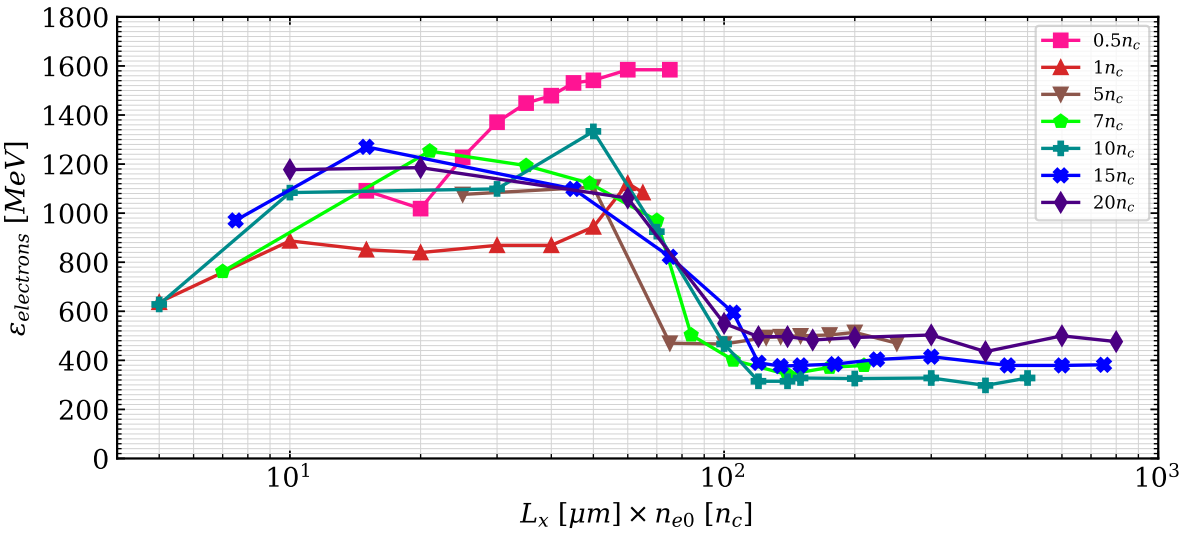

Figure 4.8: Maximum electron energy vs target areal density, as obtained in 2D PIC simulations. Target parameters: $L_y = 30\ \mu$m. Laser parameters: $\lambda = 1\ \mu$m, $a_0 = 85$, $\tau = 20$ fs FWHM and $w_0 = 12.5\ \mu$m.

In the ultra-relativistic regime, the electrons will start to lose a significant part of their energy by emitting radiation. In Section 5.1 of Chapter 5 we will describe the emission of radiation in the transparent and opaque regimes.

4.2.2 Proton acceleration mechanisms

As already explained in Section 1.3 of Chapter 1, there are two main proton acceleration mechanisms for the regime considered: RPA (radiation pressure acceleration), mainly driven by the intense light pressure, and TNSA (Target Normal Sheath Acceleration), driven by the quasi-electrostatic charge-separation field created at the back of the target, as shown in Fig.4.3. The TNSA quasi-electrostatic field appears also in the front side of the target due to plasma expansion. To study the origin of the accelerated protons, we considered a target made of two species of protons: front and rear protons, named after their position in the target structure as shown in the inset of Fig.4.9.

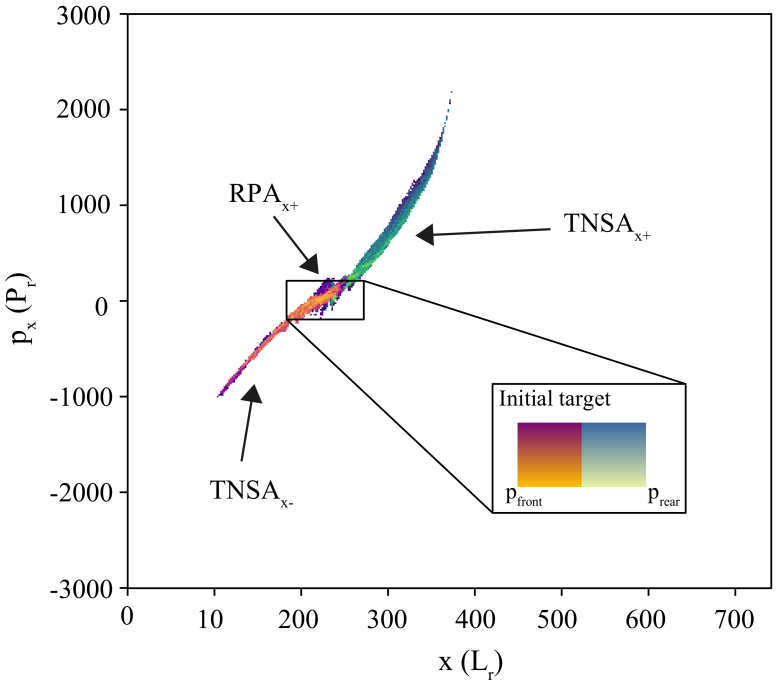

Figure 4.9: Proton phase space from a 2D PIC simulation. Target parameters: $n_{e0} = 5$ n$_c$, $L_x = 10$ μm and $L_y = 30$ μm. Laser parameters: $\lambda = 1$ μm, $a_0 = 85$, $\tau = 20$ fs FWHM and $w_0 = 12.5$ μm. The inset describes the initial repartition of protons inside the target. The main proton acceleration mechanisms are RPA and TNSA.

The protons are accelerated according to their position in the target. The front-located protons will be accelerated in the forward direction by the RPA mechanism and during their propagation, they will be re-accelerated by the electric field at the back of the target (TNSA mechanism), while the back-located protons will be accelerated only by TNSA. We observe that some front located protons are accelerated in the forward direction by the laser pressure while others are accelerated in the backward direction due to the strong expansion of the target.

The same behaviour was present in all optimum cases considered.

4.3 Proton acceleration results

The absorption coefficient of the laser energy to protons vs target areal density is shown in Fig.4.10. As it can be observed, there is a preferential areal density for which the transfer of laser energy to protons is optimized.

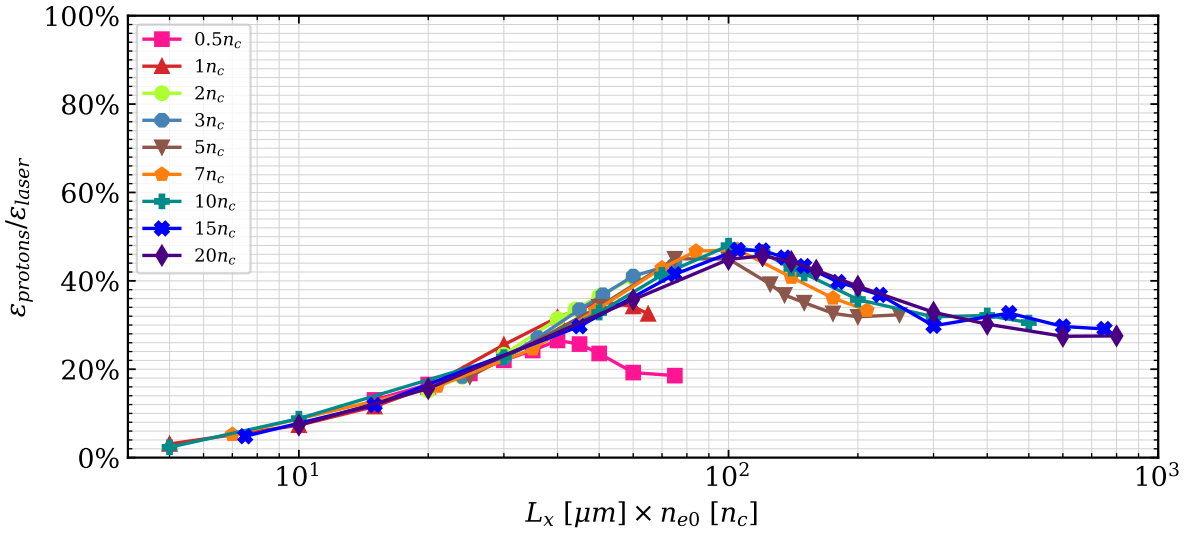

Figure 4.10: Energy conversion coefficient from the laser to protons vs target areal density as obtained in 2D PIC simulations. Target parameters: $L_y = 30\ \mu$m. Laser parameters: $\lambda = 1\ \mu$m, $a_0 = 85$, $\tau = 20$ fs FWHM and $w_0 = 12.5\ \mu$m.

In addition, the maximum proton energy is obtained for a preferential target areal density, as can be observed in Fig.4.11. This behaviour was already reported in previous studies [53, 51].

Comparing Fig.3.5 with Fig.4.11, we can observe that the optimum areal density for proton acceleration is much smaller than the optimum areal density for laser energy absorption in all plasma constituents. To maximize the absorption of the laser energy, the optimum areal density was found to be in the interval $70-120$ $n_{e0}L_x$ as shown in Fig.3.5, while to maximize the proton energies, the optimum areal density is about the half of this interval, $30-50$ $n_{e0}L_x$ as shown in Fig.4.11. After reaching optimum acceleration, the conversion coefficient grows slower, reaches a maximum value and then decreases as the areal density increases. This is due

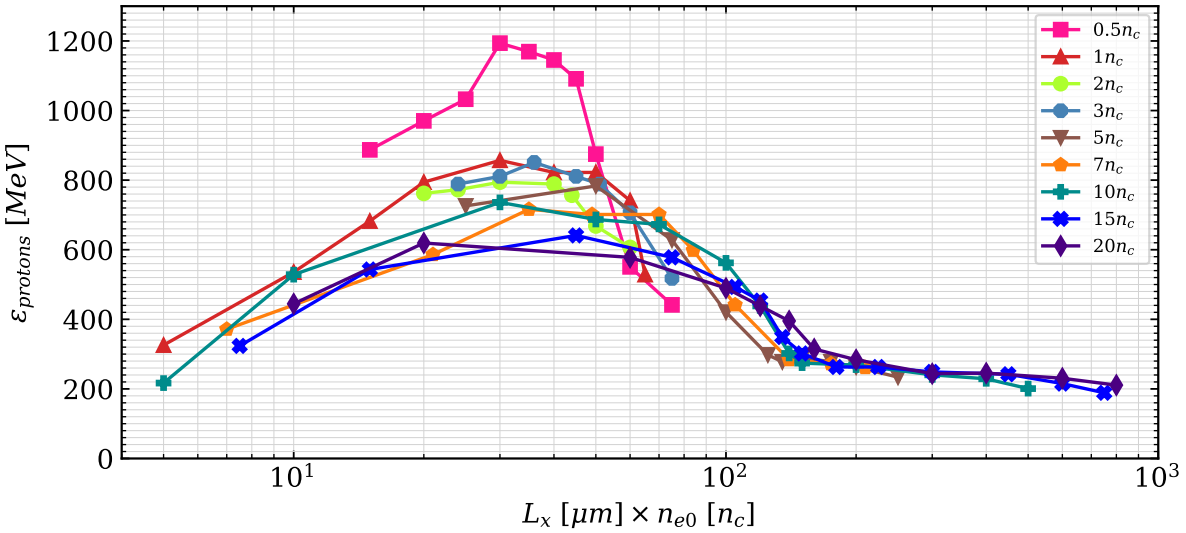

Figure 4.11: Maximum proton energy vs target areal density, as obtained in 2D PIC simulations. Target parameters: $L_y = 30$ μm. Laser parameters: $\lambda = 1$ μm, $a_0 = 85$, $\tau = 20$ fs FWHM and $w_0 = 12.5$ μm.

to the spread of the hot electrons over a larger volume in the target, which results in a lower density of hot electrons, and in turn in a lower energy for the accelerated protons. Moreover, the optimum target thickness for proton acceleration corresponds to the point where the transmission and the absorption coefficients become almost equal (see Fig.3.5 and Fig.3.6). This behaviour is related to the competition between the increase of the absorption coefficient with increasing target thickness and the increase of hot electron density with decreasing target thickness [50, 53]. For a target density 0.5 n_c, the areal density to maximize the absorption of the laser energy to protons from Fig.4.10 is almost the same with the one to maximize the proton energies from Fig.4.11. For very low target densities, we are approaching the laser wakefield acceleration regime, where we start to accelerate more efficiently the electrons, which in turn leads to a more efficient proton acceleration. At the corresponding optimum thickness for proton acceleration, for a target density of 0.5 n_c the absorption of the laser energy in electrons with the energies ≥ 1 MeV is 22%, while for the case of 1 n_c it is 11%. Moreover, for the case of 0.5 n_c, the laser is focused while propagating inside the target, a behaviour similar to the one from Fig.4.2 for 1 n_c target density, and the maximum value of its normalized field amplitude in the case of 0.5 n_c case increases from $a_0 = 85$ to $a_0 = 120$. These stronger fields lead to very high maximum proton energies, of 1.2 GeV as can be seen in Fig.4.11.

In Fig.4.12 is shown the variation of the optimum target thickness for proton acceleration with the target density. The results obtained in our simulations are in good agreement with the prediction made by Brantov et al. [51], where $L_{Brantov} = 0.5\lambda a_0 n_c/n_{e0}$. Moreover, based on the

previous made observation, we used our model (3.21) to predict the optimum target thickness for proton acceleration. As it can be seen in Fig.4.12, the half of the optimum target thickness to maximize the laser energy absorption is very close to the optimum thickness to maximize proton acceleration, as obtained in the simulations and as predicted by Brantov's model.

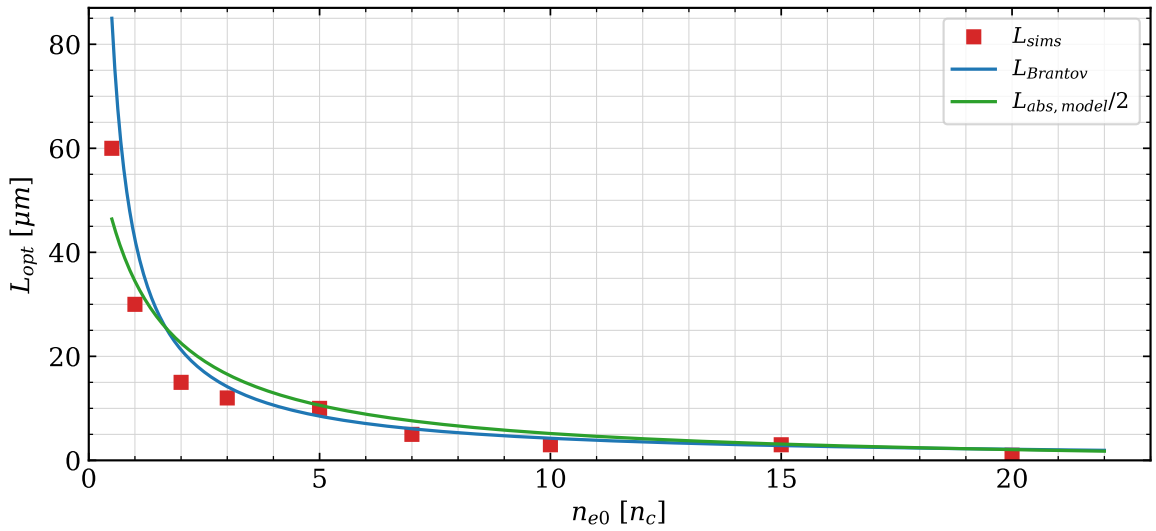

Figure 4.12: Optimum target thickness for proton acceleration vs target density. Target parameters: $L_y = 30$ μm. Laser parameters: $\lambda = 1$ μm, $a_0 = 85$, $\tau = 20$ fs FWHM and $w_0 = 12.5$ μm. The simulation results are shown with the red quares, the results given by the Brantov's model are shown with the blue line and the results obtained by equation Eq.3.21 divided by 2 are shown with the green line.

We compared the maximum proton energy from the 2D PIC simulations with the theoretical scaling proposed by Mora in 2005 [40], for each optimum target thickness for proton acceleration:

$$\varepsilon_{max} = 2T_{hot} \ln^2 \left\{ 0.8 \frac{L_x}{\lambda_D} + 8.17 \right\} \tag{4.1}$$

where T_{hot} is given by the average energy of the hot electrons, L_x is the target thickness and λ_D is the Debye length given by:

$$\lambda_D = \sqrt{\frac{\varepsilon_0 \cdot T_{hot}}{n_e \cdot e^2}} \tag{4.2}$$

where $\varepsilon_0 = 8.854 \cdot 10^{-12}$ F/m - the vacuum permittivity, $e = 1.6 \cdot 10^{-19}$ C - the elementary charge and n_e is the hot electron density:

$$n_e = \eta \cdot \frac{N}{V} \cdot \left(1 + \frac{T_{hot}}{m_e c^2} \right) \tag{4.3}$$

where the number of electrons N is computed as $\eta \varepsilon_{laser} / T_{hot}$ and the volume of the heated plasma is $V = \pi \cdot FWHM^2 \cdot L_x$.

For each density considered, we used the average energy of the hot electrons and the absorption coefficient as found in the 2D PIC simulations. In addition, we calculated the maximum proton energy using Eq.(4.1) for the optimum target thickness predicted by Brantov et al. [51] as following: T_{hot} is given by Eq.(3.20) and the Debye length is calculated using Eq.(4.2) and Eq.4.3, where we consider the absorption coefficient of the laser energy for the optimum proton acceleration being half of the total absorption coefficient from Eq.(3.19). The last assumption is based on the previous made observations and on the linear dependence between the optimum target thickness and the absorption coefficient. The results obtained are shown in Fig.4.13.

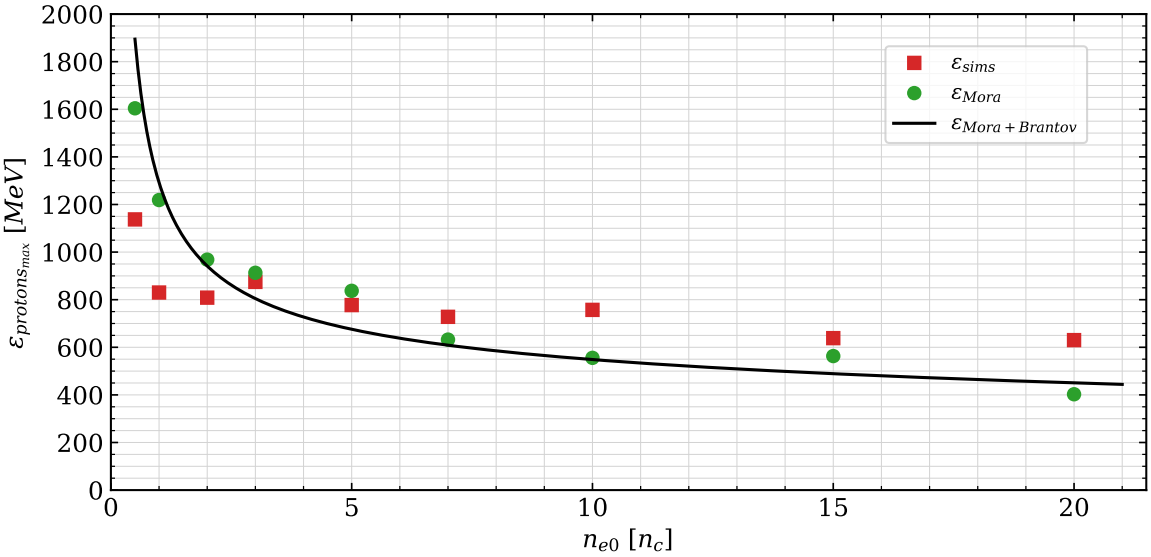

Figure 4.13: Maximum proton energy in the optimum case for proton acceleration vs target density. The simulation results are shown with the red squares, the results of Eq.(4.1) are shown with the green circles and the results of Eq.(4.1) modified by Eq.(3.19) and Eq.(3.20) are shown with the black line. Laser parameters:$\lambda = 1$ μm, $a_0 = 85$, $\tau = 20$ fs FWHM and $w_0 = 12.5$ μm.

The simulation results are in good agreement with the theoretical predictions by the modified Eq.4.1, with one exception. For very low target density, the proton energies are lower in the simulation results than in the prediction made. In this case, we are in a highly transparent regime where other acceleration mechanisms may occur.

4.3.1 Electron influence on the proton cutoff energy

We considered three different target densities, corresponding to different regimes. The maximum ion energy is obtained for similar target areal densities. The electron populations

shown in Fig.4.14 corresponding to these cases present a distribution with multiple components, some of them can be modeled with a sum of Maxwell-Jüttner distributions with multiple temperatures. Moreover, for some of the distributions we have the presence of a plateau. The spectra are taken at the point of maximum energy transfer from the laser pulse to electrons. To estimate the number of real electrons from the energy spectrum, we considered the third dimension as being the ratio between the real laser energy and the maximum laser energy as retrieved in the 2D PIC simulations, which is about $\sim 20\ \mu$m and is very close to the conservative estimate of the laser FWHM.

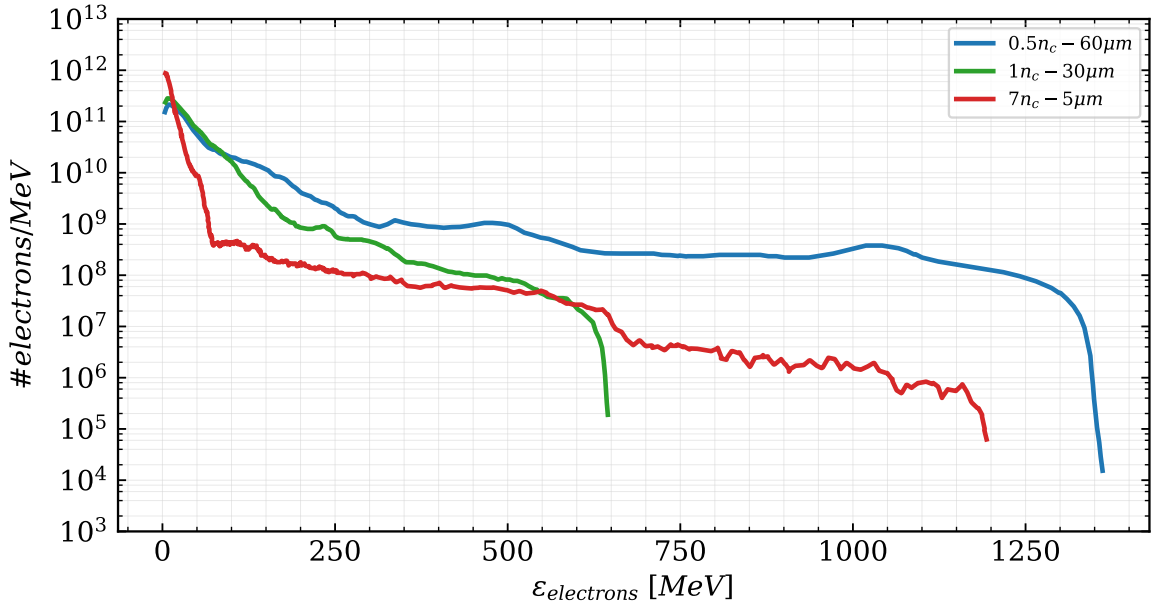

Figure 4.14: Electron spectra for 3 different target densities, at the optimum target thickness from 2D PIC simulations. Target parameters: $L_y = 30\ \mu$m. Laser parameters: $\lambda = 1\ \mu$m, $a_0 = 85$, $\tau = 20$ fs FWHM and $w_0 = 12.5\ \mu$m.

For the lower density case, the electrons present a broad energy spectrum with multiple populations, which is becoming narrower as the target density increases. The low energy population represents the electrons which are trapped in the target and recirculate. Their energy is slowly decreasing with the target density. The tail of the electron distribution represents the ultra-relativistic electrons which escape at the back of the target and travel with the laser pulse, as shown in Fig.4.15.

After setting up the quasi-electrostatic charge-separation field, the escaping electrons should not further influence the proton acceleration process. We computed the charge of two electron populations: with energy $\varepsilon_{e^-} > 5$ MeV and $\varepsilon_{e^-} > 300$ MeV. The charge of the electrons was computed using the previously mentioned assumption to calculate the number of real

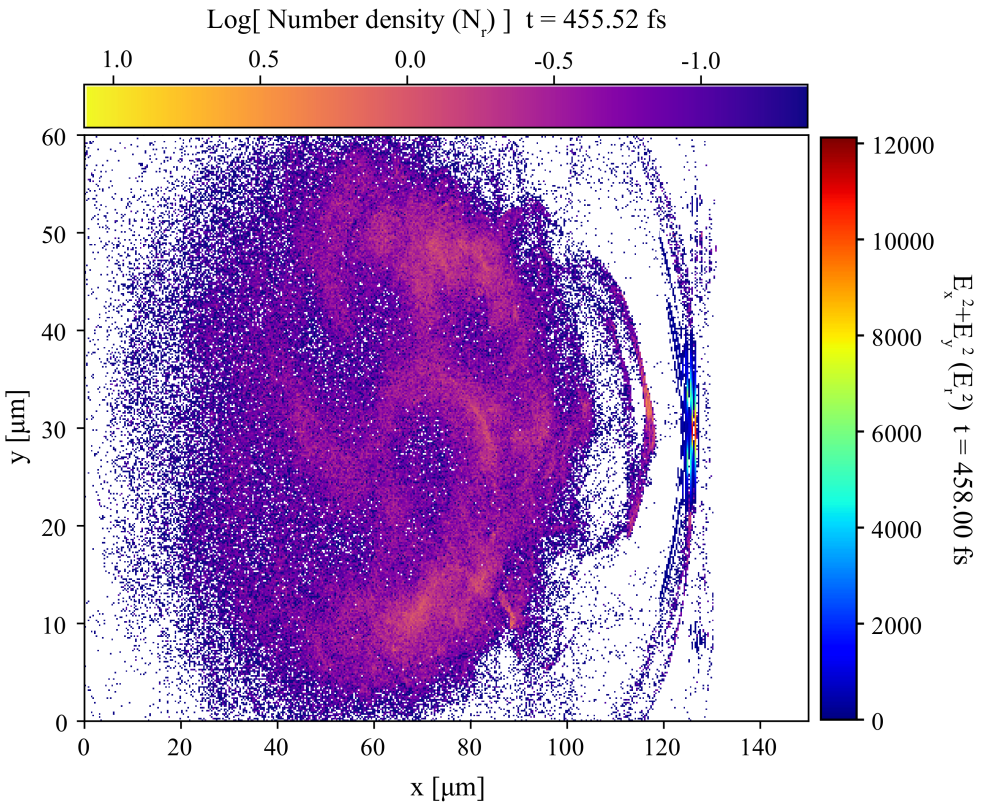

Figure 4.15: Electron density map and laser electric field from a 2D PIC simulation. Target parameters: $n_{e0} = 0.5$ n$_c$, $L_x = 60$ μm and $L_y = 30$ μm. Laser parameters: $\lambda = 1$ μm, $a_0 = 85$, $\tau = 20$ fs FWHM and $w_0 = 12.5$ μm.

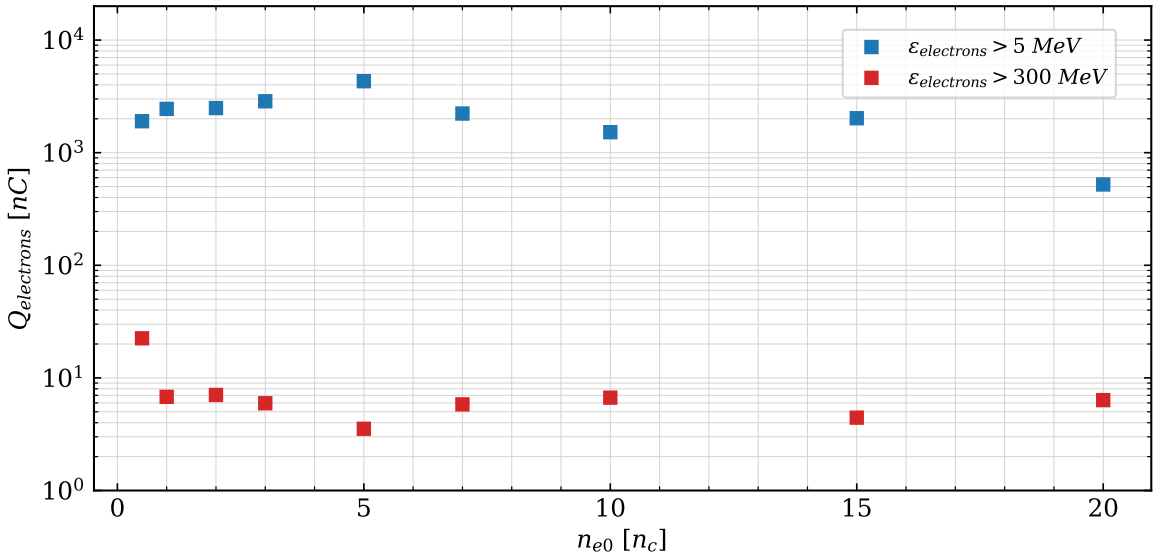

Figure 4.16: Electron charge vs target density at the optimum target thickness for proton acceleration from 2D PIC simulations. Target parameters: $L_y = 30$ μm. Laser parameters: $\lambda = 1$ μm, $a_0 = 85$, $\tau = 20$ fs FWHM and $w_0 = 12.5$ μm.

electrons, namely we considered the third dimension as being the ratio between the real laser energy and the maximum laser energy as retrieved in the 2D PIC simulations. The results are

shown in Fig.4.16. The charge of the ultra-fast electrons is not negligible (few nC) and can influence the energy of the accelerated protons.

4.3.2 Origin of the most energetic protons

In the simulations performed, the most energetic protons were originating from the rear side of the target as can also be seen in the temporal evolution of the maximum proton energy from Fig.4.17.

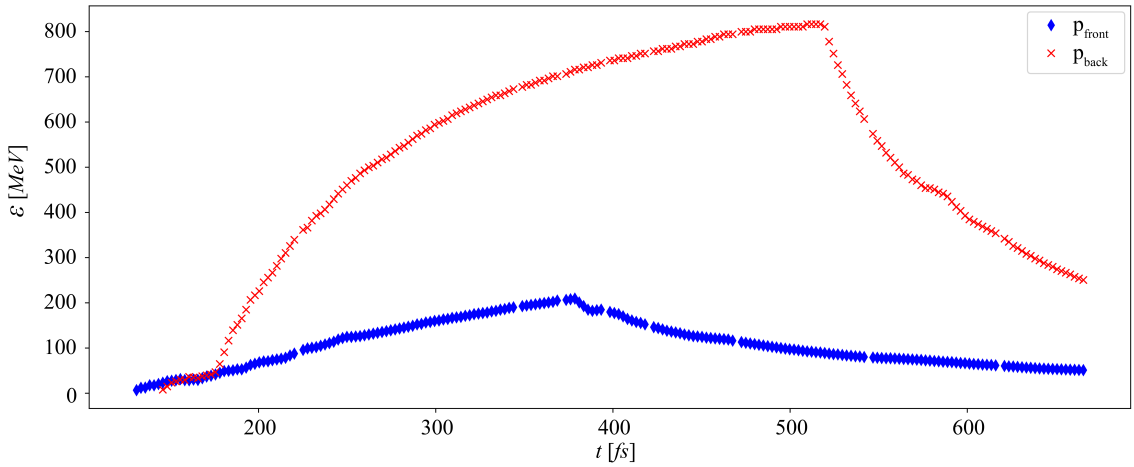

Figure 4.17: Temporal variation of the maximum proton energy from a 2D PIC simulation. Target parameters: $n_{e0} = 5$ n$_c$, $L_x = 10$ μm and $L_y = 30$ μm. Laser parameters: $\lambda = 1$ μm, $a_0 = 85$, $\tau = 20$ fs FWHM and $w_0 = 12.5$ μm. The corresponding proton phase space is shown in Fig.4.9.

We consider the case of a plasma with a density of 2 n$_c$ and a thickness of 15 μm. Following a few protons in their trajectory and energy evolution in time, we can see proton acceleration in all directions. The target, being mass limited, expands in all directions and the protons gain energies up to tens of MeV due to this expansion. The most outer protons at the rear side will experience the higher electrostatic field and will have the highest energies, as shown in Fig.4.18. As the distance from the rear side increases, the proton energies are decreasing.

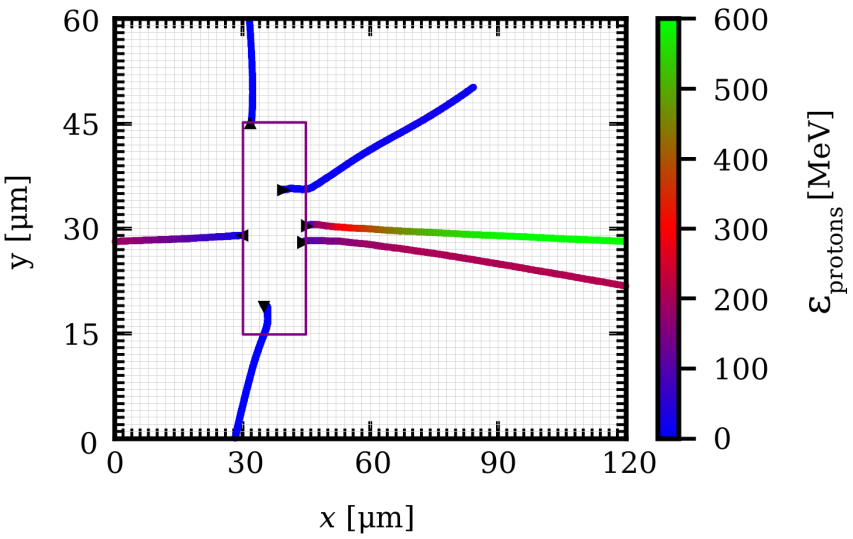

Figure 4.18: Protons trajectory and energy evolution in time from a 2D PIC simulation. Target parameters: $n_{e0} = 2$ n_c, $L_x = 15$ μm and $L_y = 30$ μm. Laser parameters: $\lambda = 1$ μm, $a_0 = 85$, $\tau = 20$ fs FWHM and $w_0 = 12.5$ μm.

4.4 Summary of the results on proton acceleration

We studied the maximum proton energy in the case of near critical density targets with the areal density in the range $5 - 800$ $n_{e0}L_x$, irradiated by an ultra intense laser pulse with $a_0 = 85$, a laser pulse duration of 20 fs FWHM and $w_0 = 12.5$ μm. The optimum areal density for proton acceleration was found to be in the interval $30 - 50$ $n_{e0}L_x$ and the maximum proton energy in the interval of $600 - 800$ MeV. Both, the optimum target thickness and maximum proton energy, are in good agreement with the theoretical predictions for an expansion like mechanism of proton acceleration. However, for a target density of 0.5 n_c, the maximum proton energy was slightly higher, 1.2 GeV. In this case, the target was completely transparent to the laser pulse and the later one, while propagating inside the target, was strongly heating the electrons. The accelerated electrons having a charge of a few nC could have influenced the proton energies in this case. In all optimum cases considered, the most energetic protons were originating from the back of the target. However, the energies found in the 2D PIC simulations can overestimate the maximum proton energies and 3D PIC simulations are required to approach the experimental results. In [133] were proposed empirical scaling laws for the ratio between the maximum proton energy as found in 2D and respetively in 3D PIC simulations. For a laser intensity in $10^{19} - 10^{21}$ W/cm^2 and a pulse duration in $\{20; 100\}$ fs, interacting with a copper plasma of density 40 n_c, the authors found that the ratio between the maximum

proton energy as found in 2D and in 3D PIC simulations is between 2 and 2.5, depending on the laser spot size. The lower proton energy in 3D PIC simulations occurs due to a reduced electron number density and average temperature, which in their turn reduce the amplitude of the accelerating sheath field.

Chapter 5

High energy synchrotron radiation and electron-positron pair creation

In this chapter we analyze the emission of high energy radiation in laser-plasma interaction with perspectives of applications for the generation of electron-positron pairs. In Section 5.1 we studied the radiation emitted by an energetic electron beam interacting with a high intensity laser pulse (Subsection 5.1.1) and the radiation emitted in a high intensity laser pulse interacting with a near-critical density plasma (Subsection 5.1.2). In optimal configuration for the maximum conversion efficiency of the laser energy to gamma photons obtained in Subsection 5.1.2, we investigated the pair production by three different processes: nonlinear Breit-Wheeler, linear Breit-Wheeler and Bethe-Heitler in Section 5.2. Further, in Section 5.3 we extended the study for higher laser intensities. Our goal is to optimize the total number of pairs produced by the linear Breit-Wheeler process and their collimation. Finally, the main findings of this study are summarized in Section 5.4.

5.1 Emission of high energy radiation

5.1.1 Study case: laser - electron beam interaction

We investigated numerically the production of high-energy γ-photons in the case of an ultra-high intensity laser pulse colliding with an electron beam. We consider the simulation setup from Fig.5.1: an ultra-high intensity laser pulse with intensity in the range $10^{19} - 10^{23}$ W/cm^2, pulse duration of 30 fs FWHM, a wavelength 1 μm and laser transveral width of $w_0 = 3$ μm interacting with an electron beam of electron density 10^{-5} n$_c$, longitudinal width $L_x = 0.8$ μm and transversal width $L_y = 0.16$ μm. The initial electron beam energy varies in $\{0.5, 1, 1.5\}$ GeV.

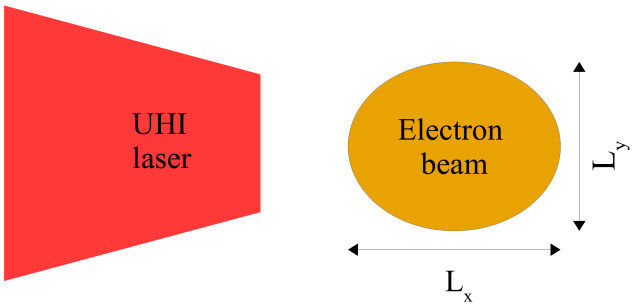

Figure 5.1: 2D simulation setup: an ultra high intensity laser pulse colliding with an energetic electron beam. Laser parameters: $\lambda = 1$ μm, $I : \{10^{19} - 10^{23}\}$ W/cm^2, $\tau = 30$ fs FWHM and $w_0 = 3$ μm. Electron beam parameters: $n_{e0} = 10^{-5}$ n$_c$, $L_x = 0.8$ μm, $L_y = 0.16$ μm and $\varepsilon_{e_0^-} : \{0.5, 1, 1.5\}$ GeV.

At the interaction with the laser pulse, the electrons are losing energy by emitting high energy radiation as explained in Section 1.4. The electron energy loss is given by [128]:

$$\frac{\Delta\varepsilon}{\varepsilon_{e_0^-}} = -\frac{k\gamma_i^2}{(\gamma_i - 1)(1 + k\gamma_i)} \tag{5.1}$$

where:

$$k = 3.2 \times 10^{-5} I_0 \left[\frac{10^{22} W}{cm^2}\right] \tau[fs] (1 - \cos\theta)^2$$

The results obtained from 2D PIC simulations and from Eq.(5.1) are given in Figure 5.2. The energy loss becomes significant for laser intensities higher than 10^{20} W/cm^2. For the high-

est intensity considered, 10^{23} W/cm^2 the electrons are losing almost all their energy in the emission of γ-photons. The electron beam energy also plays a role: the more energetic the electrons are, the more important is the emission of radiation. As introduced in Subsection 2.6.4, there are 4 models for the emission of radiation and its effects on the electron motion implemented in SMILEI: 2 continuous models (classical Landau-Lifshitz and corrected Landau-Lifshitz) and 2 stochastic models (Niel and Monte Carlo).

The classical Landau-Lifshitz model used in our simulations fits the predicted theoretical results of Eq.(5.1) up to the laser intensity of 10^{22} W/cm^2. Above this intensity, the classical model and the corrected continuous model underestimate the radiation emitted by the electrons. For ultra-high intensities, the electrons lose a significant part of their energy, and the phenomena cannot be anymore assumed to involve continuous energy transfers. To compute the transfer of energy from the electrons to the photons, stochastic models must be used. The best approximation of the theoretical results is given by the Monte Carlo model.

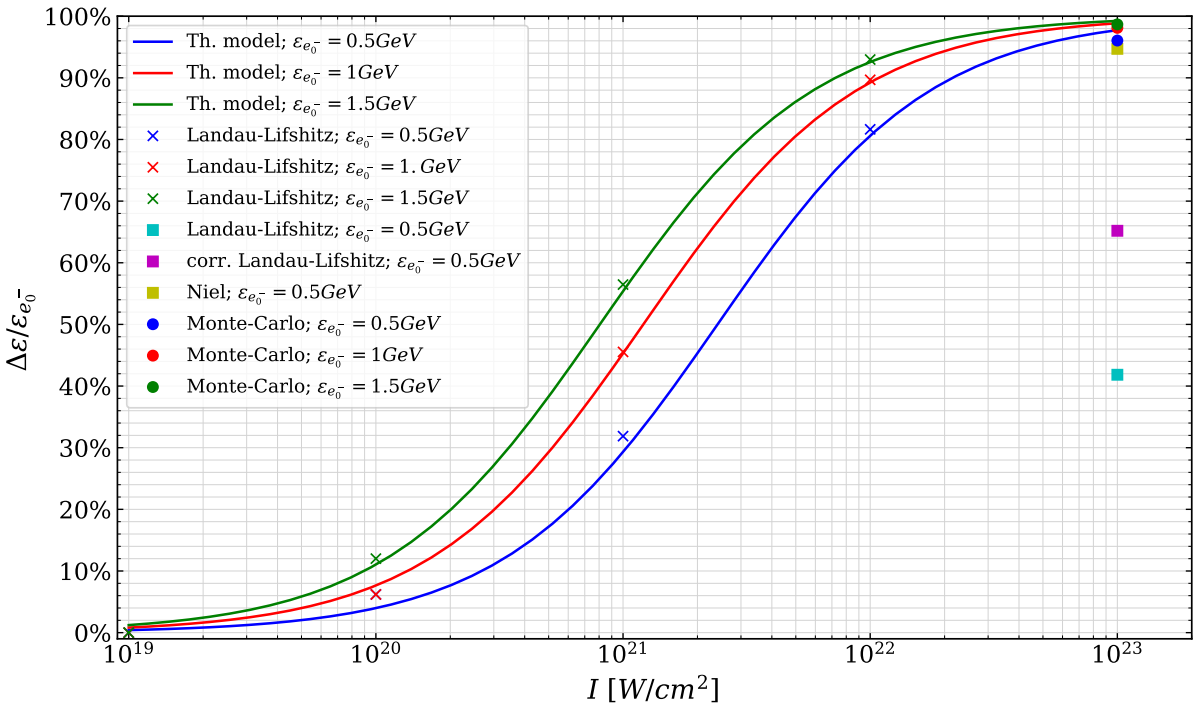

Figure 5.2: Electron energy loss vs laser intensity as obtained from 2D PIC simulations. The continuous lines (blue - $\varepsilon_e^- = 0.5$ GeV, red - $\varepsilon_e^- = 1$ GeV, green - $\varepsilon_e^- = 1.5$ GeV) represent the theoretical scaling from Eq.(5.1). The simulation results are represented as follows: the continuous Landau-Lifshitz model - crosses (blue - $\varepsilon_e^- = 0.5$ GeV, red - $\varepsilon_e^- = 1$ GeV, green - $\varepsilon_e^- = 1.5$ GeV); for $I = 10^{23}$ W/cm^2: continuous Landau-Lifhsitz model - azure square, corrected Landau-Lifshitz model - magenta square, stochastic Niel model - yellow square and stochastic Monte Carlo model - circles (blue - $\varepsilon_e^- = 0.5$ GeV, red - $\varepsilon_e^- = 1$ GeV, green - $\varepsilon_e^- = 1.5$ GeV).

Figure 5.3 shows the energy angle distribution of the emitted radiation by an energetic

electron beam of initial energy $\varepsilon_{e_0^-} = 1.5$ GeV at the interaction with a high intensity laser pulse for two intensities: 10^{22} W/cm^2 and 10^{23} W/cm^2. The emission of high energy radiation is modeled by the Monte-Carlo model. The laser propagation direction is at $\theta = 0°$, while the electrons are counterpropagating at $\theta = 180°$. The high-energy radiation is emitted mostly in the direction of the moving electrons or at small angles around their direction, as theoretically predicted by Equation (1.39). Moreover, the emission of radiation significantly increases in the case of $I = 10^{23}$ W/cm^2 in multiple directions, with the preferential direction around $\theta = 180°$.

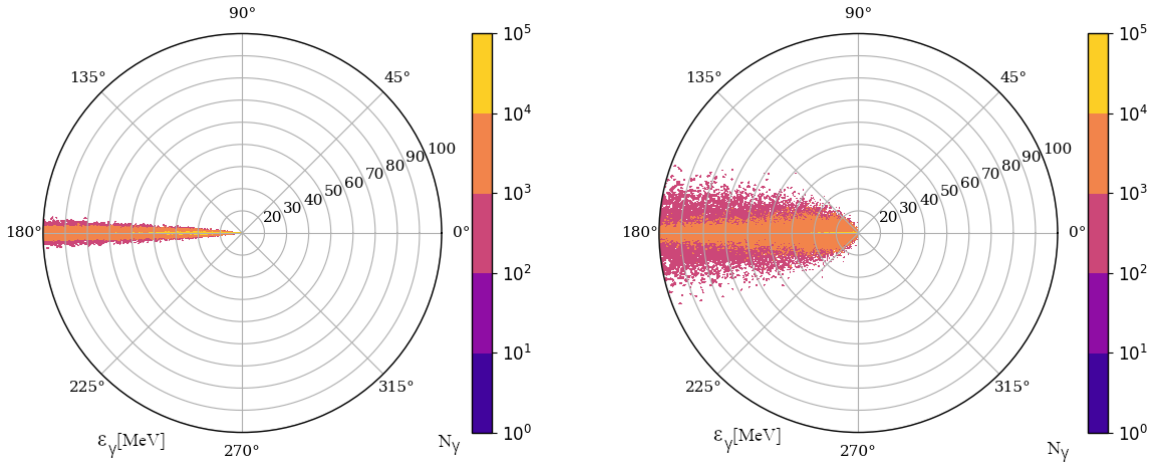

Figure 5.3: The energy angle distributions of the emitted radiation with the energy up to 100 MeV at 185 fs, integrated in time, for two laser intensities: (Left) $I = 10^{22}$ W/cm^2 (Right) $I = 10^{23}$ W/cm^2. Laser parameters: $\lambda = 1$ μm, $\tau = 30$ fs FWHM and $w_0 = 3$ μm. Electron beam parameters: $n_{e0} = 10^{-5}$ n$_c$, $L_x = 0.8$ μm, $L_y = 0.16$ μm and $\varepsilon_{e_0^-} = 1.5$ GeV. The cutoff energy of the energy angle distribution is: (Left) 1150 MeV and (Right) 1200 MeV.

5.1.2 Study case: laser - plasma interaction

To study the emission of high energy radiation in laser-plasma interaction, we consider the same simulation setup as in Chapter 4, which is similar to the one from Fig.3.2. The laser is linearly polarized and has the following characteristics: a wavelength of 1 μm, a transversal waist of 4π μm, a pulse duration of 20 fs FWHM (6 t$_0$) and a laser pulse intensity of 10^{22} W/cm^2 ($a_0 = 85$). The target is considered fully ionized, being made of protons and electrons. The density of the target varies from 0.5 n$_c$ to 20 n$_c$, the target thickness varies from 500 nm to 200 μm and the transversal width of the target is 30 μm. The simulation box has 60 μm in the y direction, while in the x direction it is changed according to the thickness L_x of the target from 120 μm to 300 μm. The cell length its $dx = dy = 15.625$ nm and the number of particles per cell is 30 for each species. The particles are deleted while crossing the domain

boundaries and the fields are absorbed. The simulations were performed with Simulating Matter Irradiated by Light at Extreme Intensities (SMILEI) [99] on the Curta machine - MCIA [106].

In all simulations which follow, the emission of radiation was modeled by two models, depending on the quantum parameter of the electrons χ_{e^-}: for $\chi_{e^-} \leq 10^{-3}$ the radiation will be emitted according to the continuous Landau Lifshitz model, otherwise a photon will be created by the Monte Carlo scheme. For example, in the 2D PIC simulations performed for a laser intensity of 10^{22} W/cm^2 and a target density of $10n_c$, we obtained a maximum χ_{e^-} parameter of 0.068, while for the laser intensity of $5 \cdot 10^{23}$ W/cm^2 and the same target density, we obtained a maximum χ_{e^-} of 1.19.

Regimes of emission of high energy radiation

We can identify two regimes of emission of high energy radiation in laser-plasma interaction, according to the target density: Reinjected Electron Synchrotron Emission [134] and Skin-depth emission [93].

Reinjected Electron Synchrotron Emission

We consider the case of an underdense target of 0.1 n_c density, interacting with a laser pulse of intensity $I = 10^{22}$ W/cm^2. The laser ponderomotive force will push the electrons in the forward direction, accelerating them up to relativistic velocities. The ions will respond slower to the laser force, while the hot electrons will be escaping the target in the forward direction. This separation of charges inside the target will set up a strong longitudinal electric field at the back of the target. This charge-separation field will in turn recirculate inside the rest of the electrons and accelerate the ions. At the interaction of the backward accelerated electrons with the laser pulse, they will suffer a strong synchrotron emission of γ-photons in their direction of propagation. Fig.5.4 shows the energy angle distribution of the emitted γ-ray energy. As the laser continuously pushes forward electrons, the charge-separation field will reinject them again, and another emission of radiation will occur. The process will repeat itself with a periodicity called 'break-down time', proportionally with the laser period. This process is known as Reinjected Electron Synchrotron Emission (RESE) and it can convert up to 15% of the laser energy into γ-photons [134].

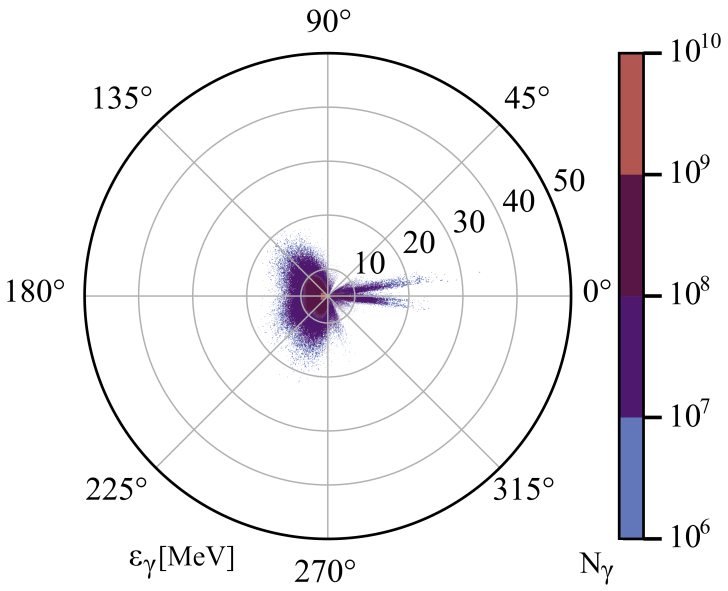

Figure 5.4: The energy angle distribution of the emitted γ-photons integrated in time, at 300 fs after the laser-plasma interaction begins, as obtained from a 2D PIC simulation. Target parameters: $n_{e0} = 0.1$ n$_c$, $L_x = 120$ μm and $L_y = 30$ μm. Laser parameters: $\lambda = 1$ μm, $a_0 = 85$, $\tau = 20$ fs FWHM and $w_0 = 12.5$ μm.

Skin-depth emission

We consider the case of an overdense target of 20 n$_c$ density, interacting with a laser pulse of intensity $I = 10^{22}$ W/cm^2. The laser pressure will create a hole-boring front over the target surface, from which a part of the laser beam will be reflected. The reflected wave will interact with the forward accelerated electrons and will give rise to an emission of radiation predominantly in the forward direction as shown in Fig.5.5. This process is known as skin-depth emission and is specific to relativistic overdense targets [93].

Results on emission of high energy radiation

The conversion of the laser energy to γ-photons vs target areal density shown in Fig.5.6 follows the same tendency as the conversion of the laser energy to plasma constituents from Fig.3.5: the conversion efficiency is increasing until reaches a plateau. The maximum value of the conversion coefficient of the laser energy to high energy photons corresponds to the optimum thickness to maximize the absorption of the laser energy in all plasma constituents with a 20% difference, except for the lowest target densities considered. In these cases, the absorption of the laser energy in γ-photons is obtained at a lower thickness than the optimum thicknesses to maximize absorption in all plasma constituents (see also Fig.3.5). For 0.5 n$_c$ and 1 n$_c$ the op-

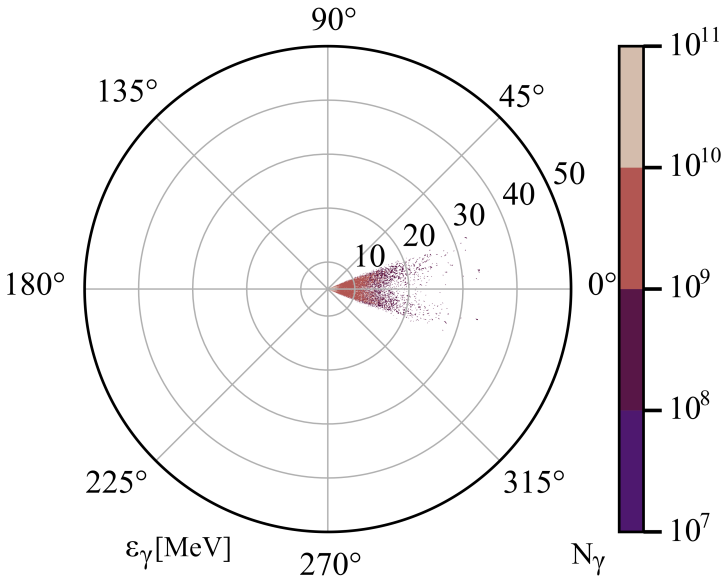

Figure 5.5: The energy angle distribution of the emitted γ-photons integrated in time, at 300 fs after the laser-plasma interaction begins, as obtained from a 2D PIC simulation. Target parameters: $n_{e0} = 20$ n$_c$, $L_x = 50$ μm and $L_y = 30$ μm. Laser parameters: $\lambda = 1\mu m$, $a_0 = 85$, $\tau = 20$ fs FWHM and $w_0 = 12.5$ μm.

timum thicknesses to maximize absorption in gamma photons are 40 μm, respectively 120 μm, while the ones to maximize absorption in all plasma constituents from Fig.3.5 are 70 μm and 190 μm.

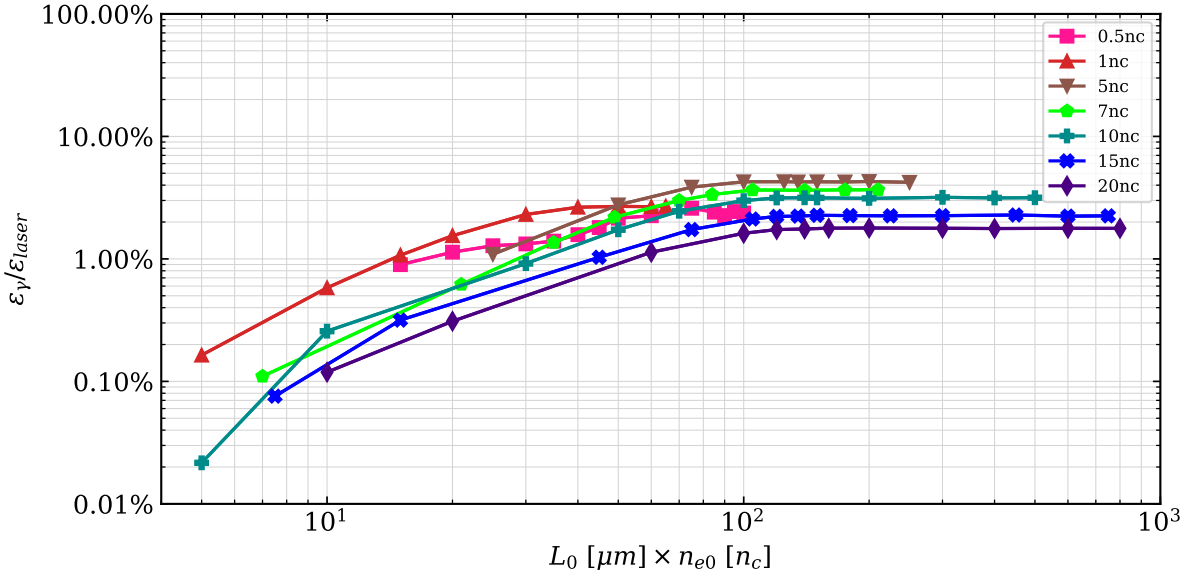

Figure 5.6: Energy conversion coefficient from the laser to photons vs target areal density as obtained in 2D PIC simulations. Target parameters: $L_y = 30$ μm. Laser parameters: $\lambda = 1$ μm, $a_0 = 85$, $\tau = 20$ fs FWHM and $w_0 = 12.5$ μm.

Even if the conversion coefficient reaches only a maximum of 4%, the energy of the

photons are close to the ones of the electrons which emitted them (hundreds of MeV - see Fig.4.8). This opens the possibility to study the process of creating electron-positron pairs via the interaction of high energy photons with the laser field, known as the multiphoton Breit-Wheeler process [82, 94].

5.2 Electron-positron pair generation

5.2.1 Experimental setup

The experimental setup for the optimization of the linear Breit Wheeler pairs detection proposed by X. Ribeyre et al. [86] is shown in Fig.5.7. Two ultra-high intensity laser pulses irradiate two targets (with a solid density or a near-critical density) and generate two high energy γ-photon beams. Further, the two γ-photon beams are transported at a given distance D from the interaction area and collide under an angle θ.

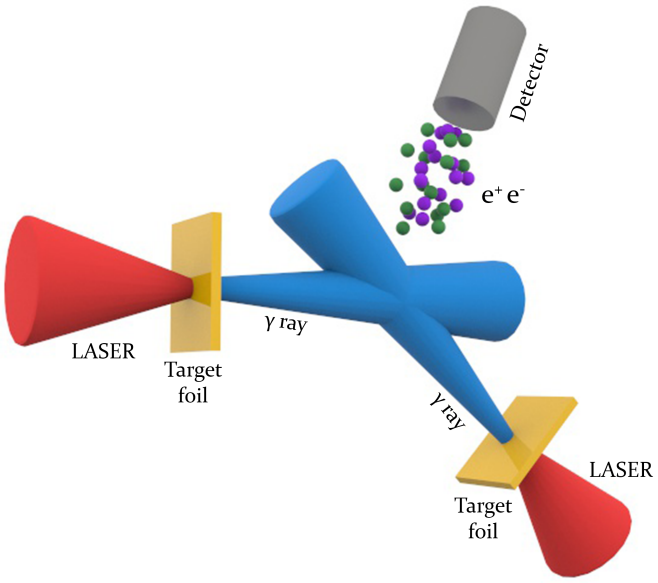

Figure 5.7: Experimental setup for linear Breit-Wheeler pair production. Credit photo: X. Ribeyre.

The laser-target interaction is studied numerically with SMILEI and the $\gamma - \gamma$ interaction is studied numerically with the code proposed by X. Ribeyre briefly explained in Subsection 1.5.1.

The electron-positron pairs will be created by the following processes:

- nonlinear Breit-Wheeler, which occurs at the interaction of the γ-photons with the electromagnetic field of the laser pulse and is numerically obtained from the PIC simulations (see Subsection 2.6.5);
- linear Breit-Wheeler, obtained from the $\gamma - \gamma$ interaction, as explained in Subsection 1.5.1 and calculated using the photon collision code described above;
- Bethe-Heitler, which occurs due to the interaction of a γ-photon with a nucleus of the target atoms and is estimated according to Subsection 1.5.3.

5.2.2 Pair creation for $a_0 = 85$

To generate the two γ-photon beams needed for the setup from Fig.5.7, we consider the laser-plasma interaction setup from Subsection 5.1.2. For each target density, we will consider the optimum target thickness to maximize the absorption coefficient of the laser energy to photons from Fig.5.6. As previously mentioned, the thickness is the same as the one found from Fig.3.5 with the exception of the lowest density cases: 0.5 n_c and 1 n_c. We also analyzed the photon beam characteristics obtained at the optimum target thickness to maximize absorption in all plasma constituents for these cases. While the absorption in high energy photons is almost the same for the case of 1 n_c for 40 μm and 70 μm (about 2.64% respectively 2.69%), the total energy of the photon beam in the forward direction varies strongly from $\sim$ 1 J up to $\sim$ 4 J. However, this strong variation was not observed for the 0.5 n_c case, where the total energy of the photon beam in the forward direction varies from 7.78 J for 120 μm to 8.68 J for 190 μm. We will further consider only the optimum thickness obtained from Fig.5.6.

In Fig.5.8 is shown the energy spectrum of the γ-photon beam and in Fig5.9 is shown the energy angle distribution of the emitted γ-photons inside a cone of 25° in the forward direction and at 150 μm distance from the original target position. To estimate the number of real photons from the energy spectrum, we considered the third dimension as being the ratio between the real laser energy and the maximum laser energy as retrieved in the 2D PIC simulations. The total energy of the γ-photon beam in the range $1 - 250$ MeV is $\sim$ 3 J and the total number of γ-photons is 10^{12}.

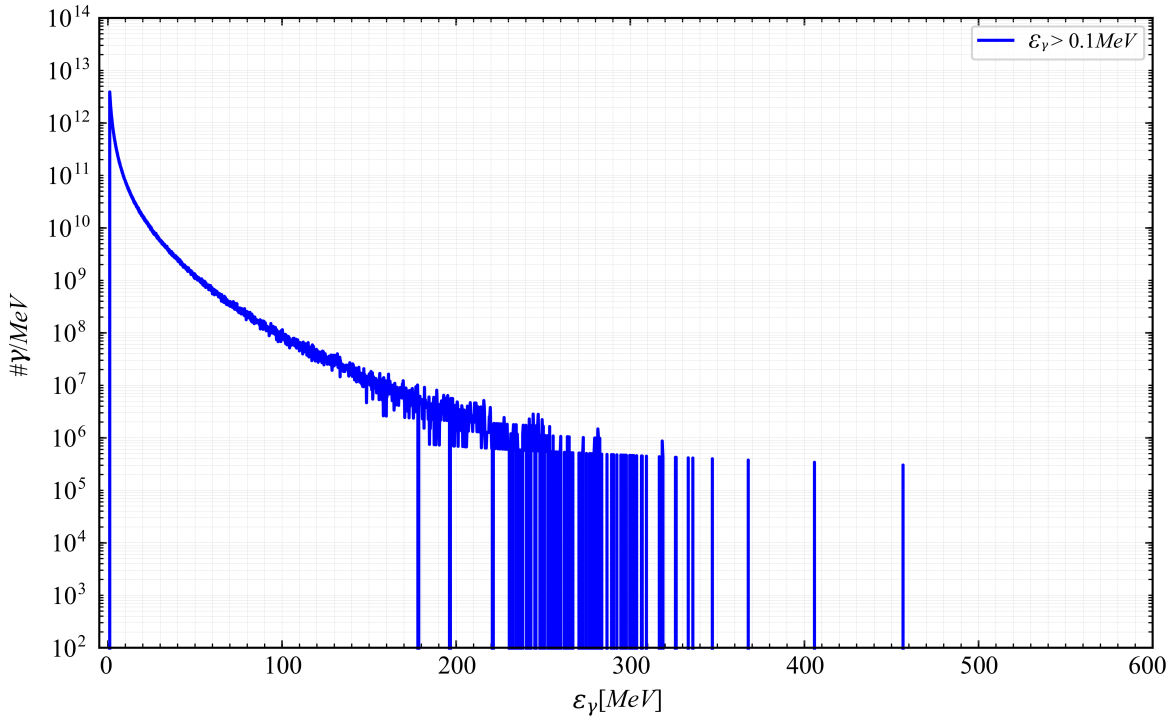

Figure 5.8: Energy spectrum of the emitted γ-photons inside a cone of 23° and at 150 μm distance from the original target position as obtained from a 2D PIC simulation. Target parameters: $n_{e0} = 1$ n$_c$, $L_x = 70$ μm and $L_y = 30$ μm. Laser parameters: $\lambda = 1$ μm, $a_0 = 85$, $\tau = 20$ fs FWHM and $w_0 = 12.5$ μm.

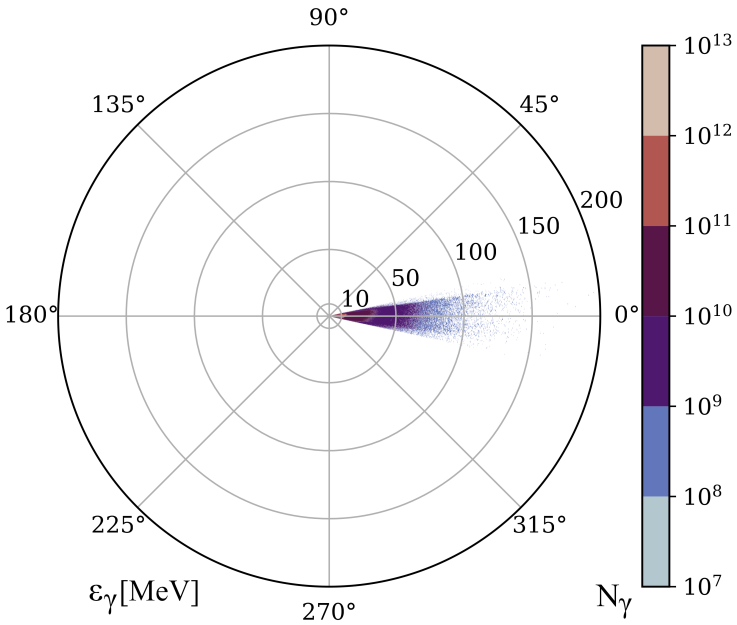

Figure 5.9: The energy angle distribution of the emitted γ-photons, integrated in time, inside a cone of 23°, at 150 μm distance from the original target position and at 740 fs after the laser-plasma interaction begins, as obtained from a 2D PIC simulation. Target parameters: $n_{e0} = 1$ n$_c$, $L_x = 70$ μm and $L_y = 30$ μm. Laser parameters: $\lambda = 1$ μm, $a_0 = 85$, $\tau = 20$ fs FWHM and $w_0 = 12.5$ μm.

For all cases considered, we analysed the γ-photons with energies ≥ 1 MeV, as the linear Breit-Wheeler process is maximum for this value. Nevertheless, it is important to note that pairs

can also be created in the collision of a high energy photon, with the energy $\varepsilon_{\gamma_1} >> 1$ MeV, with a lower energy one, with the energy $\varepsilon_{\gamma_2} << 1$ MeV, as long as the product of their energy is above the pair creation threshold $\varepsilon_{1,2} = \sqrt{2\varepsilon_{\gamma_1}\varepsilon_{\gamma_2}(1-\cos\theta)} \geq 2m_e c^2$, where θ is the angle of collision [86]. However, the limit of 1 MeV for the energy of the photons ensures that the number of linear Breit-Wheeler pairs will not be overestimated due to the overestimation of the number of low energy photons in the PIC codes.

In Table5.1 are summarized all γ-photon beam characteristics obtained from 2D PIC simulations. All photon characteristics are taken in the forward direction and at a distance of 150 μm from the initial position of the target.

Table 5.1: The γ-photon beam characteristics from 2D PIC simulations for different target characteristics. Target parameters: $L_y = 30$ μm. Laser parameters: $\lambda = 1$ μm, $a_0 = 85$, $\tau = 20$ fs FWHM and $w_0 = 12.5$ μm. The conversion coefficient of the laser energy to high energy γ-photons is $\eta_{\gamma,total}$, and the conversion coefficient of the laser energy to γ-photons with the energy ≥ 1 MeV is $\eta_{\gamma,\varepsilon_\gamma \geq 1\text{ MeV}}$. All photon characteristics, except $\eta_{\gamma,total}$, are for the photons with the energy ≥ 1 MeV.

n_{e0} [n_c] $\times$ L_0 [μm]	0.5×120	1×40	5×20	10×12	15×8	20×6
Energy range [MeV]	$1-380$	$1-200$	$1-85$	$1-90$	$1-45$	$1-35$
Total energy [J]	7.78	1.145	1.486	1.8	1.077	0.82
Average energy [MeV]	8.806	4.517	3.109	3.187	2.555	2.449
#γ-photons [10^{12}]	5.521	1.585	2.988	3.531	2.634	2.094
Opening angle [$^\circ$]	24.517	21.675	24.5	23.663	21.518	21.278
$\eta_{\gamma,\varepsilon_\gamma \geq 1\text{ MeV}}$[%]	1.487	0.219	0.284	0.344	0.206	0.157
$\eta_{\gamma,total}$[%]	2.25	2.642	4.2607	3.146	2.223	1.735

As we can observe from Table5.1, the absorption of laser energy in γ-photons with energy ≥ 1 MeV is much smaller than the total absorption of energy in γ-photons. The total energy of the γ-photon beam, with the photons with the energy ≥ 1 MeV, and its opening angle for all cases considered are shown in Fig.5.10. The beam opening angle varies slowly between 21.5° and 25° for all cases and the total energy in the photon beam varies between 0.8 J and ~ 8 J.

We consider two identical γ-photon beams interacting at different angles θ at a distance of 0.1 cm from the laser-plasma interaction area, each beam having the characteristics from Table5.1. To compute the area of beam at the $\gamma-\gamma$ interaction zone which is needed for the cross section of the interaction, we consider the initial radius of the γ-photon beam (see also

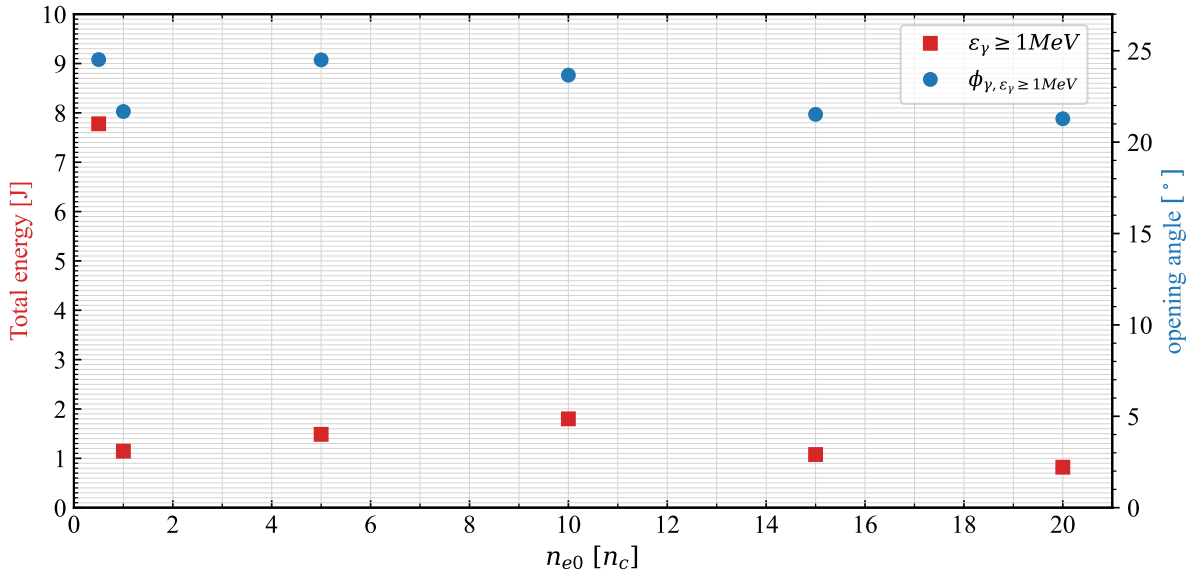

Figure 5.10: Photon beam characteristics vs target density at the optimum target thickness inside a cone of $\sim 23°$, in the forward direction, and at 150 μm distance from the original target position from 2D PIC simulations. Target parameters: $L_y = 30$ μm. Laser parameters: $\lambda = 1$ μm, $a_0 = 85$, $\tau = 20$ fs FWHM and $w_0 = 12.5$ μm. The total energy of the photon beam with energies ≥ 1 MeV is $\varepsilon_\gamma \geq 1$ MeV and the beam opening angle is $\phi_{\gamma,\varepsilon_\gamma \geq 1\text{ MeV}}$.

Fig.1.3 of Subsection 1.5.1) to be the initial radius of the target transversal width (15 μm). For all target characteristics considered, the total number of pairs created is shown in Fig.5.11.

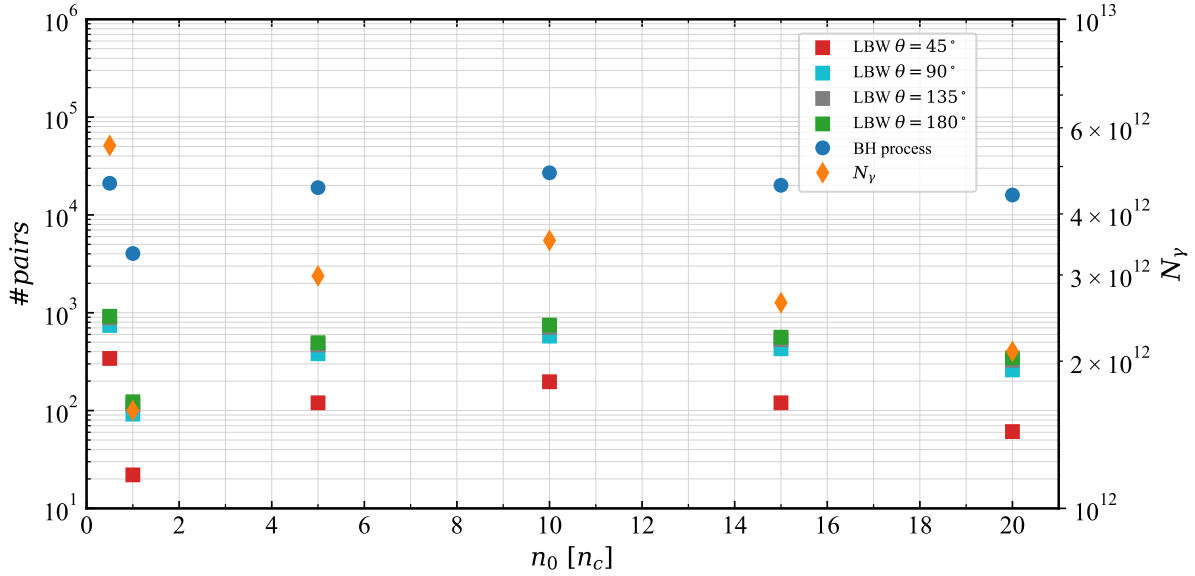

Figure 5.11: The number of electron-positron pairs created vs target density: linear Breit Wheeler (LBW) pairs at different collision angles θ (red, cyan, gray and green squares) and Bethe-Heitler (BH) pairs (blue circles), and the number of γ-photons N_γ with energies ≥ 1 MeV (orange diamonds). The interaction of the two γ-photon beams occurs at 0.1 cm from the laser - plasma interaction area. For the parameters considered, no pair was created by the nonlinear Breit-Wheeler process. Target parameters: $L_y = 30$ μm. Laser parameters: $\lambda = 1$ μm, $a_0 = 85$, $\tau = 20$ fs FWHM and $w_0 = 12.5$ μm.

The total number of linear Breit-Weeler (LBW) pairs varies from 22 for a target of 1 $n_c - 40$ μm to 341 for 0.5 $n_c - 120$ μm, both at $\theta = 45^\circ$. The total number of LBW pairs varies with the collision angle θ, for a target density of 10 $n_c - 12$ μm, as follows: from 197 pairs at $\theta = 45^\circ$ to 749 pairs at $\theta = 180^\circ$. The maximum number of LBW pairs is 921 and is obtained for a target of 0.5 $n_c - 120$ μm at $\theta = 180^\circ$. For all cases considered, the head-on collision produced the highest number of pairs.

The energy spectrum of the linear Breit-Wheeler pairs created at 135° incidence angle between two γ-photon beams, prior generated using a target of density 10 n_c and thickness of 12 μm, is shown in Fig.5.12. The maximum number of pairs is produced with an energy of 1 MeV, while the cutoff energy is 10 MeV.

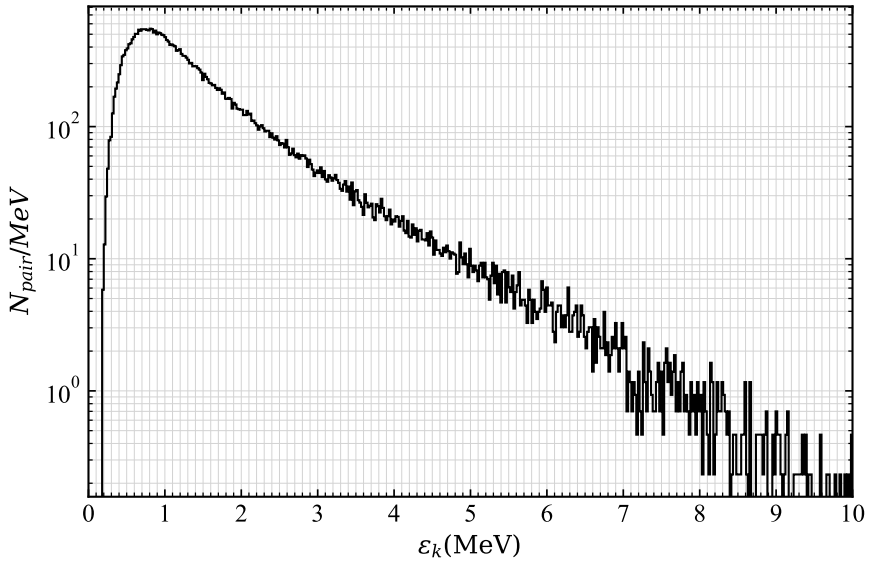

Figure 5.12: Energy spectrum of the LBW pairs created at 135° incidence angle between the two γ-photon beams. Target parameters: $n_{e0} = 10$ n_c, $L_x = 12$ μm and $L_y = 30$ μm. Laser parameters: $\lambda = 1$ μm, $a_0 = 85$, $\tau = 20$ fs FWHM and $w_0 = 12.5$ μm.

The beam collimation is important for the detection and identification of the pairs created. In Fig.5.13 is shown the energy angle distribution of the LBW pairs created at different angles θ.

For $\theta = 180^\circ$ the pairs are mostly produced along the direction of propagation of the γ-photon beams, while for lower angles the pair beam becomes collimated as already pointed out in [89]. The highest collimation is obtained for $\theta = 45^\circ$, which corresponds to the lowest number of pairs produced as a function of θ, for the collision angles considered, as can be seen

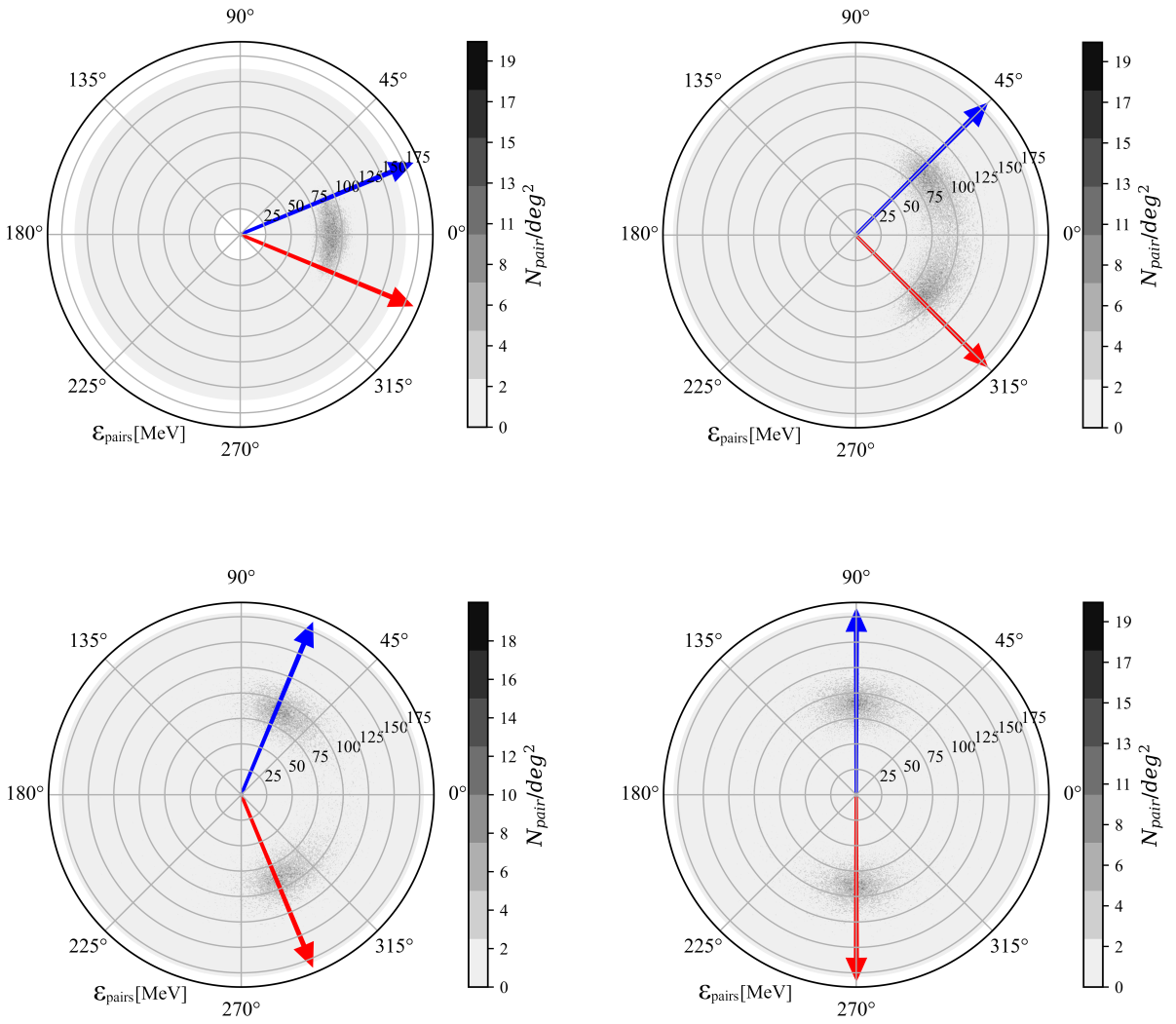

Figure 5.13: The energy angle distribution, integrated in time, of the linear Breit-Wheeler pairs created at 4 different incidence angle between the two γ-photon beams: 45° (up left), 90° (up right), 135° (down left) and 180° (down right). The red and the blue arrows represent the directions of the incident γ-photon beams. Target parameters: $n_{e0} = 10$ n$_c$, $L_x = 12$ μm and $L_y = 30$ μm. Laser parameters: $\lambda = 1$ μm, $a_0 = 85$, $\tau = 20$ fs FWHM and $w_0 = 12.5$ μm.

in Figure 5.11.

To calculate the total number of pairs created by the Bethe-Heitler process, we will use Eq.(1.59) from Subsection 1.5.3, in which we consider the target and the $\gamma-$photon beam characteristics as given in Table5.1. The total number of pairs created by the Bethe-Heitler process varies from $4 \cdot 10^3$ up to $\approx 3 \cdot 10^4$, which is up to 2 orders of magnitude higher than the linear Breit-Wheeler pairs. However, BH pairs are mostly produced in the same direction as the direction of propagation of the γ photon beam. For all simulations performed at the intensity of 10^{22} W/cm^2, the nonlinear Breit-Wheeler pairs were not produced.

5.3 High energy radiation and pair creation for higher laser intensities

We studied the production of electron-positron pairs for higher laser intensities. The laser intensity varies in the range $10^{22} - 5 \cdot 10^{23}$ W/cm^2, while the other parameters are kept constant: laser wavelength $\lambda = 1$ μm, pulse duration $\tau = 20$ fs FWHM and laser waist $w_0 = 12.5$ μm. The ultra-high intensity laser pulse irradiated a near critical density target of density 10 n_c. We will consider the target thickness to be the optimum target thickness found from 2D PIC simulations performed in Chapter 3 for the validation of the proposed theoretical model. For the laser intensity in $10^{22} - 10^{23}$ W/cm^2, the optimum target thickness from the 2D PIC simulations is $\{12, 22, 30\}$ μm, which corresponds to the theoretical prediction given by Eq.(3.21) with a 20% difference. For the highest laser intensity, we consider the optimum thickness as predicted by Eq.(3.21), which is 88 μm. The target width is in all cases 30 μm.

Fig.5.14 presents the energy angle distribution of the emitted γ-photons for a laser intensity of $5 \cdot 10^{23}$ W/cm^2 inside a cone of 27° and at 150 μm distance from the original target position. The total energy of the γ-photon beam in the range 1 MeV – 1.5 GeV is $\sim$ 550 J and the total number of γ-photons is $\sim 3 \cdot 10^{14}$.

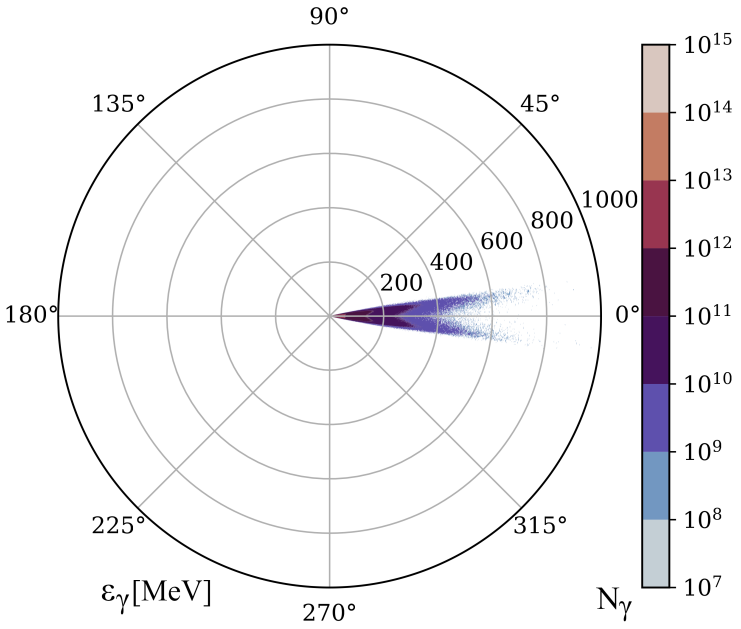

Figure 5.14: The energy angle distribution of the emitted gamma-photons, integrated in time, inside a cone of 27°, at 150 μm distance from the target and at 720 fs after the laser-plasma interaction begins, as obtained from a 2D PIC simulation. Target parameters: $n_{e0} = 10$ n_c, $L_x = 88$ μm and $L_y = 30$ μm. Laser parameters: $\lambda = 1$ μm, $a_0 = 601$, $\tau = 20$ fs FWHM and $w_0 = 12.5$ μm.

For intensities higher than 10^{23} W/cm^2, the energy angle distribution of the emitted γ-photons shows a two lobe structure. This structure is due to the two lobe structure of the electron energy angle distribution at the earlier times of the laser-plasma interaction as explained in Section C.2 of Appendix C, which can be due to the strong magnetic field which can reach up to 1 MT in some regions of the interaction zone.

To study the linear Breit-Wheeler process we consider both cases: one γ-photon beam and one lobe of the γ-photon beam. As previously mentioned, we are interested in the γ-photons with energies ≥ 1 MeV. In Table5.2 are summarized all γ-photon beam characteristics obtained from 2D PIC simulations.

Table 5.2: The γ-photon beam characteristics at the optimum target thickness for maximum absorption for different laser pulse intensities from 2D PIC simulations. Target parameters: $n_{e0} = 10\,\mathrm{n_c}$ and $L_y = 30\,\mu$m. Laser parameters: $\lambda = 1\,\mu$m, $\tau = 20$ fs FWHM and $w_0 = 12.5\,\mu$m. The conversion coefficient of the laser energy to high energy γ-photons is $\eta_{\gamma,total}$, and the conversion coefficient of the laser energy to γ-photons with the energy ≥ 1 MeV is $\eta_{\gamma,\varepsilon_\gamma \geq 1\text{ MeV}}$. All photon characteristics, except $\eta_{\gamma,total}$, are for the photons with the energy ≥ 1 MeV.

L_0 [μm]	12	22	30	88
I [W/cm^2]	10^{22}	$5\cdot 10^{22}$	10^{23}	$5\cdot 10^{23}$
Energy range [MeV]	$1-90$	$1-315$	$1-460$	$1-1500$
Total energy [J]	1.8	47.323	114.7	547.429
Average energy [MeV]	3.187	6.276	7.031	12.273
#γ-photons [10^{12}]	3.531	47.131	101.95	278.77
Opening angle [$^\circ$]	23.663	27.464	28.494	24.682
$\eta_{\gamma,\varepsilon_\gamma>1\text{ MeV}}$[%]	0.344	1.81	2.193	2.09
$\eta_{\gamma,total}$[%]	3.146	21.28	29.05	33.1

The absorption of laser energy in high energy photons increases with the laser intensity from $\leq 1\%$ (for $a_0 = 85$) to 33% (for $a_0 = 601$). The total number of photons increases by 2 orders of magnitude for $I \geq 10^{23}$ W/cm^2 and the γ-photon beam cutoff energy reaches 1.5 GeV for the highest laser intensity considered.

The total energy of the γ-photon beam, with photon energies ≥ 1 MeV, and its opening angle, for all cases considered and including the cases with one lobe are shown in Fig.5.15. As can be observed in Fig.5.15, the total energy of the γ-photon beam increases from a few Joules to > 500 J when increasing the laser intensity, and therefore the laser energy.

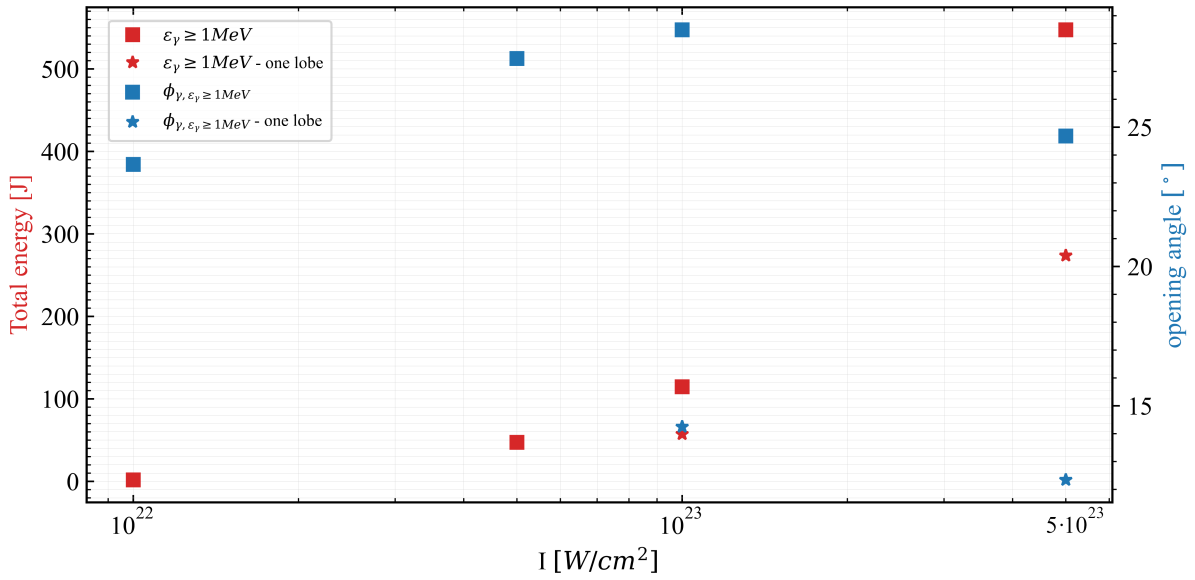

Figure 5.15: Photon beam characteristics vs target density at the optimum target thickness inside a cone of $\sim 25°$, in the forward direction, and at 150 μm distance from the original target position from 2D PIC simulations. Target parameters: $n_{e0} = 10$ n$_c$ and $L_y = 30$ μm. Laser parameters: $\lambda = 1$ μm, $\tau = 20$ fs FWHM and $w_0 = 12.5$ μm. The total energy of the photon beam with energies ≥ 1 MeV is $\varepsilon_\gamma \geq 1$ MeV and the beam opening angle is $\phi_{\gamma,\varepsilon_\gamma \geq 1 \text{ MeV}}$.

The photon beam opening angle varies slowly between 23.5° and 28.5°. For one lobe, the opening angle varies slowly between 12.5° and 14°. The duration of the γ-photon beam, with photon energies ≥ 1 MeV, varies from 28 fs for $a_0 = 85$ to 34.5 fs for $a_0 = 601$. At 150 μm distance from the initial position of the target, the γ-photon beam intensity is $9.4 \cdot 10^{17}$ W/cm^2 for $a_0 = 85$, respectively $2.1 \cdot 10^{20}$ W/cm^2 for $a_0 = 601$, and the average flux is $184 \cdot 10^{28}$ photons/cm^2/s for $a_0 = 85$, respectively $107 \cdot 10^{30}$ photons/cm^2/s for $a_0 = 601$. This leads to a γ-photon beam brightness of $6.87 \cdot 10^{19}$ photons/mm^2/s/mrad/0.1% bandwidth at 1 MeV for $a_0 = 85$, and $1.97 \cdot 10^{21}$ photons/mm^2/s/mrad/0.1% bandwidth at 1 MeV for $a_0 = 601$.

Following the same procedure, we consider two identical γ-photon beams interacting at different angles θ, each beam having the characteristics from Table5.2. Same as in the previous section, the initial radius of the γ-photon beam is considered to be the initial radius of the target transversal width 15 μm.

The interaction between the two γ-photon beams occurs at a distance of 0.1 cm from the laser - plasma interaction area. At this distance, the γ-photon beam intensity varies from $4.02 \cdot 10^{16}$ W/cm^2 for a laser intensity of 10^{22} W/cm^2 ($a_0 = 85$) up to $8.9 \cdot 10^{18}$ W/cm^2 for a laser intensity of $5 \cdot 10^{23}$ W/cm^2 ($a_0 = 601$). Figure 5.16 shows the variation of the total

number of γ-photons and the total number of pairs created by different processes with the laser intensity.

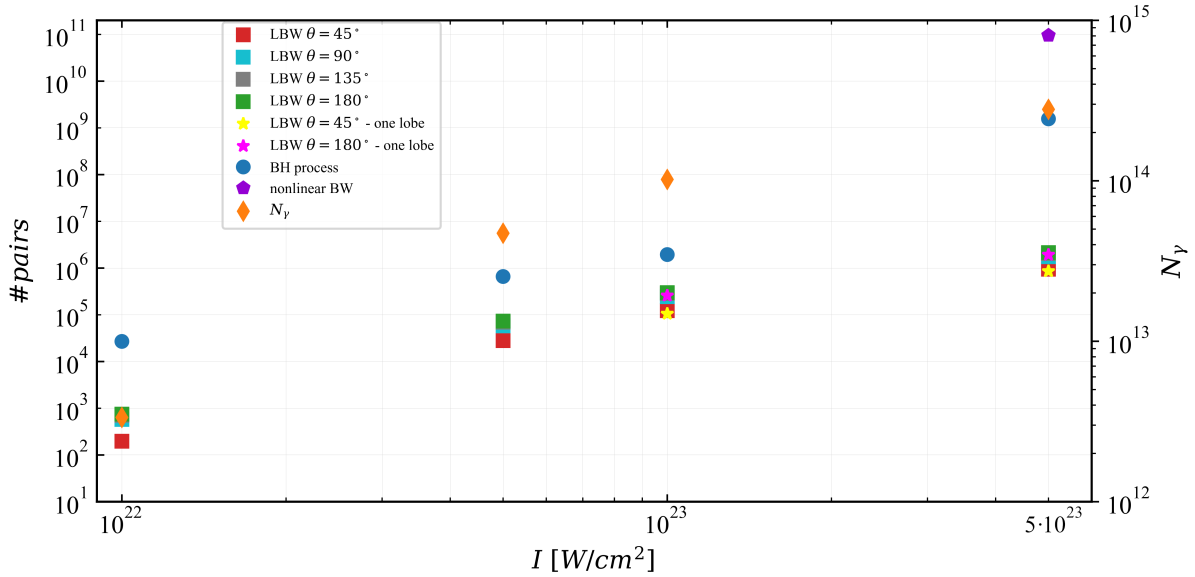

Figure 5.16: The number of electron-positron pairs created vs laser intensity: linear Breit-Wheeler (LBW) pairs at different collision angles θ (red, cyan, gray and green squares using full photon distribution, yellow and magenta stars using one lobe of the distribution), Bethe-Heitler (BH) pairs (blue circles), and nonlinear Breit-Wheeler pairs (purple pentagon) at the optimum target thickness, and the number of γ-photons with energies ≥ 1 MeV (orange diamonds). The interaction of the two γ-photon beams occurs at 0.1 cm from the laser - plasma interaction area. For $I < 5 \cdot 10^{23}$ W/cm^2, no pair was created by the nonlinear BW process. Target parameters: 10 n$_c$ at the optimum target thickness for maximum absorption. Laser parameters: $\lambda = 1$ μm, $\tau = 20$ fs FWHM and $w_0 = 12.5$ μm.

The total number of linear Breit-Wheeler pairs increases from 750 (for $a_0 = 85$) to $2 \cdot 10^6$ (for $a_0 = 601$), both at $\theta = 180^\circ$ and at 0.1 cm distance from the laser-plasma interaction area. From the total number of linear BW pairs produced, there is no significant difference between using the full γ-photon beam or one lobe of it.

The energy spectrum of the linear Breit-Wheeler pairs created at 45° incidence angle between two γ-photon beams, prior generated using a laser intensity of $5 \cdot 10^{23}$ W/cm^2 is shown in Fig.5.17. Similar to Fig.5.12, it presents a maximum for 1 MeV, but the maximum energy is 500 MeV.

In Fig.5.18 is shown the energy angle distribution of the LBW pairs. As previously mentioned, the pair beam is collimated for the lowest θ considered. Moreover, the maximum number of pairs is emitted along the direction of propagation of the γ-photon beams.

The number of Bethe-Heitler pairs also increases significantly from $2.6 \cdot 10^4$ (for $a_0 =$

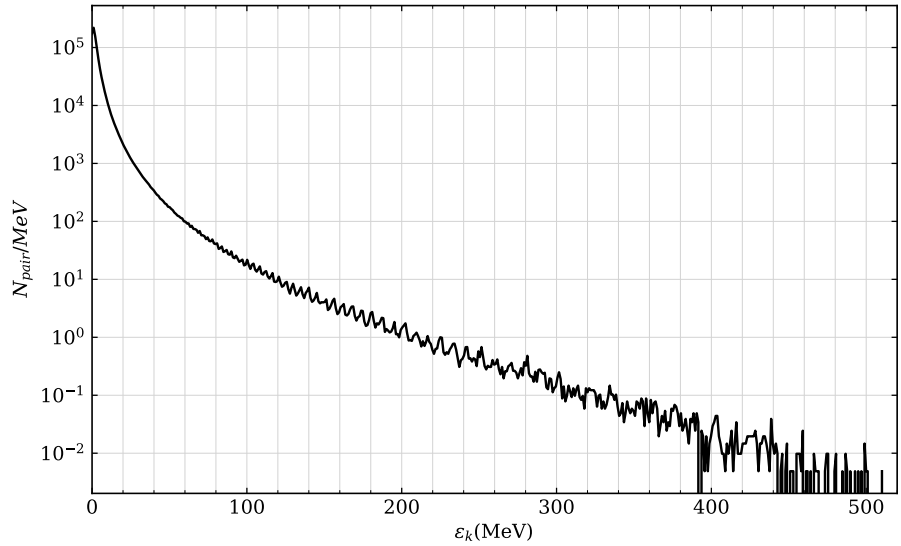

Figure 5.17: Energy spectrum of the linear BW pairs created at 45° incidence angle between the two γ-photon beams. Target parameters: $n_{e0} = 10$ n$_c$, $L_x = 88$ μm and $L_y = 30$ μm. Laser parameters: $\lambda = 1$ μm, $a_0 = 601$, $\tau = 20$ fs FWHM and $w_0 = 12.5$ μm.

85) to $1.5 \cdot 10^9$ (for $a_0 = 601$). In addition, for the highest intensity considered (for $a_0 = 601$), the nonlinear Breit-Wheeler process takes place and produces the highest number of pairs $9.5 \cdot 10^{10}$, which is about 5 orders of magnitude higher than the pairs produced by the linear BW process. The characteristics of the positrons created are detailed in Section C.1 of Appendix C. This supports the difficulty of experimental detection of the linear BW pairs. For all intensities smaller than $5 \cdot 10^{23}$ W/cm^2 ($a_0 = 601$), the nonlinear Breit-Wheeler process did not take place. The best compromise is obtained for $a_0 = 270$, where the nonlinear BW process is not present and the number of Bethe-Heitler pairs is $2 \cdot 10^6$ which is one order of magnitude higher than the ones obtained by the linear BW process, $1.2 \cdot 10^5$ at $\theta = 45°$. However, the Bethe-Heitler pairs will be created mostly in the direction of propagation of the gamma beams, while for the linear BW pairs one can control the direction of propagation, making possible to differentiate them.

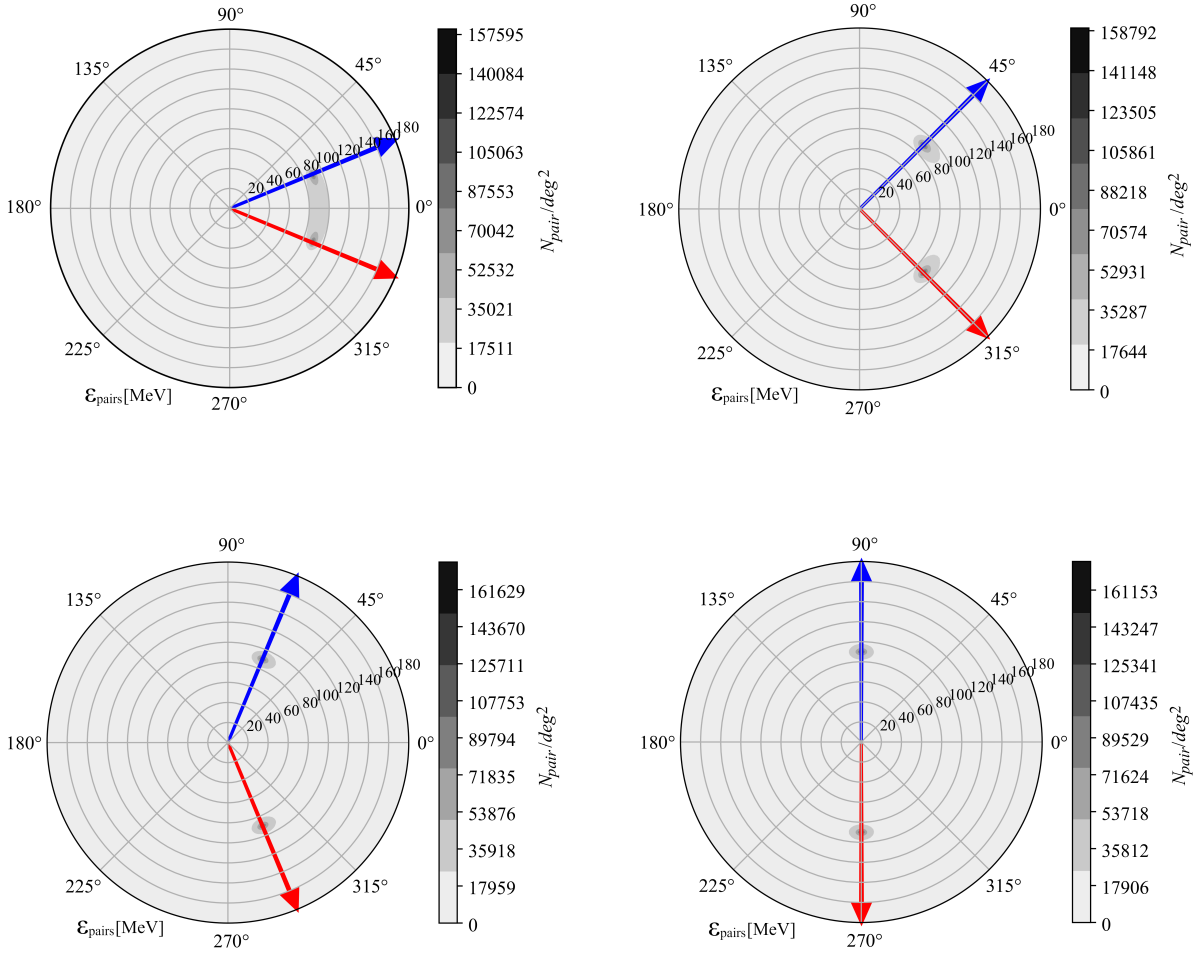

Figure 5.18: The energy angle distribution, integrated in time, of the linear Breit-Wheeler pairs created at 4 different incidence angle between the two γ-photon beams: 45° (up left), 90° (up right), 135° (down left) and 180° (down right). The red and the blue arrows represent the directions of the incident γ-photon beams. Target parameters: $n_{e0} = 10$ n$_c$, $L_x = 88$ μm and $L_y = 30$ μm. Laser parameters: $\lambda = 1$ μm, $a_0 = 601$, $\tau = 20$ fs FWHM and $w_0 = 12.5$ μm FWHM.

5.4 Summary of the results

We studied the high-energy radiation produced in two configurations: laser-electron beam interaction and laser-plasma interaction. Varying the intensity of the laser pulse in $\{10^{19} : 10^{23}\}$ W/cm^2, we studied the production of gamma photons for different initial energies of the electron beam $(0.5, 1, 1.5$ GeV) extending the results obtained by M. Vranic et al. [128]. For the highest laser intensity considered the electron are losing almost all of their energy to emitt γ-photons. In addition, we compared different models implemented in SMILEI for the emission of radiation and its effect on the electron dynamics. We found that for the highest laser intensity considered the continuous Landau-Lifshitz models cannot be used anymore and a stochastic model should be used instead. In the second configuration, we considered a laser

pulse of intensity 10^{22} W/cm^2 and pulse duration of 20 fs FWHM irradiating a near-critical density target with the density in $0.5-20$ n_c and thickness in $0.5-190$ μm. The maximum absorption coefficient obtained in 2D PIC simulations was 4% for a plasma thickness which corresponds to the optimum thickness to maximize the absorption of laser energy in all plasma constituents predicted by Eq.3.21, except for the lowest densities considered: 0.5 n_c and 1 n_c cases. However, at the optimum thickness predicted by our model for these two cases, the absorption of laser energy in γ-photons was slightly higher in the forward direction.

Further, we considered the optimal configuration for laser energy transfer to γ-photons and we analyzed the interaction of two identical γ-photons previously produced at a given distance from the laser-plasma interaction area. Our goal was to optimize the production of electron-positron pairs by the linear Breit-Wheeler process. The electron-positron pairs can also produced in the laser target interaction area by two other processes: nonlinear Breit-Wheeler and Bethe-Heitler. For $a_0 = 85$, the highest number of linear Breit-Wheeler pairs was 750 obtained for a target density of 10 n_c and 12 μm thickness, which corresponds to the optimum thickness for maximizing laser absorption in γ-photons. The number of Bethe-Heitler pairs was up to 2 orders of magnitude higher, but they are produced mostly in the direction of propagation of the γ-photon beam, while the direction of propagation of the linear Breit-Wheeler pairs can be controlled by the angle θ between the two γ-photon beams. At this laser intensity, no nonlinear Breit-Wheeler pairs were produced.

Finally, we extended our analysis to higher laser intensities: from 10^{22} W/cm^2 to $5 \cdot 10^{23}$ W/cm^2 considering a target of density 10 n_c at the optimum thickness to maximize the laser energy absorption. The highest absorption coefficient of the laser energy to γ-photons was 33% for the highest laser intensity considered. Following the previously mentioned setup, we studied the production of electron-positron pairs. The maximum number of linear Breit-Wheeler pairs was $2 \cdot 10^6$ obtained for a laser intensity of $5 \cdot 10^{23}$ W/cm^2. However, at this intensity the nonlinear Breit-Wheeler process is dominant and produces up to 5 orders of magnitude more electron-positron pairs. The optimum case to detect the linear Breit-Wheeler pairs corresponded to a laser intensity of 10^{23} W/cm^2.

As the geometry of the interaction (the collision angle and the distance from the laser-plasma interaction area) influences the total number of linear Breit-Wheeler pairs, it can be further optimized to meet the experimental setup. We performed preliminary tests for a higher

distance between the $\gamma - \gamma$ interaction area and laser-plasma interaction area to study its influence on the total number of linear Breit-Wheeler pairs created. In the case of a laser intensity of 10^{23} W/cm^2, and for a collision angle $\theta = 45^\circ$, we obtained the following results: for a distance of 0.1 cm, a total number of $1.2 \cdot 10^5$ pairs were created, and for a distance of 0.5 cm, $5.3 \cdot 10^3$ pairs were created. If we further increase the distance at 1 cm, only ~ 1000 pairs will be created. For the same laser intensity of 10^{23} W/cm^2 and at a distance of 0.1 cm from the laser-plasma interaction area, we also performed preliminary tests for the influence of the collision angle θ on the total number of linear Breit-Wheeler pairs. We obtained the following results: for $\theta = 30^\circ$, $5.6 \cdot 10^4$ pairs were created and for $\theta = 15^\circ$, 9000 pairs were created.

The 2D PIC simulations can overestimate the number of energetic photons, and consequently the number of electron-positron pairs created. 3D PIC simulations could be more appropriate to give quantitative estimates for the results obtained in experiments, and additional studies for the quantitative comparison of the number of pairs emitted in a given direction by all processes are needed. Nevertheless, these results could be useful to prepare experimental campaigns at ELI-NP, ELI-Beamlines, and Apollon [72, 71] laser facilities.

Chapter 6

Conclusions

This work discusses the interaction between an ultra-high intensity ultra short laser pulse with near-critical density targets.

The first two chapters are dedicated to an introduction to the field of laser-plasma interaction and its study through numerical simulations. In Chapter 1 we described theoretically the general laser-plasma interaction as well as the most relevant mechanisms of laser energy absorption and of particle acceleration for our regime of interest. In Chapter 2 we introduced the numerical description of a plasma, namely the Particle-in-cell method and the PIC code used for this work. All of the theoretical and numerical descriptions are inspired by the mentioned literature. In this introductory part of the thesis, the personal contributions are restricted to the study of the variation of the physical quantities with of the variation the numerical parameters and the estimation of the total consumed energy of our simulations.

In the first numerical study, we investigated the influence of the total number of particles per cell and of the cell length on the total energy absorption coefficient and on the absorption of laser energy to γ-photons coefficient. In the first case, we considered 30 particles per cell while the cell length was varying between 15.625 nm to 468.75 nm. We observed a strong dependence of the absorption in γ-photons with the cell length: while the laser energy absorption coefficient was converging to a stable value for the cell length smaller than 300 nm, the laser absorption to γ-photons coefficients was converging only for a cell length smaller than 200 nm. In the second study we fixed the cell length at 15.625 nm while we varied the total number of particles per cell

between 1 and 64. The physical quantities did not change significantly with the total number of particles per cell, which can be also due to the very small cell length.

With the help of the Energy Scope software we studied the variation of the energy consumed and the CO_2 emission of a 2D PIC simulation with the computational time. Using the total computational time for the full PhD duration, we estimated a total amount of energy consumed of 22.52 MWh and a total emission of 1.15 tonnes CO_2 (calculated for France). We also want to emphasize the importance of supercomputers in physics. The total computational time used for this thesis is about 2.6 millions CPU hours. The same amount of computational time on a workstation with 12 cores would have lasted about 25 years, which is totally unreasonable.

The following three chapters are focused on the original results obtained during the PhD program.

In Chapter 3 we propose a novel theoretical model for the optimization of the laser energy absorption in the ultra-high intensity near-critical density regime. The main goal is to find the optimum target thickness for a given density to maximize the absorption of the laser energy. There are two main parameters which influence our model: the saturation point of the absorption coefficient and the average energy of the hot electrons. We modeled these two parameters by performing multiple 2D PIC simulations with SMILEI. We considered the variation of the following parameters: the laser intensity in $10^{20} - 10^{23}$ W/cm^2 (for a pulse duration of 20 fs), the pulse duration in $6.5 - 100$ fs (for a laser intensity of 10^{22} W/cm^2), the target density in $0.5 - 24$ n_c and the target thickness in $0.5 - 200$ μm. We found a semi-empirical model for the absorption coefficient, based on the target density and the laser intensity and pulse duration, and for the average energy of the hot electrons, based on the ponderomotive scaling and our observations from the 2D PIC simulations. In addition, we found that most of the laser energy will be absorbed by the electrons with energies > 5 MeV with the exception for the laser intensity of 10^{20} W/cm^2 where only between 6% and 28% of the laser energy is transferred to these electrons. Finally, our model for the optimum target thickness to maximize the laser energy absorption shows good agreement with 2D PIC simulation results for a wide range of laser and target parameters. In addition, we discussed the applicability of our model for the generation of hot electrons and the generation of high energy radiation.

In Chapter 4 we used the theoretical model proposed in the previous chapter to optimize

proton acceleration for a laser pulse of intensity 10^{22} W/cm^2. We studied the electron heating and the creation of a quasi-electrostatic charge separation field at the back of the target and its dependence on the target density. The quasi-electrostatic charge separation field is between 30 and 40 TV/m in all cases considered and is responsible for the proton acceleration. We also investigated the maximum electron energies which can reach 1.5 GeV which explains the strong emission of high energy radiation which is further discussed in the next chapter. We observed two proton acceleration mechanisms in the simulations performed: Target Normal Sheath Acceleration, which is due to the electron heating and the quasi-electrostatic charge separation field at the back of the target, and Radiation Pressure Acceleration, which is due to the laser pressure at the front side of the target. TNSA was the main accelerating mechanism, while RPA was observed only for the higher target densities. The optimum target areal density to maximize proton acceleration was in the range of $30-50\ n_{e0}L_x$ and the maximum proton energy was found to be in 600 MeV $-$ 1.2 GeV. The optimum target thickness and the maximum proton energy were found to be in good agreement with the previous theoretical models validated for lower laser intensities. For the lowest target density considered, we observed proton energies higher than the theoretical prediction which can occur due to the influence of the most energetic electrons in the acceleration process.

Finally, in Chapter 5 we studied the emission of high energy radiation with potential applications for the generation of electron-positron pairs. First, we considered the radiation emitted by a relativistic electron beam with energies in $0.5-1.5$ GeV colliding with a high-intensity laser pulse of intensity $10^{19}-10^{23}$ W/cm^2. We found that for laser intensities higher than 10^{22} W/cm^2 the electrons can lose all of their energy by emitting γ-photons. The 2D PIC simulation results were in good agreement with the theoretical model. In addition, we tested different models implemented in SMILEI for the radiation reaction discussed in Chapter 2 and we found that for the highest laser intensity considered, the emission of radiation should be treated as a stochastic event. Further, we investigated the radiation emitted by the electrons in laser-plasma interaction for a laser pulse of intensity 10^{22} W/cm^2. The absorption coefficient from the laser pulse to the photons was found to have a maximum of 4%, which was at the same target thickness as the one maximizing the total absorption coefficient of the laser energy to plasma, with one exception for the lowest density case considered. Further, we used the characteristics of the γ-photon beam in the optimum configuration to study the creation of the electron-positron pairs. We considered an experimental setup designed for the optimization

of the linear Breit-Wheeler process, consisting of 2 γ-photon beams colliding under a given angle θ. The maximum number of pairs was 750 for $\theta = 180°$. In addition, the Bethe-Heitler process was responsible for the creation of $3 \cdot 10^4$ electron-positron pairs in the direction of propagation of the γ-photon beam. However, the direction of the propagation of the linear Breit-Wheeler pairs can be controlled by the angle θ, the highest collimation being observed for the lowest angle considered $\theta = 45°$. We extended our study for higher laser intensities, up to $5 \cdot 10^{23}$ W/cm^2, interacting with a target density of 10 n_c and a target thicknesses as predicted by our model from Chapter 3. We obtained a maximum of 33% laser to photons absorption coefficient for the highest laser intensity considered. The optimum case for maximizing the detection of the linear Breit-Wheeler pairs was found to be for a laser intensity of 10^{23} W/cm^2. In this case we obtained a total number of pairs of $1.2 \cdot 10^5$ for $\theta = 45°$. For higher laser intensities we observed that the nonlinear Breit-Wheeler process takes place and produces up to 5 orders of magnitude more electron positron-pairs.

The results obtained in this thesis were presented at various national and international conferences as mentioned in Appendix D. The results were published or submitted for publication in scientific journals as follows:

1. Preliminary results obtained on the theoretical model of the laser energy absorption and on the proton and electron acceleration for a target density of 5 n_c and a laser intensity of 10^{22} W/cm^2 were published in Proceedings of 13th International Particle Accelerator Conference [135]. The article identifiers are: I.M. Vladisavlevici, D. Vizman and E.d'Humières, *Theoretical Study of Laser Energy Absorption Towards Energetic Proton and Electron Sources*.

2. The final results on the theoretical model of the laser energy absorption in near-critical density plasmas in the ultra-high intensity regime and with an application of proton acceleration for 10^{22} W/cm^2 were accepted for publication in Plasma Physics and Controlled Fusion [136]. The article identifiers are: I.M. Vladisavlevici, D. Vizman and E.d'Humières, *Theoretical investigation of the interaction of ultra-high intensity laser pulses with near critical density plasmas*.

3. The results obtained on laser driven electron acceleration from near-critical density targets at ultra-high laser intensities with the application on the emission of high energy radiation

were published in Photonics [137]. The article identifiers are: I.M. Vladisavlevici, D. Vizman and E.d'Humières, *Laser driven electron acceleration from near-critical density targets towards the generation of high energy γ-photons*.

4. The results obtained on the emission of high energy radiation from near-critical density target at ultra-high laser intensities towards the optimization of the linear Breit-Wheeler pair creation process are under review for publication in Frontiers in Physics [138]. The article identifiers are: I.M. Vladisavlevici, X. Ribeyre, D. Vizman and E.d'Humières, *Investigation of γ-photon sources using near-critical density targets towards the optimization of the linear Breit-Wheeler process*.

Perspectives

The theoretical model proposed for the absorption of the laser energy in near-critical density plasmas in the ultra-high intensity regime can be used to prepare the first experimental campaigns for the next generation of high intensity lasers like ELI-NP, ELI-Beamlines, and Apollon [72, 71]. One limit of our theoretical model is the highly radiative regime, for a laser intensity $I > 10^{23}$ W/cm^2 and a low target density, where the radiation effects become more important and lead to an overestimation of the average energy of the electrons and of the optimum target thickness. Additional studies in this regime could improve the proposed model, and moreover bring new scaling laws for electron acceleration in the ultra high intensity, low density regime.

We discussed the application of our model for the generation of hot electrons, for studies involving the proton acceleration, for the generation of high energy radiation, and for studies involving electron-positron pair creation. However, the energies found in the 2D PIC simulations can overestimate the maximum electron, respectively proton energies, and 3D PIC simulation are needed to complete the results obtained and to give even more accurate predictions.

We investigated the total number of pairs created by various processes in a two-beam laser-plasma configuration in the ultra-high intensity near-critical density regime. The 2D PIC simulations can overestimate the number of energetic photons, and consequently the number of electron-positron pairs created. 3D PIC simulations could be more appropriate to give quan-

titative estimates for the results obtained in experiments. Moreover, to prepare experimental campaigns for the optimization of the linear Breit-Wheeler process, quantitative comparison of the number of pairs emitted in a given direction by all processes are needed.

Bibliography

[1] T.H. Maiman. Stimulated Optical Radiation in Ruby. *Nature*, 187:493–494, 1960.

[2] G. Mourou et al. Ultrahigh-Intensity Lasers: Physics of the Extreme on a Tabletop. *Physics Today*, 51(1):22–28, 1998.

[3] Donna Strickland and Gérard Mourou. Compression of amplified chirped optical pulses. *Optics Communications*, 56(3):219–221, 1985.

[4] https://www.nobelprize.org/prizes/physics/2018/press-release/, accessed on 04/09/2022.

[5] P. F. Moulton. Spectroscopic and laser characteristics of Ti:Al2O3. *Journal of the Optical Society of America B*, 3(1):125–133, 1986.

[6] J.W. Yoon et al. Realization of laser intensity over $10^{23} W/cm^2$. *Optica*, 8(5):630–635, 2021.

[7] J.P. Zou et al. Design and current progress of the Apollon 10 PW project. *High Power Laser Science and Engineering*, 3, 2015.

[8] S. Gales et al. The extreme light infrastructure - nuclear physics (ELI-NP) facility: new horizons in physics with 10 PW ultra-intense lasers and 20 MeV brilliant gamma beams. *Reports on Progress in Physics*, 81(9), 2018.

[9] E. Cartlidge. The light fantastic. *Science*, 359(6374):382–385, 2018.

[10] C. Radier et al. 10 PW peak power femtosecond laser pulses at ELI-NP. *High Power Laser Science and Engineering*, 10:e21, 2022.

[11] F. Lureau et al. High-energy hybrid femtosecond laser system demonstrating 2×10 PW capability. *High Power Laser Science and Engineering*, 8:e43, 2020.

[12] E. d'Humières et B. Dubroca V. T. Tikhonchuk. *Modélisation de la physique des plasmas et applications - Cours et travaux dirigés*. 2012-2013.

[13] Thierry Dauxois. Fermi, Pasta, Ulam, and a mysterious lady. *Physics Today*, 61(1):55, 2008.

[14] John Dawson. One Dimensional Plasma Model. *The Physics of Fluids*, 5(4):445–459, 1962.

[15] Martin H. Weik. *A Third Survey of Domestic Electronic Digital Computing Systems*. Balistic Research Laboratories Report No. 1115, 1961.

[16] https://www.olcf.ornl.gov/frontier/, accessed on 02/09/2022.

[17] https://www.top500.org/, accessed on 02/09/2022.

[18] H. Daido et al. Review of laser-driven ion sources and their applications. *Reports on Progress in Physics*, 75(056401), 2012.

[19] L. D. Landau and E. M. Lifshitz. *The Classical Theory of Fields - Third Edition*. Pergamon Press, 1971.

[20] William L. Kruer. *The Physics of Laser Plasma Interaction*. Frontiers in Physics. Westview Press, 2003.

[21] Andrea Macchi. *A Superintense Laser-Plasma Interaction Theory Primer*. SpringerBriefs in Physics. Springer Netherlands, 2013.

[22] J.C. Delagnes E. d'Humières and V. T. Tikhonchuk. *Classical Electrodynamics - Course and tutorials*. 2021-2022.

[23] James Clerk Maxwell. *A Dynamical Theory of the Electromagnetic Field*. Number 155 in Philosophical Transactions. Royal Society London, 1865.

[24] Predhiman Kaw and John Dawson. Relativistic Nonlinear Propagation of Laser Beams in Cold Overdense Plasmas. *The Physics of Fluids*, 13(472), 1970.

[25] A.I. Akhiezer and R.V. Polovin. Theory of Wave Motion of an Electron Plasma. *Soviet Physics, Journal of Experimental and Theoretical Physics*, 3(5), 1956.

[26] K.G. Estabrook, E.J. Valeo, and W.L. Kruer. Two-dimensional relativistic simulations of resonance absorption. *The Physics of Fluids*, 18(9):1151, 1975.

[27] D.W. Forslund, J.M. Kindel, and K. Lee. Theory of Hot-Electron Spectra at High Laser Intensity. *Physical Review Letters*, 39(5):284, 1977.

[28] F. Brunel. Not-So-Resonant, Resonant Absorption. *Physical Review Letters*, 59(1):52, 1987.

[29] W.L. Kruer and K. Estabrook. $\mathbf{J} \times \mathbf{B}$ heating by very intense laser light. *The Physics of Fluids*, 28(1):430, 1985.

[30] S.C. Wilks et al. Absorption of Ultra-Intense Laser Pulses. *Physical Review Letters*, 69(9):1383, 1992.

[31] E. Lefebvre and G. Bonnaud. Transparency/Opacity of a Solid Target Illuminated by an Ultrahigh-Intensity Laser Pulse. *Physical Review Letters*, 74(11):2002, 1995.

[32] J. Sanz, A. Debayle, and K. Mima. Model for ultraintense laser-plasma interaction at normal incidence. *Physical Review E*, 85(046411), 2012.

[33] A. Debayle et al. Electron heating by intense short-pulse lasers propagating through near-critical plasmas. *New Journal of Physics*, 19(123013), 2017.

[34] R.A. Snavely et al. Intense High-Energy Proton Beams from Petawatt-Laser Irradiation of Solids. *Physical Review Letter*, 85(2945), 2000.

[35] S.C. Wilks et al. Energetic proton generation in ultra-intense laser–solid interactions. *Physics of Plasma*, 8(542), 2001.

[36] P. Mora. Plasma Expansion into a Vacuum. *Physical Review Letters*, 90, 2003.

[37] J. Fuchs et al. Laser-driven proton scaling laws and new paths towards energy increase. *Nature Physics*, 2:48–54, 2006.

[38] J. Fuchs et al. Comparative spectra and efficiencies of ions laser-accelerated forward from the front and rear surfaces of thin solid foils. *Physics of Plasmas*, 14(053105), 2007.

[39] L. Robson et al. Scaling of proton acceleration driven by petawatt-laser–plasma interactions. *Nature Physics*, 3:58–62, 2007.

[40] P. Mora. Thin-foil expansion into a vacuum. *Physical Review E*, 72, 2005.

[41] M. Zimmer et al. Analysis of laser-proton acceleration experiments for development of empirical scaling laws. *Physical Review E*, 104:045210, 2021.

[42] A.P.L. Robinson et al. Radiation pressure acceleration of thin foils with circularly polarized laser pulses. *New Journal of Physics*, 10(013021), 2008.

[43] S.S. Moiseev and R.Z. Sagdeev. Collisionless shock waves in a plasma in a weak magnetic field. *Journal of Nulear Energy, Part C, Plasma Physics*, 5(1):43–47, 1963.

[44] T. Esirkepov et al. Highly Efficient Relativistic-Ion Generation in the Laser-Piston Regime. *Physical Review Letter*, 92(175003), 2004.

[45] J. Denavit. Absorption of High-Intensity Subpicosecond Lasers on Solid Density Targets. *Physical Review Letter*, 69(21):3052–3055, 1992.

[46] L.O. Silva et al. Proton Shock Acceleration in Laser-Plasma Interactions. *Physical Review Letter*, 92(015002), 2004.

[47] E. d'Humières et al. Investigation of high intensity laser proton acceleration with underdense targets. *Journal of Physics: Conference Series*, 244(042023), 2010.

[48] D. Haberberger et al. Collisionless shocks in laser-produced plasma generate monoenergetic high-energy proton beams. *Nature Physics*, 8:95–99, 2012.

[49] P. Puyuelo-Valdes et al. Proton acceleration by collisionless shocks using a supersonic H2 gas-jet target and high-power infrared laser pulses. *Physics of Plasmas*, 26(123109), 2019.

[50] E. d'Humières et al. Proton acceleration mechanisms in high-intensity laser interaction with thin foils. *Physics of Plasmas*, 12(062704), 2005.

[51] A.V. Brantov et al. Ion energy scaling under optimum conditions of laser plasma acceleration. *Physical Review Special Topics - Accelerators and Beams*, 18(021301), 2015.

[52] A.V. Brantov et al. Comparison of optimized ion acceleration from thin foils and low-density targets for linearly and circularly polarized laser pulses. *Physics of Plasmas*, 24(113102), 2017.

[53] R. Mishra et al. Enhanced ion acceleration in transition from opaque to transparent plasmas. *New Journal of Physics*, 20(043047), 2018.

[54] J.H. Bin et al. Enhanced Laser-Driven Ion Acceleration by Superponderomotive Electrons Generated from Near-Critical-Density Plasma. *Physical Review Letters*, 120(074801), 2018.

[55] W.J. Ma et al. Laser Acceleration of Highly Energetic Carbon Ions Using a Double-Layer Target Composed of Slightly Underdense Plasma and Ultrathin Foil. *Physical Review Letters*, 122(014803), 2019.

[56] A. Pazzaglia et al. A theoretical model of laser-driven ion acceleration from near-critical double-layer targets. *Communications Physics*, 3(133), 2020.

[57] Ramona Mayer Manjit Dosanjh, Ugo Amaldi and Richard Poetter. ENLIGHT: European network for Light ion hadron therapy. *Radiotherapy and Oncology*, 128(1):76–82, 2018.

[58] https://gco.iarc.fr/today/home, accessed on 02/09/2022.

[59] S.V. Bulanov et al. Laser ion acceleration for hadron therapy. *Physics-Uspekhi*, 57(12):1149–1179, 2014.

[60] S.V. Bulanov et al. Oncological hadrontherapy with laser ion accelerators. *Physics Letters A*, 299(2):240–247, 2002.

[61] V. Malka et al. Practicability of protontherapy using compact laser systems. *Medical Physics*, 31(6):1587–1592, 2004.

[62] K. Nemoto et al. Laser-triggered ion acceleration and table top isotope production. *Applied Physics Letters*, 78(5), 2001.

[63] S. Fritzler et al. Proton beams generated with high-intensity lasers: Applications to medical isotope production. *Applied Physics Letters*, 83(3039), 2003.

[64] I. Spencer et al. Laser generation of proton beams for the production of short-lived positron emitting radioisotopes. *Nuclear Instruments and Methods in Physics Research Section B: Beam Interactions with Materials and Atoms*, 183(3), 2001.

[65] M.I.K. Santala et al. Production of radioactive nuclides by energetic protons generated from intense laser-plasma interactions. *Applied Physics Letters*, 78(1), 2001.

[66] M. Yamagiwa and J. Koga. MeV ion generation by an ultra-intense short-pulse laser: application to positron emitting radionuclide production. *Journal of Physics D: Applied Physics*, 32(19), 1999.

[67] M. Barberio et al. Laser-Accelerated Proton Beams as Diagnostics for Cultural Heritage. *Scientific Reports*, 7(40415), 2017.

[68] F. Barberio et al. Integrated quantitative PIXE analysis and EDX spectroscopy using a laser-driven particle source. *Science Advances*, 7(3), 2021.

[69] M. Roth et al. Fast Ignition by Intense Laser-Accelerated Proton Beams. *Physical Review Letters*, 86:436–439, 2001.

[70] Di Piazza et al. Quantum Radiation Reaction Effects in Multiphoton Compton Scattering. *Physical Review Letters*, 105:220403, 2010.

[71] https://cilexsaclay.fr, accessed on 02/09/2022.

[72] https://eli-laser.eu/, accessed on 02/09/2022.

[73] Mathieu Lobet. *Effets radiatifs et d'électrodynamique quantique dans l'interaction laser-matière ultra-relativiste*. PhD thesis - University of Bordeaux. 2015.

[74] H.Y. Wang et al. Signatures of quantum radiation reaction in laser-electron-beam collisions. *Physics of Plasmas*, 22, 2015.

[75] M. Vranic et al. Quantum radiation reaction in head-on laser-electron beam interaction. *New Journal of Physics*, 18, 2016.

[76] S.V. Bulanov et al. On the design of experiments for the study of extreme field limits in the interaction of laser with ultrarelativistic electron beam. *Nuclear Instruments and Methods in Physics Research A*, 660, 2011.

[77] D.J. Stark et al. Enhanced Multi-MeV Photon Emission by a Laser-Driven Electron Beam in a Self-Generated Magnetic Field. *Physical Review Letters*, 116:185003, 2016.

[78] B. Martinez et al. Synchrotron radiation from ultrahigh-intensity laser-plasma interactions and competition with Bremsstrahlung in thin foil targets. *Physical Review Research*, 2, 2020.

[79] L. L. Ji et al. Energy partition, γ-ray emission, and radiation reaction in the near-quantum electrodynamical regime of laser-plasma interaction. *Physics of Plasmas*, 21, 2014.

[80] A. Gonoskov et al. Charged particle motion and radiation in strong electromagnetic fields. *Reviews of Modern Physics*, 94:045001, 2022.

[81] A. Fedotov et al. Advances in QED with intense background fields. *arXiv*, 2022.

[82] Breit, G. and Wheeler, John A. Collision of Two Light Quanta. *Physical Review*, 46:1087–1091, 1934.

[83] A. I. Nikishov. Absorption of High-Energy Photons in the Universe. *Soviet Physics, Journal of Experimental and Theoretical Physics*, 14(2):393–394, 1962.

[84] O. C. De Jager. Estimate of the intergalactic infrared radiation field from γ-ray observations of the galaxy Mrk421. *Nature*, 369:294–296, 1994.

[85] O.J. Pike et al. A photon–photon collider in a vacuum hohlraum. *Nature Photonics*, 8:434–436, 2014.

[86] X. Ribeyre et al. Pair creation in collision of γ-ray beams produced with high-intensity lasers. *Physsical Review E*, 93:013201, 2016.

[87] T. Wang et al. Power Scaling for Collimated γ-Ray Beams Generated by Structured Laser-Irradiated Targets and Its Application to Two-Photon Pair Production. *Physical Review Applied*, 13:054024, 2020.

[88] X. Ribeyre et al. Electron–positron pairs beaming in the Breit–Wheeler process. *Plasma Physics and Controlled Fusion*, 59(1):014024, 2016.

[89] X. Ribeyre et al. Effect of differential cross section in Breit–Wheeler pair production. *Plasma Physics and Controlled Fusion*, 60(10):104001, 2018.

[90] V. B. Beresteskii, E. M. Lifshitz, and L. P. Pitaevskii. *Quantum Electrodynamics*. Elsevier Butterworth-Hienmann, 1982.

[91] H. R. Reiss. Absorption of Light by Light. *Journal of Mathematical Physics*, 3(1):59–67, 1962.

[92] A. I. Nikishov and V. I. Ritus. Quantum Processes in the Field of a Plane Electromagnetic Wave and in a Constant Field. I. *Soviet Physics, Journal of Experimental and Theoretical Physics*, 19(2):529–541, 1964.

[93] C.P. Ridgers et al. Dense Electron-Positron Plasmas and Ultraintense γ rays from Laser-Irradiated Solids. *Physical Review Letters*, 108:165006, 2012.

[94] D. L. Burke et al. Positron Production in Multiphoton Light-by-Light Scattering. *Physical Review Letters*, 79:1626–1629, 1997.

[95] W. Heitler H. Bethe and P. A. M. Dirac. On the stopping of fast particles and on the creation of positive electrons. *Proceedings of the Royal Society of London*, 146(856):83–112, 1934.

[96] Hui Chen et al. Relativistic Positron Creation Using Ultraintense Short Pulse Lasers. *Physical Review Letters*, 102:105001, 2009.

[97] K. Nakashima and H. Takabe. Numerical study of pair creation by ultraintense lasers. *Physics of Plasmas*, 9(5):1505–1512, 2002.

[98] A.B. Langdon C.K. Birdsall. *Plasma Physics via Computer Simulation*. IOP Publishing Ltd, 1991.

[99] Julien Derouillat, A. Beck, F. Pérez, T. Vinci, M. Chiaramello, A. Grassi, M.Flé, G. Bouchard, I. Plotnikov, N. Aunai, J. Dargent, C. Riconda, M. Grech. SMILEI : A collaborative, open-source, multi-purpose particle-in-cell code for plasma simulation. *Computer Physics Communications*, 222:351–373, 2018.

[100] https://smileipic.github.io/smilei/index.html, accessed on 02/09/2022.

[101] J. Bonvalet et al. Energetic α-particle sources produced through proton-boron reactions by high-energy high-intensity laser beams. *Physical Review E*, 103:053202, 2021.

[102] J. Bonvalet et al. Laser-driven collisionless shock acceleration of protons from gas jets tailored by one or two nanosecond beams. *Physics of Plasmas*, 28(11):113102, 2021.

[103] F. Massimo et al. Efficient start-to-end 3D envelope modeling for two-stage laser wakefield acceleration experiments. *Plasma Physics and Controlled Fusion*, 61(12):124001, 2019.

[104] W. Yao et al. Laboratory evidence for proton energization by collisionless shock surfing. *Nature Physics*, 17:1177–1182, 2021.

[105] A. Fazzini et al. Particle energization in colliding subcritical collisionless shocks investigated in the laboratory. *Astronomy & Astrophysics*, 665:A87, 2022.

[106] https://redmine.mcia.fr/projects/cluster-curta/, accessed on 02/09/2022.

[107] http://mpd.jinr.ru/hybrilit-cluster/, accessed on 02/09/2022.

[108] J .P. Boris. Relativistic plasma simulation - optimization of a hybrid code. *Proceeding of the 4th Conference on Numerical Simulation of Plasmas*, pages 3–67, 1970.

[109] J.-L. Vay. Simulation of beams or plasmas crossing at relativistic velocity. *Physics of Plasmas*, 15(5):056701, 2008.

[110] A. V. Higuera and J. R. Cary. Structure-preserving second-order integration of relativistic charged particle trajectories in electromagnetic fields. *Physics of Plasmas*, 24(5):052104, 2017.

[111] A. Taflove, S.C. Hagness, M. Piket-May. 9 - computational electromagnetics: The finite-difference time-domain method. In *The Electrical Engineering Handbook*, pages 629–670. Academic Press, Burlington, 2005.

[112] J.-L. Vay, C.G.R. Geddes, E. Cormier-Michel, D.P. Grote. Numerical methods for instability mitigation in the modeling of laser wakefield accelerators in a Lorentz-boosted frame. *Journal of Computational Physics*, 230(15):5908–5929, 2011.

[113] R. Nuter, L. Gremillet, E. Lefebvre, A. Levy, T. Ceccotti, P. Martin. Field ionization model implemented in Particle In Cell code and applied to laser-accelerated carbon ions. *Physics of Plasmas*, 18(033107), 2011.

[114] M. V. Ammosov, N.B. Delone, V.P. Krainov. Tunnel ionization of complex atoms and of atomic ions in an alternating electromagnetic field. *Journal of Experimental and Theoretical Physics*, 64(6):1191, 1986.

[115] F. Perez, L. Gremillet, A. Decoster, M. Drouin, E. Lefebvre. Improved modeling of relativistic collisions and collisional ionization in particle-in-cell codes. *Physics of Plasmas*, 19(083104), 2012.

[116] K. Nanbu. Theory of cumulative small-angle collisions in plasmas. *Physical Review E*, 55(4):4642–4652, 1997.

[117] D.P. Higginson, A. Link, A. Schmidt. A pairwise nuclear fusion algorithm for weighted particle-in-cell plasma simulations. *Journal of Computational Physics*, 388:439–453, 2019.

[118] Fabien Niel, C. Riconda, F. Amiranoff, R. Duclous, M. Grech. From quantum to classical modelling of radiation reaction: a focus on stochasticity effects. *Physical Review E*, 97(043209), 2018.

[119] https://www.greenit.fr/environmental-footprint-of-the-digital-world/, accessed on 09/09/2022.

[120] https://sed-bso.gitlabpages.inria.fr/datacenter/energy_scope.html, accessed on 09/09/2022.

[121] Eric Maisonnave and Isabelle d'Ast. Energy consumption of the NEMO ocean model measured with the Energy Scope tool. *WN/CMGC/21/88*.

[122] Emmanuel Agullo et al. Study of the processor and memory power consumption of coupled sparse/dense solvers. *Inria Bordeaux Sud-Ouest, Research Report*, 9463, 2022.

[123] https://www.inria.fr/fr, accessed on 09/09/2022.

[124] https://fr.statista.com/statistiques/484345/distance-parcourue-en-moyenne-par-voiture-france/, accessed on 08/09/2022.

[125] https://climate.selectra.com/fr/empreinte-carbone/voiture, accessed on 08/09/2022.

[126] M. Lobet et al. Modeling of radiative and quantum electrodynamics effects in PIC simulations of ultra-relativistic laser-plasma interaction. *Journal of Physics: Conference Series*, 688(012058), 2016.

[127] S. Gordienko and A. Pukhov. Scalings for ultrarelativistic laser plasmas and quasimonoenergetic electrons. *Physics of Plasmas*, 12(4):043109, 2005.

[128] M. Vranic et al. All-Optical Radiation Reaction at $10^{21} W/cm^2$. *Physical Review Letter*, 113(134801), 2014.

[129] T. Nakamura et al. High-Power γ-Ray Flash Generation in Ultraintense Laser-Plasma Interactions. *Physical Review Letters*, 108:195001, 2012.

[130] T.G. Blackburn et al. Quantum Radiation Reaction in Laser-Electron-Beam Collisions. *Physical Review Letters*, 112:015001, 2014.

[131] A. Gonoskov et al. Anomalous Radiative Trapping in Laser Fields of Extreme Intensity. *Physical Review Letters*, 113:014801, 2014.

[132] J. Magnusson et al. Laser-Particle Collider for Multi-GeV Photon Production. *Physical Review Letters*, 122:254801, 2019.

[133] K. D. Xiao et al. Multidimensional effects on proton acceleration using high-power intense laser pulses. *Physics of Plasmas*, 25(2):023103, 2018.

[134] C.S. Brady et al. Laser Absorption in Relativistically Underdense Plasmas by Synchrotron Radiation. *Physical Review Letters*, 109:245006, 2012.

[135] I. M. Vladisavlevici, D. Vizman and E d'Humières. Theoretical Study of Laser Energy Absorption Towards Energetic Proton and Electron Sources. *Proceedings of 13th International Particle Accelerator Conference, Bangkok, Thailand*, June:1737 – 1740, 2022.

[136] I. M. Vladisavlevici, D. Vizman and E d'Humières. Theoretical investigation of the interaction of ultra-high intensity laser pulses with near critical density plasmas. *Accepted for publication in Plasma Physics and Controlled Fusion*.

[137] I. M. Vladisavlevici, D. Vizman and E d'Humières. Laser driven electron acceleration from near-critical density targets towards the generation of high energy γ-photons. *Photonics*, 9(953), 2022.

[138] I. M. Vladisavlevici, X.Ribeyre, D. Vizman and E d'Humières. Investigation of γ-photon sources using near-critical density targets towards the optimization of the linear Breit-Wheeler process . *Under Review at Frontiers in Physics*.

Acknowledgements

This work was developed within the binational PhD program between the West University of Timisoara - Faculty of Physics and University of Bordeaux - CELIA (Centre Lasers Intenses et Applications) laboratory.

First of all, I am extremely grateful to Prof. dr. Daniel Vizman and to Prof. dr. Emmanuel d'Humières for giving me the opportunity to be their student, and for their continuous confidence, advice and support during the 4 years of PhD, in normal, as well as in difficult times. I would also like to express my deepest gratitude to Prof. dr. Emmanuel d'Humières for his patience to explain me basic and complex concepts of plasma physics and of numerical simulations, for his leadership in the development of all the work presented in this thesis as well as for all motivational discussions.

I would like to express my special thanks to Xavier Ribeyre for his help for the study of electron-positron pair generation. I am very grateful for the $\gamma - \gamma$ code and for his time explaining it to me, as well as for the theoretical explanations of all pair generation processes and the estimation of the number of pairs obtained by the Bethe-Heitler pair process.

I would like to express my deepest appreciation to Mr. and Mrs. Adam for their continuous interest and dedicated support of my work, as well as for all their encouragements.

I would like to thank to the members of jury of the public defense for the honor to read and review my thesis. The initial version of this manuscript was greatly improved according to their valuable comments and suggestions.

I would also like to thank to the members of the thesis monitoring committee, Lect. dr. Alexandra Popescu, Conf. dr. Paul Barvinschi and Prof. dr. Marius Paulescu for their scientific

advices and suggestions which helped me to improve this thesis.

Many thanks to SMILEI team developers who provided an open source, very well documented and user-friendly PIC code. I am especially thankful for the help given with the installation and the running of SMILEI on supercomputers, as well as for the implementation and usage of various diagnostics.

I am also thankful to Hervé Mathieu for the opportunity to run my simulations with Energy Scope software and his help to interpret the results obtained.

I would like to express my admiration and gratitude to my physics class teacher Mariana Zaberca for inspiring me her passion for physics and motivating me to choose this journey.

I would also like to thank my friends for their support and curiosity in my work. Many thanks to Iulia Bejenariu for the moral support especially during these 4 years and even longer, and to Raluca Hodorog for her support and for believing in me since we met first time.

I would also like to thank Dragoș Tatomirescu for his help and advices in dealing with a binational program, to Andreea Sabadus for all the help with the administration and for the motivating coffee breaks, and to Andrei Cordoș for being the best officemate I have ever had.

I am very grateful to Michael Ehret for the motivational speeches and encouragements which helped me to finish this PhD. Thank you for being always there for me.

Nevertheless, I would like to special thanks to my very big family for their confidence and for giving me the moral and the financial support I needed to start as well as to continue this journey. This thesis would have been impossible without their help.

Finally, I would like to thank to all helping and inspiring people I have met in my life. Thank you for helping me to become the person I am today.

Financial support

First of all, as a scientific research would not be possible withot proper funding, I would like to thank to the main financial sources for my PhD thesis: the scholarship awarded by

the West University of Timisoara (2018 - 2021), the research working contract provided by the Romanian National Authority for Scientific Research PN 75/2018 (2019 - 2022) and the WUT - ICAM research working contract (2022 - ongoing). Also, I am grateful for the financial support of my mobility from April - June 2022 provided by the Centre National de la Recherche Scientifique - CELIA France.

Along my way in the computer simulations, I was often proved the importance of supercomputers. I would like to thank to the CELIA laboratory for the access to the computing facilities MCIA (Mésocentre de Calcul Intensif Aquitain) of the Université de Bordeaux and of the Université de Pau et des Pays de l'Adour. I am very grateful to MCIA - Curta machine for more than 2.6 million CPU hours which allowed me to conduct my work.

I am very thankful to the Department of International Relations of the WUT for their flexibility in helping me to access Erasmus+ Student Grants. The Erasmus+ program changed my way of thinking well before the PhD and transformed me in an European citizien. I am very grateful to the European Union for the implemention of this program which covered 12 months of my research visits in Bordeaux (grants: 2018/2019, 2019/2020 and 2020/2021).

Most of the time, a research contract does not come accompanied with financial support for conferences or summer schools, and a research project is needed.

I am very grateful to the Agence Nationale de la Recherche project ANR-17-CE30-0026-Pinnacle which allowed me the participation to 8 scientific events (EPS2022, SFP-Plasmas, ILP Forum, GdR APPEL, SMILEI 3rd workshop, JRA meeting, Short-pulse lasers and applications Summer School, SMILEI 2nd workshop) as well as for my first week in Bordeaux (2019). In addition, I am also thankful for supporting all travel costs for all my stays in Bordeaux.

I am very thankful to the international collaboration WUT - JINR collaboration project 05-6-1119-2014/2023 (2/2019; 86/2020; 103/2021) for granting my access to HybriLIT supercomputer and the financial support of my mobilities in LIT - JINR, as well as my participation at Nuclear physics with high power lasers Summer School.

I would like to thank WUT for the financial support provided for the participation at the conferences ECAART14 and TIM19.

I am very grateful for the awarded IPAC22 Student Grant which provided me the par-

ticipation in a prestigious international conference and the opportunity to discover a different culture.

Nevertheless, I would like to thank the organizers of the following online conferences TIM20-21, EPS2020, CSDCU-MIF2020 for providing free access and participation in difficult times.

Appendix A

A.1 Variation of the absorption coefficient with target density and laser pulse duration

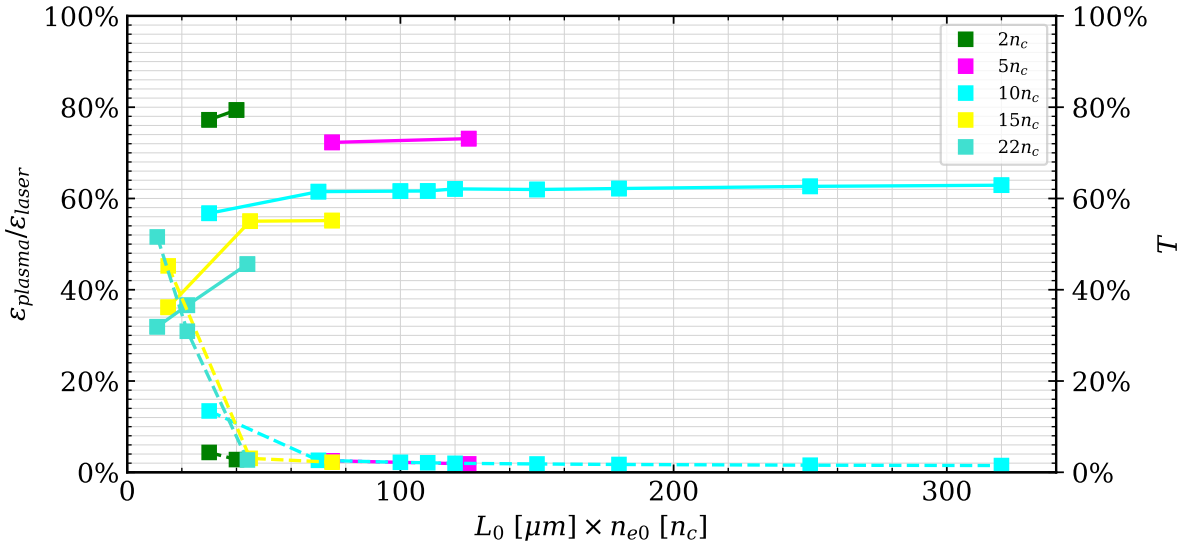

Figure A.1: Absorption coefficient vs initial target areal density from 2D PIC simulations. Target parameters: $L_y = 30$ μm. Laser parameters: $a_0 = 85$, $\tau = 2$ t$_0$, $\lambda = 1$ μm, w$_0 = 12.5$ μm.

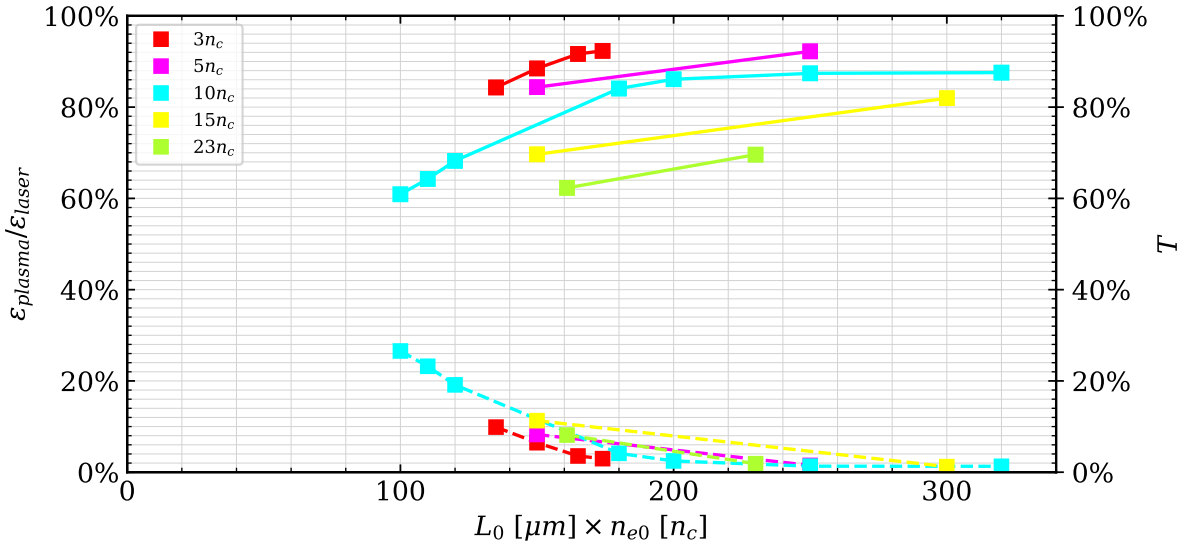

Figure A.2: Absorption coefficient vs initial target areal density from 2D PIC simulations. Target parameters: $L_y = 30\ \mu$m. Laser parameters: $a_0 = 85,\ \tau = 12\ \mathrm{t_0},\ \lambda = 1\ \mu$m, $\mathrm{w_0} = 12.5\ \mu$m.

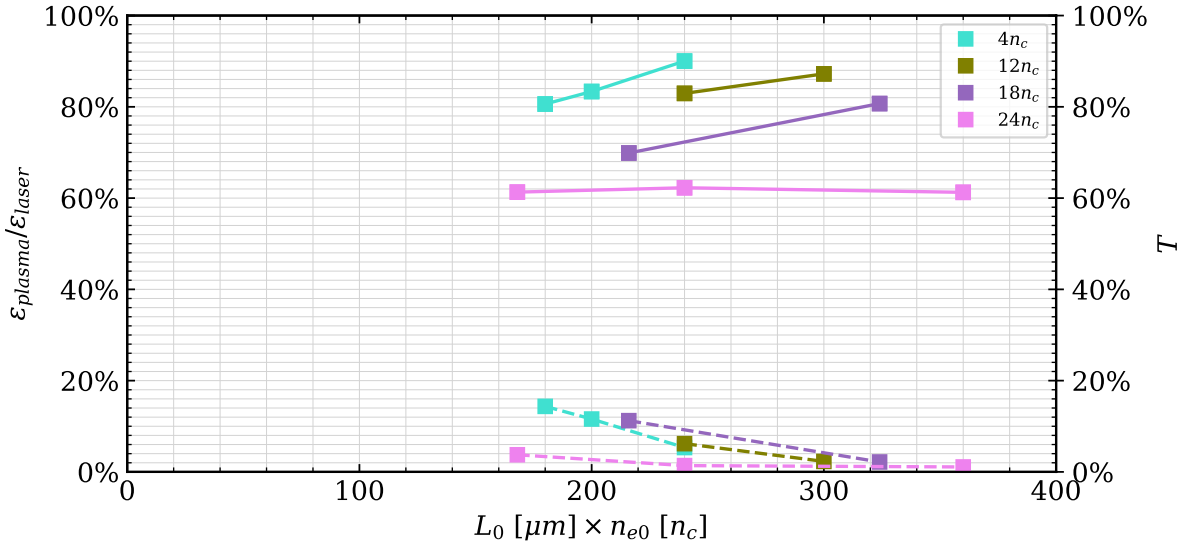

Figure A.3: Absorption coefficient vs initial target areal density from 2D PIC simulations. Target parameters: $L_y = 30\ \mu$m. Laser parameters: $a_0 = 85,\ \tau = 18\ \mathrm{t_0},\ \lambda = 1\ \mu$m, $\mathrm{w_0} = 12.5\ \mu$m.

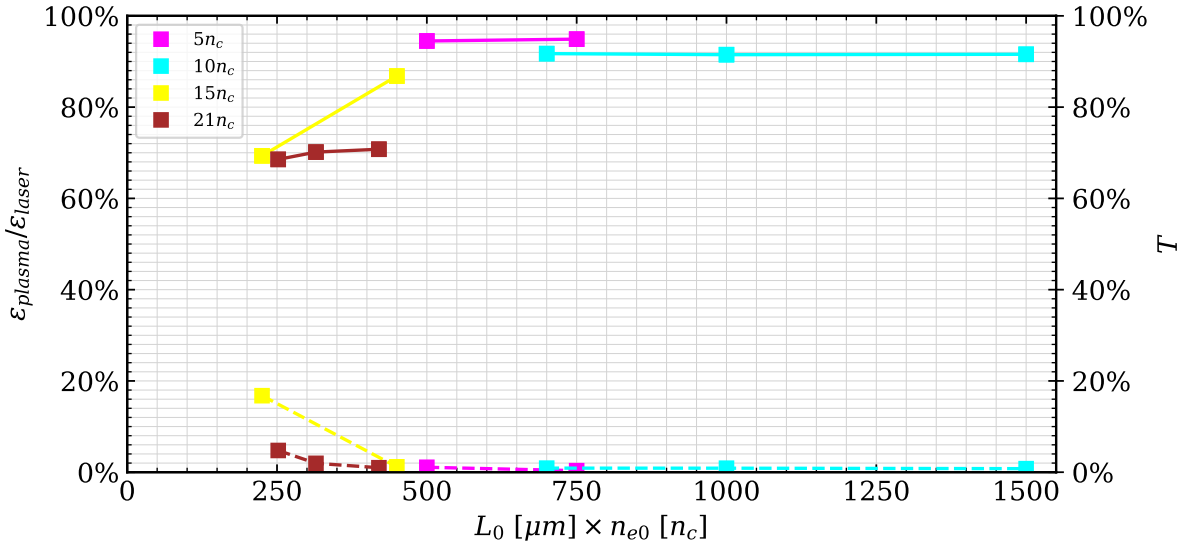

Figure A.4: Absorption coefficient vs initial target areal density from 2D PIC simulations. Target parameters: $L_y = 30\ \mu$m. Laser parameters: $a_0 = 85,\ \tau = 24\ \mathrm{t_0},\ \lambda = 1\ \mu$m, $\mathrm{w_0} = 12.5\ \mu$m.

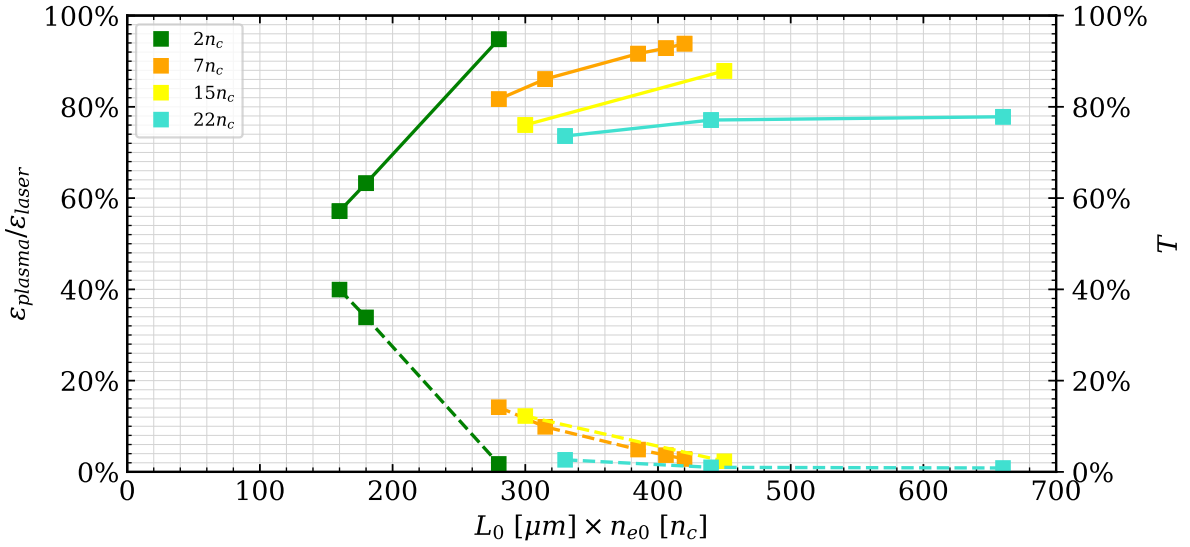

Figure A.5: Absorption coefficient vs initial target areal density from 2D PIC simulations. Target parameters: $L_y = 30\ \mu$m. Laser parameters: $a_0 = 85,\ \tau = 30\ \mathrm{t_0},\ \lambda = 1\ \mu$m, $\mathrm{w_0} = 12.5\ \mu$m.

A.2 Variation of the absorption coefficient with target density and laser normalized field amplitude

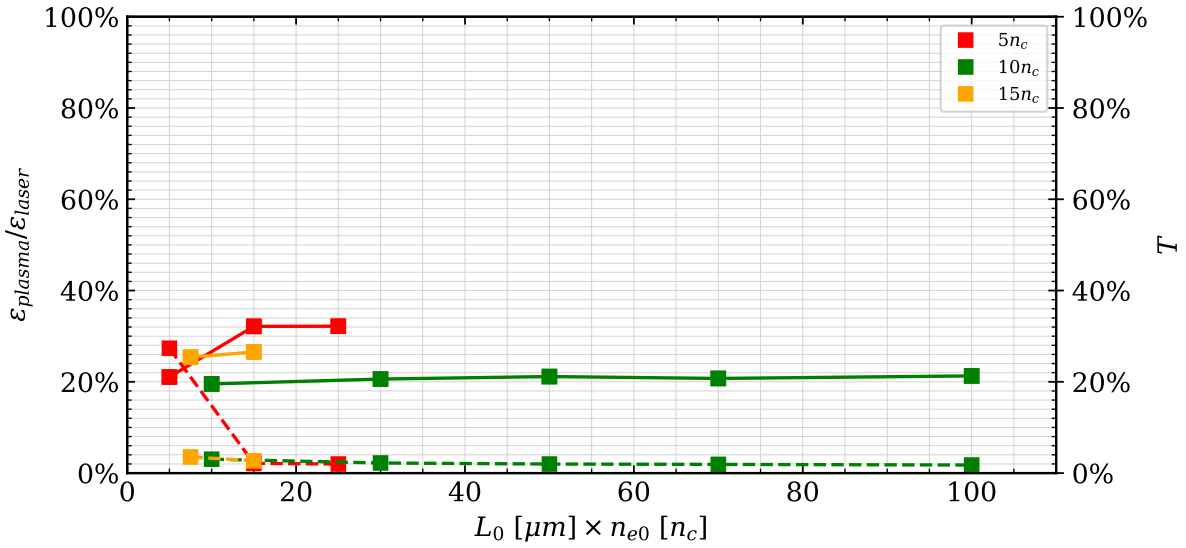

Figure A.6: Absorption coefficient vs initial target areal density from 2D PIC simulations. Target parameters: $L_y = 30\ \mu$m. Laser parameters: $a_0 = 8.5$, $\tau = 6\ t_0$, $\lambda = 1\ \mu$m, $w_0 = 12.5\ \mu$m.

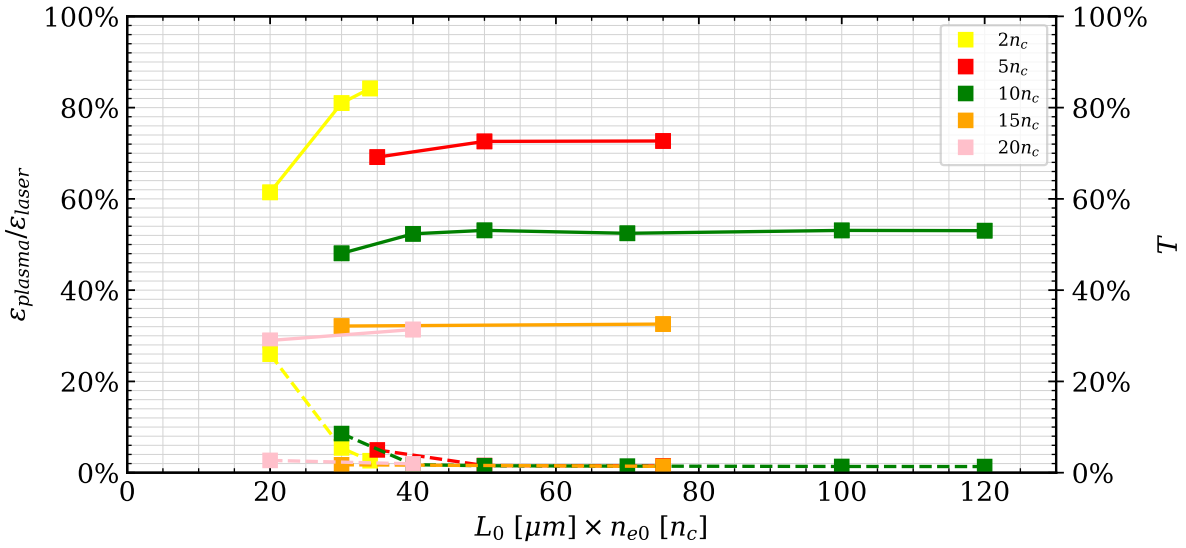

Figure A.7: Absorption coefficient vs initial target areal density from 2D PIC simulations. Target parameters: $L_y = 30\ \mu$m. Laser parameters: $a_0 = 26.88$, $\tau = 6\ t_0$, $\lambda = 1\ \mu$m, $w_0 = 12.5\ \mu$m.

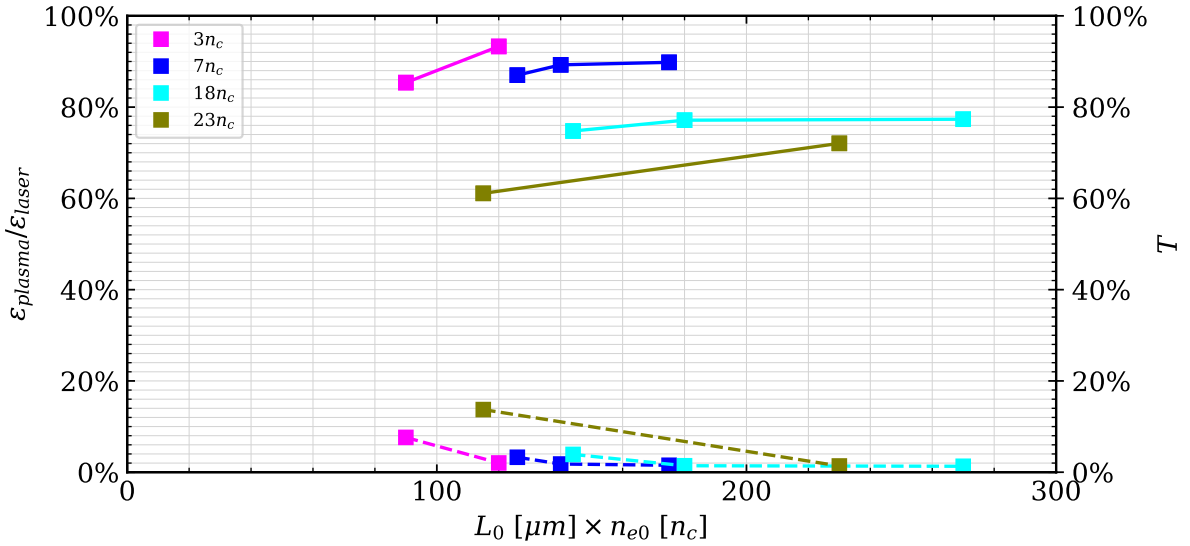

Figure A.8: Absorption coefficient vs initial target areal density from 2D PIC simulations. Target parameters: $L_y = 30\ \mu$m. Laser parameters: $a_0 = 120,\ \tau = 6$ t$_0$, $\lambda = 1\ \mu$m, w$_0 = 12.5\ \mu$m.

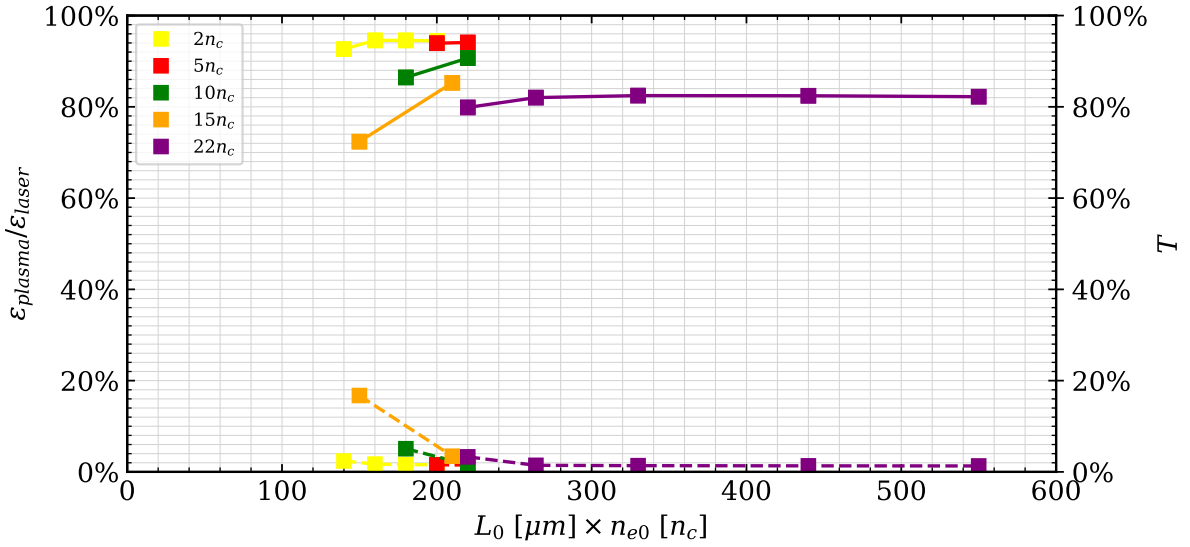

Figure A.9: Absorption coefficient vs initial target areal density from 2D PIC simulations. Target parameters: $L_y = 30\ \mu$m. Laser parameters: $a_0 = 190,\ \tau = 6$ t$_0$, $\lambda = 1\ \mu$m, w$_0 = 12.5\ \mu$m.

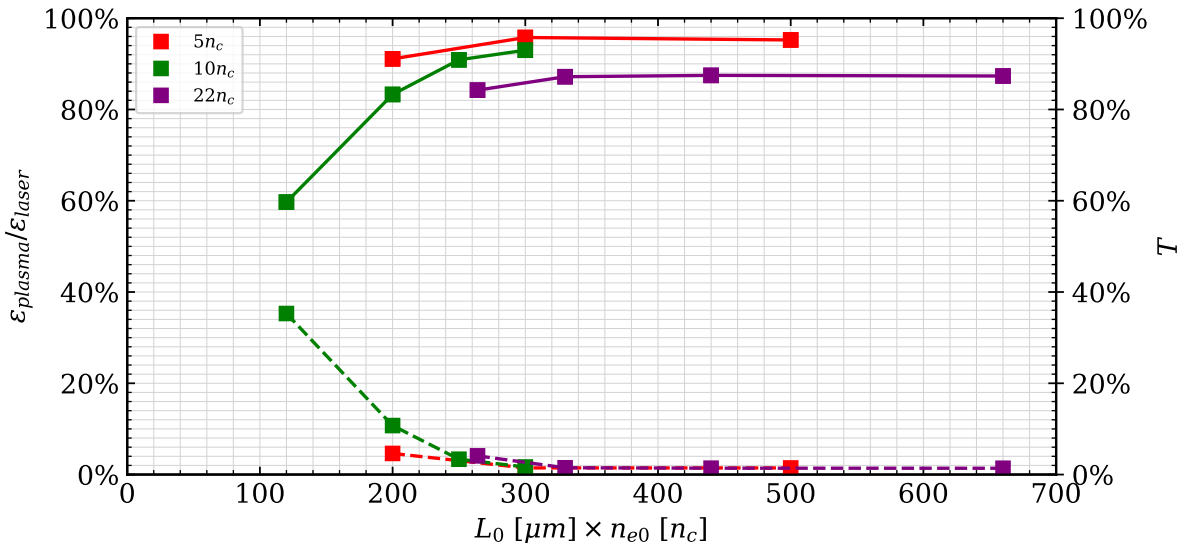

Figure A.10: Absorption coefficient vs initial target areal density from 2D PIC simulations. Target parameters: $L_y = 30\ \mu$m. Laser parameters: $a_0 = 268.8,\ \tau = 6\ \mathrm{t}_0,\ \lambda = 1\ \mu$m, $\mathrm{w}_0 = 12.5\ \mu$m.

A.3 Variation of the saturation point of the absorption coefficient with target density and laser parameters

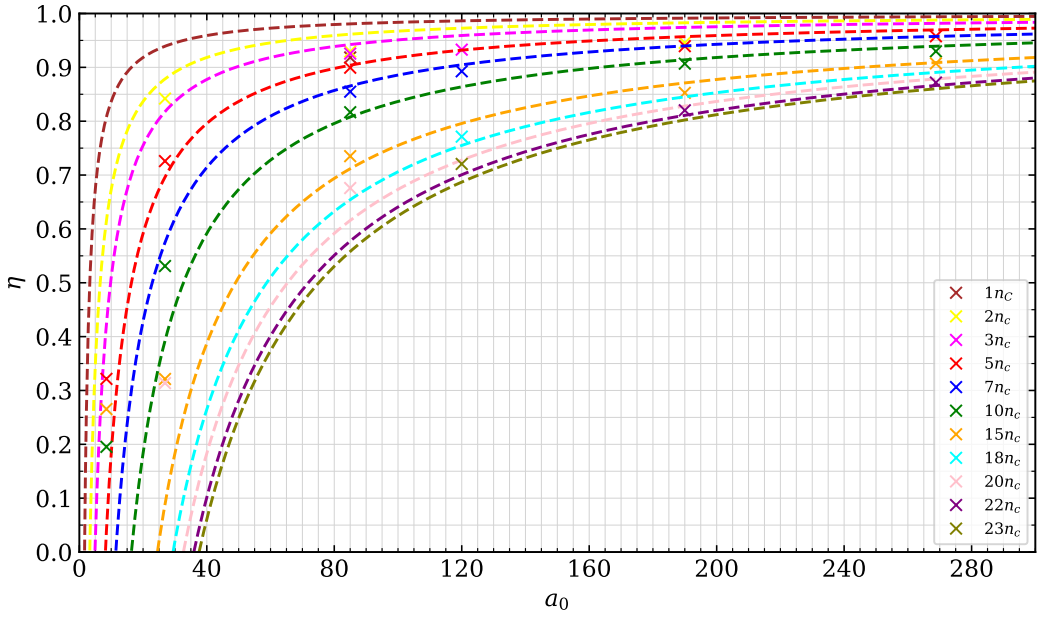

Figure A.11: Saturation point of the absorption coefficient vs laser normalized field amplitude for various target densities at the optimum target thickness. Target parameters: $L_y = 30\ \mu$m. Laser parameters are $\lambda = 1\ \mu$m, $\tau = 6$ t$_0$ and $w_0 = 12.5\ \mu$m. The simulation results are represented with crosses, and the results of Eq.(3.19) are shown with the dashed lines.

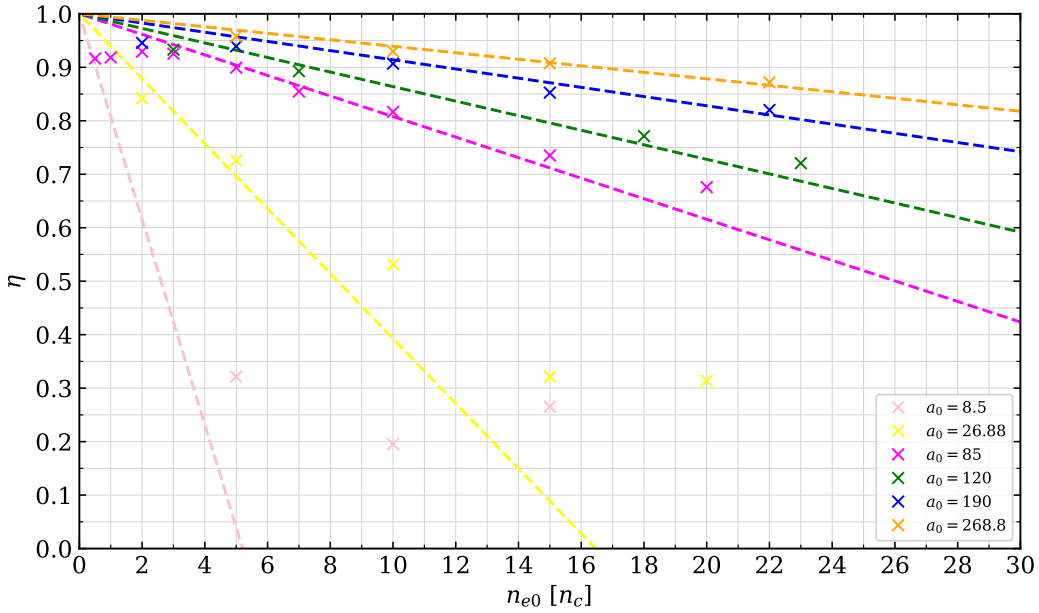

Figure A.12: Saturation point of the absorption coefficient vs target density for various laser normalized field amplitudes at the optimum target thickness. Target parameters: $L_y = 30\ \mu$m. Laser parameters are $\lambda = 1\ \mu$m, $\tau = 6$ t$_0$ and $w_0 = 12.5\ \mu$m. The simulation results are represented with crosses, and the results of Eq.(3.19) are shown with the dashed lines.

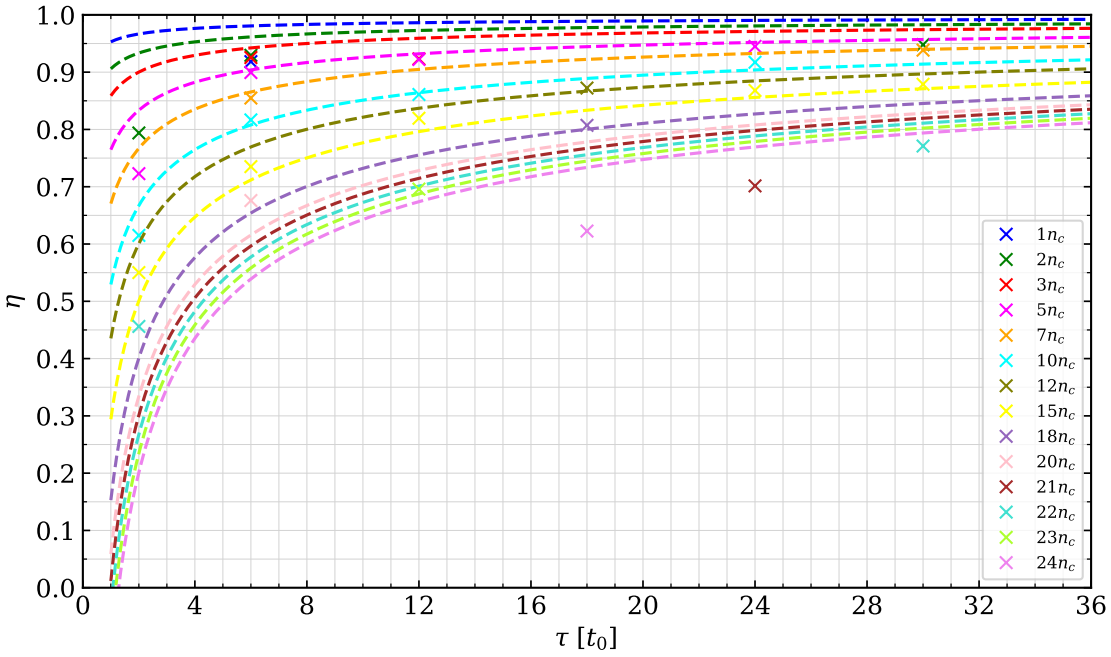

Figure A.13: Saturation point of the absorption coefficient vs laser pulse duration for various target densities at the optimum target thickness. Target parameters: $L_y = 30$ μm. Laser parameters are $\lambda = 1$ μm, $a_0 = 85$ and $w_0 = 12.5$ μm. The simulation results are represented with crosses, and the results of Eq.(3.19) are shown with the dashed lines.

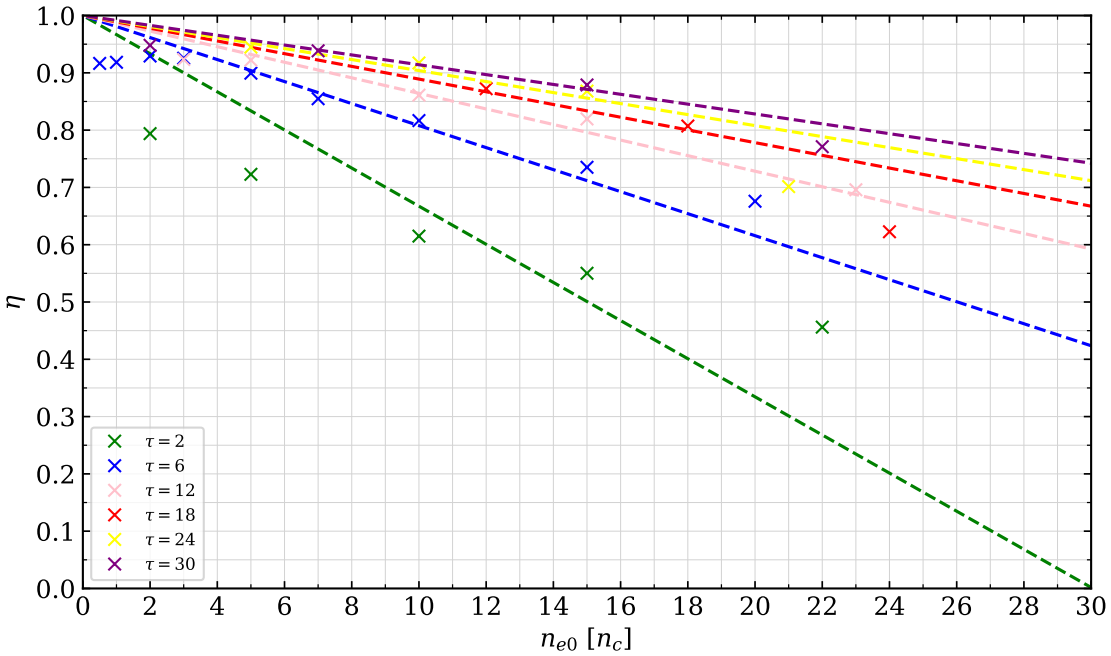

Figure A.14: Saturation point of the absorption coefficient vs target density for various laser pulse durations at the optimum target thickness. Target parameters: $L_y = 30$ μm. Laser parameters are $\lambda = 1$ μm, $a_0 = 85$ and $w_0 = 12.5$ μm. The simulation results are represented with crosses, and the results of Eq.(3.19) are shown with the dashed lines.

A.4 Variation of the average energy of hot electrons with target density and laser parameters

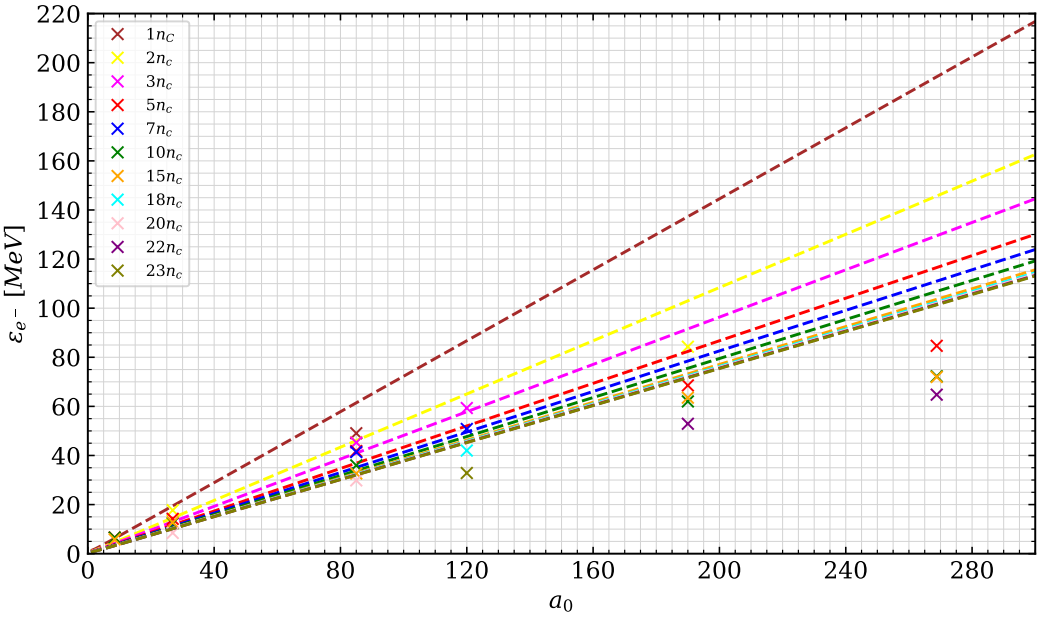

Figure A.15: Average energy of the hot electrons vs laser normalized field amplitude for various target densities at the optimum target thickness. Target parameters: $L_y = 30\ \mu$m. Laser parameters are $\lambda = 1\ \mu$m, $\tau = 6$ t$_0$ and $w_0 = 12.5\ \mu$m. The simulation results are represented with crosses, and the results of Eq.(3.20) are shown with the dashed lines.

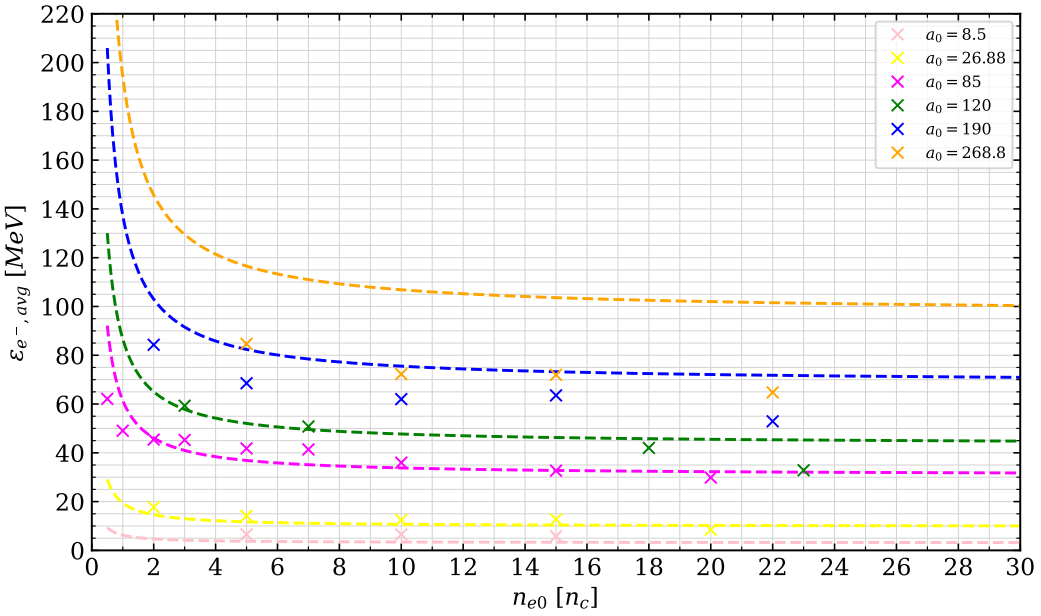

Figure A.16: Average energy of the hot electrons vs target density for various laser normalized field amplitudes at the optimum target thickness. Target parameters: $L_y = 30\ \mu$m. Laser parameters are $\lambda = 1\ \mu$m, $\tau = 6$ t$_0$ and $w_0 = 12.5\ \mu$m. The simulation results are represented with crosses, and the results of Eq.(3.20) are shown with the dashed lines.

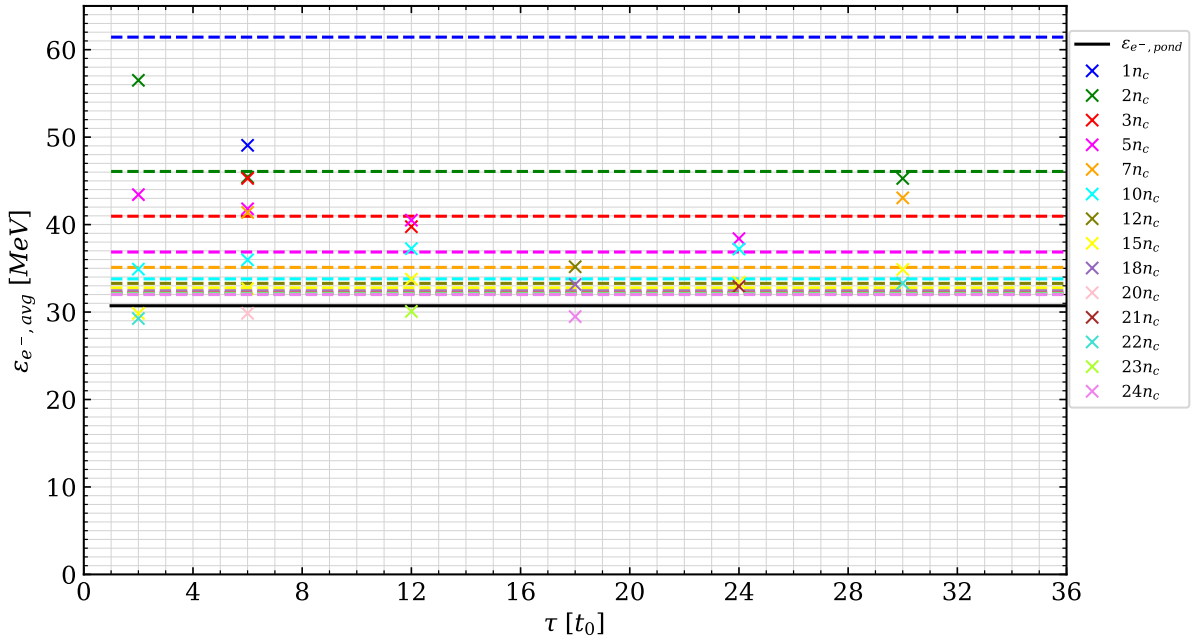

Figure A.17: Average energy of the hot electrons vs laser pulse duration for various target densities at the optimum target thickness. Target parameters: $L_y = 30$ μm. Laser parameters are $\lambda = 1$ μm, $a_0 = 85$ and $w_0 = 12.5$ μm. The simulation results are represented with crosses, and the results of Eq.(3.20) are shown with the dashed lines. The continuous black line represents the ponderomotive scaling.

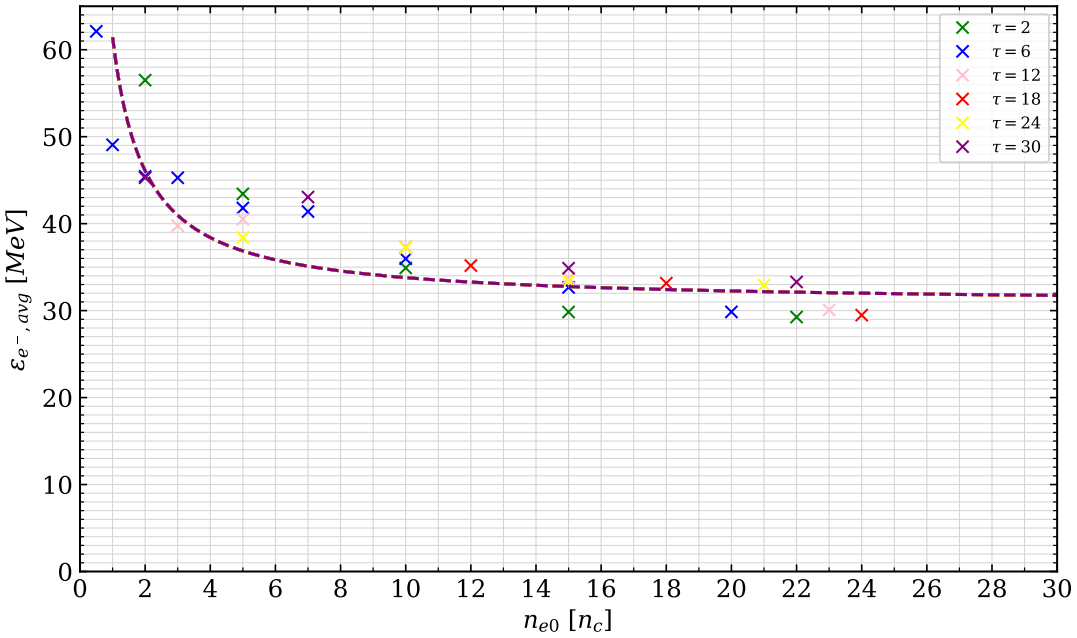

Figure A.18: Average energy of the hot electrons vs target density for various laser pulse durations at the optimum target thickness. Target parameters: $L_y = 30$ μm. Laser parameters are $\lambda = 1$ μm, $a_0 = 85$ and $w_0 = 12.5$ μm. The simulation results are represented with crosses, and the results of Eq.(3.20) are shown with the dashed line.

A.5 Variation of the optimum target thickness with target density and laser parameters

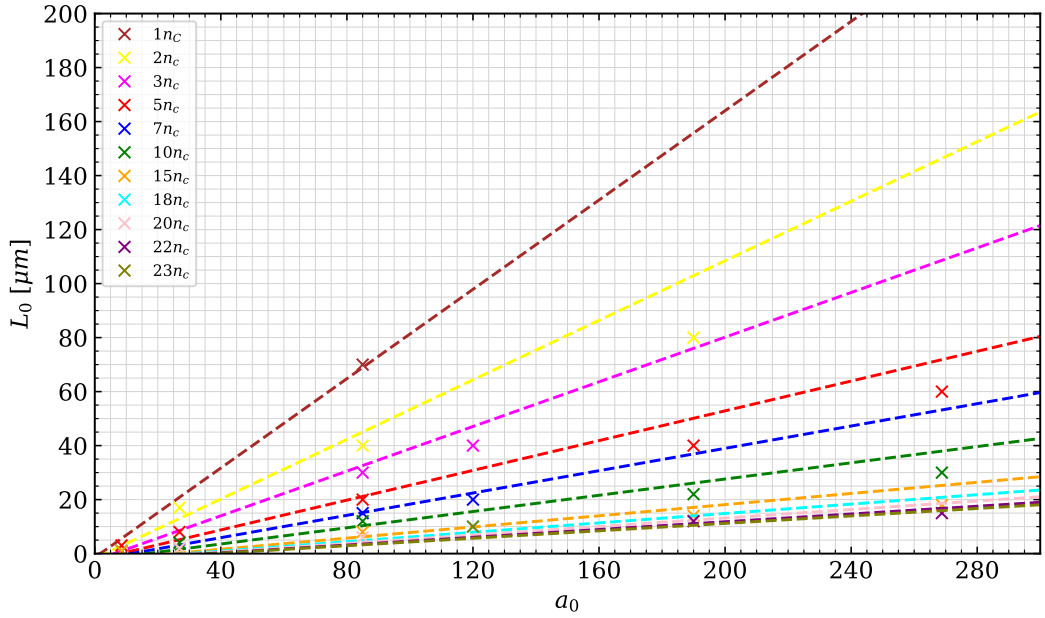

Figure A.19: Optimum target thickness vs laser normalized field amplitude for various target densities. Target parameters: $L_y = 30$ μm. Laser parameters are $\lambda = 1$ μm, $\tau = 6$ t$_0$ and $w_0 = 12.5$ μm. The simulation results are represented with crosses, and the results of Eq.(3.21) are shown with the dashed lines.

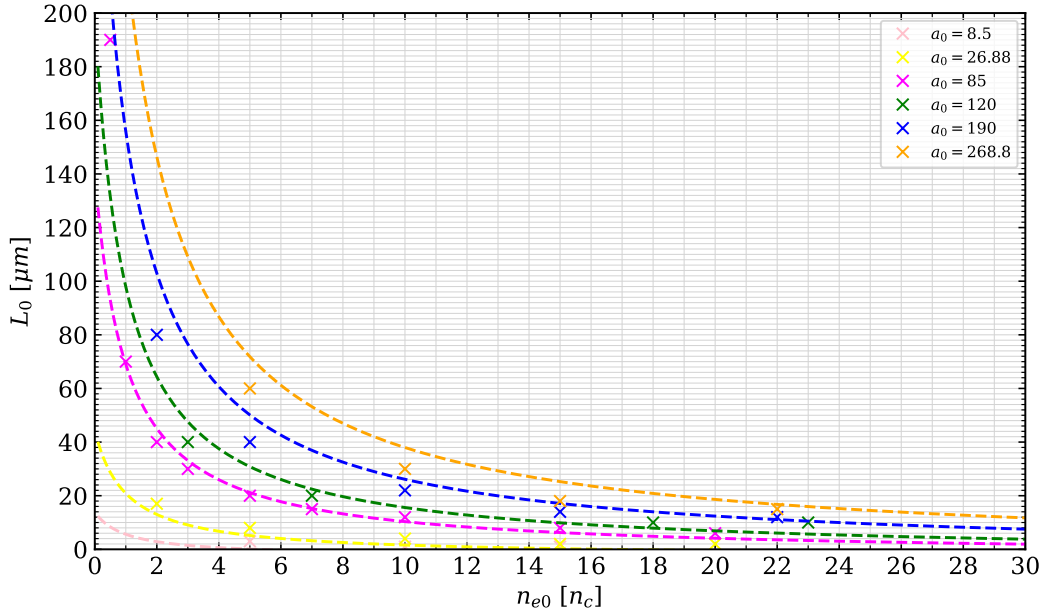

Figure A.20: Optimum target thickness vs target density for various laser normalized field amplitudes. Target parameters: $L_y = 30$ μm. Laser parameters are $\lambda = 1$ μm, $\tau = 6$ t$_0$ and $w_0 = 12.5$ μm. The simulation results are represented with crosses, and the results of Eq.(3.21) are shown with the dashed lines.

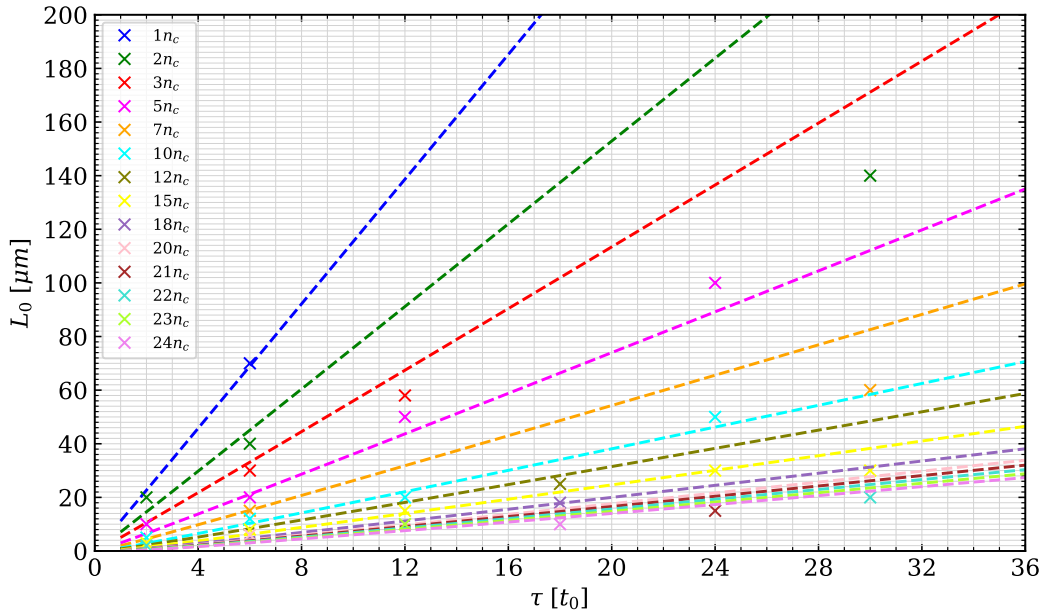

Figure A.21: Optimum target thickness vs laser pulse duration for various target densities. Target parameters: $L_y = 30$ μm. Laser parameters are $\lambda = 1$ μm, $a_0 = 85$ and $w_0 = 12.5$ μm. The simulation results are represented with crosses, and the results of Eq.(3.21) are shown with the dashed lines.

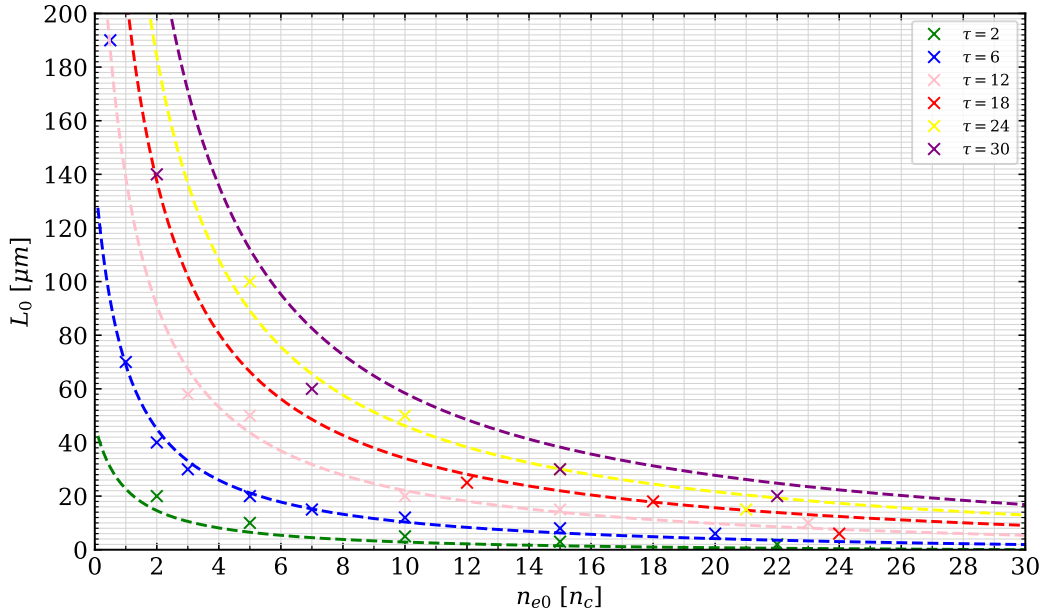

Figure A.22: Optimum target thickness vs target density for various laser pulse durations. Target parameters: $L_y = 30$ μm. Laser parameters are $\lambda = 1$ μm, $a_0 = 85$ and $w_0 = 12.5$ μm. The simulation results are represented with crosses, and the results of Eq.(3.21) are shown with the dashed lines.

Appendix B

B.1 Typical electron trajectories from 2D PIC simulations

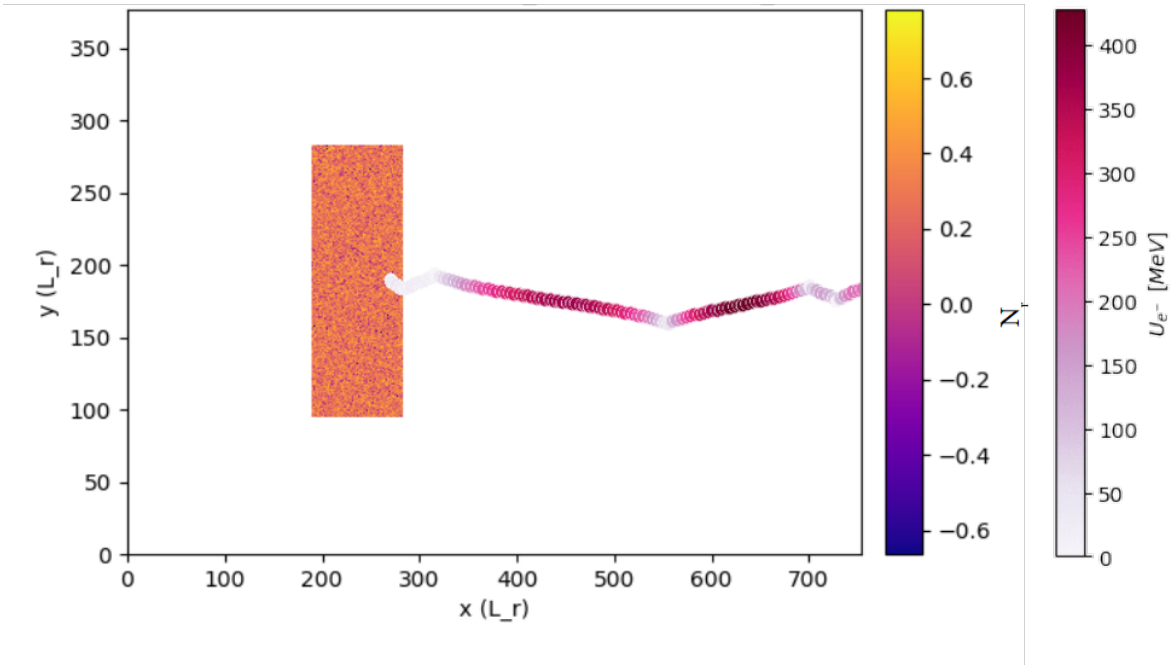

Figure B.1: The trajectory and the energy evolution in time of an electron accelerated by the ponderomotive force from a 2D PIC simulation. Target parameters: $n_{e0} = 2$ n$_c$, $L_x = 15$ μm and $L_y = 30$ μm. Laser parameters: $\lambda = 1$ μm, $a_0 = 85$, $\tau = 20$ fs FWHM and $w_0 = 12.5$ μm.

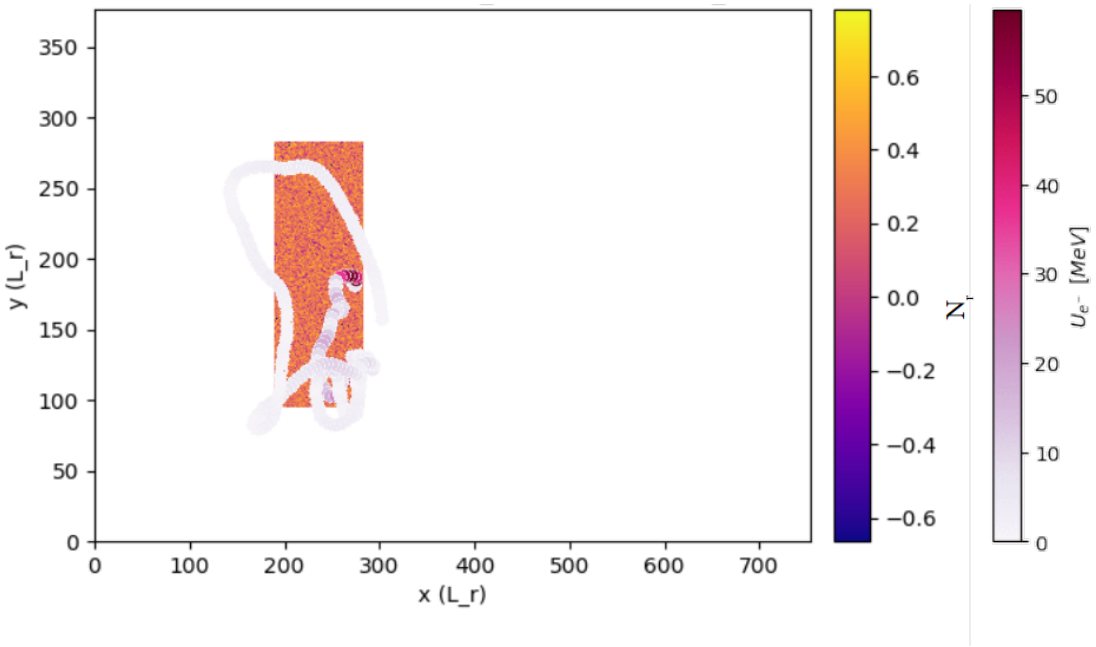

Figure B.2: The trajectory and the energy evolution in time of an electron which recirculates inside the target from a 2D PIC simulation. Target parameters: $n_{e0} = 2$ n$_c$, $L_x = 15$ μm and $L_y = 30$ μm. Laser parameters: $\lambda = 1$ μm, $a_0 = 85$, $\tau = 20$ fs FWHM and $w_0 = 12.5$ μm.

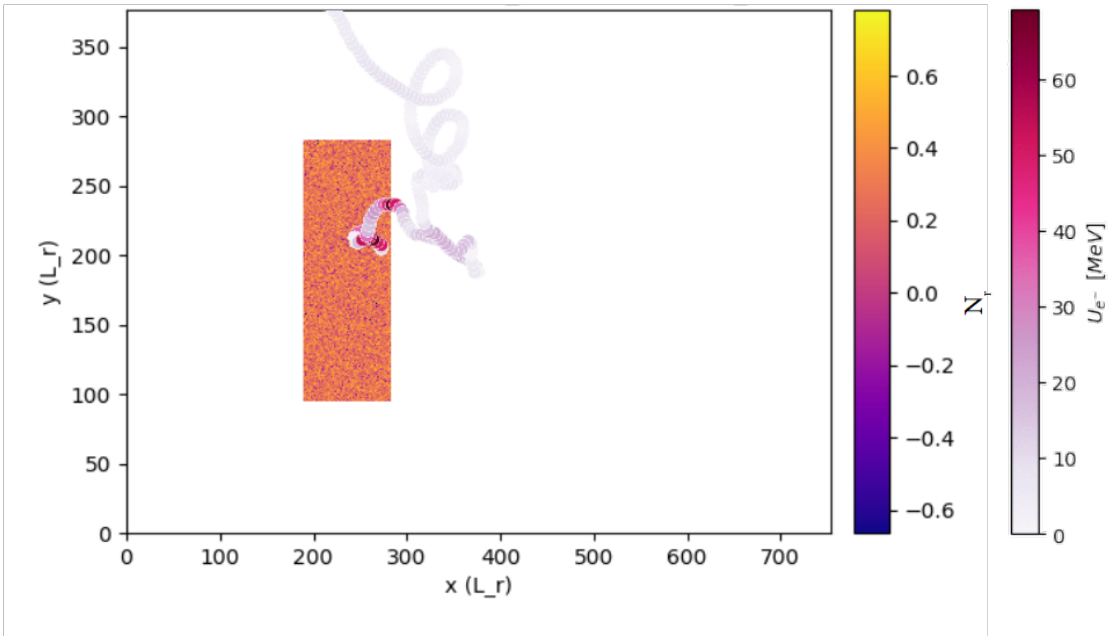

Figure B.3: The trajectory and the energy evolution in time of an electron confined by the magnetic field from a 2D PIC simulation. Target parameters: $n_{e0} = 2$ n$_c$, $L_x = 15$ μm and $L_y = 30$ μm. Laser parameters: $\lambda = 1$ μm, $a_0 = 85$, $\tau = 20$ fs FWHM and $w_0 = 12.5$ μm.

B.2 Density change in laser-plasma interaction

As can be seen in Fig.B.4 (left), the laser pushes the electrons and forms a denser area ahead of the laser pulse. This effect can be also seen in the temporal evolution of the maximum electron density, which increases when most of the laser-to-plasma energy transfer takes place as shown in Fig.B.4 (right).

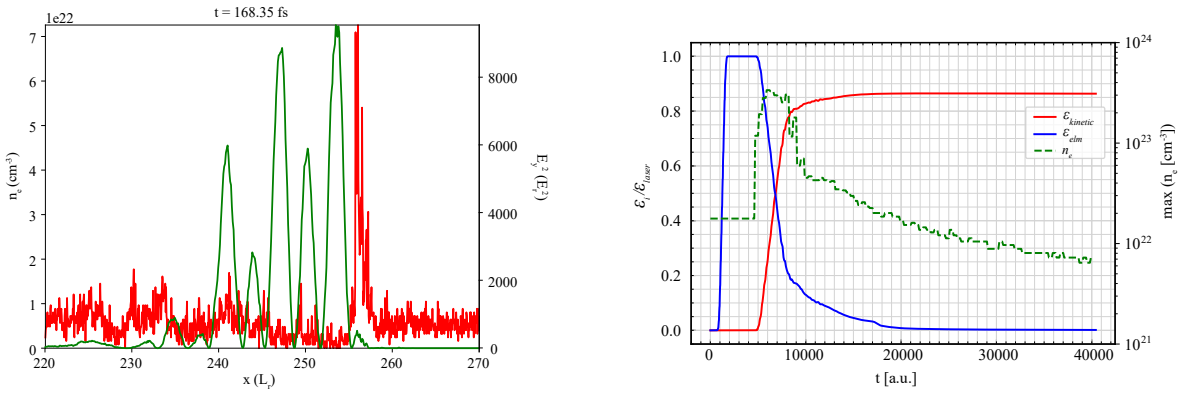

Figure B.4: Profile of the target density (red) and transversal component of the laser electric field (green) vs target position from a 2D PIC simulation (left); temporal evolution of the electromagnetic and kinetic energies and temporal evolution of the maximum of target density from a 2D PIC simulation (right). Target parameters: $n_{e0} =$ 5 n_c, $L_x = 20$ μm and $L_y = 30$ μm. Laser parameters: $\lambda = 1$ μm, $a_0 = 85$, $\tau = 20$ fs FWHM and $w_0 = 12.5$ μm.

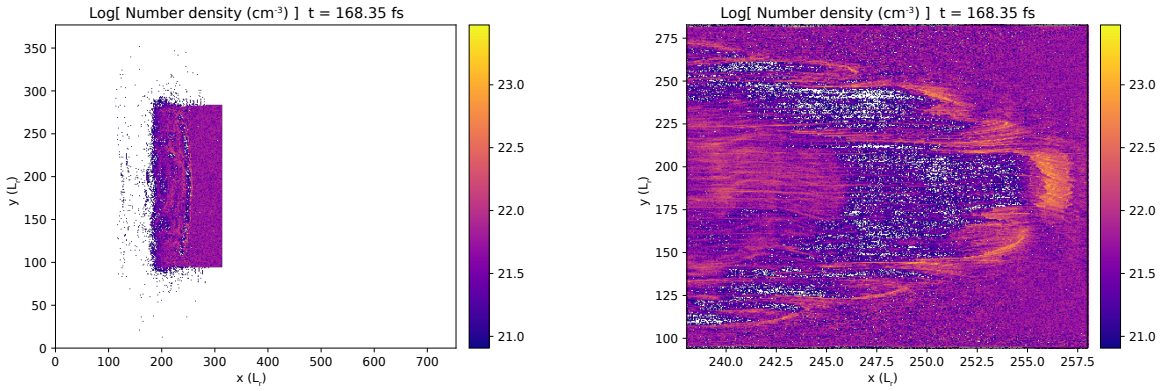

Figure B.5: Electron density map (left) and electron density map in the interaction area (right) for a time corresponding to 7000 a.u. from Fig.B.4. Target parameters: $n_{e0} = 5$ n_c, $L_x = 20$ μm and $L_y = 30$ μm. Laser parameters: $\lambda = 1$ μm, $a_0 = 85$, $\tau = 20$ fs FWHM and $w_0 = 12.5$ μm.

To quantify the effect of the density change, we calculated the average electron density in the interaction area at a given time. In Fig.B.5 (right) is shown the 2D density map corresponding to the time at which the density increase gets maximum, at $t = 7000$ a.u. from Fig.B.4 (left). The average density in the interaction area from Fig.B.5 (right) is $6.35 \cdot 10^{21}$ cm^{-3},

which represents an increase of about 27% of the initial target density. The average density from Fig.B.5 (right), starting with the position $x = 255$ L_r, which corresponds to the dense peak from Fig.B.4 (left), is $8.42 \cdot 10^{21}$ cm^{-3}.

Appendix C

C.1 Positron characteristics from 2D PIC simulations

In Fig.C.1 is shown the positron spectrum obtained from a 2D PIC simulation. The total number of positrons obtained in the 2D PIC simulation is $9.5 \cdot 10^{10}$ with a total energy of 8.5 J, representing 0.047% of the initial laser energy.

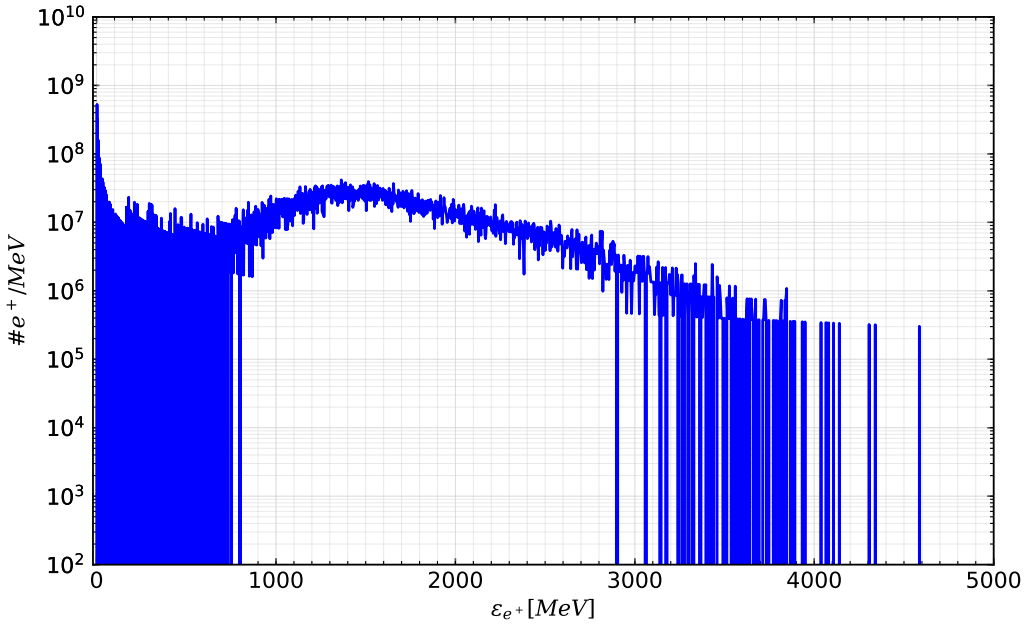

Figure C.1: Energy spectrum of the nonlinear BW pairs created from a 2D PIC simulation. Target parameters: $n_{e0} = 10$ n$_c$, $L_x = 88$ μm and $L_y = 30$ μm. Laser parameters: $\lambda = 1$ μm, $a_0 = 601$, $\tau = 20$ fs FWHM and $w_0 = 12.5$ μm.

Fig.C.2 shows the temporal evolution of the total number of macroparticles from a 2D PIC simulation. As can be seen the total number of macro-positrons is increasing rapidly due

to the nonlinear Breit-Wheeler process and saturates after the $\gamma-$photons escaped from the area of strong electromagnetic field. As the total number of macro-positrons is a few orders of magnitude lower than the one of macro-electrons, the nonlinear Breit-Wheeler process takes place only once per $\gamma-$photon.

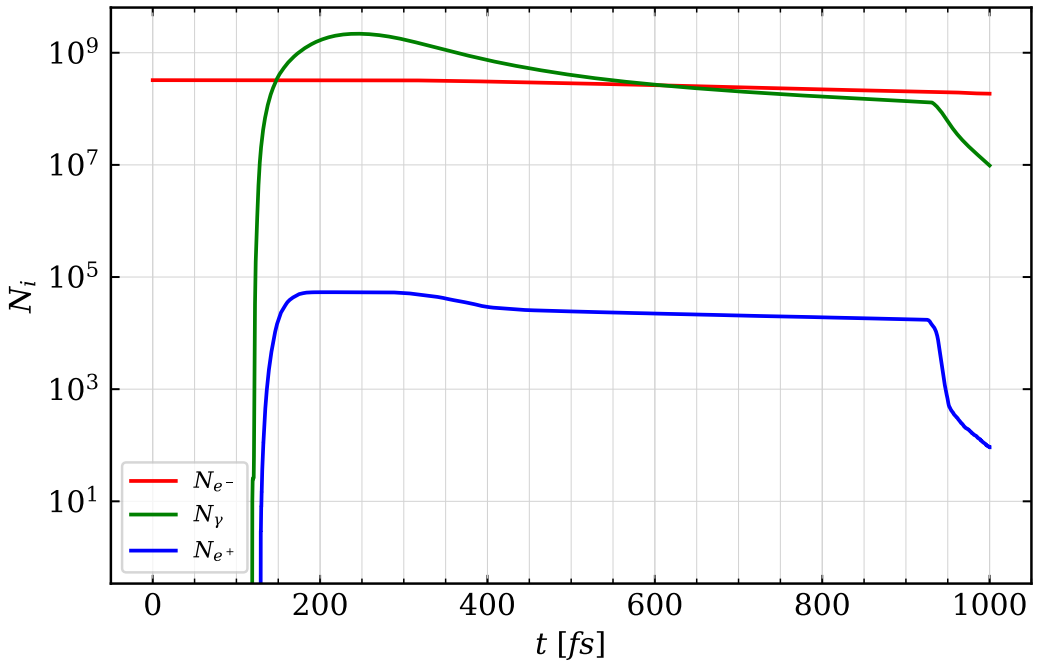

Figure C.2: Temporal evolution of the macroparticles from a 2D PIC simulation. Target parameters: $n_{e0} = 10$ n$_c$, $L_x = 88$ μm and $L_y = 30$ μm. Laser parameters: $\lambda = 1$ μm, $a_0 = 601$, $\tau = 20$ fs FWHM and $w_0 = 12.5$ μm.

C.2 Electron energy angle distribution

As mentioned in Section 5.3, for intensities higher than 10^{23} W/cm^2, the energy angle distribution of the $\gamma-$photons shows a two lobe structure which occurs because of the two lobe structure of the energy angle distribution of the electrons, which is shown in Fig.C.3.

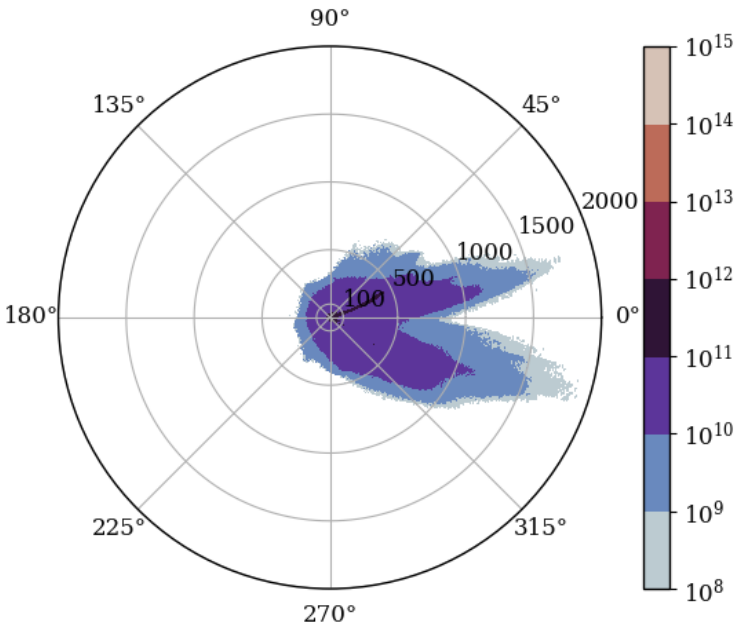

Figure C.3: The energy angle distribution of the electrons from a 2D PIC simulation. Target parameters: $n_{e0} = 10\ \mathrm{n_c}$, $L_x = 88\ \mu$m and $L_y = 30\ \mu$m. Laser parameters: $\lambda = 1\ \mu$m, $a_0 = 601$, $\tau = 20$ fs FWHM and $w_0 = 12.5\ \mu$m.

As most of the high energy electrons are emitted at the beginning of the laser-plasma interaction, in the direction of propagation of high energy electrons, the two lobe structure of the electron energy angle distribution will be observed in the later times in the energy angle distribution of the $\gamma-$photons. The emission which occurs at a later time does not influence enough the two lobe structure, which is preserved in the energy angle distribution of the $\gamma-$photons until the end of the simulation.

The two lobes of the energy angle distribution of the electrons can occur due to the presence of a strong magnetic field in the interaction zone which can reach up to 1 MT.

Appendix D

Scientific Activity

D.1 Articles

1. **I. M. Vladisavlevici**, D. Vizman, E. d'Humières, *Theoretical Study of Laser Energy Absorption Towards Energetic Proton and Electron Sources*, in Proceedings of 13th International Particle Accelerator Conference, Bangkok, Thailand, June 2022, pages 1737 - 1740, doi:10.18429/JACoW-IPAC2022-WEPOST021.

2. **I. M. Vladisavlevici**, D. Vizman, E. d'Humières, *Theoretical investigation of the interaction of ultra-high intensity laser pulses with near critical density plasmas*, - Accepted for publication in Plasma Physics and Controlled Fusion, doi:10.1088/1361-6587/acbe63.
   IF: 2.532; AIS: 0.909

3. **I. M. Vladisavlevici**, D. Vizman, E. d'Humières, *Laser driven electron acceleration from near-critical density targets towards the generation of high energy γ-photons*, Photonics, vol. 9(12):953, 2022, doi:10.3390/photonics9120953.
   IF: 2.536; AIS: 0.444

4. **I.M. Vladisavlevici**, X. Ribeyre, D. Vizman, E. d'Humières, *Investigation of γ-photon sources using near-critical density targets towards the optimization of the linear Breit-Wheeler process*, - Under Review at Frontiers in Physics.
   IF: 3.718; AIS: 0.891

D.2 International Conferences

D.2.1 Oral Presentations

1. **ECAART14** 14th European Conference on Accelerators in Applied Research and Technology, 17 - 23 July 2022, Sibiu, Romania

    - **I.M. Vladisavlevici**, D. Vizman, E. d'Humières, *Theoretical Study of Laser Energy Absorption towards Novel Bright Proton and Electron Sources*

2. **TIM20-21** Physics Conference, 11-13 November 2021, Online Conference

    - **I.M. Vladisavlevici**, E. d'Humières, D. Vizman, *Computational study of ultra-high intensity laser pulse interacting with near-critical density plasmas*

D.2.2 Poster Presentations

1. **EPS2022**, 48th European Conference on Plasma Physics, 27 June - 1 July 2022, Online Conference

    - **I.M. Vladisavlevici**, X. Ribeyre, D. Vizman, E. d'Humières, *Optimization of γ-photon sources using near-critical density targets towards electron-positron pairs generation through the linear and nonlinear Breit-Wheeler processes*

2. **IPAC22**, 13th International Particle Accelerator Conference, 12 - 17 June 2022, Bangkok, Thailand

    - **I.M. Vladisavlevici**, E. d'Humières, D. Vizman, *Theoretical Study of Laser Energy Absorption Towards Novel Bright Proton and Electron Sources*

3. **EPS2020**, 47th European Conference on Plasma Physics, 21-25 June 2021, Online Conference

    - **I.M. Vladisavlevici**, E. d'Humières, D. Vizman, *Computational study of ultra-high intensity laser pulse interacting with near-critical density plasmas*

4. **TIM19** Physics Conference, 28 - 31 May 2019, Timisoara, Romania

- **I.M. Vladisavlevici**, E. d'Humières, D. Vizman, *Optimization of high energy radiation produced in ultra high intensity laser plasma interaction*

D.3 French National Conferences

1. **GdR APPEL**, Assemblée Générale, 11 - 13 May 2022, Bordeaux, France

    - **I.M. Vladisavlevici**, E. d'Humières, D. Vizman, *Computational study of ultra-high intensity laser pulse interacting with near-critical density plasmas*

2. **SFP-Plasmas**, 16ème Congrès de la division Plasmas de la Société Française de Physique, 6 - 8 July 2022, Marseille, France

    - **I.M. Vladisavlevici**, X. Ribeyre, D. Vizman, E. d'Humières, *Optimization of γ-photon sources using near-critical density targets towards electron-positron pairs generation through the linear and nonlinear Breit-Wheeler processes*

3. **ILP forum**, Le 11ème Forum Lasers et Plasmas, 27 September - 1 October 2021, Belgodere, Corsica

    - **I.M. Vladisavlevici**, E. d'Humières, D. Vizman, *Computational study of ultra-high intensity laser pulse interacting with near-critical density plasmas*

D.4 Romanian National Conferences

1. **CSDCU-MIF2020**, Conferința Școlilor Doctorale din Consorțiul Universitaria pe domeniile Matematică, Informatică, Fizică, 22 - 24 October 2020, Online Conference

    - **Iuliana-Mariana Vladisavlevici**, Emmanuel d'Humières, Daniel Vizman, *Computational study of ultra-high intensity laser pulse interacting with near-critical density plasmas* - Oral Presentation

D.5 Seminars

1. Seminar of the scientific department of computational physics, JINR - MLIT, Dubna, Russia Thursday, 25 January 2022:

    - **Iuliana-Mariana Vladisavlevici**, Emmanuel d'Humières, Daniel Vizman, *Optimization of laser energy absorption in near-critical density plasmas*

D.6 Summer Schools

1. ELI-NP, *Nuclear physics with high power lasers*, 09-13 September 2019, Sinaia, Romania
2. University of Bordeaux, *Short-pulse lasers and applications*, 25 - 28 June 2019, Bordeaux, France
3. Max Planck Institute for Plasma Physics, *International Summer University for Plasma Physics and Fusion Research*, 17-21 September, 2018, Greifswald, Germany

D.7 Workshops

1. École Polytechnique, *The 3rd SMILEI user & training workshop*, 9 – 11 March 2022, Palaiseau, France

    - **Iuliana-Mariana Vladisavlevici**, Emmanuel d'Humières, Daniel Vizman, *Theoretical study of laser energy absorption in near-critical density plasmas at ultra-high intensity* - Oral Presentation

2. JRA, *Joint Research Activity Meeting - Laserlab Europe*, 9-10 October 2019, Florence, Italy
3. Maison de la Simulation, *The 2nd SMILEI Training Workshop*, 7 – 8 March 2019, Saclay, France

D.8 International collaborations

1. **Short term trip at LIT - JINR** (Laboratory of Information Technologies - Joint Institute for Nuclear Research), 24 November - 14 December 2019, Dubna, Russia

2. **Long term trip at LIT - JINR** (Laboratory of Information Technologies - Joint Institute for Nuclear Research), 3 October 2021 - 3 February 2022, Dubna, Russia

Appendix E

Résumé détaillé

E.1 Introduction

Un laser est un appareil optique qui permet l'amplification de la lumière par émission stimulée de rayonnement (LASER). Une propriété importante du rayonnement émis est sa cohérence, c'est-à-dire que tous les photons émis ont la même fréquence et la même phase ce qui permet son amplification. Le premier laser au monde a été fabriqué par Mainman en 1960 [1]. La configuration consistait en une lampe flash haute puissance qui irradiait un cristal de rubis de 1 cm recouvert sur deux faces parallèles d'argent irradié par une lampe flash haute puissance. Les ions chrome étaient excités par l'énergie de la lampe flash et par désexcitation ils émettent spontanément un doublet aux longueurs d'onde 6929Å et 6943Å. En augmentant la puissance de la lampe, l'émission à 6943Å augmentait considérablement.

Les lasers construits en 1960 avaient une durée d'impulsion de 10 μs et une puissance de l'ordre du kW [2]. Les progrès sur l'augmentation de la puissance sont venus avec la réduction de la durée des impulsions en changeant les modes de la cavité laser. De 1960 à 1964, les lasers ont atteint l'échelle de la picoseconde, correspondant à une puissance dans la gamme GW. Malgré une diminution supplémentaire de la durée de l'impulsion laser, l'intensité de puissance maximale du laser obtenue était d'environ 10^{15} W/cm^2 en raison des effets non linéaires qui endommageaient les optiques. Le changement est survenu en 1985, lorsque Donna Strickland et Gérard Mourou ont proposé une nouvelle méthode pour créer des impulsions laser plus courtes,

plus énergétiques et, par conséquent, plus intenses [3]. Ils ont utilisé une impulsion laser Nd YAG courte et basse énergie à modulation linéaire d'une durée d'impulsion de 300 ps. Dans une première étape du processus, l'impulsion est étirée par un premier ensemble de réseaux pour obtenir une impulsion laser plus longue avec un pic de puissance plus petit. Dans la deuxième étape, l'impulsion étirée est amplifiée et en outre, dans une troisième étape, elle est comprimée par un deuxième ensemble de réseaux. Les auteurs ont obtenu une impulsion laser de 2 ps avec une énergie de quelques mJ. Ce processus est appelé Amplification par dérive de fréquence et est aujourd'hui utilisé dans les laboratoires du monde entier pour créer les impulsions laser les plus courtes et les plus intenses. Les auteurs ont reçu le prix Nobel de physique en 2018 [4].

De nos jours, les lasers les plus puissants au monde sont les lasers Ti :Sapphire [5]. Le laser le plus intense est le laser CoReLS - PW qui a atteint en 2021 une intensité maximale de $\approx 10^{23}$ W/cm^2 et une courte durée d'impulsion de ≈ 19 fs FWHM correspondant à une puissance de $2,7$ PW [6]. Plusieurs lasers dans le monde au niveau PW ont atteint une intensité de 10^{22} W/cm^2 et de nouveaux projets visent une puissance plus élevée comme le système Apollon (puissance de 10 PW ; intensité $\approx 2 \cdot 10^{22}$ W/cm^2, durée d'impulsion 15 fs FWHM) [7] et ELI-NP (puissance de $2 \cdot 10$ PW ; intensité de $10^{22} - 10^{23}$ W/cm^2, durée d'impulsion $15 - 22,5$ fs FWHM) [8] et SEL (puissance de 100 PW ; intensité maximale 10^{24} W/cm^2) [9].

Lors de l'interaction d'un laser de haute intensité avec une cible (solide, liquide ou gazeuse), un plasma composé d'électrons et d'ions est créé. Le plasma est par définition le quatrième état de la matière dans lequel les électrons et les ions se déplacent librement. Plus de 99% de l'univers visible sont constitués de plasmas, de l'éclairage terrestre à l'ionosphère terrestre jusqu'aux étoiles, aux galaxies ou à l'espace intergalactique [12]. En laboratoire, un plasma peut être créé en augmentant la température d'un objet jusqu'à son ionisation. A l'intérieur d'une étoile, la température et la densité sont si élevées que les ions commencent à fusionner en formant des éléments plus lourds et en libérant de l'énergie. Si l'on pouvait contrôler le processus de fusion nucléaire sur Terre, les problèmes énergétiques du 21er siècle seraient résolus. Des plasmas très chauds sont créés de nos jours en laboratoire avec les tokamaks ou avec les lasers. Cependant, d'autres études expérimentales et théoriques sont nécessaires pour atteindre le processus de fusion nucléaire auto-entretenu et obtenir des gains en énergie.

Comme mentionné précédemment, lorsqu'un laser irradie une cible, un plasma est créé par chauffage et ionisation de la cible. En outre, les constituants du plasma sont accélérés,

l'accélération dépendant des caractéristiques initiales du laser et de la cible. Pour des intensités $> 10^{18}$ W/cm^2, le mouvement des électrons est relativiste. Par exemple, pour une intensité laser de 10^{19} W/cm^2 et une longueur d'onde de 1 μm, l'énergie moyenne des électrons est d'environ 1 MeV. L'augmentation de l'intensité laser s'accompagne d'un changement du régime d'interaction, ouvrant de nouveaux régimes d'interaction laser-plasma où les effets relativistes sont importants et peuvent dominer le mouvement des particules [2].

Les simulations numériques sont un outil puissant pour étudier des systèmes réels et obtenir des informations détaillées sur les phénomènes physiques. Peu de temps après la première expérience numérique d'un système physique en 1955 [13], la première simulation numérique d'un plasma fut publiée par Dawson en 1962 [14]. La configuration de simulation unidimensionnelle consistait en 1000 feuilles représentant des particules chargées se déplaçant dans une direction. L'objectif était d'étudier des phénomènes physiques comme la relaxation thermique du système, l'écrantage de Debye et l'amortissement de Landau. Les résultats de calcul obtenus ont montré un bon accord avec la théorie avec des erreurs relativement faibles.

Depuis lors, la configuration informatique a évolué ainsi que les codes plasma. L'ordinateur utilisé en 1955 était MANIAC I (Mathematical Analyzer Numerical Integrator and Automatic Computer Model I) qui avait une puissance de traitement de 2048 instructions par seconde [15]. De nos jours, la machine informatique la plus puissante est le système Frontier du Laboratoire National d'Oak Ridge, aux États-Unis, qui est composé de plus de 8,7 millions de cœurs et d'une vitesse de calcul de 1,102 Exaflops correspondant à plus de 10^{18} instructions par seconde [16]. C'est le premier ordinateur à dépasser la barrière exascale [17]. Les simulations numériques pour la physique des plasmas nécessitent des codes de calcul complexes et performants pour avoir une description complète de milliards de particules et de leurs interactions. Les simulations numériques du plasma peuvent être soit cinétiques, en résolvant le système d'équations de Maxwell-Vlasov, soit fluides, en résolvant les équations fluides d'un plasma, selon l'échelle temporelle des processus que l'on veut étudier. Comme nous nous intéressons à l'échelle de temps très courte de l'interaction laser-plasma, de l'ordre de centaines de fs jusqu'à une ps, nous considérerons plus loin l'approche cinétique.

E.2 Objectifs de la thèse

L'accélération de particules avec une impulsion laser est une alternative aux accélérateurs radio-fréquence conventionnels. Les énormes gradients d'accélération dans un accélérateur à base de laser sont de l'ordre de $\mathrm{MeV}/\mu\mathrm{m}$, comparés à ceux d'un accélérateur radiofréquence de l'ordre de $100\ \mathrm{MeV}/\mathrm{m}$. Par conséquent, les particules peuvent être accélérées à des énergies très élevées sur des distances inférieures au millimètre, de plusieurs ordres de grandeur plus courtes que requis dans les accélérateurs conventionnels. Cela offre l'opportunité d'étudier de nouvelles applications des faisceaux accélérés. Cependant, des problèmes tels que l'efficacité de conversion de l'énergie laser aux particules, la distribution spectrale et angulaire des faisceaux de particules ainsi que leur énergie restent à résoudre [18].

L'objectif principal de cette thèse est d'étudier théoriquement et numériquement l'interaction des impulsions laser haute puissance de nouvelle génération avec des cibles de densité quasi-critique. On peut identifier trois sujets interconnectés :

1. *Le transfert d'énergie du laser aux constituants du plasma.* Notre objectif principal est de décrire et de modéliser le transfert d'énergie du laser aux particules, du régime transparent au régime moins transparent de l'interaction laser-plasma dans le régime des ultra-haute intensités laser.

2. *Accélération des protons par laser.* Notre objectif principal est de prédire l'épaisseur optimale pour l'accélération des protons et les énergies maximales des protons en fonction de l'absorption de l'énergie laser.

3. *Émission de rayonnement de haute énergie et création de paires.* Notre objectif principal est d'étudier le rayonnement de haute énergie émis par les électrons dans l'interaction laser-plasma, conduisant éventuellement à la production de paires électron-positron via le processus linéaire et non linéaire Breit-Wheeler.

E.3 Résultats de la thèse

1. *Le transfert d'énergie du laser aux constituants du plasma.*

   Nous avons étudié à l'aide de simulations Particle-In-Cell (PIC) 2D réalisées avec le code SMILEI l'absorption maximale de l'énergie laser dans le cas de cibles de densité quasi critique avec des densités surfaciques comprises entre $5-800$ $n_{e0}L_x$. La densité surfacique optimale se situe dans l'intervalle $70-120$ $n_{e0}L_x$, correspondant à un coefficient d'absorption maximum de $67-95\%$. En minimisant le coefficient de transmission à saturation, nous avons trouvé un modèle semi-empirique pour le coefficient d'absorption, dépendant de la densité de la cible, de l'intensité du laser et de la durée de l'impulsion. Pour une même densité surfacique, nous avons estimé l'énergie moyenne des électrons chauds avec la température pondéromotrice, corrigée d'un facteur qui dépend de la densité cible. Enfin, nous avons formulé un modèle pour maximiser l'absorption d'énergie laser dans le cas de cibles de densité quasi critique.

   Le modèle théorique proposé montre un bon accord avec les résultats de simulation obtenus pour un large ensemble de paramètres : durée d'impulsion laser $\tau : 2-30$ t_0 (pour $a_0 = 85$) où t_0 est la période laser, amplitude de champ laser normalisée $a_0 : 26,88-268,8$ (pour $\tau = 6$ t_0) et densité cible $n_{e0} : 0,5-24$ n_c où n_c est la densité critique. Le modèle proposé par Eq.(3.21) est utile pour guider l'absorption maximale dans le plasma, pour les études impliquant la génération d'électrons chauds et la génération de rayonnement de haute énergie [129, 93, 130, 131, 77, 132, 87].

2. *Accélération des protons par laser.*

   Nous avons étudié l'énergie maximale des protons dans le cas de cibles de densité quasi critique avec une densité surfacique comprise entre $5-800$ $n_{e0}L_x$. La densité surfacique optimale pour l'accélération des protons se situe dans l'intervalle $30-50$ $n_{e0}L_x$ et l'énergie maximale des protons dans l'intervalle $600-800$ MeV. L'épaisseur optimale de la cible et l'énergie maximale du proton sont toutes deux en bon accord avec les prédictions théoriques d'un mécanisme d'accélération du proton semblable à celui de l'expansion d'un plasma. Cependant, pour une densité cible de la cible de $0,5$ n_c, l'énergie maximale des protons est légèrement supérieure, à $1,2$ GeV. Dans ce cas, la cible est complètement transparente à l'impulsion laser et celle-ci, en se propageant à l'intérieur de la cible, chauffe fortement les électrons. Les électrons accélérés les plus énergétiques ayant une

charge de quelques nC peuvent influencer les énergies des protons dans ce cas. Dans tous les cas optimaux considérés, les protons les plus énergétiques proviennent de l'arrière de la cible.

3. *Émission de rayonnement de haute énergie et création de paires.*

   Nous avons étudié le rayonnement de haute énergie produit dans deux configurations : l'interaction laser-faisceau d'électrons et l'interaction laser-plasma. En faisant varier l'intensité de l'impulsion laser dans la gamme $\{10^{19} - 10^{23}\}$ W/cm^2, nous avons étudié la production de photons gamma pour différentes énergies initiales du faisceau d'électrons ($\{0,5; 1; 1,5\}$ GeV) prolongeant les résultats obtenus par M. Vranic et al. [128]. Pour l'intensité laser la plus élevée considérée, les électrons perdent la quasi-totalité de leur énergie pour émettre des photons γ. De plus, nous avons comparé différents modèles mis en œuvre dans le code Particle-In-Cell SMILEI pour l'émission de rayonnement et son effet sur la dynamique des électrons. Nous avons constaté que pour l'intensité laser la plus élevée considérée, les modèles continus de Landau-Lifshitz ne peuvent plus être utilisés, un modèle stochastique doit être utilisé à la place. Dans la deuxième configuration, nous avons considéré une impulsion laser d'intensité 10^{22} W/cm^2 et une durée d'impulsion de 20 fs FWHM irradiant une cible de densité quasi-critique avec une densité de $0,5 - 20$ n$_c$ et une épaisseur de $0,5 - 190$ μm. Le coefficient d'absorption maximal obtenu dans les simulations PIC 2D était 4%, ce qui correspond à l'épaisseur optimale pour maximiser l'absorption de l'énergie laser dans tous les constituants du plasma prédite par Eq.3.21 à une exception près. Cependant, à l'épaisseur optimale prédite par notre modèle, l'absorption de l'énergie laser dans les photons γ était prédominante vers l'avant.

   De plus, nous avons considéré la configuration optimale du transfert d'énergie laser vers les photons γ et nous avons analysé l'interaction de deux faisceaux de photons γ identiques précédemment produits à une distance donnée de la zone d'interaction laser-plasma. Notre objectif était d'optimiser la production de paires électron-positron par le procédé linéaire de Breit-Wheeler. Les paires électron-positon sont également produites dans la zone d'interaction par deux autres processus : Breit-Wheeler non linéaire et Bethe-Heitler. Pour $a_0 = 85$, le plus grand nombre de paires de Breit-Wheeler linéaires était de 750 obtenu pour une densité de cible de 10 n$_c$ et une épaisseur de 12 μm, ce qui correspond à l'épaisseur optimale pour maximiser l'absorption laser dans les photons γ. Le nombre de paires de Bethe-Heitler était jusqu'à 2 ordres de grandeur plus élevé, mais elles sont

produites principalement dans la direction de propagation des faisceaux de photons γ. La direction de propagation des paires de Breit-Wheeler peut être contrôlée par l'angle θ entre les deux faisceaux de photons γ.

Enfin, nous avons étendu notre analyse à des intensités laser plus élevées : de 10^{22} W/cm^2 à $5 \cdot 10^{23}$ W/cm^2 en considérant une cible de densité 10 n_c à l'épaisseur optimale pour maximiser l'absorption d'énergie laser. Le coefficient d'absorption le plus élevé de l'énergie laser aux photons γ était de 33% pour la plus haute intensité laser considérée. Suivant le montage mentionné précédemment, nous avons étudié la production de paires électron-positron. Le nombre maximum de paires de Breit-Wheeler linéaires était de $2 \cdot 10^6$ obtenu pour une intensité laser de $5 \cdot 10^{23}$ W/cm^2. Cependant, à cette intensité, le processus Breit-Wheeler non linéaire est dominant et produit jusqu'à 5 ordres de grandeur plus de paires électron-positron. Le cas optimal pour détecter les paires Breit-Wheeler linéaires correspondait à une intensité laser de 10^{23} W/cm^2.

E.4 Conclusions

Ce travail traite de l'interaction entre une impulsion laser ultra-courte à ultra-haute intensité avec des cibles de densité quasi-critique.

Les deux premiers chapitres sont consacrés à une introduction dans le domaine de l'interaction laser-plasma et à son étude par des simulations numériques. Dans le chapitre 1 nous avons décrit théoriquement l'interaction laser-plasma ainsi que les mécanismes les plus pertinents d'absorption d'énergie laser et d'accélération des particules pour notre régime d'intérêt. Dans le chapitre 2 nous avons introduit la description numérique d'un plasma, à savoir la méthode Particle-in-cell et le code PIC utilisé pour ce travail. Toutes les descriptions théoriques et numériques sont inspirées de la littérature mentionnée. Dans cette partie introductive de la thèse, les contributions personnelles se limitent à l'étude de la variation des grandeurs physiques avec la variation des paramètres numériques et l'estimation de l'énergie totale consommée de nos simulations.

Dans la première étude numérique, nous avons étudié l'influence du nombre total de particules par cellule et de la longueur de la cellule sur le coefficient d'absorption d'énergie totale et sur le coefficient d'absorption de l'énergie laser dans les photons γ. Dans le premier cas, nous avons considéré 30 particules par cellule alors que la longueur des cellules variait entre $15,625$ nm et $468,75$ nm. Nous avons observé une forte dépendance du coefficient d'absorption de l'énergie laser dans les photons gamma avec la longueur de cellule : alors que le coefficient d'absorption d'énergie laser convergeait vers une valeur stable pour une longueur de cellule inférieure à 300 nm, le coefficient d'absorption de l'énergie laser dans les photons gamma ne converge que pour une longueur de cellule inférieure à 200 nm. Dans la deuxième étude, nous avons fixé la longueur de la cellule à 15,625 nm tandis que nous avons fait varier le nombre total de particules par cellule entre 1 et 64. Les quantités physiques n'ont pas changé de manière significative avec le nombre total de particules par cellule, ce qui peut également être dû à la très petite longueur de cellule utilisée.

A l'aide du logiciel Energy Scope nous avons étudié la variation de l'énergie consommée et de l'émission de CO_2 d'une simulation PIC 2D avec le temps de calcul. En utilisant le temps de calcul total pour la durée complète du doctorat, nous avons estimé une quantité totale d'énergie consommée de $22,52$ MWh et une émission totale de 1,15 tonnes de CO_2 (calculées

pour la France). Nous voulons également souligner l'importance des supercalculateurs en physique. Le temps de calcul total utilisé pour cette thèse est d'environ 2,6 millions d'heures CPU. La même quantité de calculs sur une station de travail à 12 cœurs aurait duré environ 25 ans, ce qui est totalement déraisonnable.

Les trois chapitres suivants se concentrent sur les résultats originaux obtenus au cours de la thèse.

Dans le chapitre 3 nous proposons un nouveau modèle théorique pour l'optimisation de l'absorption d'énergie laser dans le régime de densité quasi-critique à ultra-haute intensité. L'objectif principal est de trouver l'épaisseur de cible optimale pour une densité donnée afin de maximiser l'absorption de l'énergie laser. Deux paramètres principaux influencent notre modèle : le point de saturation du coefficient d'absorption et l'énergie moyenne des électrons chauds. Nous avons modélisé ces deux paramètres en effectuant plusieurs simulations PIC 2D avec SMILEI. Nous avons considéré la variation des paramètres suivants : l'intensité du laser dans la gamme $10^{20} - 10^{23}$ W/cm^2 (pour la durée de l'impulsion de 20 fs), la durée de l'impulsion dans la gamme $6,5 - 100$ fs (pour l'intensité du pic laser de 10^{22} W/cm^2), la densité cible dans la gamme $0,5 - 24$ n$_c$ et l'épaisseur cible dans la gamme $0,5 - 200$ μm. Nous avons trouvé un modèle semi-empirique pour le coefficient d'absorption, basé sur la densité de la cible et l'intensité du laser et la durée d'impulsion ainsi que pour l'énergie moyenne des électrons chauds, basé sur la température pondéromotrice et nos observations des simulations PIC 2D. De plus, nous avons constaté que la majeure partie de l'énergie laser sera absorbée par les électrons avec des énergies > 5 MeV à l'exception de l'intensité laser de 10^{20} W/cm^2 où seulement entre 6% et 28% de l'énergie laser sont transférés à ces électrons. Enfin, notre modèle d'épaisseur de cible optimale pour maximiser l'absorption de l'énergie laser montre un bon accord pour une large gamme de paramètres de l'impulsion laser et de la cible. De plus, nous avons discuté de l'applicabilité de notre modèle pour la génération d'électrons chauds et la génération de rayonnement à haute énergie.

Dans le chapitre 4 nous avons utilisé le modèle théorique proposé dans le chapitre précédent pour optimiser l'accélération de protons pour une impulsion laser d'intensité 10^{22} W/cm^2. Nous avons étudié le chauffage des électrons et la création d'un champ de séparation de charge quasi-électrostatique à l'arrière de la cible et sa dépendance à la densité de la cible. Le champ de séparation de charge quasi-électrostatique est compris entre 30 et 40 TV/m dans tous les cas

considérés et est responsable de l'accélération des protons. Nous avons également étudié les énergies maximales des électrons qui peuvent atteindre $1,5$ GeV ce qui explique la forte émission de rayonnement de haute énergie qui sera discutée plus en détail dans le chapitre suivant. Nous avons observé deux mécanismes d'accélération des protons dans les simulations effectuées : l'accélération dans la gaine normale à la cible qui est due au chauffage des électrons et au champ de séparation de charge quasi-électrostatique à l'arrière de la cible et l'accélération par la pression de radiation qui est due à la pression du laser à l'avant de la cible. L'accélération par le champ de séparation de charge à l'arrière de la cible était le principal mécanisme d'accélération, tandis que l'accélération par la pression de radiation n'a été observée que pour les densités de cibles plus élevées. La densité surfacique de la cible optimale pour maximiser l'accélération des protons a été obtenue pour une densité surfacique de $30-50\ n_{e0}L_x$ et l'énergie maximale des protons s'est avérée être de 600 MeV $-\ 1,2$ GeV. L'épaisseur optimale de la cible et l'énergie maximale des protons se sont avérées en bon accord avec les modèles théoriques précédents validés pour des intensités laser inférieures. Pour la densité de cible la plus faible considérée, nous avons observé des énergies de protons inférieures à la prédiction théorique qui peuvent se produire en raison de l'influence des électrons relativistes dans le processus d'accélération.

Enfin, dans le chapitre 5 nous avons étudié l'émission de rayonnement de haute énergie avec des applications potentielles pour la génération de paires électron-positron. Premièrement, nous avons considéré le rayonnement émis par un faisceau d'électrons relativistes avec des énergies de $0,5-1,5$ GeV entrant en collision avec une impulsion laser d'intensité $10^{19}-10^{23}$ W/cm^2. Nous avons constaté que pour des intensités laser $> 10^{22}$ W/cm^2, les électrons peuvent perdre toute leur énergie en émettant des photons γ. Les résultats de la simulation PIC 2D étaient en bon accord avec le modèle théorique. De plus, nous avons testé différents modèles implémentés dans SMILEI pour la réaction de rayonnement discutée dans le chapitre 2 et nous avons constaté que pour l'intensité laser la plus élevée considérée, l'émission de rayonnement doit être traitée comme un événement stochastique. De plus, nous avons étudié le rayonnement émis par les électrons dans l'interaction laser-plasma pour une impulsion laser d'intensité 10^{22} W/cm^2. Le coefficient d'absorption de l'impulsion laser vers les photons s'est avéré avoir un maximum de 4%, et il est obtenu pour la même épaisseur cible que celle pour maximiser le coefficient d'absorption total de l'énergie laser vers le plasma, à une exception près pour le cas de la densité la plus faible considérée. De plus, nous avons utilisé

les caractéristiques du faisceau de photons γ dans la configuration optimale pour la création de paires électron-positron. Nous avons considéré une configuration expérimentale conçue pour l'optimisation du processus de Breit-Wheeler linéaire, consistant en 2 faisceaux de photons γ entrant en collision sous un angle donné θ. Le nombre maximum de paires était de 750 pour $\theta = 180°$. De plus, le processus Bethe-Heitler était responsable de la création de $3 \cdot 10^4$ paires électron-positron dans la direction de propagation des faisceaux de photons γ. Cependant, la direction de propagation des paires produites par le processus Breit-Wheeler linéaire peut être contrôlée par l'angle θ, la collimation la plus élevée étant observée pour l'angle le plus bas considéré $\theta = 45°$. Nous avons étendu notre étude pour des intensités laser plus élevées, jusqu'à $5 \cdot 10^{23}$ W/cm^2, interagissant avec une densité cible de 10 n_c et une épaisseur cible telle que prédite par notre modèle du chapitre 3. Nous avons obtenu un maximum de 33% pour le coefficient d'absorption de l'énergie laser dans les photons pour la plus haute intensité laser considérée. Le cas optimal pour maximiser la détection des paires produites par le processus Breit-Wheeler linéaire s'est avéré être pour une intensité laser de 10^{23} W/cm^2. Dans ce cas, nous avons obtenu un nombre total de paires produites par le processus Breit-Wheeler linéaire de $1,2 \cdot 10^5$ pour $\theta = 45°$. Pour des intensités laser plus élevées, nous avons observé que le processus Breit-Wheeler non linéaire se produit et produit un nombre de paires jusqu'à 5 ordres de grandeur plus élevé.

Les résultats de cette thèse ont été présentés lors de conférences nationales et internationales comme mentionné dans le annexe D.